AGGREGATION BEHAVIOR OF NANOMATERIALS IN WATER: ROLES OF MATERIAL INTRINSIC PROPERTY AND ENGINEERED DNA SURFACE COATING

BO PENG

PhD

The Hong Kong Polytechnic University

2023

The Hong Kong Polytechnic University

Department of Civil and Environmental Engineering

Aggregation Behavior of Nanomaterials in Water: Roles of Material Intrinsic Property and Engineered DNA Surface Coating

Bo PENG

A thesis submitted in partial fulfilment of the requirements for the degree of Doctor of Philosophy

January 2023

CERTIFICATE OF ORIGINALITY

I hereby declare that this thesis is my own work and that, to the best of my knowledge and belief, it reproduces no material previously published or written, nor material that has been accepted for the award of any other degree or diploma, except where due acknowledgement has been made in the text.

__________________________ (Signed)

_____Bo Peng_____________ (Name of Student)

Abstract

Engineered nanomaterials (ENMs) are manufactured materials with at least one nanoscale dimension (*ca.* 1−100 nm). Their high surface area-to-volume ratio often leads to high surface energy and colloidal instability (i.e., aggregation) compared to their bulk counterparts. Aggregation of ENMs affects not only their functionality, but also their toxicity, bioavailability, fate and transport in the environment. Understanding the aggregation behavior of ENMs in water remains challenging because of their complex physicochemical properties and dynamic transformations in aquatic environments. Discrepancies on the effect of certain physicochemical properties (e.g., size, zeta potential, surface functionality) of ENMs on their aggregation behavior are often observed among studies, and there is also a critical knowledge gap in understanding the role of (transformed) engineered single-stranded DNA (ssDNA) coating in the aggregation of coated nanomaterials, despite their rapidly emerging applications (e.g., sensors, hydraulic tracers).

Therefore, this thesis aims to (1) resolve the seemingly contradictory effects of specific physicochemical properties on nanomaterial aggregation and examine the corresponding predictions by the Derjaguin-Landau-Verwey-Overbeek (DLVO) theory, based on a meta-analysis of previous individual studies; and (2) understand the transformation(s) of the engineered ssDNA coating in typical aquatic environments at a molecular-level and reveal the subsequent impact on the aggregation behavior of coated nanomaterials.

Through a meta-analytic approach, this thesis reveals that, for graphene oxide and carbon nanotube, a threshold hydrodynamic size of *ca.* 200 nm exists, below which their critical coagulation concentration (CCC) increases with decreasing material size. This finding is consistent with the early prediction of the DLVO theory, but the observed threshold size is smaller (i.e., 200 nm vs. 2 μm). Beyond the threshold size, the effect of size is minimum on CCC, and material zeta potential can be mathematically correlated to CCC as predicted by the

DLVO theory. However, this correlation is only observed for nanomaterials with moderate/low surface charge but not high surface charge, which is likely due to the underestimation of surface charge by zeta potential for the highly charged nanomaterials. A positive correlation between CCC and material surface oxidation degree is also observed.

Through experimental work combined with molecular dynamics simulations, this thesis reveals that transformations of the engineered ssDNA coating significantly affect the aggregation of coated nanomaterials. The ssDNA coating shows distinct features compared to conventional polymer coatings when interacting with surrounding counterions and natural organic matter (NOM). The strong interaction of cations with guanine bases affects the ion distribution along the DNA strand and the guanine-rich DNA strand leads to a thicker DNA coating on the coated nanomaterials, thereby substantially mitigating their aggregation. Furthermore, the ssDNA coating preferentially interacts with NOM of high aromaticity via strong π-π interaction. Divalent cations facilitate a complete shielding of the ssDNA coating by highly aromatic NOM (i.e., Aldrich humic acid), whereas NOM with low aromaticity (e.g., Suwannee River humic acid) only partially shields the ssDNA coating. The extent of ssDNA shielding by NOM has a major impact not only on the aggregation behavior of coated nanomaterials, but also on the performance of engineered DNA-based applications.

Altogether, this thesis resolves the inconsistency among previous observations of certain physicochemical properties on ENM aggregation and provides new knowledge regarding the unconventional ssDNA coating, thereby considerably improving our understanding of the aggregation behavior of ENMs in water. Knowledge obtained from this thesis will facilitate the rational design of ENMs and engineered DNA for their sustainable applications.

Acknowledgement

I sincerely thank my chief supervisor, Dr. Yi Jiang, for his continued guidance and support throughout my entire PhD study. His passion for research and curiosity about fundamental scientific issues have shaped my education and research and inspired me to go further. I would also like to express my gratitude to my co-supervisor, Prof. Xiang-dong Li, for his guidance in refining this thesis. My deep gratitude also goes to my examination committee, Prof. Ben Shao-Yuan Leu, Prof. Yandi Hu, and Prof. Danmeng Shuai, for their time and efforts in reviewing this thesis. All the discussions, comments, and suggestions from the committee were invaluable in improving this thesis.

I appreciate the opportunity to work with many colleagues. I thank Dr. Zhu Liu, Dr. Peng Liao, and Zhiying Deng for their contributions to this work. My thanks also go to other members of Dr. Jiang’s research group, including Dr. Delai Zhong, Dr. Zhenyu Zhao, Dr. Yangtao Wu, Zhishang Wan, Lihong Gan, Yuchen Wu, Beizhao Chen, Yanni Weng, and Jin Zhang. I would also like to thank the technicians, W.S. Lam, Y.H. Jonathan Chan, and Celine Che, in the Water Lab for their assistance with my laboratory work.

Finally, I must give my appreciation to my beloved wife, Fan Yang, and parents, Guifa Peng and Qiaoling Tang. Thank you for all the unconditional love and support.

This PhD journey was not easy, and we made it together.

Table of Content

List of Figures

List of Tables

Chapter 1 Introduction

1.1 Background

Nanotechnology provides revolutionary solutions in various scientific fields, such as chemistry, biology, physics, and materials science. The global nanotechnology market size was estimated at 1.76 billion US dollars in 2020 and is projected to reach $33.63 billion by 2030 (Divyanshi, 2021). Such advancement of nanotechnology has been accompanied by the development and manufacturing of a wide spectrum of engineered nanomaterials (ENMs). ENMs are manufactured materials with at least one nanoscale dimension (*ca.* 1−100 nm), and they are of particular interest compared to their bulk counterparts because of their novel properties, such as increased reactivity and surface energy. However, the high surface energy of ENMs also leads to their colloidal instability (i.e., aggregation).

Aggregation of ENMs refers to the formation of clusters by primary particles of the same (i.e., homoaggregation) or different nature (i.e., heteroaggregation), and this process alters their physicochemical properties (e.g., reduced accessible surface area and increased aggregate size up to micrometer scale), in turn affecting their functionality in applications (Hotze et al., 2010; Zhang, 2014). For example, in polymer nanocomposites, aggregation of nanoparticles weakens their interactions with the polymer matrix, leading to poor tensile strength of the composite (Ashraf et al., 2018); the aggregation behavior of polymeric nanoparticles affects their cellular uptake and intracellular transport, posing a significant impact on the drug delivery efficiency to living cells and ultimately the therapeutic efficacy (Zhang et al., 2020); furthermore, attaching drug (Paclitaxel) to nanoparticle surface via DNA linkers increases the stability and solubility of the drug, leading to enhanced drug effectiveness (Zhang et al., 2011). Besides the impacts on material functionality, aggregation of ENMs also changes their behavior in the environment (Lowry et al., 2012; Petosa et al., 2010). For instance, aggregation of Fe(0) nanoparticles forms micrometer-sized aggregates, accelerating their deposition in the subsurface and sedimentation in surface water (Phenrat et al., 2007; Saleh et al., 2008); the dissolution rate of dispersed 14 nm PbS nanoparticles is one order of magnitude faster than the aggregated particles (4.4×10^{-9} mol m^{-2} s^{-1} vs. 4.7×10^{-10} mol m^{-2} s^{-1}) (Liu et al., 2009); aggregation of nanoparticles alters their sizes, in turn affecting their exposure pathway and mode of cellular uptake in the organisms, with larger particles accumulating in the alveolar region and smaller particles in the upper respiratory tract (Oberdörster et al., 2007). Therefore, understanding the factors controlling the aggregation behavior of ENMs has been a hot research topic.

According to the Web of Science, the number of annual publications on nanomaterial aggregation increased from fewer than 10 in 2005 to 96 in 2021 (Figure 1.1). Various types of ENMs have been investigated, including but not limited to fullerene (Chen and Elimelech, 2006), carbon nanotube (Smith et al., 2009), graphene (oxide) (Chowdhury et al., 2013), metal-related (e.g., gold (Pamies et al., 2014), silver (Gunsolus et al., 2015), iron (Phenrat et al., 2008), titanium carbide (Xie et al., 2020), molybdenum disulfide (Mohona et al., 2019)), and more recently nanoplastics (Wang et al., 2021). Although significant progress has been achieved, challenges remain in understanding the aggregation process due to the complex physicochemical properties of ENMs and their dynamic transformations in aquatic environments. More efforts are needed to gain a comprehensive and in-depth understanding of the aggregation behavior of ENMs.

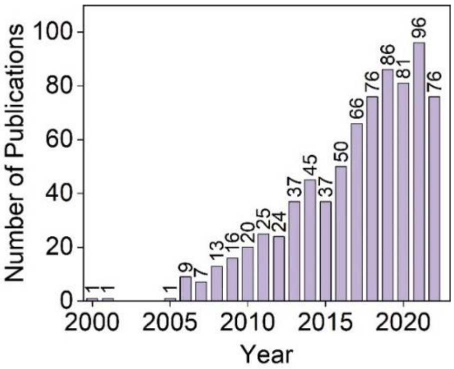

Figure 1.1 Number of publications on nanomaterial aggregation indexed by the Web of Science as of November 17, 2022.

1.2 Challenges in Understanding the Aggregation Behavior of ENMs

The physicochemical properties of ENMs (size, shape, surface chemistry, surface coating, etc.) may diversify by orders of magnitude and pose significant impacts on the aggregation of ENMs. However, whether there is a consistent relationship between a specific material property and the aggregation of nanomaterials remains unclear. For instance, the colloidal stability of nanomaterials was reported to have increased (Mulvihill et al., 2010) or decreased (He et al., 2008) with reducing nanomaterial size, or even to be independent of material size (Liu et al., 2012). A positive correlation ($R^2 = 0.94-0.99$) between the zeta potential (which is usually used to represent surface charge) and nanomaterial stability was reported by Jiang et al. (2016), while Qi et al. (2016) observed a two-fold difference in the colloidal stability of nanomaterials with similar zeta potential. These study-to-study variations suggest that research synthesis efforts are needed to identify whether there is a consistent relationship between a specific material property and the aggregation behavior of nanomaterials. However, such work has been rarely performed. Additionally, analytical expressions have been derived from the classic Derjaguin-Landau-Verwey-Overbeek (DLVO) theory of colloid science, which describe the relationships between the aggregation of nanomaterials and their properties, such as material size and zeta potential (Hsu and Kuo, 1997; Hsu and Liu, 1998; Trefalt et al., 2017). A few studies found these early predictions to be consistent with experimental observations (Jiang et al., 2016; Omija et al., 2021), while others suggested that these early models need to be improved considering the unique properties of nanomaterials (e.g., the two-dimensional nature of nanosheets (Gudarzi, 2016)). The predictions of the DLVO theory were often made under certain assumptions, e.g., the Derjaguin approximation and the Debye−Hückel approximation. The properties of nanomaterials (such as small size and non-spherical shape) may not satisfy those assumptions and challenge the applicability of relevant analytical expressions. Therefore, the early predictions of the DLVO theory need to be revisited based on a larger set of experimental data.

Furthermore, engineered surface coatings have been an important research topic in studying ENM aggregation because they are commonly applied to achieve specific functionality and/or reduce nanomaterial aggregation (Gambinossi et al., 2015). Previous studies mainly focused on conventional polymer coatings, which are organic macromolecules consisting of repeating monomer units. The effect(s) of conventional polymer coating on the aggregation behavior of coated nanomaterial have been correlated with the properties of the polymer coating, such as molecular weight (Moore et al., 2003; Phenrat et al., 2008), coating layer thickness (Dederichs et al., 2009; Stenkamp and Berg, 1997), surface coverage (Afshinnia et al., 2017; Gebauer et al., 2012), and coating layer conformation (Krueger et al., 2007), among others. Engineered DNA emerges as an important type of surface coating since the 1990s (Alivisatos et al., 1996; Mirkin et al., 1996), and the applications of such composite nanomaterials range across diverse scientific and technological fields, such as materials synthesis (Macfarlane et al., 2011), diagnostics (Taton et al., 2000), and therapeutics (Rosi et al., 2006), and so forth. While engineered DNA is also a long-chain polyelectrolyte (i.e., charged polymer), it differs from conventional polymer coating by its unique structural complexity, i.e., the DNA sequence (Figure 1.2). Different interaction/reaction potentials of the nucleobases with the coated nanomaterial and water matrices (e.g., counterions and natural organic matter) would affect the coating structure. For example, the higher surface coverage of DNA strands with a thymine spacer on gold nanoparticle surface was attributed to the lower affinity of thymine towards gold compared to other bases (Hurst et al., 2006); the varied interaction affinities of the nucleobases with counterions (e.g., Na^+, Mg^{2+}, Ca^{2+}) influenced the folding structure of DNA strands (Kolev et al., 2018); the position of nucleobases in a DNA strand affects the surface coverage of DNA strands on a nanoparticle (Brown et al., 2008) and the height of surface-bound DNA strands (Holland and Geiger, 2012). These molecular-level heterogeneities can add extreme complexity to the transformations of the engineered DNA coating in water, and the impact of such heterogeneity on the aggregation behavior of DNA-coated nanomaterials has yet to be systematically investigated.

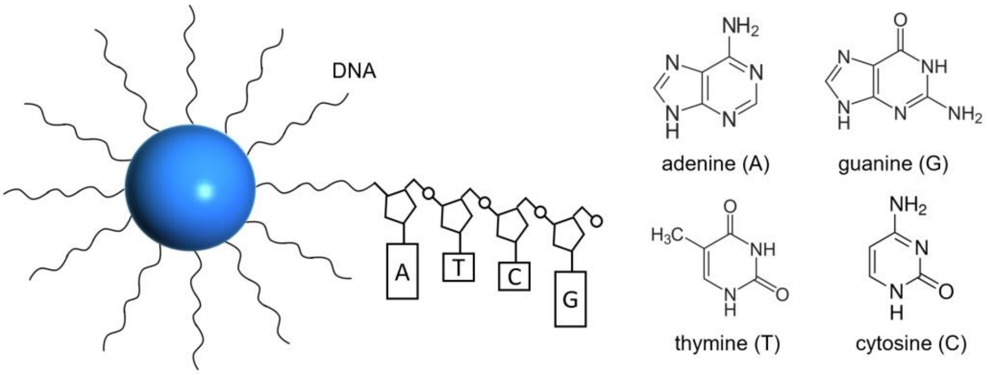

Figure 1.2 Schematic of an engineered single-stranded DNA-coated nanoparticle and the molecular structure of the four nitrogenous bases. The schematics are not drawn to scale and for illustrative purposes only.

1.3 Research Objectives

The interplay of nanomaterial physicochemical properties (e.g., material morphology and surface characteristics) and solution chemistry (e.g., pH, ionic strength, and natural organic matter) largely determines the aggregation behavior of nanomaterials. Therefore, the overarching goals of this thesis are to reveal: (1) the relationship between specific physicochemical properties of nanomaterials and their aggregation based on a meta-analysis of data from multiple individual studies (Chapter 3); (2) the transformation(s) of engineered DNA coating in typical aquatic environment at a molecular-level, and the subsequent impact on the aggregation behavior of coated nanomaterial (Chapter 4 and 5).

The first objective of this thesis is to resolve the seemingly contradictory effects of specific physicochemical properties (i.e., material size, zeta potential, and surface chemistry) on nanomaterial aggregation and to examine the applicability of the relevant predictions of the

DLVO theory. Instead of drawing conclusions from a small set of data based on exemplary studies, this thesis uses a meta-analytic approach to quantitatively synthesize the results from multiple studies on the aggregation of carbon nanomaterials (graphene (oxide) and carbon nanotube) to reach broad generalization.

The second objective is to obtain a molecular-level understanding of the structural change(s) of the ssDNA coating on nanomaterial upon interactions with two ubiquitous aquatic components, namely cations (Na^+, Mg^{2+}, Ca^{2+}) (Chapter 4) and natural organic matter (Chapter 5). The understanding of such molecular-level transformation is used to interpret the change of aggregation behavior of the ssDNA-coated nanomaterial. The impacts on the environmental applications of such nanomaterials (e.g., as sensors) are also discussed.

1.4 Thesis Organization

This thesis comprises six chapters. The current chapter introduces the background information on the aggregation of nanomaterials and identifies the challenges posed by the complex physicochemical properties of nanomaterials in understanding their aggregation behavior. The objectives of this doctoral research project are stated, which correspond to the key scientific issues to be addressed.

Chapter 2 gives a holistic review of current works on the aggregation of nanomaterials as functions of material property, engineered surface coating, and water matrix. The need for a comprehensive analysis of published studies is highlighted. Furthermore, previous works on the transformations of DNA (both natural and engineered) in aquatic environment are discussed to emphasize the need for a more in-depth, molecular-level understanding of those transformations. Lastly, the commonly used DLVO theory for the interpretation of nanomaterial aggregation is briefly introduced, along with the challenges raised from the properties of nanomaterial to the DLVO theory.

Chapter 3 examines the relationship between the critical coagulation concentration (CCC) of nanomaterials and their physicochemical properties (i.e., size, surface charge, and surface functionalities) based on a meta-analytic approach. The CCCs and physicochemical properties of carbon nanomaterials (graphene (oxide) and carbon nanotube) reported in 46 individual studies are collected and analyzed to resolve the seemingly contradictory results from different studies. The predictions of CCC as a function of size and surface charge from earlier theoretical works based on the DLVO theory are examined.

Chapter 4 addresses the structural change of engineered ssDNA coating induced by ubiquitous cations in water, and the subsequent impact on the aggregation behavior of DNA-coated gold nanoparticles (DNA-Au NPs). Four DNA strands with systematically varied properties (i.e., DNA length and sequence) are studied. Both experimental and computational (molecular dynamics simulation) approaches are used to reveal the role of nucleobase-cation specific interactions in affecting the ssDNA coating structure and the aggregation behavior of DNA-Au NPs.

Chapter 5 further addresses the transformation of the engineered ssDNA coating induced by natural organic matter (NOM), another ubiquitous component in water. The preferential interaction of ssDNA with highly aromatic NOM is discovered, and the detailed, molecular-level interaction mechanisms are obtained by using a suite of microscopic and spectroscopic techniques. The extent of ssDNA shielding by NOM depends on the property of NOM and cations, and it has a major impact on the aggregation behavior of DNA-Au NPs.

Finally, Chapter 6 summarizes this thesis’s key research findings and details its novel contributions and impacts. Concluding remarks discuss future research directions as well as the implications of the obtained findings for the rational design and applications of ENMs in practical scenarios.

References

Afshinnia, K., Sikder, M., Cai, B. and Baalousha, M. 2017. Effect of nanomaterial and media physicochemical properties on ag nm aggregation kinetics. J. Colloid Interface Sci. 487, 192-200.

Alivisatos, A.P., Johnsson, K.P., Peng, X., Wilson, T.E., Loweth, C.J., Bruchez Jr, M.P. and Schultz, P.G. 1996. Organization of 'nanocrystal molecules' using DNA. Nature 382, 609.

Ashraf, M.A., Peng, W., Zare, Y. and Rhee, K.Y. 2018. Effects of size and aggregation/agglomeration of nanoparticles on the interfacial/interphase properties and tensile strength of polymer nanocomposites. Nanoscale Res. Lett. 13(1), 214.

Brown, K.A., Park, S. and Hamad-Schifferli, K. 2008. Nucleotide−surface interactions in DNA-modified Au−nanoparticle conjugates: Sequence effects on reactivity and hybridization. J. Phys. Chem. C 112(20), 7517-7521.

Chen, K.L. and Elimelech, M. 2006. Aggregation and deposition kinetics of fullerene (C60) nanoparticles. Langmuir 22(26), 10994-11001.

Chowdhury, I., Duch, M.C., Mansukhani, N.D., Hersam, M.C. and Bouchard, D. 2013. Colloidal properties and stability of graphene oxide nanomaterials in the aquatic environment. Environ. Sci. Technol. 47(12), 6288-6296.

Dederichs, T., Möller, M. and Weichold, O. 2009. Colloidal stability of hydrophobic nanoparticles in ionic surfactant solutions: Definition of the critical dispersion concentration. Langmuir 25(4), 2007-2012.

Divyanshi, T. 2021 Nanotechnology market: Global opportunity analysis and industry forecast, 2021-2030, Allied Market Research.

Gambinossi, F., Mylon, S.E. and Ferri, J.K. 2015. Aggregation kinetics and colloidal stability of functionalized nanoparticles. Adv. Colloid Interface Sci. 222, 332-349.

Gebauer, J.S., Malissek, M., Simon, S., Knauer, S.K., Maskos, M., Stauber, R.H., Peukert, W. and Treuel, L. 2012. Impact of the nanoparticle–protein corona on colloidal stability and protein structure. Langmuir 28(25), 9673-9679.

Gudarzi, M.M. 2016. Colloidal stability of graphene oxide: Aggregation in two dimensions. Langmuir 32(20), 5058-5068.

Gunsolus, I.L., Mousavi, M.P.S., Hussein, K., Bühlmann, P. and Haynes, C.L. 2015. Effects of humic and fulvic acids on silver nanoparticle stability, dissolution, and toxicity. Environ. Sci. Technol. 49(13), 8078-8086.

He, Y.T., Wan, J. and Tokunaga, T. 2008. Kinetic stability of hematite nanoparticles: The effect of particle sizes. J. Nanopart. Res. 10(2), 321-332.

Holland, J.G. and Geiger, F.M. 2012. Importance of length and sequence order on magnesium binding to surface-bound oligonucleotides studied by second harmonic generation and atomic force microscopy. J. Phys. Chem. B 116(22), 6302-6310.

Hotze, E.M., Phenrat, T. and Lowry, G.V. 2010. Nanoparticle aggregation: Challenges to understanding transport and reactivity in the environment. J. Environ. Qual. 39(6), 1909-1924.

Hsu, J.-P. and Kuo, Y.-C. 1997. The critical coagulation concentration of counterions: Spherical particles in asymmetric electrolyte solutions. J. Colloid Interface Sci. 185(2), 530-537.

Hsu, J.-P. and Liu, B.-T. 1998. Effect of particle size on critical coagulation concentration. J. Colloid Interface Sci. 198(1), 186-189.

Hurst, S.J., Lytton-Jean, A.K.R. and Mirkin, C.A. 2006. Maximizing DNA loading on a range of gold nanoparticle sizes. Anal. Chem. 78(24), 8313-8318.

Jiang, Y., Raliya, R., Fortner, J.D. and Biswas, P. 2016. Graphene oxides in water: Correlating morphology and surface chemistry with aggregation behavior. Environ. Sci. Technol. 50(13), 6964-6973.

Kolev, S.K., Petkov, P.S., Rangelov, M.A., Trifonov, D.V., Milenov, T.I. and Vayssilov, G.N. 2018. Interaction of Na^+, K^+, Mg^{2+} and Ca^{2+} counter cations with RNA. Metallomics 10(5), 659-678.

Krueger, K.M., Al-Somali, A.M., Mejia, M. and Colvin, V.L. 2007. The hydrodynamic size of polymer stabilized nanocrystals. Nanotechnology 18(47), 475709.

Liu, J., Aruguete, D.M., Murayama, M. and Hochella, M.F., Jr. 2009. Influence of size and aggregation on the reactivity of an environmentally and industrially relevant nanomaterial (PbS). Environ. Sci. Technol. 43(21), 8178-8183.

Liu, J., Legros, S., Ma, G., Veinot, J.G.C., von der Kammer, F. and Hofmann, T. 2012. Influence of surface functionalization and particle size on the aggregation kinetics of engineered nanoparticles. Chemosphere 87(8), 918-924.

Lowry, G.V., Gregory, K.B., Apte, S.C. and Lead, J.R. 2012. Transformations of nanomaterials in the environment. Environ. Sci. Technol. 46(13), 6893-6899.

Macfarlane, R.J., Lee, B., Jones, M.R., Harris, N., Schatz, G.C. and Mirkin, C.A. 2011. Nanoparticle superlattice engineering with DNA. Science 334(6053), 204-208.

Mirkin, C.A., Letsinger, R.L., Mucic, R.C. and Storhoff, J.J. 1996. A DNA-based method for rationally assembling nanoparticles into macroscopic materials. Nature 382, 607-609.

Mohona, T.M., Gupta, A., Masud, A., Chien, S.-C., Lin, L.-C., Nalam, P.C. and Aich, N. 2019. Aggregation behavior of inorganic 2D nanomaterials beyond graphene: Insights from molecular modeling and modified DLVO theory. Environ. Sci. Technol. 53(8), 4161-4172.

Moore, V.C., Strano, M.S., Haroz, E.H., Hauge, R.H., Smalley, R.E., Schmidt, J. and Talmon, Y. 2003. Individually suspended single-walled carbon nanotubes in various surfactants. Nano Lett. 3(10), 1379-1382.

Mulvihill, M.J., Habas, S.E., Jen-La Plante, I., Wan, J. and Mokari, T. 2010. Influence of size, shape, and surface coating on the stability of aqueous suspensions of cdse nanoparticles. Chem. Mater. 22(18), 5251-5257.

Oberdörster, G., Stone, V. and Donaldson, K. 2007. Toxicology of nanoparticles: A historical perspective. Nanotoxicology 1(1), 2-25.

Omija, K., Hakim, A., Masuda, K., Yamaguchi, A. and Kobayashi, M. 2021. Effect of counter ion valence and pH on the aggregation and charging of oxidized carbon nanohorn (CNHox) in aqueous solution. Colloids Surf. A Physicochem. Eng. Asp. 619, 126552.

Pamies, R., Cifre, J.G.H., Espín, V.F., Collado-González, M., Baños, F.G.D. and de la Torre, J.G. 2014. Aggregation behaviour of gold nanoparticles in saline aqueous media. J. Nanopart. Res. 16(4), 2376.

Petosa, A.R., Jaisi, D.P., Quevedo, I.R., Elimelech, M. and Tufenkji, N. 2010. Aggregation and deposition of engineered nanomaterials in aquatic environments: Role of physicochemical interactions. Environ. Sci. Technol. 44(17), 6532-6549.

Phenrat, T., Saleh, N., Sirk, K., Kim, H.-J., Tilton, R.D. and Lowry, G.V. 2008. Stabilization of aqueous nanoscale zerovalent iron dispersions by anionic polyelectrolytes: Adsorbed anionic polyelectrolyte layer properties and their effect on aggregation and sedimentation. J. Nanopart. Res. 10(5), 795-814.

Phenrat, T., Saleh, N., Sirk, K., Tilton, R.D. and Lowry, G.V. 2007. Aggregation and sedimentation of aqueous nanoscale zerovalent iron dispersions. Environ. Sci. Technol. 41(1), 284-290.

Qi, Y., Xia, T., Li, Y., Duan, L. and Chen, W. 2016. Colloidal stability of reduced graphene oxide materials prepared using different reducing agents. Environ. Sci.: Nano 3(5), 1062-1071.

Rosi, N.L., Giljohann, D.A., Thaxton, C.S., Lytton-Jean, A.K.R., Han, M.S. and Mirkin, C.A. 2006. Oligonucleotide-modified gold nanoparticles for intracellular gene regulation. Science 312(5776), 1027-1030.

Saleh, N., Kim, H.-J., Phenrat, T., Matyjaszewski, K., Tilton, R.D. and Lowry, G.V. 2008. Ionic strength and composition affect the mobility of surface-modified Fe0 nanoparticles in water-saturated sand columns. Environ. Sci. Technol. 42(9), 3349-3355.

Smith, B., Wepasnick, K., Schrote, K.E., Bertele, A.R., Ball, W.P., O'Melia, C. and Fairbrother, D.H. 2009. Colloidal properties of aqueous suspensions of acid-treated, multi-walled carbon nanotubes. Environ. Sci. Technol. 43(3), 819-825.

Stenkamp, V.S. and Berg, J.C. 1997. The role of long tails in steric stabilization and hydrodynamic layer thickness. Langmuir 13(14), 3827-3832.

Taton, T.A., Mirkin, C.A. and Letsinger, R.L. 2000. Scanometric DNA array detection with nanoparticle probes. Science 289(5485), 1757-1760.

Trefalt, G., Szilagyi, I., Téllez, G. and Borkovec, M. 2017. Colloidal stability in asymmetric electrolytes: Modifications of the Schulze–Hardy rule. Langmuir 33(7), 1695-1704.

Wang, J., Zhao, X., Wu, A., Tang, Z., Niu, L., Wu, F., Wang, F., Zhao, T. and Fu, Z. 2021. Aggregation and stability of sulfate-modified polystyrene nanoplastics in synthetic and natural waters. Environ. Pollut. 268, 114240.

Xie, Y., Gao, Y., Ren, X., Song, G., Alsaedi, A., Hayat, T. and Chen, C. 2020. Colloidal behaviors of two-dimensional titanium carbide in natural surface waters: The role of solution chemistry. Environ. Sci. Technol. 54(6), 3353-3362.

Zhang, C., Liu, T., Wang, W., Bell, C.A., Han, Y., Fu, C., Peng, H., Tan, X., Král, P., Gaus, K., Gooding, J.J. and Whittaker, A.K. 2020. Tuning of the aggregation behavior of fluorinated polymeric nanoparticles for improved therapeutic efficacy. ACS Nano 14(6), 7425-7434.

Zhang, W. (2014). Nanoparticle aggregation: principles and modeling. In: Capco, D., Chen, Y. (eds) Nanomaterial: Advances in experimental medicine and biology, vol 811. Springer, Dordrecht.

Zhang, X.-Q., Xu, X., Lam, R., Giljohann, D., Ho, D. and Mirkin, C.A. 2011. Strategy for increasing drug solubility and efficacy through covalent attachment to polyvalent DNA–nanoparticle conjugates. ACS Nano 5(9), 6962-6970.

Chapter 2 Literature Review

2.1 Aggregation of Nanomaterials in Water

The aggregation behavior of nanomaterials has been widely studied and can be quantitatively assessed by their critical coagulation concentrations (CCC) in electrolytes (under controlled laboratory settings). Most studies mainly focused on the effect of water matrices (pH, ionic strength, ion valency, natural organic matter (NOM), etc.) on the aggregation behavior of nanomaterial, while fewer studies probed the effect of nanomaterial physicochemical properties in a systematic manner. With more studies reporting the CCC of nanomaterials, wide discrepancies in the reported values are often encountered, even for the same type of nanomaterial. For example, the reported CCC values of graphene oxide (GO) in NaCl electrolyte varied by ten-fold, from as low as 36 mM (Yang et al., 2016) to as high as 387 mM (Kim et al., 2020). The varied physicochemical properties of the nanomaterials used in each study may have contributed to the observed distinctions in the CCC values, as many nanomaterials, such as GO, should be more accurately identified as a family of nanomaterials with different physicochemical properties. Overall, the aggregation behavior of nanomaterials in water is collectively affected by the physicochemical properties of the nanomaterial (e.g., size, charge, surface coating) and water matrices (e.g., counterion type and concentration, pH, natural organic matter). In this section, the impacts of material intrinsic property, engineered surface coating, and water matrix on the aggregation behavior of nanomaterials are briefly reviewed.

2.1.1 Effect of Material Intrinsic Property

Material Composition. Nanomaterial composition affects the aggregation through (changing) the van der Waals attraction between particles, which can be described by the variations in the Hamaker constants. Nanomaterial with a large Hamaker constant, thus stronger van der Waals attraction, is less stable than that with a low Hamaker constant under the same solution chemistry. Typically, a bulk material with an electronic or molecular structure that favors the generation of permanent or induced dipoles possesses a large Hamaker constant (Hotze et al., 2010). For example, the Hamaker constant of Au (27×10^{-20} J) is around 20-times larger than that of SiO_2 (1.2×10^{-20} J) (Petosa et al., 2010; Zhang et al., 2008). The Hamaker constant shows a strong dependence on the material composition and is typically in the range of 10^{-21} –10^{-19} J (Baalousha, 2017). Furthermore, some materials can originate additional attractive force(s) that promote the aggregation, such as the magnetic attraction of nanoscale zerovalent iron (nZVI) particles (Phenrat et al., 2008).

Size. The effect of material size on the aggregation behavior of nanomaterials has been widely studied. Sun et al. (2020) examined the effect of lateral size (around 1000, 500, 350 and 200 nm, respectively) on the stability of GO with similar structure and surface chemistry and found a negative correlation between the material stability and lateral size. Similar effect of size on the stability of graphene-based nanomaterials has been observed in the publications from different research groups (Liu et al., 2018; Su et al., 2017; Szabo et al., 2020). The negative correlation has also been reported for cadmium selenide (CdSe) (Mulvihill et al., 2010), hematite (Sheng et al., 2016), and silver nanomaterials (Afshinnia et al., 2017). However, contradictory results have also been observed. Hematite (He et al., 2008) and titanium dioxide (TiO_2) nanomaterials (Zhou et al., 2013) were reported to be more prone to aggregation as the size of nanomaterial became smaller. Additionally, the aggregation behavior of gold nanomaterials was reported to be independent of nanomaterial size (Liu et al., 2012). The observed discrepancy in the relationship between material size and aggregation behavior possibly arises from the varied surface charge along with the change of size during nanomaterial synthesis (Afshinnia et al., 2017). Another potential cause of the discrepancy might be the varied Hamaker constants due to the changes in size (Pinchuk and Jiang, 2015; Szabo et al., 2020).

Shape. Engineered nanomaterials come in a variety of shapes, such as spheres, rods, triangles, ellipses, and more. Variations in the shape affect both the van der Waals and electrostatic interactions between nanomaterials (Elimelech et al., 1995). For example, theoretical work by Vold (1954) suggested that the van der Waals attraction of anisometric particles (e.g., plates, rectangular rods, cylinders) is larger than that of spherical particles due to the larger number of atoms on the anisometric particle surface. Experimentally, Zhou and Keller (2010) reported that the nearly spherical ZnO nanomaterials were more stable than the irregularly shaped ZnO nanomaterials in NaCl electrolyte. Jiang et al. (2016) reported that the crumpling of GO from two-dimensional nanosheet to three-dimensional structure increased its colloidal stability due to the reduced π−π interaction between discrete sheets. Nevertheless, another study suggested that the shape of TiO_2 nanomaterials (spherical anatase and rutile rod) is not an influential factor on their aggregation in water, but the different chemical compositions are, which affect the surface charge of nanomaterials (Liu et al., 2011a).

Crystal Structure. The crystal structure of nanomaterials impacts their aggregation behaviors through altering the van der Waals and electrostatic interactions between nanomaterials. Varied crystal structures yielded different Hamaker constants, thereby the van der Waals attraction between nanomaterials. For example, the Hamaker constants for iron oxide nanoparticles depended on the phases and followed the order of magnetite (3.3×10^{-20} J) < maghemite (3.6×10^{-20} J) < hematite (3.9×10^{-20} J) (Faure et al., 2011); the higher stability of single-walled carbon nanotube (SWNT) with (6,5) chiral enrichment than the (7,6) armchair SWNT in electrolytes ($NaCl/CaCl_2$) was due to the stronger van der Waals attraction of the (7,6) SWNT (Khan et al., 2013). Furthermore, the crystal structure also alters the surface charge of nanomaterials, thereby the electrostatic interaction. For instance, the three different phases of crystallinity of TiO_2 nanomaterial possessed different zeta potential at pH 7.5; that was -20 mV for anatase and brookite and -35 mV for rutile (French et al., 2009; Lebrette et al., 2004).

Surface Chemical Composition. Nanomaterial surface may acquire impurities from the synthesis process either intentionally or unintentionally, which could affect the surface charge and Hamaker constant of nanomaterial (Baalousha, 2017). For example, the zeta potential of the Fe^0/Fe_3O_4 core-shell NPs transitioned from -32 mV to -38 mV as the Fe^0 core was oxidized to magnetite (in 1 mM $NaHCO_3$, pH 7.5) (Phenrat et al., 2007); the negative surface of gold nanoparticles synthesized via citrate reduction was due to the adsorbed citrate acid molecules on the particle surface (Sardar et al., 2009). On the other hand, surface oxidation of nanomaterials is purposedly applied to achieve enhanced colloidal stability, such as for carbon nanomaterials. Surface oxidation degree could affect the Hamaker constant (Gudarzi, 2016; Xia et al., 2019) and the surface charge (Bai et al., 2014; Jiang et al., 2016; Smith et al., 2009b) of these nanomaterials, and the oxidation degree has been reported to increase nanomaterial stability (Bai et al., 2014; Xia et al., 2019), or pose little impact (Gao et al., 2020).

Study-to-study variations on the effect of material properties on the aggregation of nanomaterials are often observed. Research synthesis efforts are needed to identify whether there is a consistent relationship between a specific material property and the aggregation behavior of nanomaterials. Meta-analysis is an objective, quantitative, and powerful approach to synthesize findings across studies (Gurevitch et al., 2018). Instead of drawing conclusions from a small set of data based on exemplary studies, meta-analysis that quantitatively synthesizes the results across studies into a larger sample size can be performed to reach broad generalizations and to resolve seemingly contradictory outcomes (Gurevitch et al., 2018; Mantilla-Calderon et al., 2022). However, such efforts have rarely been conducted to study the aggregation of ENMs.

2.1.2 Effect of Engineered Surface Coating

Applying engineered coatings to nanomaterial surface is a common measure to reduce nanomaterial aggregation and/or achieve specific functionality in manufacturing engineered nanomaterials (Gambinossi et al., 2015; Zhang, 2014). Common surface coatings include small molecules, synthetic polymers, and biomacromolecules, among others. Surfactants are typically small molecules with relatively low molecular weights, such as sodium dodecyl sulfate (SDS) and cetrimonium bromide (CTAB). Depending on the ionic head groups, surfactants can be classified into four groups: cationic, anionic, zwitterionic, and nonionic (Schramm et al., 2003). In contrast to the low molecular weight of surfactants, polymers are high molecular weight organic macromolecules consisting of repeating monomer units, and polyelectrolytes are charged polymers. Biomacromolecules (e.g., protein, polysaccharide, and DNA) can also serve as surface coatings. These coatings alter the aggregation behavior of engineered nanomaterials (mostly to stabilize the nanomaterials) by providing extra (electro)steric repulsion, and the magnitude of which is determined by the properties and structure of the polymer coating (Petosa et al., 2010).

Molecular Weight. Typically, surface coating with a higher molecular weight (MW) provides stronger stabilization against nanomaterial aggregation. For example, the nonionic surfactant Brij 78 (MW = 1198 g/mol) stabilized 4.3% of SWNT, while Brij 700 (MW = 4670 g/mol) stabilized 6.4% of SWNT (Moore et al., 2003); the dispersion stability of SWNT increased when the MW of Pluronic increased from 4950 to 14600 g/mol (Moore et al., 2003); carboxymethyl cellulose (CMC) with MW of 90 kg/mol did not prevent the aggregation of nZVI nanoparticles, but CMC with MW of 700 kg/mol stabilized 52% of the particles (Phenrat et al., 2008). Additionally, physiosorbed low MW molecules may desorb or be displaced by higher molecular weight molecules (Louie et al., 2013; Rosen and Kunjappu, 2012). The molecules with high MW can adsorb to nanomaterial surface with multiple anchoring sites compared to molecules of low MW, thereby making the adsorption much stronger and less reversible. For instance, the polyelectrolyte coatings (polyaspartate (PAP) or CMC) on nZVI nanoparticles with a higher MW desorbed slower than their counterparts with lower MW after four months (Kim et al., 2009).

Layer Thickness. Layer thickness is the main factor determining the stabilization effect of the surface coating on nanomaterials (Elimelech et al., 1995). Stenkamp and Berg (1997) revealed that polystyrene latex particles with a thicker Pluronics polymer coating were more stable in electrolytes and the most outward-extending tails in the coating largely played a determinant role even when the tail density was quite low. Phenrat et al. (2008) estimated the layer thickness of polyelectrolyte-coated nZVI particles using the Oshima's soft particle theory and found a good correlation between the stable fractions of the coated particles and the adsorbed polyelectrolyte thickness. Dederichs et al. (2009) used *n*-alkyltrimethylammonium bromide (C_nTAB, alkyl chain lengths 10-16) to coat the surface of boehmite nanoparticles and observed a linear relationship between the surfactant chain length (or coating thickness) and particle dispersion stability. They revealed that the surfactants with longer chains (i.e., thicker coating layer) were more efficient in dispersing nanoparticles than those with shorter chains. Goodwin et al. (2013) observed that the span of the adsorbed surface coating layer, which takes into account the contribution from the tails, plays a significant role in the colloidal stability of the coated nanoparticles.

Surface Coverage. Surface coverage by the engineered surface coating affects the aggregation behavior of coated nanomaterials. For example, SWNTs were more stable in NaCl electrolyte as more SDS (from 0.001 to 0.1 %) was used to stabilize the nanomaterials (Bouchard et al., 2012); stability of polyvinylpyrrolidone (PVP) coated-silver nanomaterials increased with the surface coverage of PVP molecules due to stronger steric stabilization (Afshinnia et al., 2017); the aggregation of silver nanomaterial in K_2SO_4 electrolyte decreased with an increasing amount of adsorbed human serum albumin protein and the attachment efficiency reached zero when the protein formed a monolayer on material surface (Gebauer et al., 2012). Additionally, the surface coverage impacts the structure of the coating layer, thereby the coating layer thickness and the ability of coating to stabilize nanomaterial (Figure 2.1a). Krueger et al. (2007) showed that with increasing surface coverage, the structure of polystyrene grafted on nanomaterials transitioned from mushroom (random coil) to brush (extended) conformation; the polymer in brush conformation was 44% longer than the unbound polymer in solution. Another factor affecting the structure of surface coating is the specific interaction with water matrices. For instance, the valency of surrounding counterions affected the conformation of polystyrenesulfonate (PSS) brushes tethered on a surface (Yu et al., 2016). The PSS brushes underwent a homogeneous shrinkage (i.e., less collapsed) when interacting with monovalent counterions, but formed a thinner pinned micelle-like heterogeneous structure upon interaction with multivalent counterions (Figure 2.1b).

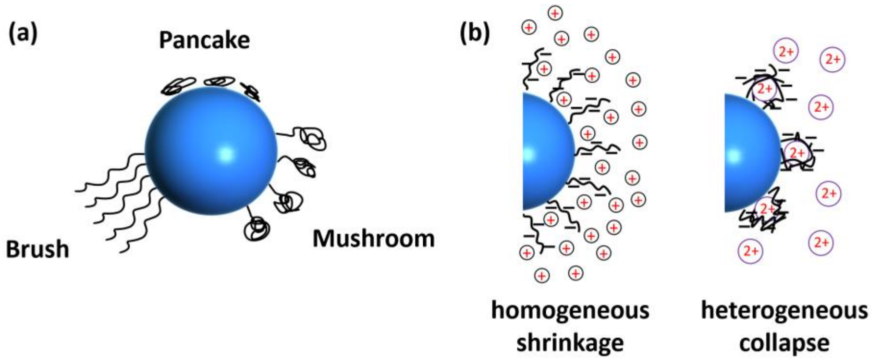

Figure 2.1 Conformation of the polymer coating on an engineered nanomaterial surface (not drawn to scale). (a) The conformation of the polymer coating transitions from a pancake layer at low surface coverage, to a mushroom layer at medium surface coverage, and to a brush layer at high surface coverage. The diagram is drawn based on Louie et al. (2016). (b) Conformational change of the polyelectrolyte coating upon interaction with surrounding counterions; monovalent counterions induce a homogeneous shrinkage of the layer, while divalent (or multivalent) counterions induce a heterogeneous collapse. The polyelectrolyte coatings are negatively charged as shown. The diagram is drawn based on Yu et al. (2016).

Overall, the effects of engineered surface coating on the aggregation behavior of coated nanomaterial are highly dependent on the physicochemical properties of the coating and could be more prominent than the effect of nanomaterial intrinsic properties (Liu et al., 2012). Furthermore, the coating properties affect the interactions of the coating among themselves and with the nanomaterial surface and the aquatic constituents (Surette and Nason, 2019), which will be further discussed in the following section. Understanding the interactions, desirably at the molecular level, is a prerequisite to accurately predict the aggregation behavior of coated nanomaterial in water.

2.1.3 Effect of Water Matrix

pH. pH plays an important role in affecting the aggregation behavior of nanomaterial as the change of pH influences the surface charge of nanomaterial. The surface charge of nanomaterial typically stems from the surface functional groups (e.g., hydroxyl, carboxyl, etc.), which are titratable by H^+ or OH^- (Hotze et al., 2010). Considering the case of a negatively charged nanomaterial, lowering the pH (i.e., more H^+) may result in a positively charged surface and increasing the pH (i.e., more OH^-) normally yields a more negatively charged surface due to deprotonation. The pH at which the surface charge becomes neutral is called the point of zero charge (PZC). For instance, the aggregation of ZnO (Zhou and Keller, 2010) and TiO_2 (Snoswell et al., 2005) nanomaterials were inhibited as the pH was away from the pH_{PZC} as the surface charge became stronger, therefore more resistant to aggregation; the CCC of GO in NaCl electrolytes increased with pH (24, 188, 482 mM at pH 2, 5, 12, respectively) since the nanomaterial possessed a more negatively charged surface at a higher pH (Wu et al., 2013).

Ions. The co-existing ions in water also affect the aggregation behavior of nanomaterials. Typical factors include ionic strength, ion species, and ion valency. Counterions screen the surface charge of nanomaterial and higher ionic strength decreases the Debye length, thereby decreasing the electrostatic repulsion between nanomaterials. The varied electronegativity and hydration shell thickness of different ion species affect their interactions with nanomaterials, thereby the aggregation behavior of nanomaterials (Philippe and Schaumann, 2014). For example, heavy metal cations (Cr^{3+}, Pb^{2+}, Cu^{2+}, Cd^{2+}, Ag^{+}) induced the aggregation of GO more aggressively than common cations (Ca^{2+}, Mg^{2+}, Na^{+}, K^{+}) (Yang et al., 2016). It is also a consensus that multivalent counterions are more effective in screening the surface charge of nanomaterial than monovalent counterions (Baalousha, 2017). This could be widely observed in the lower CCC of nanomaterials in a multivalent electrolyte than in a monovalent electrolyte solution (Chen and Elimelech, 2007; Jiang et al., 2016; Khan et al., 2013; Omija et al., 2021; Saleh et al., 2010; Xia et al., 2019). More importantly, the specific interaction between counterions and nanomaterial/engineered surface coating may significantly change the aggregation behavior of nanomaterial. For example, cation bridging interaction between divalent cations and the carboxyl groups has been reported to accelerate the aggregation of nanomaterials (Chen and Elimelech, 2007; Huynh and Chen, 2011; Liu et al., 2011b; Yu et al., 2019); multivalent counterions could induce a heterogeneous collapse of the polystyrenesulfonate (PSS) surface layer, resulting a thinner polyelectrolyte layer compared to the homogeneous shrunk layer induced by monovalent counterions (Yu et al., 2016); strong ion-specific interaction was reported between the divalent cations and the PSS coating, where Mg^{2+} and Ca^{2+} caused relatively homogeneous shrinkage and Ba^{2+} led to pinned-micelle like heterogeneous collapse (Xu et al., 2019).

Natural Organic Matter. NOM is a general term that includes humic substances, proteins, polysaccharides, etc. (de Melo et al., 2016). It is ubiquitous in typical aquatic environments and its impact on the aggregation behavior of nanomaterial has been broadly investigated. Typically, the presence of NOM inhibits the aggregation of nanomaterial by imparting (electro)steric repulsion, nevertheless, enhanced aggregation may also occur due to charge neutralization (when nanomaterial and NOM are oppositely charged) (Louie et al., 2016). The properties of NOM (e.g., concentration or NOM-to-nanomaterial ratio, chemistry, and molecular weight) are important in their interaction with nanomaterials. For example, the aggregation of nanomaterials (TiO_2, ZnO, and CeO_2) was increasingly inhibited with more NOM present, which was attributed to the (more) adsorption of NOM onto nanomaterial surface, resulting in more negative surface charge and stronger steric repulsion of the coated nanomaterials (Keller et al., 2010). Similar effect of the NOM concentration has been widely reported (Jiang et al., 2017; Ottofuelling et al., 2011; Qi et al., 2016; Sun et al., 2020; Wang et al., 2018). The bulk properties of NOM determine the interaction with nanomaterial. In a study comparing the effect of nine different NOM isolates on the aggregation of zinc sulfide nanomaterial, the aromaticity and average molecular weight of NOM were found to be the major factors in inhibiting nanomaterial aggregation (Deonarine et al., 2011). The results are consistent with the observation that humic acid provided stronger stabilization than fulvic acid against aggregation of nanomaterial, because fulvic acid typically has lower molecular weight and aromaticity than humic acid (Furman et al., 2013; Nason et al., 2012). However, since NOM is a complex mixture and different components in the mixture could have different chemistry, using bulk or average properties to fully describe the interaction(s) between NOM and nanomaterials turns out to be inaccurate (Louie et al., 2016). For example, the NOM fraction of high molecular weight provided better stabilization to nanomaterial than the bulk NOM or NOM fraction of low molecular weight (Hyung and Kim, 2008; Li et al., 2020; Louie et al., 2013; Shen et al., 2019; Yin et al., 2015). However, a few studies have also observed that Pony Lake fulvic acid (PLFA) with a low molecular weight provided a similar stabilization effect as the high molecular weight NOM to gold and silver nanomaterials (Gunsolus et al., 2015; Louie et al., 2015; Nason et al., 2012). The cause was attributed to the high sulfur and nitrogen contents of PLFA, which may result in a stronger adsorption affinity to gold and silver nanomaterials (Gunsolus et al., 2015; Louie et al., 2015). These studies highlight the importance of specific interactions (e.g., chemical bonding or reaction) between NOM and nanomaterials in affecting the loading and configurations of NOM on nanomaterials surface.

Overall, the effect of water matrices on the aggregation behavior is complex and determined by multiple interdependent factors. The interaction(s) between water matrices and nanomaterial is a key process affecting the aggregation behavior of nanomaterial, and more research efforts are required to disentangle the property-dependent interaction(s) in typical aquatic environment.

2.2 Engineered DNA as an Emerging Nanomaterial Coating

DNA is a polyelectrolyte consisting of polynucleotide chain(s) in a specific order. Each nucleotide contains a deoxyribose sugar, a phosphate group, and one of the four nitrogenous bases, namely adenine (A), thymine (T), cytosine (C), and guanine (G). Other than being a genetic information carrier, many other functions of DNA are being discovered. For example, aptamer, a short-chain single-stranded DNA (ssDNA), can bind to targets with high sensitivity and selectivity, thereby being a very promising sensing platform (Akki et al., 2015; Qing et al., 2017; Yu et al., 2018). The unique properties of DNA, such as biological functions, biocompatibility, molecular recognition capability, and controllability on the nanoscale (Xu et al., 2021), render its broad application across diverse scientific and technological fields, e.g., bioimaging (Zhang et al., 2018), sensing (Wang et al., 2019), therapeutics (Xu et al., 2018), information storage (Erlich and Zielinski, 2017), hydraulic tracers (Liao et al., 2018), among others. Engineered DNA can be synthesized with desired sequences and a wide range of useful modifications, such as fluorescent tags and linkage molecules, to achieve specific functionality (Seeman and Sleiman, 2017), and the cost of synthesizing engineered DNA has been decreasing as the technology getting more mature and sophisticated (Xu et al., 2021).

The Uniqueness of Engineered DNA Coating. The introduction of engineered DNA, especially ssDNA, as a surface coating for nanomaterial started from the 1990s (Alivisatos et al., 1996; Mirkin et al., 1996). This combination, on one hand, provides DNA greater stability, nanoplasmonic properties, and new catalytic activities, on the other hand gives the nanomaterial core improved biocompatibility and precise targeting ability, and changes the charge characteristics (Mirkin, 2021). Like many other conventional polymers, the structure of the engineered DNA coating depends on polymer length and surface coverage as well as interaction(s) with water matrices (Figure 2.2a). For example, progressively increasing surface coverage shifted the structure of the end-grafted DNA from a flat-lying conformation to a more upright and random coil conformation, and eventually to a stretched shape with DNA standing perpendicularly to the surface (Parak et al., 2003). For densely packed DNA strands on nanomaterial surface, short DNA (< 30 bases) was fully stretched on particle surface, while longer DNA had a mixture of fully stretched inner parts and randomly coiled outer parts (Parak et al., 2003). However, engineered DNA differs from conventional polymer in its intrinsic structural complexity, i.e., DNA sequence (Figure 2.2b).

Each nucleobase has different interaction/reaction potentials towards the nanoparticle core and water matrices, which in turn affects the structure of the DNA coating. For example, the low affinity of thymine towards gold nanoparticle surface allowed a higher surface coverage of the DNA strands with thymine as a spacer (Hurst et al., 2006); the folding structure of DNA strands was affected by the varied interactions of nucleobases with surrounding counterions because each nucleobase has different affinities to ions (Kolev et al., 2018); the position of nucleobases in DNA strand affected the surface coverage (Brown et al., 2008) and the thickness of the DNA coating (Holland and Geiger, 2012). The molecular-level heterogeneity of the engineered DNA can add extreme complexity to its transformation in water and the subsequent impact on the aggregation behavior of engineered DNA-coated nanoparticles.

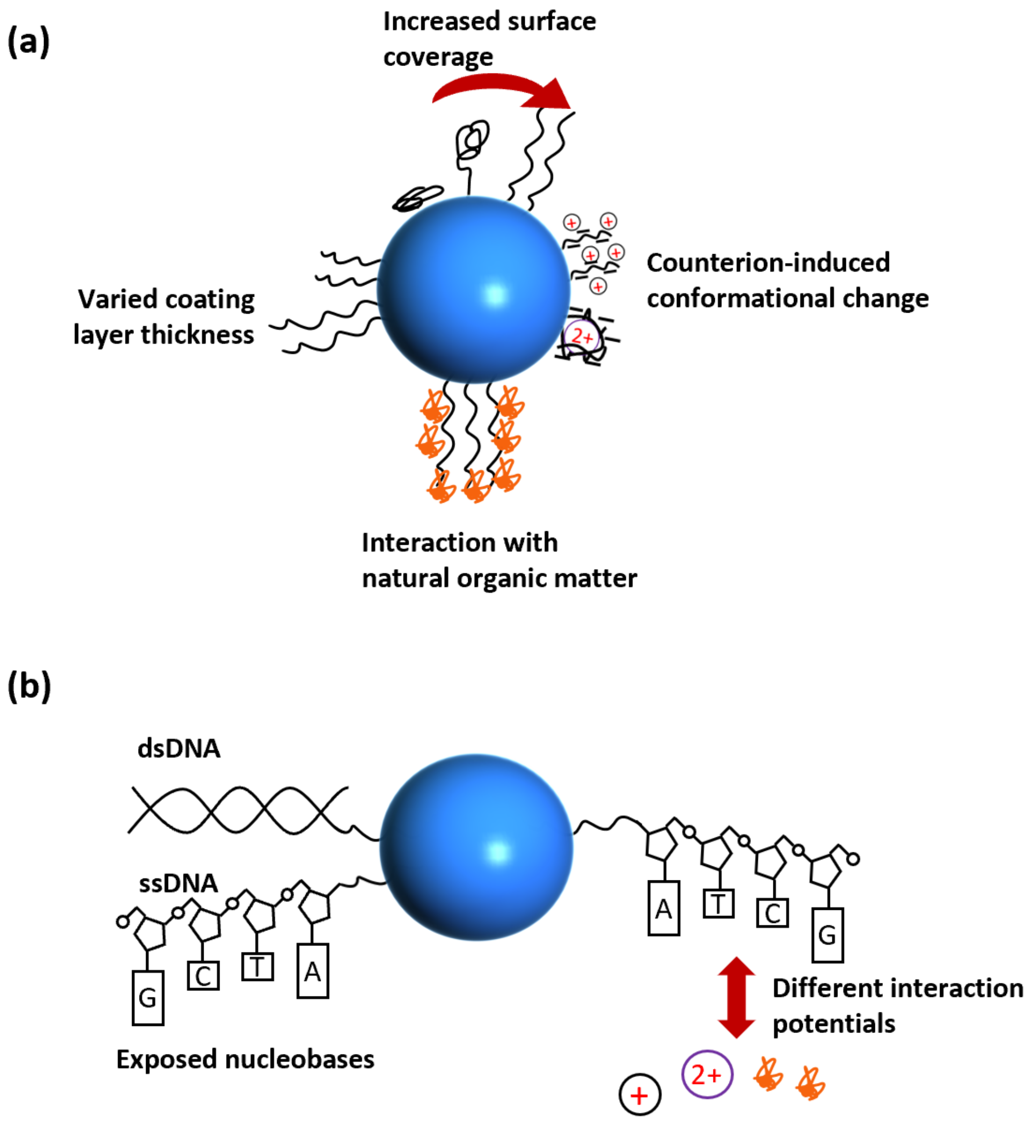

Figure 2.2 Possible transformations of the engineered DNA coating on a nanoparticle. (a) Like conventional polymer coating, conformation of the engineered DNA coating could be influenced by surface coverage, polymer length, and interaction with water matrices (e.g., counterions and natural organic matter). (b) Engineered DNA coating differs from conventional polymer due to the uniqueness of DNA sequence; the nucleobases are exposed in single-stranded DNA (ssDNA) but shielded in double-stranded DNA (dsDNA); different nucleobases have different interaction potentials with water matrices.

Transformations of DNA in Water. Natural double-stranded DNA (dsDNA) with a long chain (thousands of base pairs) was commonly used in previous studies to investigate their aquatic transformations (Lu et al., 2012; Nguyen and Chen, 2007; Nguyen and Elimelech, 2007; Qin et al., 2018). For example, the phosphate groups of dsDNA were deemed as the binding site for divalent cations to form bridges with NOM (Nguyen and Chen, 2007; Nguyen and Elimelech, 2007); DNA fragments that have faster diffusion rates and smaller size (2.69 kbp) preferentially adsorbed to soil compared to larger fragments (11.19 and 23 kbp) (Ogram et al., 1994). However, the varied properties of (engineered) DNA (e.g., double- or single-stranded, length, and sequence) may complicate its transformation in water. Especially, little attention was paid to (engineered) short-chain ssDNA (e.g., < 100 nucleobases, the typical length of a DNA aptamer (Zhou et al., 2010)), which may behave distinctively from natural dsDNA in aquatic systems. For instance, the ion-nucleotide specific interactions observed in surface-bound ssDNA affected the ion distribution along the DNA strands (Holland and Geiger, 2012; Holland et al., 2011). The exposed nucleobases of ssDNA have been reported as important binding sites for their interaction with GO (He et al., 2010; Liu et al., 2020). The surfaces of NOM and GO are both considered as a mixture of highly oxidized, hydrophilic domains, which are rich in oxygen-containing functional groups (e.g., epoxides, hydroxyl, carboxyl, and carbonyl groups), and less oxidized, hydrophobic domains (Chen et al., 2012; de Melo et al., 2016). Similar interactions between ssDNA and NOM may also be observed. To date, few studies have investigated the effect of the ssDNA coating on the aggregation behavior of the coated particles. Storhoff et al. (2002) reported the aggregation of DNA-coated gold nanoparticles in $MgCl_2$ electrolyte to be DNA sequence-dependent. However, the study was only limited to homo-base strands (poly-adenine/thymine/cytosine) and did not consider the heterogeneous nature of DNA. The cation-induced structural changes of the (heterogeneous) DNA coating remain largely unknown.

Altogether, there is a critical knowledge gap in understanding the transformation of the engineered ssDNA coating in water, in the context of its rapidly emerging applications in various fields, including many environmental applications such as sensors, hydraulic tracers, and so forth. A fundamental understanding of the transformation not only facilitates the understanding of the aggregation behavior of engineered DNA-coated nanomaterial in water, but also benefits the design and applications of engineered DNA-based applications in realistic scenarios.

2.3 Theoretical Understanding of Nanomaterial Aggregation

Aggregation of nanomaterials is often interpreted based on colloid science principles, i.e., the Derjaguin-Landau-Verwey-Overbeek (DLVO) theory (Gudarzi, 2016; Jiang et al., 2016; Omija et al., 2021). The classic DLVO theory simplifies the surface interactions of particles by assuming that van der Waals attraction and electrical double layer repulsion (or electrostatic repulsion) are additive and combined to yield the total interaction energy between particles (Figure 2.3) (Elimelech et al., 1995). Essential assumptions made in derivation of the classic DLVO theory are summarized below:

1. Particle: the particle is spherical with solid core and smooth surface, with electric charges uniformly distributed over the solid surface. The thickness of diffuse double layer is much smaller than the particle radius (i.e., Derjaguin approximation).
2. Solution: particles are dispersed in a structureless and uniform continuum characterized only by its dielectric constant. The ions are point charges (i.e., without any particle size) and the distribution of which is determined by electrostatic force, Brownian motion, and entropic dispersion.
3. Forces: only van der Waals attraction and electrostatic repulsion are considered, and these forces are treated independently and assumed additive.

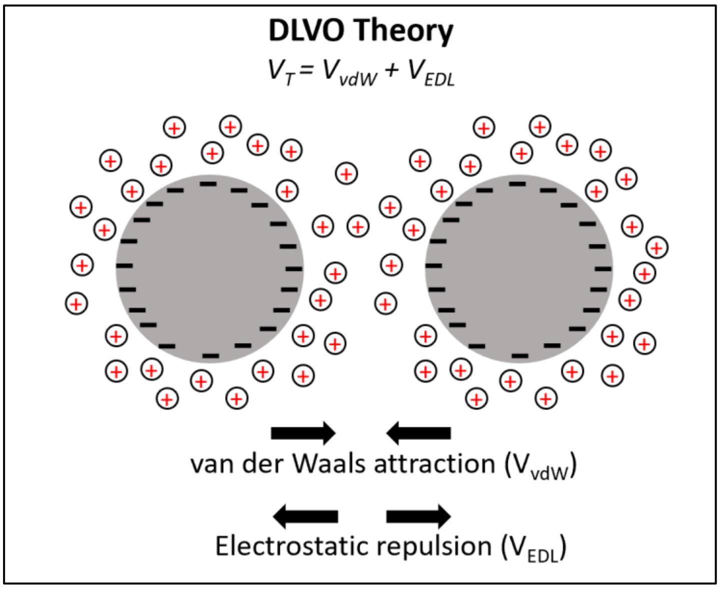

Figure 2.3 Schematic illustration of the classic DLVO theory. V_T is the total interaction energy of two particles.

As the ionic strength of solution increases, the electrostatic repulsion between particles decreases and the aggregation of particles occurs more readily. Depending on the ionic strength, aggregation occurs in reaction- or diffusion-limited regimes (RLA and DLA, respectively) (Figure 2.4). The attachment efficiency (α) describes the probability of two particles sticking together after collision and is used to differentiate RLA ($0 < \alpha < 1$) and DLA ($\alpha = 1$) regimes. In the RLA regime, an increase of the ionic strength leads to faster aggregation rates and larger attachment efficiencies of the particles, while in the DLA regime, the aggregation rate is independent of the ionic strength and limited by Brownian motion. The transition from RLA to DLA regimes occurs over a narrow range of ionic strength, and the concentration of electrolyte observing the transition is called the *critical coagulation concentration* (CCC) (Elimelech et al., 1995).

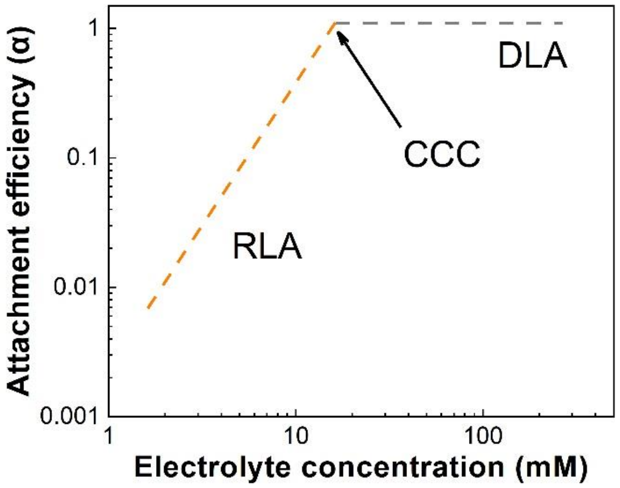

Figure 2.4 Schematic diagram showing the impact of increasing electrolyte concentration on the attachment efficiency (α) according to the DLVO theory. RLA, reaction-limited aggregation regime; DLA, diffusion-limited aggregation regime; CCC, critical coagulation concentration. This diagram is for illustrative purposes only.

Theoretically, before the electrolyte concentration reaches the CCC, the electrostatic repulsion outweighs the van der Waals attraction between particles and there is an energy barrier that tends to prevent particle aggregation (Figure 2.5). The increase of electrolyte concentration lowers the energy barrier, and the aggregation occurs more readily (i.e., the RLA regime). At the CCC, the total interaction energy V_T and the gradient dV_T/dh are equal to zero and the energy barrier disappears, which means that the particles are fully destabilized (i.e., the DLA regime). Experimentally, the CCC of nanomaterials could be determined by monitoring the rate of aggregation as a function of electrolyte concentration using time-resolved dynamic light scattering (Chen and Elimelech, 2006; Saleh et al., 2008).

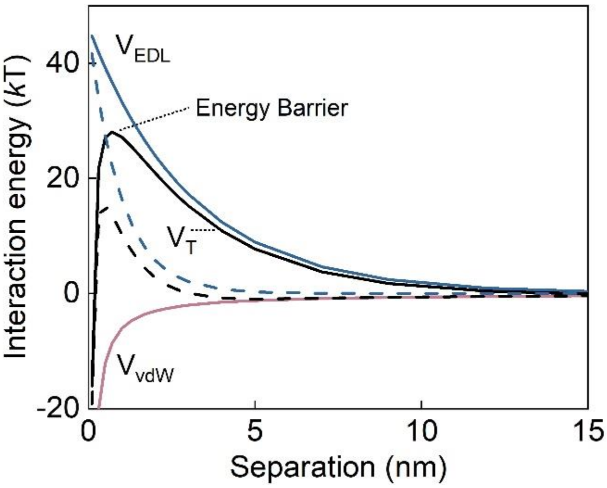

Figure 2.5 Schematic diagram of interaction energy profile between two spherical particles based on the DLVO theory. V_{vdW} is the van der Waals attraction (pink solid line), V_{EDL} is the electrostatic repulsion (blue solid and dash lines), and V_T is the total interaction energy (black solid and dash lines). Dash lines represent a higher electrolyte concentration than the solid lines for V_{EDL} and V_T, respectively. This diagram is for illustrative purposes only.

Classic DLVO Theory to Interpret Nanomaterial Aggregation. DLVO-type aggregation behavior in simple electrolytes (e.g., NaCl, $MgCl_2$, and $CaCl_2$) is observed for a variety of nanomaterials (Chen and Elimelech, 2006; Chowdhury et al., 2013; Li and Huang, 2010; Mohona et al., 2019; Omija et al., 2021; Pamies et al., 2014), and the classic DLVO theory has been commonly used to interpret the experimental observations of electrostatically stabilized nanomaterials. For example, Smith et al. (2009a) determined the CCC of multi-walled carbon nanotube (MWNT) as 93 mM NaCl, 1.8 mM $MgCl_2$, and 1.2 mM $CaCl_2$, respectively. The ratios of CCC in divalent electrolytes to CCC in monovalent electrolyte were $2^{-5.7}$ (Mg^{2+}/Na^+) and $2^{-6.3}$ (Ca^{2+}/Na^+), which were close to the Schulze-Hardy rule and the DLVO theory prediction of 2^{-6}. Jiang et al. (2016) observed that the CCCs of GO in NaCl, $CaCl_2$, and $MgCl_2$ electrolytes could be correlated to material zeta potential, being mathematically consistent with the classic DLVO theory. Omija et al. (2021) reported a semi-quantitative relationship between the surface charge density of oxidized carbon nanohorn (CNHox) and its CCCs in KCl, $CaCl_2$, and $LaCl_3$ electrolytes.

Extended DLVO Theory to Include Non-DLVO Forces. In addition to the van der Waals force and electrostatic forces, non-DLVO force(s) also exist between nanomaterials, further complicating the analysis of nanomaterial aggregation with the classic DLVO theory. For example, nanomaterials with an engineered surface coating (such as polymer) or adsorbed NOM (such as humic acid) from water matrix give rise to (electro)steric stabilization (Figure 2.6) (Moore et al., 2003; Phenrat et al., 2008; Surette et al., 2019; Zhang et al., 2012); the steric stabilization rises from the excluded volume energy due to overlap of polymers and the elastic energy due to the compression of polymers (Napper, 1983); the grafting of polyelectrolyte also induces the osmotic repulsive energy from the trapped counterions inside the polyelectrolyte layer (Jusufi et al., 2002; Kegler et al., 2007). Other non-DLVO forces include, but not limited to, magnetic attraction (Phenrat et al., 2008; Phenrat et al., 2007), hydrophobic (Lewis acid-base) interaction (Hoek and Agarwal, 2006; Huang et al., 2021; Wu et al., 1999), polymer bridging (Chen and Elimelech, 2007; Domingos et al., 2009), hydration repulsion (Israelachvili, 2015). These non-DLVO interactions could either enhance or alleviate nanomaterial aggregation, depending on the nature of the interaction(s).

A few studies include non-DLVO interactions into the classic DLVO theory (i.e., extended DLVO theory) to match experimental data and describe the aggregation behavior of nanomaterials. For instance, the experimentally measured attachment efficiency of poly(methacrylic acid)-grafted nanoparticles (a core of polystyrene-poly(butyl acrylate)) was quantitatively described by an extended DLVO theory that included osmotic and elastic repulsion (Fritz et al., 2002); an extended DLVO theory that included magnetic attraction and steric repulsion was used to semi-quantitatively explain the effects of adsorbed polyelectrolytes on the aggregation behavior of nZVI particles (Phenrat et al., 2008); the predicted CCCs of Janus GO with asymmetrically grafted dodecylamine, which were calculated via an extended DLVO model that included hydrophobic interaction, fitted well with the experimental values

(Huang et al., 2021). These studies suggest that additional non-DLVO force(s) may operate on an equivalent or even larger magnitude as van der Waals attraction and electrostatic repulsion, and the force types strongly depend on the tested system.

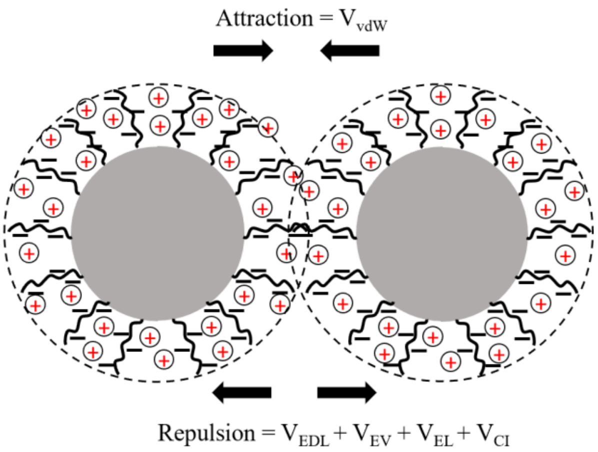

Figure 2.6 Schematic representation of the forces acting on polyelectrolyte-coated nanomaterials, including van der Waals attraction (V_{vdW}), electrostatic repulsion (V_{EDL}), excluded volume repulsion (V_{EV}), elastic repulsion (V_{EL}), and osmotic repulsion of counterions (V_{CI}).

Limitation(s) of DLVO Model to Describe Nanomaterial Aggregation. Novel properties of nanomaterials (e.g., small size, varied shape, and high surface curvature) may challenge the interpretation of nanomaterial aggregation via the DLVO theory of colloidal science (Louie et al., 2016; Zhang, 2014). For instance, theoretical work by Hsu and Liu (1998) based on the DLVO theory predicts the CCC to be independent of particle size when the particle radius is larger than 1 μm. For particles with a radius smaller than 1 μm, the CCC is inversely proportional to their size. Gudarzi (2016) found the dimensionality of nanomaterials affects the aggregation behavior GO. Due to the two-dimensional (2D) nature of GO (and other 2D nanomaterials), proper scaling laws are required to calculate the DLVO forces and interpret the aggregation behavior. For nanomaterials with engineered surface coating, the assumption of uniform segment distribution of the coating used in the extended DLVO theory could result in an overestimation of the steric interactions, especially for nanoparticles with high surface curvature (Louie et al., 2016). Overall, the DLVO theory has been mostly used to qualitatively explain, rather than quantitatively predict the aggregation behavior of nanomaterials.

Furthermore, the DLVO theory has difficulties in recognizing the (specific) interactions between nanomaterials at the molecular level. In such cases, new tools shall be used to gain a full understanding of the aggregation process. For example, a molecular modeling approach was used to calculate the molecular-level interaction energies between individual two-dimensional nanosheets (i.e., MoS_2, WS_2, and h-BN nanosheets) (Mohona et al., 2019). Tang et al. (2021) employed molecular dynamics simulations to reveal the aggregation mechanisms of GO in alkaline solution and discovered the important role of oxidation debris on GO in facilitating the aggregation of GO when $pH > 10$. With the aid of modern computational techniques, a more comprehensive understanding of the nanomaterial aggregation process could be achieved.

References

Afshinnia, K., Sikder, M., Cai, B. and Baalousha, M. 2017. Effect of nanomaterial and media physicochemical properties on Ag NM aggregation kinetics. J. Colloid Interface Sci. 487, 192-200.

Akki, S.U., Werth, C.J. and Silverman, S.K. 2015. Selective aptamers for detection of estradiol and ethynylestradiol in natural waters. Environ. Sci. Technol. 49(16), 9905-9913.

Alivisatos, A.P., Johnsson, K.P., Peng, X., Wilson, T.E., Loweth, C.J., Bruchez Jr, M.P. and Schultz, P.G. 1996. Organization of 'nanocrystal molecules' using DNA. Nature 382, 609.

Baalousha, M. 2017. Effect of nanomaterial and media physicochemical properties on nanomaterial aggregation kinetics. NanoImpact 6, 55-68.

Bai, Y., Wu, F., Lin, D. and Xing, B. 2014. Aqueous stabilization of carbon nanotubes: Effects of surface oxidization and solution chemistry. Environ. Sci. Pollut. Res. 21(6), 4358-4365.

Bouchard, D., Zhang, W., Powell, T. and Rattanaudompol, U.-s. 2012. Aggregation kinetics and transport of single-walled carbon nanotubes at low surfactant concentrations. Environ. Sci. Technol. 46(8), 4458-4465.

Brown, K.A., Park, S. and Hamad-Schifferli, K. 2008. Nucleotide−surface interactions in DNA-modified Au−nanoparticle conjugates: Sequence effects on reactivity and hybridization. J. Phys. Chem. C 112(20), 7517-7521.

Chen, D., Feng, H. and Li, J. 2012. Graphene oxide: Preparation, functionalization, and electrochemical applications. Chem. Rev. 112(11), 6027-6053.

Chen, K.L. and Elimelech, M. 2006. Aggregation and deposition kinetics of fullerene (C60) nanoparticles. Langmuir 22(26), 10994-11001.

Chen, K.L. and Elimelech, M. 2007. Influence of humic acid on the aggregation kinetics of fullerene (C60) nanoparticles in monovalent and divalent electrolyte solutions. J. Colloid Interface Sci. 309(1), 126-134.

Chowdhury, I., Duch, M.C., Mansukhani, N.D., Hersam, M.C. and Bouchard, D. 2013. Colloidal properties and stability of graphene oxide nanomaterials in the aquatic environment. Environ. Sci. Technol. 47(12), 6288-6296.

de Melo, B.A.G., Motta, F.L. and Santana, M.H.A. 2016. Humic acids: Structural properties and multiple functionalities for novel technological developments. Mater. Sci. Eng., C 62, 967-974.

Dederichs, T., Möller, M. and Weichold, O. 2009. Colloidal stability of hydrophobic nanoparticles in ionic surfactant solutions: Definition of the critical dispersion concentration. Langmuir 25(4), 2007-2012.

Deonarine, A., Lau, B.L.T., Aiken, G.R., Ryan, J.N. and Hsu-Kim, H. 2011. Effects of humic substances on precipitation and aggregation of zinc sulfide nanoparticles. Environ. Sci. Technol. 45(8), 3217-3223.

Domingos, R.F., Tufenkji, N. and Wilkinson, K.J. 2009. Aggregation of titanium dioxide nanoparticles: Role of a fulvic acid. Environ. Sci. Technol. 43(5), 1282-1286.

Elimelech, M., Gregory, J. and Jia, X. (1995) Particle deposition and aggregation: Measurement, modelling and simulation, Butterworth-Heinemann.

Erlich, Y. and Zielinski, D. 2017. DNA fountain enables a robust and efficient storage architecture. Science 355(6328), 950-954.

Faure, B., Salazar-Alvarez, G. and Bergström, L. 2011. Hamaker constants of iron oxide nanoparticles. Langmuir 27(14), 8659-8664.

French, R.A., Jacobson, A.R., Kim, B., Isley, S.L., Penn, R.L. and Baveye, P.C. 2009. Influence of ionic strength, pH, and cation valence on aggregation kinetics of titanium dioxide nanoparticles. Environ. Sci. Technol. 43(5), 1354-1359.

Fritz, G., Schädler, V., Willenbacher, N. and Wagner, N.J. 2002. Electrosteric stabilization of colloidal dispersions. Langmuir 18(16), 6381-6390.

Furman, O., Usenko, S. and Lau, B.L.T. 2013. Relative importance of the humic and fulvic fractions of natural organic matter in the aggregation and deposition of silver nanoparticles. Environ. Sci. Technol. 47(3), 1349-1356.

Gambinossi, F., Mylon, S.E. and Ferri, J.K. 2015. Aggregation kinetics and colloidal stability of functionalized nanoparticles. Adv. Colloid Interface Sci. 222, 332-349.

Gao, Y., Ren, X., Song, G., Chen, D., Zhang, X. and Chen, C. 2020. Colloidal properties and stability of UV-transformed graphene oxide in aqueous solutions: The role of disorder degree. J. Hazard. Mater. 382, 121097.

Gebauer, J.S., Malissek, M., Simon, S., Knauer, S.K., Maskos, M., Stauber, R.H., Peukert, W. and Treuel, L. 2012. Impact of the nanoparticle–protein corona on colloidal stability and protein structure. Langmuir 28(25), 9673-9679.

Goodwin, D.J., Sepassi, S., King, S.M., Holland, S.J., Martini, L.G. and Lawrence, M.J. 2013. Characterization of polymer adsorption onto drug nanoparticles using depletion measurements and small-angle neutron scattering. Mol. Pharmaceutics 10(11), 4146-4158.

Gudarzi, M.M. 2016. Colloidal stability of graphene oxide: Aggregation in two dimensions. Langmuir 32(20), 5058-5068.

Gunsolus, I.L., Mousavi, M.P.S., Hussein, K., Bühlmann, P. and Haynes, C.L. 2015. Effects of humic and fulvic acids on silver nanoparticle stability, dissolution, and toxicity. Environ. Sci. Technol. 49(13), 8078-8086.

Gurevitch, J., Koricheva, J., Nakagawa, S. and Stewart, G. 2018. Meta-analysis and the science of research synthesis. Nature 555(7695), 175-182.

He, S., Song, B., Li, D., Zhu, C., Qi, W., Wen, Y., Wang, L., Song, S., Fang, H. and Fan, C. 2010. A graphene nanoprobe for rapid, sensitive, and multicolor fluorescent DNA analysis. Adv. Funct. Mater. 20(3), 453-459.

He, Y.T., Wan, J. and Tokunaga, T. 2008. Kinetic stability of hematite nanoparticles: The effect of particle sizes. J. Nanopart. Res. 10(2), 321-332.

Hoek, E.M.V. and Agarwal, G.K. 2006. Extended DLVO interactions between spherical particles and rough surfaces. J. Colloid Interface Sci. 298(1), 50-58.

Holland, J.G. and Geiger, F.M. 2012. Importance of length and sequence order on magnesium binding to surface-bound oligonucleotides studied by second harmonic generation and atomic force microscopy. J. Phys. Chem. B 116(22), 6302-6310.

Holland, J.G., Malin, J.N., Jordan, D.S. and Geiger, F.M. 2011. Specific and nonspecific metal ion−nucleotide interactions at aqueous/solid interfaces functionalized with adenine, thymine, guanine, and cytosine oligomers. J. Am. Chem. Soc. 133(8), 2567-2570.

Hotze, E.M., Phenrat, T. and Lowry, G.V. 2010. Nanoparticle aggregation: Challenges to understanding transport and reactivity in the environment. J. Environ. Qual. 39(6), 1909-1924.

Hsu, J.-P. and Liu, B.-T. 1998. Effect of particle size on critical coagulation concentration. J. Colloid Interface Sci. 198(1), 186-189.

Huang, P., Jia, H., Wang, T., Xu, Y., Zhang, L., Wei, X., Jia, H., Wen, S., Lv, K. and Liu, D. 2021. Effects of modification degrees on the colloidal stability of amphiphilic Janus graphene oxide in aqueous solution with and without electrolytes. Langmuir 37(33), 10061-10070.

Hurst, S.J., Lytton-Jean, A.K.R. and Mirkin, C.A. 2006. Maximizing DNA loading on a range of gold nanoparticle sizes. Anal. Chem. 78(24), 8313-8318.

Huynh, K.A. and Chen, K.L. 2011. Aggregation kinetics of citrate and polyvinylpyrrolidone coated silver nanoparticles in monovalent and divalent electrolyte solutions. Environ. Sci. Technol. 45(13), 5564-5571.

Hyung, H. and Kim, J.-H. 2008. Natural organic matter (NOM) adsorption to multi-walled carbon nanotubes: Effect of NOM characteristics and water quality parameters. Environ. Sci. Technol. 42(12), 4416-4421.

Israelachvili, J.N. (2015) Intermolecular and surface forces, Academic Press.

Jiang, Y., Raliya, R., Fortner, J.D. and Biswas, P. 2016. Graphene oxides in water: Correlating morphology and surface chemistry with aggregation behavior. Environ. Sci. Technol. 50(13), 6964-6973.

Jiang, Y., Raliya, R., Liao, P., Biswas, P. and Fortner, J.D. 2017. Graphene oxides in water: Assessing stability as a function of material and natural organic matter properties. Environ. Sci.: Nano 4(7), 1484-1493.

Jusufi, A., Likos, C.N. and Löwen, H. 2002. Counterion-induced entropic interactions in solutions of strongly stretched, osmotic polyelectrolyte stars. J. Chem. Phys. 116(24), 11011-11027.

Kegler, K., Salomo, M. and Kremer, F. 2007. Forces of interaction between DNA-grafted colloids: An optical tweezer measurement. Phys. Rev. Lett. 98(5), 058304.

Keller, A.A., Wang, H., Zhou, D., Lenihan, H.S., Cherr, G., Cardinale, B.J., Miller, R. and Ji, Z. 2010. Stability and aggregation of metal oxide nanoparticles in natural aqueous matrices. Environ. Sci. Technol. 44(6), 1962-1967.

Khan, I.A., Afrooz, A.R.M.N., Flora, J.R.V., Schierz, P.A., Ferguson, P.L., Sabo-Attwood, T. and Saleh, N.B. 2013. Chirality affects aggregation kinetics of single-walled carbon nanotubes. Environ. Sci. Technol. 47(4), 1844-1852.

Kim, C., Lee, J., Wang, W. and Fortner, J. 2020. Organic functionalized graphene oxide behavior in water. Nanomaterials 10(6), 1228.

Kim, H.-J., Phenrat, T., Tilton, R.D. and Lowry, G.V. 2009. Fe^0 nanoparticles remain mobile in porous media after aging due to slow desorption of polymeric surface modifiers. Environ. Sci. Technol. 43(10), 3824-3830.

Kolev, S.K., Petkov, P.S., Rangelov, M.A., Trifonov, D.V., Milenov, T.I. and Vayssilov, G.N. 2018. Interaction of Na^+, K^+, Mg^{2+} and Ca^{2+} counter cations with RNA. Metallomics 10(5), 659-678.

Krueger, K.M., Al-Somali, A.M., Mejia, M. and Colvin, V.L. 2007. The hydrodynamic size of polymer stabilized nanocrystals. Nanotechnology 18(47), 475709.

Lebrette, S., Pagnoux, C. and Abélard, P. 2004. Stability of aqueous TiO_2 suspensions: Influence of ethanol. J. Colloid Interface Sci. 280(2), 400-408.

Li, M. and Huang, C.P. 2010. Stability of oxidized single-walled carbon nanotubes in the presence of simple electrolytes and humic acid. Carbon 48(15), 4527-4534.

Li, Z., Shakiba, S., Deng, N., Chen, J., Louie, S.M. and Hu, Y. 2020. Natural organic matter (NOM) imparts molecular-weight-dependent steric stabilization or electrostatic destabilization to ferrihydrite nanoparticles. Environ. Sci. Technol. 54(11), 6761-6770.

Liao, R., Yang, P., Wu, W., Luo, D. and Yang, D. 2018. A DNA tracer system for hydrological environment investigations. Environ. Sci. Technol. 52(4), 1695-1703.

Liu, B., Zhao, Y., Jia, Y. and Liu, J. 2020. Heating drives DNA to hydrophobic regions while freezing drives DNA to hydrophilic regions of graphene oxide for highly robust biosensors. J. Am. Chem. Soc. 142(34), 14702-14709.

Liu, J., Legros, S., Ma, G., Veinot, J.G.C., von der Kammer, F. and Hofmann, T. 2012. Influence of surface functionalization and particle size on the aggregation kinetics of engineered nanoparticles. Chemosphere 87(8), 918-924.

Liu, X., Chen, G. and Su, C. 2011a. Effects of material properties on sedimentation and aggregation of titanium dioxide nanoparticles of anatase and rutile in the aqueous phase. J. Colloid Interface Sci. 363(1), 84-91.

Liu, X., Wazne, M., Chou, T., Xiao, R. and Xu, S. 2011b. Influence of Ca^{2+} and suwannee river humic acid on aggregation of silicon nanoparticles in aqueous media. Water Res. 45(1), 105-112.

Liu, X., Xu, X., Sun, J., Duan, S., Sun, Y., Hayat, T. and Li, J. 2018. Interaction between Al_2O_3 and different sizes of GO in aqueous environment. Environ. Pollut. 243, 1802-1809.

Louie, S.M., Spielman-Sun, E.R., Small, M.J., Tilton, R.D. and Lowry, G.V. 2015. Correlation of the physicochemical properties of natural organic matter samples from different sources to their effects on gold nanoparticle aggregation in monovalent electrolyte. Environ. Sci. Technol. 49(4), 2188-2198.

Louie, S.M., Tilton, R.D. and Lowry, G.V. 2013. Effects of molecular weight distribution and chemical properties of natural organic matter on gold nanoparticle aggregation. Environ. Sci. Technol. 47(9), 4245-4254.

Louie, S.M., Tilton, R.D. and Lowry, G.V. 2016. Critical review: Impacts of macromolecular coatings on critical physicochemical processes controlling environmental fate of nanomaterials. Environ. Sci.: Nano 3(2), 283-310.

Lu, N., Mylon, S.E., Kong, R., Bhargava, R., Zilles, J.L. and Nguyen, T.H. 2012. Interactions between dissolved natural organic matter and adsorbed DNA and their effect on natural transformation of Azotobacter vinelandii. Sci. Total Environ. 426, 430-435.

Mantilla-Calderon, D., Huang, K., Li, A., Chibwe, K., Yu, X., Ye, Y., Liu, L. and Ling, F. 2022. Emerging investigator series: Meta-analyses on SARS-COV-2 viral RNA levels in wastewater and their correlations to epidemiological indicators. Environ. Sci. Water Res. Technol. 8(7), 1391-1407.

Mirkin, C.A. (2021) Spherical nucleic acids: Volume 2, Jenny Stanford Publishing.

Mirkin, C.A., Letsinger, R.L., Mucic, R.C. and Storhoff, J.J. 1996. A DNA-based method for rationally assembling nanoparticles into macroscopic materials. Nature 382, 607-609.

Mohona, T.M., Gupta, A., Masud, A., Chien, S.-C., Lin, L.-C., Nalam, P.C. and Aich, N. 2019. Aggregation behavior of inorganic 2D nanomaterials beyond graphene: Insights from molecular modeling and modified DLVO theory. Environ. Sci. Technol. 53(8), 4161-4172.

Moore, V.C., Strano, M.S., Haroz, E.H., Hauge, R.H., Smalley, R.E., Schmidt, J. and Talmon, Y. 2003. Individually suspended single-walled carbon nanotubes in various surfactants. Nano Lett. 3(10), 1379-1382.

Mulvihill, M.J., Habas, S.E., Jen-La Plante, I., Wan, J. and Mokari, T. 2010. Influence of size, shape, and surface coating on the stability of aqueous suspensions of CdSe nanoparticles. Chem. Mater. 22(18), 5251-5257.

Napper, D.H. (1983) Polymeric stabilization of colloidal dispersions, Academic Press, London; New York.

Nason, J.A., McDowell, S.A. and Callahan, T.W. 2012. Effects of natural organic matter type and concentration on the aggregation of citrate-stabilized gold nanoparticles. J. Environ. Monit. 14(7), 1885-1892.

Nguyen, T.H. and Chen, K.L. 2007. Role of divalent cations in plasmid DNA adsorption to natural organic matter-coated silica surface. Environ. Sci. Technol. 41(15), 5370-5375.

Nguyen, T.H. and Elimelech, M. 2007. Adsorption of plasmid DNA to a natural organic matter-coated silica surface: Kinetics, conformation, and reversibility. Langmuir 23(6), 3273-3279.

Ogram, A.V., Mathot, M.L., Harsh, J.B., Boyle, J. and Pettigrew, C.A. 1994. Effects of DNA polymer length on its adsorption to soils. Appl. Environ. Microbiol. 60(2), 393-396.

Omija, K., Hakim, A., Masuda, K., Yamaguchi, A. and Kobayashi, M. 2021. Effect of counter ion valence and pH on the aggregation and charging of oxidized carbon nanohorn (CNHox) in aqueous solution. Colloids Surf. A Physicochem. Eng. Asp. 619, 126552.

Ottofuelling, S., Von Der Kammer, F. and Hofmann, T. 2011. Commercial titanium dioxide nanoparticles in both natural and synthetic water: Comprehensive multidimensional testing and prediction of aggregation behavior. Environ. Sci. Technol. 45(23), 10045-10052.

Pamies, R., Cifre, J.G.H., Espín, V.F., Collado-González, M., Baños, F.G.D. and de la Torre, J.G. 2014. Aggregation behaviour of gold nanoparticles in saline aqueous media. J. Nanopart. Res. 16(4), 2376.

Parak, W.J., Pellegrino, T., Micheel, C.M., Gerion, D., Williams, S.C. and Alivisatos, A.P. 2003. Conformation of oligonucleotides attached to gold nanocrystals probed by gel electrophoresis. Nano Lett. 3(1), 33-36.

Petosa, A.R., Jaisi, D.P., Quevedo, I.R., Elimelech, M. and Tufenkji, N. 2010. Aggregation and deposition of engineered nanomaterials in aquatic environments: Role of physicochemical interactions. Environ. Sci. Technol. 44(17), 6532-6549.

Phenrat, T., Saleh, N., Sirk, K., Kim, H.-J., Tilton, R.D. and Lowry, G.V. 2008. Stabilization of aqueous nanoscale zerovalent iron dispersions by anionic polyelectrolytes: Adsorbed anionic polyelectrolyte layer properties and their effect on aggregation and sedimentation. J. Nanopart. Res. 10(5), 795-814.

Phenrat, T., Saleh, N., Sirk, K., Tilton, R.D. and Lowry, G.V. 2007. Aggregation and sedimentation of aqueous nanoscale zerovalent iron dispersions. Environ. Sci. Technol. 41(1), 284-290.

Philippe, A. and Schaumann, G.E. 2014. Interactions of dissolved organic matter with natural and engineered inorganic colloids: A review. Environ. Sci. Technol. 48(16), 8946-8962.

Pinchuk, P. and Jiang, K. (2015) Size-dependent hamaker constants for silver and gold nanoparticles, SPIE.

Qi, Y., Xia, T., Li, Y., Duan, L. and Chen, W. 2016. Colloidal stability of reduced graphene oxide materials prepared using different reducing agents. Environ. Sci.: Nano 3(5), 1062-1071.

Qin, C., Zhang, W., Yang, B., Chen, X., Xia, K. and Gao, Y. 2018. DNA facilitates the sorption of polycyclic aromatic hydrocarbons on montmorillonites. Environ. Sci. Technol. 52(5), 2694-2703.

Qing, Z., Zhu, L., Li, X., Yang, S., Zou, Z., Guo, J., Cao, Z. and Yang, R. 2017. A target-lighted dsDNA-indicator for high-performance monitoring of mercury pollution and its antagonists screening. Environ. Sci. Technol. 51(20), 11884-11890.

Rosen, M.J. and Kunjappu, J.T. (2012) Surfactants and interfacial phenomena, John Wiley & Sons.

Saleh, N.B., Pfefferle, L.D. and Elimelech, M. 2008. Aggregation kinetics of multiwalled carbon nanotubes in aquatic systems: Measurements and environmental implications. Environ. Sci. Technol. 42(21), 7963-7969.

Saleh, N.B., Pfefferle, L.D. and Elimelech, M. 2010. Influence of biomacromolecules and humic acid on the aggregation kinetics of single-walled carbon nanotubes. Environ. Sci. Technol. 44(7), 2412-2418.

Sardar, R., Funston, A.M., Mulvaney, P. and Murray, R.W. 2009. Gold nanoparticles: Past, present, and future. Langmuir 25(24), 13840-13851.

Schramm, L.L., Stasiuk, E.N. and Marangoni, D.G. 2003. 2 Surfactants and their applications. Annual Reports Section "C" (Physical Chemistry) 99(0), 3-48.

Seeman, N.C. and Sleiman, H.F. 2017. DNA nanotechnology. Nat. Rev. Mater. 3(1), 17068.

Shen, M., Hai, X., Shang, Y., Zheng, C., Li, P., Li, Y., Jin, W., Li, D., Li, Y., Zhao, J., Lei, H., Xiao, H., Li, Y., Yan, G., Cao, Z. and Bu, Q. 2019. Insights into aggregation and transport of graphene oxide in aqueous and saturated porous media: Complex effects of cations with different molecular weight fractionated natural organic matter. Sci. Total Environ. 656, 843-851.

Sheng, A., Liu, F., Shi, L. and Liu, J. 2016. Aggregation kinetics of hematite particles in the presence of outer membrane cytochrome OmcA of Shewanella oneidenesis MR-1. Environ. Sci. Technol. 50(20), 11016-11024.

Smith, B., Wepasnick, K., Schrote, K.E., Bertele, A.R., Ball, W.P., O'Melia, C. and Fairbrother, D.H. 2009a. Colloidal properties of aqueous suspensions of acid-treated, multi-walled carbon nanotubes. Environ. Sci. Technol. 43(3), 819-825.

Smith, B., Wepasnick, K., Schrote, K.E., Cho, H.-H., Ball, W.P. and Fairbrother, D.H. 2009b. Influence of surface oxides on the colloidal stability of multi-walled carbon nanotubes: A structure−property relationship. Langmuir 25(17), 9767-9776.

Snoswell, D.R.E., Duan, J., Fornasiero, D. and Ralston, J. 2005. Colloid stability of synthetic titania and the influence of surface roughness. J. Colloid Interface Sci. 286(2), 526-535.

Stenkamp, V.S. and Berg, J.C. 1997. The role of long tails in steric stabilization and hydrodynamic layer thickness. Langmuir 13(14), 3827-3832.

Storhoff, J.J., Elghanian, R., Mirkin, C.A. and Letsinger, R.L. 2002. Sequence-dependent stability of DNA-modified gold nanoparticles. Langmuir 18(17), 6666-6670.

Su, Y., Yang, G., Lu, K., Petersen, E.J. and Mao, L. 2017. Colloidal properties and stability of aqueous suspensions of few-layer graphene: Importance of graphene concentration. Environ. Pollut. 220, 469-477.

Sun, B., Zhang, Y., Liu, Q., Yan, C., Xiao, B., Yang, J., Liu, M. and Zhu, L. 2020. Lateral size dependent colloidal stability of graphene oxide in water: Impacts of protein properties and water chemistry. Environ. Sci.: Nano 7(2), 634-644.

Surette, M.C. and Nason, J.A. 2019. Nanoparticle aggregation in a freshwater river: The role of engineered surface coatings. Environ. Sci.: Nano 6(2), 540-553.

Surette, M.C., Nason, J.A. and Kaegi, R. 2019. The influence of surface coating functionality on the aging of nanoparticles in wastewater. Environ. Sci.: Nano 6(8), 2470-2483.

Szabo, T., Maroni, P. and Szilagyi, I. 2020. Size-dependent aggregation of graphene oxide. Carbon 160, 145-155.

Tang, H., Zhang, S., Huang, T., Zhang, J. and Xing, B. 2021. Mechanisms of the aggregation of graphene oxide at high pH: Roles of oxidation debris and metal adsorption. Environ. Sci. Technol. 55(21), 14639-14648.

Vold, M.J. 1954. Van der waals' attraction between anisometric particles. J. of Colloid Sci. 9(5), 451-459.

Wang, M., Gao, B., Tang, D., Sun, H., Yin, X. and Yu, C. 2018. Effects of temperature on aggregation kinetics of graphene oxide in aqueous solutions. Colloids Surf. A Physicochem. Eng. Asp. 538, 63-72.

Wang, X., Yang, D., Liu, M., Cao, D., He, N. and Wang, Z. 2019. Highly sensitive fluorescence biosensor for intracellular telomerase detection based on a single patchy gold/carbon nanosphere via the combination of nanoflare and hybridization chain reaction. Biosens. Bioelectron. 137, 110-116.

Wu, L., Liu, L., Gao, B., Muñoz-Carpena, R., Zhang, M., Chen, H., Zhou, Z. and Wang, H. 2013. Aggregation kinetics of graphene oxides in aqueous solutions: Experiments, mechanisms, and modeling. Langmuir 29(49), 15174-15181.

Wu, W., Giese, R.F. and van Oss, C.J. 1999. Stability versus flocculation of particle suspensions in water—correlation with the extended DLVO approach for aqueous systems, compared with classical DLVO theory. Colloids Surf. B: Biointerfaces 14(1), 47-55.

Xia, T., Guo, X., Lin, Y., Xin, B., Li, S., Yan, N. and Zhu, L. 2019. Aggregation of oxidized multi-walled carbon nanotubes: Interplay of nanomaterial surface O-functional groups and solution chemistry factors. Environ. Pollut. 251, 921-929.

Xu, H., Liao, C., Zuo, P., Liu, Z. and Ye, B.-C. 2018. Magnetic-based microfluidic device for on-chip isolation and detection of tumor-derived exosomes. Anal. Chem. 90(22), 13451-13458.

Xu, W., He, W., Du, Z., Zhu, L., Huang, K., Lu, Y. and Luo, Y. 2021. Functional nucleic acid nanomaterials: Development, properties, and applications. Angew. Chem. Int. Ed. 60(13), 6890-6918.

Xu, X., Mastropietro, D., Ruths, M., Tirrell, M. and Yu, J. 2019. Ion-specific effects of divalent ions on the structure of polyelectrolyte brushes. Langmuir 35(48), 15564-15572.

Yang, K., Chen, B., Zhu, X. and Xing, B. 2016. Aggregation, adsorption, and morphological transformation of graphene oxide in aqueous solutions containing different metal cations. Environ. Sci. Technol. 50(20), 11066-11075.

Yin, Y., Shen, M., Tan, Z., Yu, S., Liu, J. and Jiang, G. 2015. Particle coating-dependent interaction of molecular weight fractionated natural organic matter: Impacts on the aggregation of silver nanoparticles. Environ. Sci. Technol. 49(11), 6581-6589.

Yu, J., Mao, J., Yuan, G., Satija, S., Jiang, Z., Chen, W. and Tirrell, M. 2016. Structure of polyelectrolyte brushes in the presence of multivalent counterions. Macromolecules 49(15), 5609-5617.

Yu, S., Shen, M., Li, S., Fu, Y., Zhang, D., Liu, H. and Liu, J. 2019. Aggregation kinetics of different surface-modified polystyrene nanoparticles in monovalent and divalent electrolytes. Environ. Pollut. 255, 113302.

Yu, X., Chen, F., Wang, R. and Li, Y. 2018. Whole-bacterium selex of DNA aptamers for rapid detection of E.coli O157:H7 using a QCM sensor. J Biotechnol 266, 39-49.

Zhang, H., Smith, J.A. and Oyanedel-Craver, V. 2012. The effect of natural water conditions on the anti-bacterial performance and stability of silver nanoparticles capped with different polymers. Water Res. 46(3), 691-699.

Zhang, K., Song, S., Huang, S., Yang, L., Min, Q., Wu, X., Lu, F. and Zhu, J.-J. 2018. Lighting up microrna in living cells by the disassembly of lock-like DNA-programmed UCNPs-AuNPs through the target cycling amplification strategy. Small 14(40), 1802292.

Zhang, W. (2014). Nanoparticle aggregation: principles and modeling. In: Capco, D., Chen, Y. (eds) Nanomaterial: Advances in experimental medicine and biology, vol 811. Springer, Dordrecht.

Zhang, Y., Chen, Y., Westerhoff, P., Hristovski, K. and Crittenden, J.C. 2008. Stability of commercial metal oxide nanoparticles in water. Water Res. 42(8), 2204-2212.

Zhou, D., Ji, Z., Jiang, X., Dunphy, D.R., Brinker, J. and Keller, A.A. 2013. Influence of material properties on TiO_2 nanoparticle agglomeration. PLOS ONE 8(11), e81239.

Zhou, D. and Keller, A.A. 2010. Role of morphology in the aggregation kinetics of ZnO nanoparticles. Water Res. 44(9), 2948-2956.

Zhou, J., Battig, M.R. and Wang, Y. 2010. Aptamer-based molecular recognition for biosensor development. Anal. Bioanal. Chem. 398(6), 2471-2480.

Chapter 3 A Meta-analysis to Revisit the Property-Aggregation Relationships of Carbon Nanomaterials: Experimental Observations Versus Predictions of the DLVO Theory

(This chapter has been written into a research article, Peng, B. and Jiang, Y. A meta-analysis to revisit the property-aggregation relationships of carbon nanomaterials: Experimental observations versus predictions of the DLVO theory. To be submitted)

Abstract

Contradicting relationships between physicochemical properties of nanomaterials (e.g., size and zeta potential) and their aggregation behavior have been constantly reported in previous literature, and such contradictions deviate from the predictions of the DLVO theory. To resolve such controversies, in this work, we employed a meta-analytic approach to synthesize the data from 46 individual studies reporting the critical coagulation concentration (CCC) of two carbon nanomaterials, namely, graphene oxide (GO) and carbon nanotube (CNT). The correlations between CCC and material physicochemical properties (i.e., size, zeta potential, and surface functionalities) were examined and compared with the theoretical predictions. Results showed that the CCC of electrostatically stabilized carbon nanomaterials increased with decreasing nanomaterial size when their hydrodynamic sizes were smaller than *ca.* 200 nm. This is qualitatively consistent with the prediction of the DLVO theory, but with a smaller threshold size than the predicted 2 μm. Above the threshold size, material zeta potential can be correlated to CCC by $CCC/\lambda \propto \tanh^4\left(\frac{a\psi_0}{4}\right)$ for nanomaterials with moderate/low surface charge, in agreement with the DLVO theory. The correlation was not observed for highly charged nanomaterials because of their underestimated surface charge by zeta potential. Furthermore,

a correlation between the C/O ratio and CCC was observed, where a lower C/O ratio resulted in a higher CCC. Overall, our findings rationalized the inconsistency between experimental observation and theoretical prediction, and provided essential insights into the aggregation behavior of nanomaterials in water, which could facilitate their rational design.

3.1 Introduction

Engineered nanomaterials are manufactured materials with at least one nanoscale dimension (*ca.* 1−100 nm). The high surface energy of nanomaterial often leads to uncontrolled aggregation, which affects not only their (designed) functionality (e.g., reduced reactivity (Hotze et al., 2010; Vikesland et al., 2007)), but also their toxicity, bioavailability, fate and transport in the environment (Baalousha, 2017). As such, the aquatic aggregation behavior of various nanomaterials has been extensively studied over the past two decades (Chen et al., 2006; Peng et al., 2022b; Saleh et al., 2008; Sano et al., 2001; Wu et al., 2013). Quantitative assessment of the aggregation behavior of nanomaterials could be performed by estimating their critical coagulation concentration (CCC) in electrolytes, which is typically achieved by monitoring the growth of nanomaterial size at the early stage of aggregation using time-resolved dynamic light scattering (Chen and Elimelech, 2006). The CCC represents the minimum concentration of counterions required to fully destabilize the nanomaterial, where the aggregation is limited by Brownian diffusion (Elimelech et al., 1995).

As the number of studies investigating the CCC of nanomaterials continues to grow, wide discrepancies in the reported CCC values are often observed, even for the same type of nanomaterial. For example, Yang et al. (2016) reported the CCC of graphene oxide (GO) in NaCl electrolyte as 36 mM, while Kim et al. (2020) reported a value of 387.2 mM NaCl; Xia et al. (2019) determined the CCC of multi-wall carbon nanotube (MWNT) to be 8.8 mM NaCl, while Yi and Chen (2011) reported the CCC of MWNT as 210 mM NaCl. Such variations are likely induced by the different physicochemical properties of the nanomaterials (varied size, surface charge, surface chemistry, etc.) in each study. Many nanomaterials, such as GO, can be more accurately recognized as a family of nanomaterials with different physicochemical properties.

Contradictory relationships between certain physicochemical properties of nanomaterials and their colloidal stability are often observed among studies. For instance, the CCC of GO was found to be negatively correlated to its material size (Sun et al., 2020; Szabo et al., 2020). Similar effect of size on the CCC has also been reported for other nanomaterials, such as CdSe (Mulvihill et al., 2010), hematite (Sheng et al., 2016), and silver nanomaterials (Afshinnia et al., 2017). The observed negative correlation between CCC and material size is consistent with an early prediction from the classic Derjaguin-Landau-Verwey-Overbeek (DLVO) theory (Hsu and Liu, 1998). However, the opposite trend has also been observed. Hematite (He et al., 2008) and TiO_2 nanomaterials (Zhou et al., 2013) were reported to be more prone to aggregation as the size of nanomaterials became smaller, and the colloidal stability of gold nanomaterials was reported to be independent of their material size (Liu et al., 2012).

In addition to material size, zeta potential, which is often used to infer the surface charge of nanomaterials (Lowry et al., 2016), has also been correlated to the CCC of nanomaterials based on the DLVO theory. The CCC is predicted to be proportional to the material surface potential, which is often approximated by the zeta potential, and a higher zeta potential results in a higher CCC (Hsu and Kuo, 1997). This proportionality was demonstrated in our previous work, in which the CCCs of five reduced GOs were mathematically related to their zeta potential as predicted by the DLVO theory (Jiang et al., 2016). However, a few studies also observed significantly varied CCC of nanomaterials with similar zeta potential, deviating from the theoretical prediction. For example, Qi et al. (2016) reported that the CCC of GO in NaCl electrolyte was almost twice that of the L-ascorbic acid-reduced GO, whereas the zeta potentials of these nanomaterials were similar (*ca.* -40 mV). Likewise, although the zeta potential of three oxidized MWNTs were similar (*ca.* -60 mV), the CCC of these materials in NaCl electrolyte were 22.5, 57.9, and 108.1 mM, respectively (Bai et al., 2014).

Studies have also been trying to correlate the material stability and surface chemistry, such as the surface oxidation degree for carbon nanomaterials. Both positive and negative correlations have been observed. For example, Qi et al. (2016) reported that the CCC of GO in NaCl electrolyte gradually decreased from 210 mM to 41 mM along with the increasing C/O ratio from 2.1 to 5.7, whereas Gao et al. (2020) observed that GO with a lower C/O ratio (2.3) was more stable than the one with a higher C/O ratio (2.6) in three common electrolytes (NaCl, $MgCl_2$, and $CaCl_2$). Azizighannad and Mitra (2018) found similar stability for GO with different oxidation degrees (C/O ratio = 1.0 and 2.1, respectively) in NaCl and $MgCl_2$ electrolytes. Jiang et al. (2016) observed a positive correlation between the oxidation degree and the CCC of GO in $CaCl_2$ electrolyte, while Xia et al. (2019) reported the opposite for MWNT.

Altogether, the above-mentioned study-to-study variations on the property-aggregation relationships of nanomaterials suggest that research synthesis efforts are needed to identify whether there is a consistent relationship between a specific property of nanomaterials and their aggregation, and such work has been rarely performed. Furthermore, although the analytical expressions of the classic DLVO theory of colloid science are commonly used to interpret the aggregation behavior of nanomaterials (Chowdhury et al., 2013; Gudarzi, 2016; Omija et al., 2021), it must be noted that these analytical expressions were obtained under certain assumptions, such as the Derjaguin approximation and/or the Debye−Hückel approximation (Hsu and Kuo, 1997; Hsu and Liu, 1998; Trefalt et al., 2017). Nanomaterial properties (such as small size and non-spherical shape) may not satisfy these assumptions, thus challenging the applicability of these analytical expressions (Baalousha, 2017; Hotze et al., 2010). An examination of such applicability based on a large data set is required to resolve the inconsistency between theoretical prediction and experimental observation. Over the past two decades, the increase of nanomaterial aggregation research generates a large set of valuable experimental data, and meta-analysis is an objective, quantitative, and powerful approach to synthesize findings across studies (Gurevitch et al., 2018). To date, according to the best of our knowledge, the use of a meta-analytic approach to examine the validity/applicability of the theoretical framework in interpreting the aggregation behavior of nanomaterials has yet to be performed.

In this study, we conducted a meta-analysis of 46 individual studies reporting the CCC of carbon nanomaterials and correlated their CCC in electrolytes and material intrinsic properties (i.e., size, zeta potential, and surface chemistry; the three most characterized properties). Specifically, we selected two types of carbon nanomaterials (i.e., graphene-based nanomaterials and carbon nanotubes) for analysis because these materials with different physicochemical properties have been widely studied by multiple groups of researchers over the past two decades. We aim to resolve the seemingly contradictory effects of physicochemical properties of nanomaterials on their aggregation behavior and examine the applicability of related theoretical predictions of CCC with regard to size and surface charge based on the DLVO theory. Overall, this meta-analytic approach will allow us to gain an improved understanding of the role of material physicochemical properties in determining the aggregation behavior of nanomaterials in water.

3.2 Experimental

3.2.1 Data Sources

We searched the Google Scholar database for publications that reported the critical coagulation concentration (CCC) of carbon nanomaterials (i.e., GO, multi- and single-wall carbon nanotubes (MWNT and SWNT)) by August 29th, 2022. Studies were identified with the search term “material critical coagulation concentration” (material refers to the carbon nanomaterials mentioned above). In the searching, only original research articles (i.e., excluding reviews) were retained and the language was restricted to English.

3.2.2 Study Selection and Eligibility Criteria

After the studies were retrieved, full-text records were examined to assess their eligibility for analysis. Specifically, we applied two selection criteria: (1) the critical coagulation concentration (CCC) of nanomaterials was determined by time-resolved dynamic light scattering (TR-DLS) at pH 5-8; (2) nanomaterials were electrostatically stabilized (i.e., no surface coating of surfactant/polymer, etc.). Rationale for criterion 1 is that the CCC of nanomaterials could be determined by the TR-DLS method (Chen and Elimelech, 2006; Saleh et al., 2008) or the UV-vis method (Lin et al., 2009; Sano et al., 2001). Both methods measure the aggregation of nanomaterials at different electrolyte concentrations; the former obtains the CCC as the minimum electrolyte concentration at which nanomaterial aggregation is limited by Brownian motion, while the latter determines the CCC at which the loss of absorbance reaches 0.5. The varied experimental approach could weaken the validity of comparison among studies. Rationale for criterion 2 is that the aggregation behavior of coated nanomaterials is largely determined by the properties of the surface coating rather than those of the 'bare' nanomaterial (Bouchard et al., 2012; Chang et al., 2015; Huang et al., 2021; Liu et al., 2016; Louie et al., 2013; Peng et al., 2022a; Peng et al., 2022b).

3.2.3 Data Extraction

Nanomaterials properties and CCC in NaCl/$MgCl_2$/$CaCl_2$ electrolytes were extracted from the tables or from figures in selected publications using PlotDigitizer (https://plotdigitizer.com/). Typically, the physicochemical properties of nanomaterial reported in the literature include shape, size (hydrodynamic size measured by DLS and/or physical dimension examined by TEM/SEM/AFM), surface charge (zeta potential or electrophoretic mobility), and surface functionalities. Since the CCC was determined by TR-DLS, the hydrodynamic size determined by DLS was used for analysis in this study. The measured electrophoretic mobility is typically used to calculate the zeta potential using the

Smoluchowski equation (Jiang et al., 2016; Wu et al., 2013). This estimated zeta potential is often used to infer the surface charge and predict the aggregation behavior of nanomaterials (Lowry et al., 2016). Surface functionalities, including the C/O ratio and fraction of functional groups, were characterized by X-ray photoelectron spectroscopy (XPS). The fractions of functional groups (C-C/C-O/C=O/O-C=O) were obtained by deconvoluting the C1s spectra. The CCC of nanomaterial in NaCl/$MgCl_2$/$CaCl_2$ electrolytes, as well as the corresponding pH under which CCC was determined, was recorded for analysis. All the data are summarized in Table S3.1-S3.4 and Figure S3.1 (Appendix A).

The surface charge of GO/rGO/MWNT obtained from potentiometric titration experiments from individual studies were collected and analyzed (Dimiev et al., 2013; Gaidukevic et al., 2021; Gao et al., 2011; Konkena and Vasudevan, 2012; Smith et al., 2009b; Sun et al., 2012; Tang et al., 2021; Tombácz et al., 2020; Zhang et al., 2021; Zhao et al., 2011; Zhao et al., 2018). Titration experiment measures the number of ionized groups on material. For GO and rGO, the surface charge density was calculated by assuming each ionized group carries one negative charge and a surface area of 1800 m^2/g (Gudarzi, 2016). For MWNT, the surface charge density was retrieved from Smith et al. (2009b).

3.2.4 Data Analysis

Based on the C/O ratio from XPS measurement, graphene-based nanomaterials were further classified as GO and reduced GO (rGO). Materials with C/O ratio > 2.5 were classified as rGO, and those with C/O ratio < 2.5 were considered as GO (Araújo et al., 2017). For those studies that did not report XPS data, GO/rGO as indicated by the article was used for the classification.

The CCC values among different nanomaterials were compared using one-way ANOVA followed by the Tukey test. The correlation between the reported CCC values and material physicochemical properties was examined by the Spearman's rank correlation coefficient (ρ) for GO/rGO/MWNT (Table S3.5-S3.7), and SWNT was excluded for such analysis due to limited data. Value of the coefficient varies between 1.0 (a perfect positive correlation) and -1.0 (a perfect negative correlation), and a value of 0 indicates no association between ranks. The results of the Spearman correlation are reported in the format of ρ [sample size], followed by the *p* value.

3.2.5 Analytical Expressions from the DLVO Theory

The DLVO theory assumes that the total interaction energy (V_T) of two particles is the sum of electric double layer repulsion (V_{EDL}) and van der Waals attraction (V_{vdW}). Since the methods used to characterize the hydrodynamic size and zeta potential of non-spherical nanomaterials treated them as spherical nanoparticles that have the same average translational diffusion coefficients (Sun et al., 2020), we therefore used analytical expressions of interaction energy derived for spherical particles in the modeling. The use of sphere-sphere DLVO model for non-spherical nanomaterials has been demonstrated in previous individual studies and satisfactory results were reported (Huang et al., 2021; Jiang et al., 2016; Kim et al., 2020).

Assuming that the thickness of the electrical double layer is much smaller than the particle size, the Derjaguin approximation was applied to obtain the electrical potential energy between two spherical particles in *a:b* electrolyte (Hsu and Kuo, 1997):

$$V_{EDL} = \frac{32(a+b)\pi X_0 n k_B T}{a k_3^2 \kappa^3}\left[\tanh^2\left(\frac{a\psi_0}{4}\right)\right]\exp(-k_3 L)\left[1-\frac{1}{2k_3 X_0}\left(1-\exp(-2k_3 X_0)\right)\right] \tag{3.1}$$

$$\psi_0 = \frac{e\Phi_0}{k_B T} \tag{3.2}$$

$$X_0 = \kappa r_0 \tag{3.3}$$

$$\kappa^2 = \frac{a(a+b)ne^2}{\varepsilon_0 \varepsilon_r k_B T} \tag{3.4}$$

where ψ_0 is dimensionless surface potential and Φ_0 is surface potential; X_0 is the dimensionless radius of particle and r_0 is particle radius; L is the surface-to-surface distance; κ is the reciprocal Debye length, ε_0 and ε_r are the permeability of vacuum and the relative permeability of water, respectively, T is the absolute temperature, e is the elementary charge,

k_B is the Boltzmann constant; n is the number concentration of cations (nanomaterials surveyed in this study were all negatively charged) in bulk phase, and k_3 is a parameter related to valences of electrolyte: for NaCl, $k_3 = 1$; for $CaCl_2$ and $MgCl_2$, $k_3 \approx 1.078$.

The van der Waals potential can be estimated by (Hsu and Kuo, 1997):

$$V_{vdW} = \frac{-A_{121}X_0}{12L} \tag{3.5}$$

where A_{121} is the Hamaker constant for the nanomaterial-water-nanomaterial system.

The total interaction energy V_T is the sum of V_{EDL} and V_{vdW}, and at CCC

$$V_T = 0 \text{ and } \frac{dV_T}{dL} = 0 \tag{3.6}$$

By solving equations (3.3), (3.5), and (3.6), CCC can be obtained:

$$n = \frac{\lambda \tanh^4\left(\frac{a\psi_0}{4}\right)}{a^5(a+b)k_3^6}\frac{(4\pi\varepsilon_0\varepsilon_r)^3(k_BT)^5 48^2}{e^6 {A_{121}}^2 \pi \exp{(2)}} \tag{3.7}$$

$$\lambda = \left[1 - \frac{1}{2k_3X_0}\left(1 - exp(-2k_3X_0)\right)\right]^2 \tag{3.8}$$

That is, CCC is proportional to the Hamaker constant and surface potential:

$$\frac{n}{\lambda} \propto \frac{1}{A_{121}^2}\tanh^4\left(\frac{a\psi_0}{4}\right) \tag{3.9}$$

For $X_0 \gg 1$, i.e., the assumption that the thickness of the electrical double layer (κ^{-1}) is much smaller than the particle radius (r_0), $\lambda \to 1$.

In the case when the thickness of an electrical double layer is not much smaller than the particle radius ($\kappa r_0 > 1$), the van der Waals potential between two spherical particles in Z:Z symmetric electrolyte can be estimated by (Hsu and Liu, 1998):

$$V_{vdW} = \frac{-A_{121}}{6}\left\{\frac{2r_0^2}{R^2-4r_0^2} + \frac{2r_0^2}{R^2} + \ln(\frac{R^2-4r_0^2}{R^2})\right\} \tag{3.10}$$

where R is the center-to-center distance between two particles. The electrical potential energy can be approximated as (Hsu and Liu, 1998):

$$V_{EDL} = B\frac{r_0^2}{R}\ln\{1 + exp(-\kappa L)\}) \tag{3.11}$$

$$B = \varepsilon_0 \varepsilon_r (\frac{k_B T}{Ze})^2 \left\{4 \exp\left(\frac{\kappa L}{2}\right) \tanh^{-1}[\exp\left(\frac{-\kappa L}{2}\right) \tanh\,(\frac{Ze\psi_0}{4k_B T})]\right\}^2 \tag{3.12}$$

An approximate solution of the inverse Debye length (κ) at CCC could be obtained by solving Equation 3.6, 3.10, and 3.11 (Hsu and Liu, 1998):

$$\kappa \cong \frac{8}{7} Q - \frac{80 + 128 \ln(\frac{L_m}{r_0})}{56 r_0} \tag{3.13}$$

$$Q = \frac{6B}{A_{121}} \ln\left[1 + exp\left(-\frac{8}{7}\right)\right] \tag{3.14}$$

L_m is the closest surface-to-surface distance between two particles.

3.3 Results and Discussion

Our search identified a total of 62 individual studies, and after the screening, 46 studies were included in our analysis (An et al., 2021; Azizighannad and Mitra, 2018; Bouchard et al., 2012; Chowdhury et al., 2013; Chowdhury et al., 2015; Du et al., 2018; Feng et al., 2017; Gao et al., 2020; Gao et al., 2022; Huang et al., 2016; Jiang et al., 2016; Jiang et al., 2017; Khan et al., 2013; Kim et al., 2020; Li and Huang, 2010; Li et al., 2022; Liu et al., 2016; Liu et al., 2018; Ntim et al., 2012; Ntim et al., 2011; Park et al., 2018; Qi et al., 2016; Saleh et al., 2008; 2010; Shen et al., 2019; Smith et al., 2009a; Smith et al., 2009b; Song et al., 2022; Sotirelis and Chrysikopoulos, 2017; Story et al., 2020; Su et al., 2017; Sun et al., 2018; Sun et al., 2021; Sun et al., 2020; Szabo et al., 2020; Tang et al., 2017; Wang et al., 2018; Wu et al., 2013; Wu and Mitra, 2014; Wu et al., 2017; Xia et al., 2019; Yang et al., 2016; Yang et al., 2017; Yi and Chen, 2011; Zeng et al., 2019; Zhao et al., 2015). These studies reported the CCC of (electrostatically stabilized) nanomaterials in NaCl/$MgCl_2$/$CaCl_2$ electrolytes using TR-DLS. Figure 3.1 describes the details of the search and Tables S3.1-S3.4 summarize the basic characteristics of nanomaterials studied in the included studies.

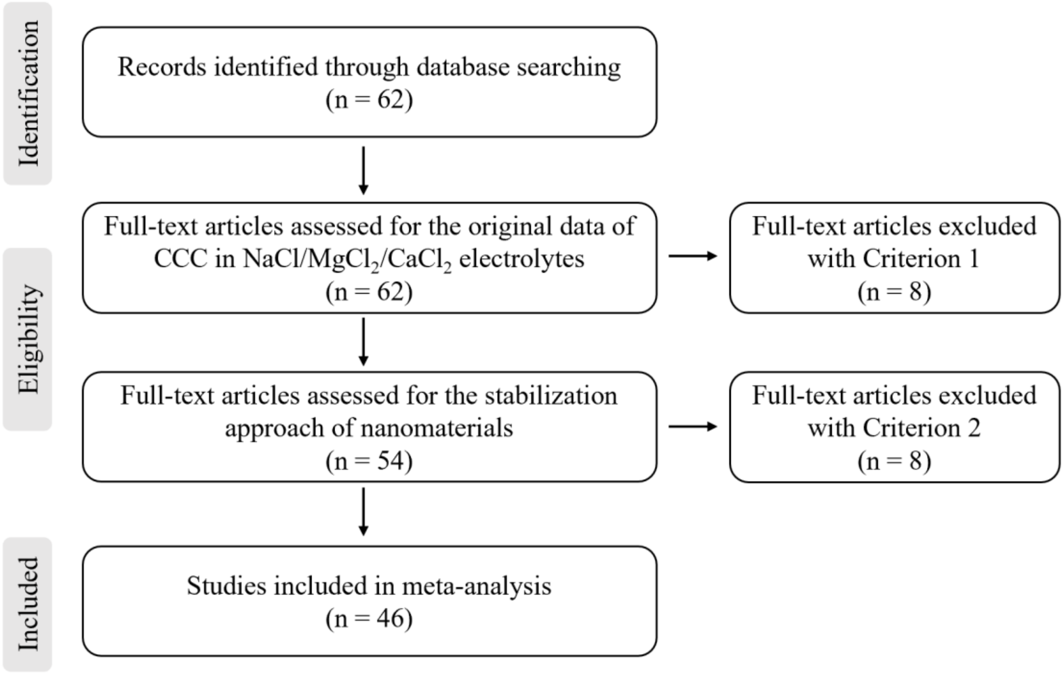

Figure 3.1 Study selection flow diagram. The two criteria used in the screening for eligibility are: Criterion 1, the critical coagulation concentration (CCC) of nanomaterials was determined in pH 5-8 via time-resolved dynamic light scattering; Criterion 2, nanomaterials were electrostatically stabilized (i.e., no surface coating of surfactant/polymer, etc.).

Figure 3.2 depicts the box plots of the CCC of each nanomaterial reported in these studies. The figures show that the CCC of the same type of nanomaterial could vary significantly from study to study, e.g., the NaCl CCC of GO ranged from 28 to 387.2 mM (Figure 3.2a). The CCC variations in divalent electrolytes ($MgCl_2$ and $CaCl_2$) were much smaller compared to those in NaCl electrolyte (Figure 3.2b-c). For instance, the $MgCl_2$ CCC of GO ranged from 1.2 to 19 mM and the $CaCl_2$ CCC ranged from 0.3 to 4.2 mM. The smaller variation of $MgCl_2$/$CaCl_2$ CCC than NaCl CCC could be attributed to that divalent counterions screen the electric double layer more efficiently than monovalent counterions and possible divalent cation bridging (Stankus et al., 2011). The experimental conditions for CCC determination were limited to a simple system consisting of nanomaterial and electrolyte, and the pH was in the range of 5-8. In the collected data, 18 out of 48 records reported the CCC of GO in pH 5.0-6.0, 12 out of 48 in pH 6.0-7.0, and 20 out of 48 in pH 7.0-8.0; 18 out of 21 records reported the rGO CCC in pH 6.0-7.0; all 42 records reported the CCC of MWNT in pH 6.0-7.2; and all 4 records reported the CCC of SWNT in pH 6.0-7.0. Deprotonation of carboxyl and phenolic functional groups on the surface of these carbon nanomaterials mainly contribute to their surface charge (Jiang et al., 2016; Smith et al., 2009b). The pK_a of carboxyl group on aromatic rings is lower than 4.2 and the pK_a of phenolic group is around 10 (Jiang et al., 2016). Therefore, within the pH range of 5-8, most of the carboxyl functional groups are deprotonated and the impact of pH on the CCC is minimum (Li and Huang, 2010). Furthermore, we have also analyzed the property-aggregation relationships of nanomaterials with a narrower pH range of 6.0-8.0 (data not shown) and the conclusions were consistent with those shown later in this work. As such, the varied CCC of the same type of nanomaterial was mainly attributed to the difference in the material intrinsic physicochemical properties. The Spearman's rank correlation coefficient between CCC and material physicochemical properties for GO/rGO/MWNT are presented in Table S3.5-S3.7, respectively. SWNT is excluded due to limited data. Below we discuss the correlation between the CCC and the varied physicochemical properties of nanomaterials.

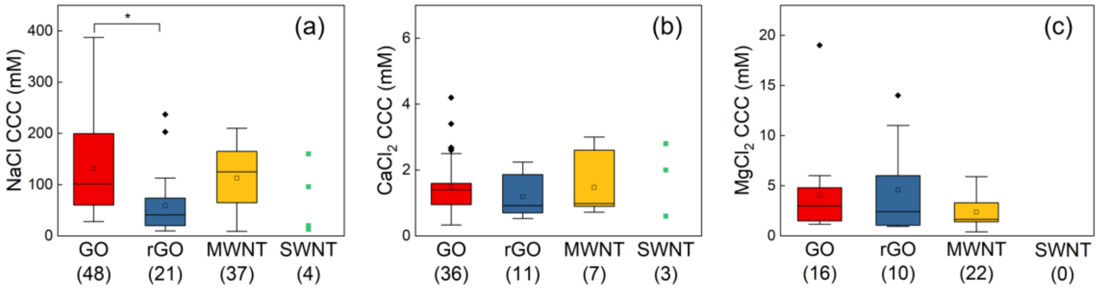

Figure 3.2 Box plots of critical coagulation concentrations (CCC) of carbon nanomaterial in (a) NaCl, (b) $CaCl_2$, and (c) $MgCl_2$ electrolytes. Sample size of each box is shown in the corresponding bracket. Asterisks indicate a significant difference (one-way ANOVA test followed by the Tukey test for multiple comparisons, $p < 0.05$).

3.3.1 Correlation between CCC and Nanomaterial Size

Figure S3.2 plots the CCC of each nanomaterial as a function of its reported hydrodynamic size. Results of the Spearman correlation analysis indicated that there was a significant negative correlation between the NaCl CCC and hydrodynamic size of GO (ρ [40] = -0.54, $p < 0.001$) and MWNT (ρ [22] = -0.82, $p < 0.001$), but the negative correlation was not statistically significant for rGO (ρ [20] = -0.34, $p = 0.138$). Due to the limited data of SWNT, the Spearman correlation analysis was not performed. The insignificant correlation observed for rGO was because that the varied zeta potential of rGO (from *ca.* -5 to -50 mV, Figure S3.1e) could influence the correlation between NaCl CCC and hydrodynamic size (Afshinnia et al., 2017). To minimize the interference from zeta potential, we analyzed rGO with similar zeta potential (Figure 3.3b) and observed a significant negative correlation between NaCl CCC and material size (ρ [9] = -0.84, $p = 0.009$). The negative correlation between the NaCl CCC and hydrodynamic size also existed for GO (ρ [21] = -0.48, $p = 0.033$) and MWNT (ρ [13] = -0.86, $p < 0.001$) when the condition of similar zeta potential was applied (Figure 3.3a and c). Due to the limited data and varied surface charges of SWNT of different sizes (Figure S3.1j), the relationship between NaCl CCC and material size cannot be established.

In divalent electrolytes, a negative correlation between the $MgCl_2$/$CaCl_2$ CCC and the hydrodynamic size can also be observed for GO, rGO, and MWNT by analyzing the nanomaterials with similar zeta potential (Figure 3.3d-i). The Spearman correlation analysis indicated a significant negative correlation between the CCC and hydrodynamic size for GO in $MgCl_2$ (ρ [9] = -0.69, $p = 0.038$) and $CaCl_2$ (ρ [26] = -0.64, $p = 0.002$), rGO in $MgCl_2$ (ρ [5] = -0.97, $p = 0.005$), and MWNT in $MgCl_2$ (ρ [9] = -0.80, $p = 0.009$). rGO and MWNT in $CaCl_2$ were not analyzed due to limited data. If the condition of similar zeta potential was not applied, the correlation between $MgCl_2$/$CaCl_2$ CCC and hydrodynamic size became weaker (Table

S3.5-3.7), since both surface charge and material size were influencing the nanomaterial stability.

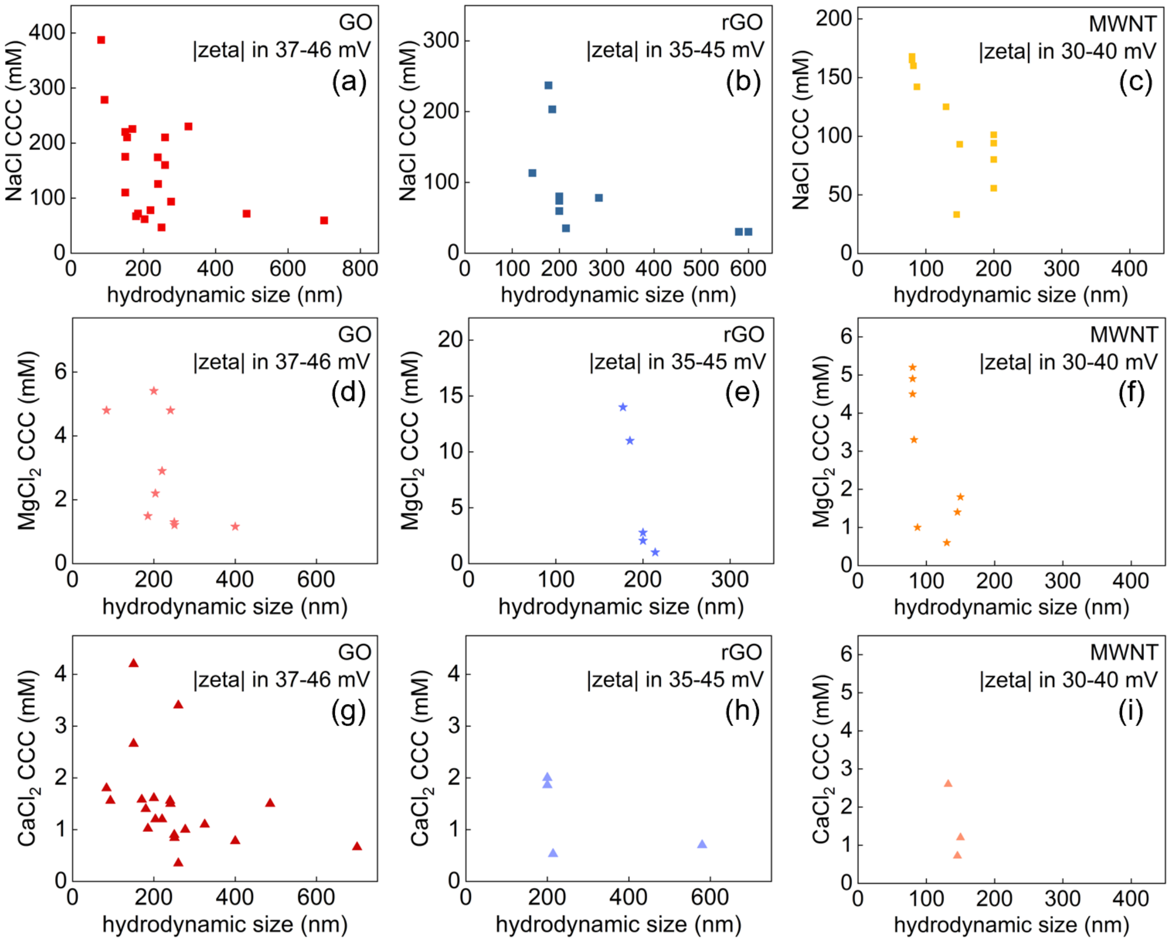

Figure 3.3 The critical coagulation concentration (CCC) of GO, rGO, and MWNT in (a-c) NaCl, (d-f) $MgCl_2$, and (g-i) $CaCl_2$ electrolytes are plotted as a function of their hydrodynamic size.

The relationship between CCC and nanomaterial size has also been investigated in previous individual studies. Sun et al. (2020) reported an increased NaCl CCC with decreasing lateral size of GO (from 1000 to 200 nm, corresponding to hydrodynamic size from 240 to 93 nm), and the zeta potentials of these nanomaterials with different sizes were similar (*ca.* -42 mV). Our conclusion was consistent with theirs. For MWNT, contradicting effects of material size were reported. While Ntim et al. (2012) observed the shorter MWNT (correspondingly smaller hydrodynamic size) possessed a higher CCC than the longer one, Wu and Mitra (2014) reported the longer MWNT was more stable in electrolyte. The contradiction was likely due to the varied zeta potentials of MWNT along with size (*ca.* -30 mV for the short one and -38 mV for the long one) in Wu and Mitra's work, whereas the zeta potential of nanomaterials with different sizes were similar (*ca.* -27 mV) in Ntim et al.'s work. The negative correlation between NaCl CCC and particle size has also been observed for non-carbon nanomaterials (Afshinnia et al., 2017; Mulvihill et al., 2010; Sheng et al., 2016). For example, Afshinnia et al. (2017) examined the CCC of silver nanomaterials (Ag NMs) from 11 research articles and concluded that the CCC of Ag NMs increased with decreasing particle size at fixed zeta potential.

Nanomaterial aggregation is often interpreted based on the DLVO theory. Theoretical work by Hsu and Liu based on the DLVO theory predicted the CCC to be inversely related to particle size when the particle is smaller than 2 μm (Equation 3.13) (Hsu and Liu, 1998). However, we observed that the effect of size on CCC became prominent below *ca.* 200 nm. A few reasons contribute to the observed discrepancy on the threshold size. Firstly, it should be noted that the hydrodynamic size determined by DLS was used in our analysis. For non-spherical nanomaterials, this approach reports the size of equivalent spherical nanoparticles with the same translational diffusion coefficient as the non-spherical nanomaterials, therefore the hydrodynamic size is not the actual physical size of non-spherical nanomaterials, which is different from the physical size used in the theoretical work of Hsu and Liu. For example, GO with hydrodynamic sizes of 240, 170, 128, 93 nm corresponded to the average lateral sizes of 1000, 500, 350, 200 nm determined by FESEM, respectively (Sun et al., 2020). Also, the hydrodynamic size of long MWNT (10-20 μm) increased from *ca.* 200 nm to 500 nm as the tube diameter increased from *ca.* 10 nm to 50 nm (Ntim et al., 2012). Nevertheless, the change in the hydrodynamic size generally coincides with the change in the actual physical size of the nanomaterials. Secondly, the observed discrepancy from the theoretical prediction may be due to the lower dimensionality of carbon nanomaterials, which differs from the three-dimensional (3D) nanoparticles used in the theoretical work of Hsu and Liu (1998). For example, the 2D nature of GO and rGO has been shown to significantly affect the van der Waals forces, and the colloidal stability of 2D nanomaterials is less sensitive to the changes in the surface charge density compared to the 3D nanomaterials (Gudarzi, 2016). Although the 1D/2D nature of carbon nanomaterials might contribute to the deviation from the theoretical prediction, the threshold (hydrodynamic) size of spherical 3D silver nanomaterials was observed to be *ca.* 50 nm (Afshinnia et al., 2017). The deviation of experimental observations from the prediction of the DLVO theory thus requires more (theoretical) efforts to uncover the cause(s).

3.3.2 Correlation between CCC and Surface Charge (Zeta Potential)

3.3.2.1 Experimental Observation vs. Prediction Based on the DLVO Theory

Based on the DLVO theory, the CCC of nanomaterials could be mathematically correlated with material surface potential (Elimelech et al., 1995; Hsu and Kuo, 1997; Hunter, 2001; Trefalt et al., 2017) and zeta potential is typically used as an approximation of surface potential in practice (Gudarzi, 2016; Jiang et al., 2016; Luo et al., 2017). However, it should be noted that assumptions were made to simplify the derivation and to obtain the analytical expressions. While these assumptions are valid for (large) colloidal nanoparticles, they may fail for nanomaterials (Hotze et al., 2010). For example, Equation 3.9 was obtained by applying the Derjaguin approximation, which only holds when the thickness of the electrical double layer is much smaller than the particle size (i.e., $\kappa r_0 >> 1$) (Elimelech et al., 1995). Under such assumption, the analytical expression of CCC is independent of nanomaterial size (Hsu and Liu, 1998). This seemingly contradicts our observed effect of size on CCC as discussed above. Nevertheless, the theoretical work by Hsu and Liu (1998) suggests that there is a threshold size, beyond which the effect of size is minimum on the CCC. We observed a threshold (hydrodynamic) size of *ca.* 200 nm (Figure 3.3).

The NaCl CCC of rGO with hydrodynamic size larger than 200 nm (solid squares in Figure 3.4b) was proportional to $\tanh^4\left(\frac{a\psi_0}{4}\right)$ when assuming the same Hamaker constant (A_{121}) values for the rGO (dash line in Figure 3.4b). However, the inclusion of rGO with a size smaller than 200 nm (open squares in Figure 3.4b) significantly weakened the correlation (dash dot line in Figure 3.4b). A similar trend was observed for MWNT as well, but with a smaller threshold size of *ca.* 150 nm (Figure 3.4c). However, GO was an exception. A poor correlation between the CCC and zeta potential was observed even for GO with a hydrodynamic size larger than 200 nm (Figure 3.4a). The deviation from the theoretical prediction was likely due to the underestimated zeta potential of GO, which will be discussed in detail in the next section. The observed correlation between material zeta potential and CCC of rGO and MWNT is consistent with our earlier work, in which we observed a good correlation between the NaCl CCC and zeta potential of five rGO with similar hydrodynamic size of *ca.* 200 nm (Jiang et al., 2016).

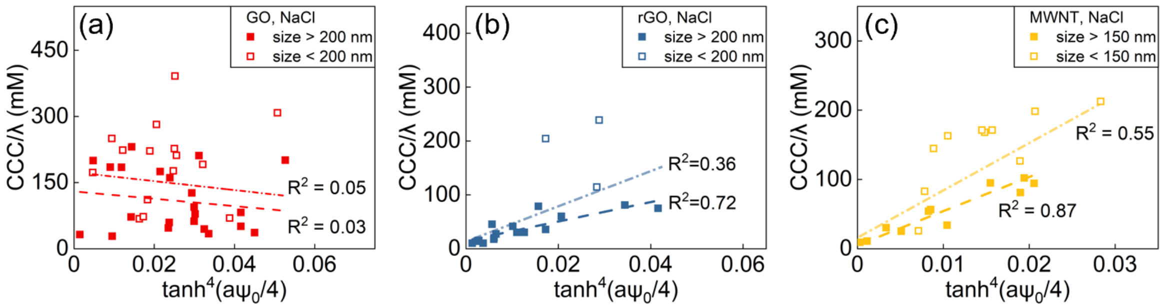

Figure 3.4 Correlation between the NaCl CCC and zeta potential of (a) GO, (b) rGO, and (c) MWNT based on the DLVO theory. Dash lines are the regression lines for solid squares only and dash dot lines are the regression lines for all data (solid and open squares).

The relationship between CCC and material zeta potential in divalent electrolytes was not mathematically consistent with the theoretical prediction, except for MWNT in $MgCl_2$ electrolyte (Figure S3.3). Nevertheless, a qualitative trend was observed for both rGO and MWNT in $MgCl_2$ electrolyte, that is, a higher zeta potential leads to a higher $MgCl_2$ CCC of the nanomaterials (Figure S3.3a-b). However, distinct effects of Ca^{2+} on the CCC of rGO and MWNT were observed (Figure S3.3c-d). The $CaCl_2$ CCC of rGO tended to increase with zeta potential, whereas the $CaCl_2$ CCC of MWNT tended to be independent with zeta potential. This discrepancy was likely because the oxygen-containing functional groups on carbon nanomaterials surface could serve as effective binding sites for cation bridging (Sun et al., 2020; Xia et al., 2019), and such interaction was not considered in the classic DLVO theory. It should be noted that the mechanism of divalent cation bridging has yet to be explicitly revealed. Previous studies suggest that the density (Lu et al., 2012) and position (Labille et al., 2005) of carboxyl groups play a role, as well as the species and concentration of divalent cations (Peng et al., 2022b). More efforts are required to fully understand the bridging mechanism(s).

3.3.2.2 Underestimated Surface Charge of GO by Zeta Potential

The negative surface charges of carbon nanomaterials are generally considered to originate from the oxygen-containing functional groups (e.g., carboxyl and hydroxyl groups) (Jiang et al., 2016; Smith et al., 2009b; Tang et al., 2021). The higher the oxidation degree, the more negative the surface charge of nanomaterials. However, by comparing the oxidation degree (indicated by the C/O ratio measured by XPS) of nanomaterials (only GO/rGO/MWNT have sufficient data for a quantitative comparison) and their zeta potential, we observed that the absolute zeta potential of graphene-based nanomaterial (GO and rGO) first increased with decreasing C/O ratio (from *ca.* 6 to 3), then reached a plateau and did not change with further decrease of the C/O ratio (from *ca.* 3-1) (Figure 3.5a). This plateau was not observed for MWNT, whose C/O ratio was all higher than 8 (Figure 3.5b). The Spearman correlation results also indicated that there was a significant correlation between the C/O ratio and zeta potential for rGO (ρ [15] = 0.55, $p = 0.033$) and MWNT (ρ [18] = 0.68, $p = 0.002$), but not for GO (ρ [31] = 0.25, $p = 0.195$). Therefore, we hypothesized that the measured zeta potential of highly charged nanomaterials may have underestimated their actual surface charge (e.g., C/O ratio <

3 for GO/rGO). To support this hypothesis, we synthesized the data of surface charges of GO/rGO/MWNT obtained from potentiometric titration experiments in published individual studies (Dimiev et al., 2013; Gaidukevic et al., 2021; Gao et al., 2011; Gudarzi, 2016; Konkena and Vasudevan, 2012; Smith et al., 2009b; Sun et al., 2012; Tang et al., 2021; Tombácz et al., 2020; Zhang et al., 2021; Zhao et al., 2011; Zhao et al., 2018) and plotted them against the C/O ratios in Figure 3.5c-d. Results from the titration method suggested the surface charge of both graphene-based nanomaterials (GO and rGO) (Spearman's ρ [15] = -0.78, $p < 0.001$) and MWNT (Spearman's ρ [11] = -0.95, $p < 0.001$) increased monotonically with the decreasing C/O ratio. The observed relationship is consistent with previous individual studies (Smith et al., 2009b; Zhang et al., 2014).

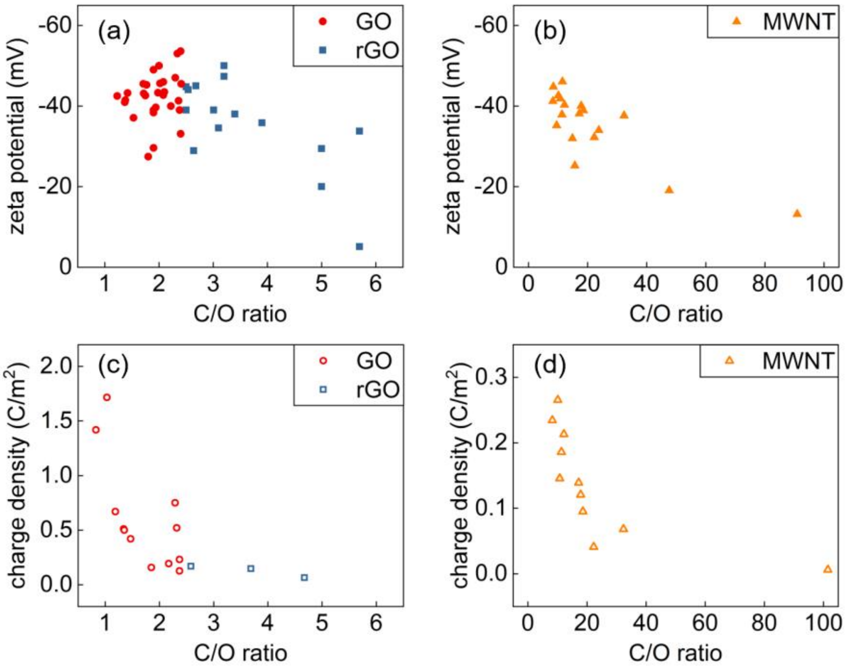

Figure 3.5 (a-b) Zeta potential are plotted against C/O ratio determined by XPS: (a) GO and rGO and (b) MWNT; (c-d) surface charge density against C/O ratio: (c) GO and rGO and (d) MWNT.

The disagreement between zeta potential from the DLS measurement and charge density from the titration measurement may be due to two reasons. On one hand, the measurement of zeta potential depends on the light scattering of nanomaterials, but small nanomaterials (< 2-3 nm) do not scatter light. It should be noted that the oxidation of graphene and CNT not only generates oxygen-containing functional group on material surface, but also produces molecular debris (i.e., oxidation debris, OD) that strongly adhere to the oxidized material (Fogden et al., 2008; Rourke et al., 2011; Verdejo et al., 2007). These OD are too small to scatter light, therefore the charges from OD might not be detected in a zeta potential measurement, yet the charges of OD could be measured by titration (Tang et al., 2021). On the other hand, it might not be appropriate to use the Smoluchowski equation to estimate the zeta potential of nanomaterial with high surface charge. Although this equation has been widely used in the literature to calculate the zeta potential from electrophoretic mobility for various nanomaterials (Afshinnia et al., 2017; Chowdhury et al., 2013; Liu et al., 2016; Mulvihill et al., 2010; Omija et al., 2021), it must be noted that there are limitations to its use. The equation can be applied to a particle of arbitrary shape provided that the radii of surface curvature were everywhere much larger than the double layer thickness (κ^{-1}) (Hunter, 2001). Only in the case of $\kappa r_0 > 20$ and moderate/low surface charge (e.g., absolute zeta potential ≤ 50 mV) can one safely apply the Smoluchowski equation (Delgado et al., 2005). If the surface charge is rather high (absolute zeta potential > 50 mV), the zeta potential is underestimated using the Smoluchowski equation and one needs to use more elaborate models (e.g., the numerical solutions by O’Brien and White) (Delgado et al., 2005). Therefore, the inappropriate use of the Smoluchowski equation for GO with high surface charge (i.e., C/O ratio < 3) may contribute to the disagreement of measured zeta potential and charge density results.

3.3.3 Correlation between CCC and Surface Functionalities

Previous individual studies have observed a linear correlation between the carboxyl group and aqueous stability (i.e., CCC) of these carbon nanomaterials and their surface functionalities (Bai et al., 2014; Jiang et al., 2016; Smith et al., 2009b; Tang et al., 2017; Wu et al., 2017). For example, we previously observed that the carboxyl groups (from *ca*. 3-5%) were highly correlated to the CCC of GO with different degrees of reduction (C/O ratio from *ca*. 2-5) (Jiang et al., 2016). This positive correlation between the carboxyl groups and GO stability was supported by molecular dynamics simulation by Tang et al. (2017). Similarly, the correlation between carboxyl groups and the CCC of MWNT has also been reported, in which the carboxyl content varied from *ca.* 1.5-5.5% for MWNT with different oxidation degrees (C/O ratio from 8-32) (Smith et al., 2009b). However, in this meta-analysis we did not observe a significant correlation between the CCC and the carboxyl functional groups for none of these carbon nanomaterials (Figure S3.4 and Table S3.5-3.7). We postulated that this discrepancy might be caused by the varied approaches in deconvoluting the XPS spectra across studies. For example, the deconvolution of high resolution C1s spectra were performed to account for either three oxygen-containing functional groups (i.e., C-C, C-O, and C=O) (An et al., 2021; Liu et al., 2018), or four functional groups (i.e., C-C, C-O, C=O, and COOH) (Chowdhury et al., 2015; Sun et al., 2020), or five functional groups (i.e., C-C, C-OH, C-O-C, C=O, and COOH) (Jiang et al., 2016; Jiang et al., 2017). Varied rules applied in each study may cause errors in recognizing the surface functionalities of nanomaterials, especially when the carboxyl content only varied in a small range, e.g., from *ca.* 2-5% of GO (Jiang et al., 2016) and *ca.* 1.5-5.5% of MWNT (Smith et al., 2009b). Therefore, unless a unified deconvolution method is applied to analyze the XPS spectra in each study, solid conclusion(s) on the correlation between the fractions of surface functionalities of nanomaterials and their aqueous stability might not be obtained.

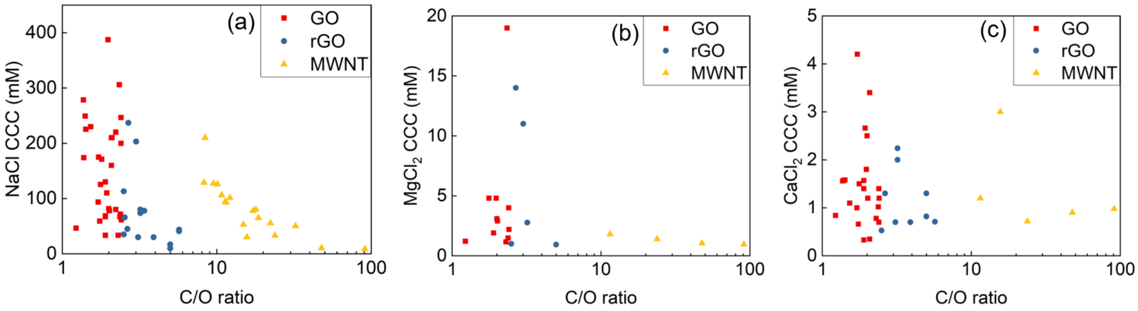

Figure 3.6 The critical coagulation concentration (CCC) of GO/rGO/MWNT in (a) NaCl, (b) $MgCl_2$, and (c) $CaCl_2$ electrolytes are plotted against the C/O ratios of these materials.

Nevertheless, the C/O ratio obtained by XPS did not require sophisticated deconvolution as the surface functionalities did, and we observed a general trend that the smaller the C/O ratio, the higher the NaCl CCC values for GO, rGO, and MWNT (Figure 3.6a). This is consistent with the observations in individual studies (Jiang et al., 2016; Smith et al., 2009b; Xia et al., 2019; Yi and Chen, 2011). Nonetheless, the correlation became weaker with decreasing C/O ratio (i.e., a higher oxidation degree) as indicated by the Spearman correlation (MWNT: ρ [18] = -0.92, $p < 0.001$; rGO: ρ [15] = -0.46, $p = 0.082$; GO: ρ [31] = -0.10, $p = 0.586$). In divalent electrolytes, the correlation between CCC and C/O ratio was much weaker (Figure 3.6b-c and Table S3.5-3.7). Compared with monovalent counterion, divalent cation has a stronger association with the nanomaterial and can possibly form bridges with the carboxyl groups (Tang et al., 2017). On one hand, the carboxyl group stabilizes the nanomaterial by providing negative charges. On the other hand, bridging interaction promotes nanomaterial aggregation. Therefore, in divalent electrolytes, the correlation between CCC and the C/O ratios become blurred.

3.4 Implications

Data-driven research has received wide attention in the scientific community and has great potential in improving the design of materials (Gao et al., 2023; Wang et al., 2023; Yang et al., 2023). This study serves as a proof-of-concept for applying a meta-analytic approach to synthesize pre-existing data to determine patterns and make predictions, thereby obtaining a better understanding of the property-aggregation relationships of nanomaterials, which will be required for the development of accurate predictive models to estimate nanomaterial aggregation. This meta-analysis focused on the carbon nanomaterials, future analysis can include more types of nanomaterials (e.g., metal nanoparticles and nanoplastics) to not only evaluate the generalizability of the findings in this analysis, but also to evaluate the impact(s) of more physicochemical properties of nanomaterials (e.g., shape and surface coating) on their aggregation behavior. Other than the aggregation behavior of nanomaterials, their electronic structure and chemical activity are also property-dependent, and leveraging a meta-analytic approach to discover and define such relationships is well-suited (Yang et al., 2023). Also, with more data being generated, future studies could utilize more advanced meta-analytic techniques, such as machine learning (Gao et al., 2023; Wang et al., 2023) to better understand the interplay of multiple properties on the aggregation of nanomaterials and to provide potential practical aid in the design of nanomaterials.

3.5 Conclusions

In this work, we employed a meta-analytic approach to synthesize the available data from 46 individual studies and examined the correlation between material physicochemical properties (i.e., size, surface charge, surface functionalities) and their CCC in three electrolytes (i.e., NaCl/$MgCl_2$/$CaCl_2$). We conclude that the CCC of these carbon nanomaterials increases with decreasing nanomaterial size, and the effect of size becomes prominent when the hydrodynamic size is smaller than *ca.* 200 nm. This observation is qualitatively consistent with the early prediction of the DLVO theory, but with a smaller threshold size. Above the threshold size, material zeta potential can be correlated to CCC in NaCl electrolyte ($CCC/\lambda \propto \tanh^4\left(\frac{a\psi_0}{4}\right)$). The correlation is not observed in the divalent electrolytes, because divalent cation bridging, which may have occurred, was not considered in the framework of the DLVO theory. Although the zeta potential (obtained via the Smoluchowski equation) is commonly used to represent material surface charge, it only remains valid for nanomaterial with moderate/low surface charge (e.g., GO with C/O ratio > *ca.* 3 and MWNT with C/O ratio > 8). For GO with C/O ratio smaller than *ca.* 3, the measured zeta potential may underestimate the actual surface charge, thereby leading to the deviation of experimental observations from the prediction of the DLVO theory. With more oxygen-containing functional groups (i.e., lower C/O ratio), these carbon nanomaterials are more stable. However, the correlation with a specific functional group could not be established unless they are identified with a unified characterization approach across studies. Overall, our findings rationalize the inconsistency among previous observations of certain physicochemical properties on nanomaterial aggregation and provide essential insights into their aggregation behavior in water, thereby assisting their rational design for various applications.

Acknowledgement

This work was supported by Hong Kong Research Grants Council's Early Career Award (25209819) and Science, Technology and Innovation Commission of Shenzhen Municipality (SGDX20210823103401009).

References

Afshinnia, K., Sikder, M., Cai, B. and Baalousha, M. 2017. Effect of nanomaterial and media physicochemical properties on Ag NM aggregation kinetics. J. Colloid Interface Sci. 487, 192-200.

An, S., Zeng, Q., Li, W. and Fortner, J. 2021. A graphene oxide Cookbook: Exploring chemical and colloidal properties as a function of synthesis parameters. J. Colloid Interface Sci. 588, 725-736.

Araújo, M.P., Soares, O.S.G.P., Fernandes, A.J.S., Pereira, M.F.R. and Freire, C. 2017. Tuning the surface chemistry of graphene flakes: new strategies for selective oxidation. RSC Advances 7(23), 14290-14301.

Azizighannad, S. and Mitra, S. 2018. Stepwise reduction of graphene oxide (GO) and its effects on chemical and colloidal properties. Sci. Rep. 8(1), 10083.

Baalousha, M. 2017. Effect of nanomaterial and media physicochemical properties on nanomaterial aggregation kinetics. NanoImpact 6, 55-68.

Bai, Y., Wu, F., Lin, D. and Xing, B. 2014. Aqueous stabilization of carbon nanotubes: effects of surface oxidization and solution chemistry. Environ. Sci. Pollut. Res. 21(6), 4358-4365.

Bouchard, D., Zhang, W., Powell, T. and Rattanaudompol, U.s. 2012. Aggregation kinetics and transport of single-walled carbon nanotubes at low surfactant concentrations. Environ. Sci. Technol. 46(8), 4458-4465.

Chang, X., Henderson, W.M. and Bouchard, D.C. 2015. Multiwalled carbon nanotube dispersion methods affect their aggregation, deposition, and biomarker response. Environ. Sci. Technol. 49(11), 6645-6653.

Chen, K.L. and Elimelech, M. 2006. Aggregation and deposition kinetics of fullerene (C60) nanoparticles. Langmuir 22(26), 10994-11001.

Chen, K.L., Mylon, S.E. and Elimelech, M. 2006. Aggregation kinetics of alginate-coated hematite nanoparticles in monovalent and divalent electrolytes. Environ. Sci. Technol. 40(5), 1516-1523.

Chowdhury, I., Duch, M.C., Mansukhani, N.D., Hersam, M.C. and Bouchard, D. 2013. Colloidal properties and stability of graphene oxide nanomaterials in the aquatic environment. Environ. Sci. Technol. 47(12), 6288-6296.

Chowdhury, I., Mansukhani, N.D., Guiney, L.M., Hersam, M.C. and Bouchard, D. 2015. Aggregation and stability of reduced graphene oxide: complex roles of divalent cations, pH, and natural organic matter. Environ. Sci. Technol. 49(18), 10886-10893.

Delgado, A.V., González-Caballero, F., Hunter, R.J., Koopal, L.K. and Lyklema, J. 2005. Measurement and interpretation of electrokinetic phenomena (IUPAC Technical Report). Pure Appl. Chem. 77(10), 1753-1805.

Dimiev, A.M., Alemany, L.B. and Tour, J.M. 2013. Graphene oxide. Origin of acidity, its instability in water, and a new dynamic structural model. ACS Nano 7(1), 576-588.

Du, T., Adeleye, A.S., Zhang, T., Jiang, C., Zhang, M., Wang, H., Li, Y., Keller, A.A. and Chen, W. 2018. Influence of light wavelength on the photoactivity, physicochemical transformation, and fate of graphene oxide in aqueous media. Environ. Sci.: Nano 5(11), 2590-2603.

Elimelech, M., Gregory, J. and Jia, X. (1995) Particle Deposition and Aggregation: Measurement, Modelling and Simulation, Butterworth-Heinemann.

Feng, Y., Liu, X., Huynh, K.A., McCaffery, J.M., Mao, L., Gao, S. and Chen, K.L. 2017. Heteroaggregation of graphene oxide with nanometer- and micrometer-sized hematite colloids: Influence on nanohybrid aggregation and microparticle sedimentation. Environ. Sci. Technol. 51(12), 6821-6828.

Fogden, S., Verdejo, R., Cottam, B. and Shaffer, M. 2008. Purification of single walled carbon nanotubes: The problem with oxidation debris. Chem. Phys. Lett. 460(1), 162-167.

Gaidukevic, J., Aukstakojyte, R., Navickas, T., Pauliukaite, R. and Barkauskas, J. 2021. A novel approach to prepare highly oxidized graphene oxide: structural and electrochemical investigations. Appl. Surf. Sci. 567, 150883.

Gao, H., Zhong, S., Dangayach, R., Chen, Y. 2023. Understanding and designing a high-performance ultrafiltration membrane using machine learning. Environ. Sci. Technol.

Gao, Y., Ren, X., Song, G., Chen, D., Zhang, X. and Chen, C. 2020. Colloidal properties and stability of UV-transformed graphene oxide in aqueous solutions: The role of disorder degree. J. Hazard. Mater. 382, 121097.

Gao, Y., Yip, H.-L., Chen, K.-S., O’Malley, K.M., Acton, O., Sun, Y., Ting, G., Chen, H. and Jen, A.K.-Y. 2011. Surface doping of conjugated polymers by graphene oxide and its application for organic electronic devices. Adv. Mater. 23(16), 1903-1908.

Gao, Y., Zeng, X., Zhang, W., Zhou, L., Xue, W., Tang, M. and Sun, S. 2022. The aggregation behaviour and mechanism of commercial graphene oxide in surface aquatic environments. Sci. Total Environ. 806, 150942.

Gudarzi, M.M. 2016. Colloidal stability of graphene oxide: Aggregation in two dimensions. Langmuir 32(20), 5058-5068.

Gurevitch, J., Koricheva, J., Nakagawa, S. and Stewart, G. 2018. Meta-analysis and the science of research synthesis. Nature 555(7695), 175-182.

He, Y.T., Wan, J. and Tokunaga, T. 2008. Kinetic stability of hematite nanoparticles: The effect of particle sizes. J. Nanopart. Res. 10(2), 321-332.

Hotze, E.M., Phenrat, T. and Lowry, G.V. 2010. Nanoparticle aggregation: Challenges to understanding transport and reactivity in the environment. J. Environ. Qual. 39(6), 1909-1924.

Hsu, J.-P. and Kuo, Y.-C. 1997. The critical coagulation concentration of counterions: Spherical particles in asymmetric electrolyte solutions. J. Colloid Interface Sci. 185(2), 530-537.

Hsu, J.-P. and Liu, B.-T. 1998. Effect of particle size on critical coagulation concentration. J. Colloid Interface Sci. 198(1), 186-189.

Huang, G., Guo, H., Zhao, J., Liu, Y. and Xing, B. 2016. Effect of co-existing kaolinite and goethite on the aggregation of graphene oxide in the aquatic environment. Water Res. 102, 313-320.

Huang, P., Jia, H., Wang, T., Xu, Y., Zhang, L., Wei, X., Jia, H., Wen, S., Lv, K. and Liu, D. 2021. Effects of modification degrees on the colloidal stability of amphiphilic Janus graphene oxide in aqueous solution with and without electrolytes. Langmuir 37(33), 10061-10070.

Hunter, R.J. (2001) Foundations of Colloid Science, Oxford University Press.

Jiang, Y., Raliya, R., Fortner, J.D. and Biswas, P. 2016. Graphene oxides in water: Correlating morphology and surface chemistry with aggregation behavior. Environ. Sci. Technol. 50(13), 6964-6973.

Jiang, Y., Raliya, R., Liao, P., Biswas, P. and Fortner, J.D. 2017. Graphene oxides in water: assessing stability as a function of material and natural organic matter properties. Environ. Sci.: Nano 4(7), 1484-1493.

Khan, I.A., Afrooz, A.R.M.N., Flora, J.R.V., Schierz, P.A., Ferguson, P.L., Sabo-Attwood, T. and Saleh, N.B. 2013. Chirality affects aggregation kinetics of single-walled carbon nanotubes. Environ. Sci. Technol. 47(4), 1844-1852.

Kim, C., Lee, J., Wang, W. and Fortner, J. 2020. Organic functionalized graphene oxide behavior in water. Nanomaterials 10(6), 1228.

Konkena, B. and Vasudevan, S. 2012. Understanding aqueous dispersibility of graphene oxide and reduced graphene oxide through pKa measurements. J. Phys. Chem. Lett. 3(7), 867-872.

Labille, J., Thomas, F., Milas, M. and Vanhaverbeke, C. 2005. Flocculation of colloidal clay by bacterial polysaccharides: Effect of macromolecule charge and structure. J. Colloid Interface Sci. 284(1), 149-156.

Li, M. and Huang, C.P. 2010. Stability of oxidized single-walled carbon nanotubes in the presence of simple electrolytes and humic acid. Carbon 48(15), 4527-4534.

Li, W., Yu, J., Zhang, S., Tang, H. and Huang, T. 2022. The fate of aggregated graphene oxide upon the increasing of pH: An experimental and molecular dynamic study. Sci. Total Environ. 851, 157954.

Lin, D., Liu, N., Yang, K., Zhu, L., Xu, Y. and Xing, B. 2009. The effect of ionic strength and pH on the stability of tannic acid-facilitated carbon nanotube suspensions. Carbon 47(12), 2875-2882.

Liu, J., Legros, S., Ma, G., Veinot, J.G.C., von der Kammer, F. and Hofmann, T. 2012. Influence of surface functionalization and particle size on the aggregation kinetics of engineered nanoparticles. Chemosphere 87(8), 918-924.

Liu, W., Zhao, X., Cai, Z., Han, B. and Zhao, D. 2016. Aggregation and stabilization of multiwalled carbon nanotubes in aqueous suspensions: influences of carboxymethyl cellulose, starch and humic acid. RSC Advances 6(71), 67260-67270.

Liu, X., Xu, X., Sun, J., Duan, S., Sun, Y., Hayat, T. and Li, J. 2018. Interaction between Al_2O_3 and different sizes of GO in aqueous environment. Environ. Pollut. 243, 1802-1809.

Louie, S.M., Tilton, R.D. and Lowry, G.V. 2013. Effects of molecular weight distribution and chemical properties of natural organic matter on gold nanoparticle aggregation. Environ. Sci. Technol. 47(9), 4245-4254.

Lowry, G.V., Hill, R.J., Harper, S., Rawle, A.F., Hendren, C.O., Klaessig, F., Nobbmann, U., Sayre, P. and Rumble, J. 2016. Guidance to improve the scientific value of zeta-potential measurements in nanoEHS. Environ. Sci.: Nano 3(5), 953-965.

Lu, N., Mylon, S.E., Kong, R., Bhargava, R., Zilles, J.L. and Nguyen, T.H. 2012. Interactions between dissolved natural organic matter and adsorbed DNA and their effect on natural transformation of Azotobacter vinelandii. Sci. Total Environ. 426, 430-435.

Luo, D., Wang, F., Alam, M.K., Yu, F., Mishra, I.K., Bao, J., Willson, R.C. and Ren, Z. 2017. Colloidal stability of graphene-based amphiphilic Janus nanosheet fluid. Chem. Mater. 29(8), 3454-3460.

Mulvihill, M.J., Habas, S.E., Jen-La Plante, I., Wan, J. and Mokari, T. 2010. Influence of size, shape, and surface coating on the stability of aqueous suspensions of CdSe nanoparticles. Chem. Mater. 22(18), 5251-5257.

Ntim, S.A., Sae-Khow, O., Desai, C., Witzmann, F.A. and Mitra, S. 2012. Size dependent aqueous dispersibility of carboxylated multiwall carbon nanotubes. J. Environ. Monit. 14(10), 2772-2779.

Ntim, S.A., Sae-Khow, O., Witzmann, F.A. and Mitra, S. 2011. Effects of polymer wrapping and covalent functionalization on the stability of MWCNT in aqueous dispersions. J. Colloid Interface Sci. 355(2), 383-388.

Omija, K., Hakim, A., Masuda, K., Yamaguchi, A. and Kobayashi, M. 2021. Effect of counter ion valence and pH on the aggregation and charging of oxidized carbon nanohorn (CNHox) in aqueous solution. Colloids Surf. A Physicochem. Eng. Asp. 619, 126552.

Park, C.M., Wang, D., Heo, J., Her, N. and Su, C. 2018. Aggregation of reduced graphene oxide and its nanohybrids with magnetite and elemental silver under environmentally relevant conditions. J. Nanopart. Res. 20(4), 93.

Peng, B., Liao, P. and Jiang, Y. 2022a. Preferential interactions of surface-bound engineered single stranded DNA with highly aromatic natural organic matter: Mechanistic insights and implications for optimizing practical aquatic applications. Water Res. 223, 119015.

Peng, B., Liu, Z. and Jiang, Y. 2022b. Aggregation of DNA-grafted nanoparticles in water: the critical role of sequence-dependent conformation of DNA coating. J. Phys. Chem. B 126(4), 847-857.

Qi, Y., Xia, T., Li, Y., Duan, L. and Chen, W. 2016. Colloidal stability of reduced graphene oxide materials prepared using different reducing agents. Environ. Sci.: Nano 3(5), 1062-1071.

Rourke, J.P., Pandey, P.A., Moore, J.J., Bates, M., Kinloch, I.A., Young, R.J. and Wilson, N.R. 2011. The real graphene oxide revealed: Stripping the oxidative debris from the graphene-like sheets. Angew. Chem. Int. Ed. 50(14), 3173-3177.

Saleh, N.B., Pfefferle, L.D. and Elimelech, M. 2008. Aggregation kinetics of multiwalled carbon nanotubes in aquatic systems: Measurements and environmental implications. Environ. Sci. Technol. 42(21), 7963-7969.

Saleh, N.B., Pfefferle, L.D. and Elimelech, M. 2010. Influence of biomacromolecules and humic acid on the aggregation kinetics of single-walled carbon nanotubes. Environ. Sci. Technol. 44(7), 2412-2418.

Sano, M., Okamura, J. and Shinkai, S. 2001. Colloidal nature of single-walled carbon nanotubes in electrolyte solution: The Schulze−Hardy rule. Langmuir 17(22), 7172-7173.

Shen, M., Hai, X., Shang, Y., Zheng, C., Li, P., Li, Y., Jin, W., Li, D., Li, Y., Zhao, J., Lei, H., Xiao, H., Li, Y., Yan, G., Cao, Z. and Bu, Q. 2019. Insights into aggregation and transport of graphene oxide in aqueous and saturated porous media: Complex effects of cations with different molecular weight fractionated natural organic matter. Sci. Total Environ. 656, 843-851.

Sheng, A., Liu, F., Shi, L. and Liu, J. 2016. Aggregation kinetics of hematite particles in the presence of outer membrane Cytochrome OmcA of Shewanella oneidenesis MR-1. Environ. Sci. Technol. 50(20), 11016-11024.

Smith, B., Wepasnick, K., Schrote, K.E., Bertele, A.R., Ball, W.P., O'Melia, C. and Fairbrother, D.H. 2009a. Colloidal Properties of aqueous suspensions of acid-treated, multi-walled carbon nanotubes. Environ. Sci. Technol. 43(3), 819-825.

Smith, B., Wepasnick, K., Schrote, K.E., Cho, H.-H., Ball, W.P. and Fairbrother, D.H. 2009b. Influence of surface oxides on the colloidal stability of multi-walled carbon nanotubes: A structure−property relationship. Langmuir 25(17), 9767-9776.

Song, J., Zeng, Y., Liu, Y. and Jiang, W. 2022. Retention of graphene oxide and reduced graphene oxide in porous media: Diffusion-attachment, interception-attachment and straining. J. Hazard. Mater. 431, 128635.

Sotirelis, N.P. and Chrysikopoulos, C.V. 2017. Heteroaggregation of graphene oxide nanoparticles and kaolinite colloids. Sci. Total Environ. 579, 736-744.

Stankus, D.P., Lohse, S.E., Hutchison, J.E. and Nason, J.A. 2011. Interactions between natural organic matter and gold nanoparticles stabilized with different organic capping agents. Environ. Sci. Technol. 45(8), 3238-3244.

Story, S.D., Boggs, S., Guiney, L.M., Ramesh, M., Hersam, M.C., Brinker, C.J. and Walker, S.L. 2020. Aggregation morphology of planar engineered nanomaterials. J. Colloid Interface Sci. 561, 849-853.

Su, Y., Yang, G., Lu, K., Petersen, E.J. and Mao, L. 2017. Colloidal properties and stability of aqueous suspensions of few-layer graphene: Importance of graphene concentration. Environ. Pollut. 220, 469-477.

Sun, B., Zhang, Y., Chen, W., Wang, K. and Zhu, L. 2018. Concentration Dependent Effects of Bovine Serum Albumin on Graphene Oxide Colloidal Stability in Aquatic Environment. Environ. Sci. Technol. 52(13), 7212-7219.

Sun, B., Zhang, Y., Li, R., Wang, K., Xiao, B., Yang, Y., Wang, J. and Zhu, L. 2021. New insights into the colloidal stability of graphene oxide in aquatic environment: Interplays of photoaging and proteins. Water Res. 200, 117213.

Sun, B., Zhang, Y., Liu, Q., Yan, C., Xiao, B., Yang, J., Liu, M. and Zhu, L. 2020. Lateral size dependent colloidal stability of graphene oxide in water: impacts of protein properties and water chemistry. Environ. Sci.: Nano 7(2), 634-644.

Sun, Y., Wang, Q., Chen, C., Tan, X. and Wang, X. 2012. Interaction between Eu(III) and Graphene Oxide Nanosheets Investigated by Batch and Extended X-ray Absorption Fine Structure Spectroscopy and by Modeling Techniques. Environ. Sci. Technol. 46(11), 6020-6027.

Szabo, T., Maroni, P. and Szilagyi, I. 2020. Size-dependent aggregation of graphene oxide. Carbon 160, 145-155.

Tang, H., Zhang, S., Huang, T., Zhang, J. and Xing, B. 2021. Mechanisms of the aggregation of graphene oxide at high pH: Roles of oxidation debris and metal adsorption. Environ. Sci. Technol. 55(21), 14639-14648.

Tang, H., Zhao, Y., Yang, X., Liu, D., Shao, P., Zhu, Z., Shan, S., Cui, F. and Xing, B. 2017. New insight into the aggregation of graphene oxide using molecular dynamics simulations and extended Derjaguin–Landau–Verwey–Overbeek theory. Environ. Sci. Technol. 51(17), 9674-9682.

Tombácz, E., Tóth, I.Y., Kovács, K., Illés, E., Szekeres, M., Barna, B., Csicsor, A. and Szabó, T. 2020. Striking analogies and dissimilarities between graphene oxides and humic acids: pH-dependent charging and colloidal stability. J. Mol. Liq. 306, 112948.

Trefalt, G., Szilagyi, I., Téllez, G. and Borkovec, M. 2017. Colloidal stability in asymmetric electrolytes: Modifications of the Schulze–Hardy rule. Langmuir 33(7), 1695-1704.

Verdejo, R., Lamoriniere, S., Cottam, B., Bismarck, A. and Shaffer, M. 2007. Removal of oxidation debris from multi-walled carbon nanotubes. Chem. Commun. (5), 513-515.

Vikesland, P.J., Heathcock, A.M., Rebodos, R.L. and Makus, K.E. 2007. Particle size and aggregation effects on magnetite reactivity toward carbon tetrachloride. Environ. Sci. Technol. 41(15), 5277-5283.

Wang, M., Gao, B., Tang, D., Sun, H., Yin, X. and Yu, C. 2018. Effects of temperature on aggregation kinetics of graphene oxide in aqueous solutions. Colloids Surf. A Physicochem. Eng. Asp. 538, 63-72.

Wang, R., Zhang, S., Chen, H., He, Z., Cao, G., Wang, K., Li, F., Ren, N., Xing, D., Ho, S.H. 2023. Enhancing biochar-based nonradical persulfate activation using data-driven techniques. Environ. Sci. Technol. 57 (9), 4050-4059.

Wu, L., Liu, L., Gao, B., Muñoz-Carpena, R., Zhang, M., Chen, H., Zhou, Z. and Wang, H. 2013. Aggregation kinetics of graphene oxides in aqueous solutions: experiments, mechanisms, and modeling. Langmuir 29(49), 15174-15181.

Wu, Z. and Mitra, S. 2014. Length reduction of multi-walled carbon nanotubes via high energy ultrasonication and its effect on their dispersibility. J. Nanopart. Res. 16(8), 2563.

Wu, Z., Wang, Z., Yu, F., Thakkar, M. and Mitra, S. 2017. Variation in chemical, colloidal and electrochemical properties of carbon nanotubes with the degree of carboxylation. J. Nanopart. Res. 19(1), 16.

Xia, T., Guo, X., Lin, Y., Xin, B., Li, S., Yan, N. and Zhu, L. 2019. Aggregation of oxidized multi-walled carbon nanotubes: Interplay of nanomaterial surface O-functional groups and solution chemistry factors. Environ. Pollut. 251, 921-929.

Yang, K., Chen, B., Zhu, X. and Xing, B. 2016. Aggregation, adsorption, and morphological transformation of graphene oxide in aqueous solutions containing different metal cations. Environ. Sci. Technol. 50(20), 11066-11075.

Yang, R. X., McCandler, C.A., Andriuc, O., Siron, M., Woods-Robinson, R., Horton, M.K., Persson, K.A. 2022. Big data in a nano world: A review on computational, data-driven design of nanomaterials structures, properties, and synthesis. ACS Nano, 16 (12), 19873-19891.

Yang, X., Wang, Q., Qu, X. and Jiang, W. 2017. Bound and unbound humic acids perform different roles in the aggregation and deposition of multi-walled carbon nanotubes. Sci. Total Environ. 586, 738-745.

Yi, P. and Chen, K.L. 2011. Influence of surface oxidation on the aggregation and deposition kinetics of multiwalled carbon nanotubes in monovalent and divalent electrolytes. Langmuir 27(7), 3588-3599.

Zeng, Z., Wang, Y., Zhou, Q., Yang, K. and Lin, D. 2019. New insight into the aggregation of graphene oxide in synthetic surface water: Carbonate nanoparticle formation on graphene oxide. Environ. Pollut. 250, 366-374.

Zhang, J., Xiong, C., Li, Y., Tang, H., Meng, X. and Zhu, W. 2021. The critical contribution of oxidation debris on the acidic properties of graphene oxide in an aqueous solution. J. Hazard. Mater. 402, 123552.

Zhang, Z., Pfefferle, L. and Haller, G.L. 2014. Comparing characterization of functionalized multi-walled carbon nanotubes by potentiometric proton titration, NEXAFS, and XPS. Chinese J. Catal. 35(6), 856-863.

Zhao, G., Li, J., Ren, X., Chen, C. and Wang, X. 2011. Few-layered graphene oxide nanosheets as superior sorbents for heavy metal ion pollution management. Environ. Sci. Technol. 45(24), 10454-10462.

Zhao, J., Liu, F., Wang, Z., Cao, X. and Xing, B. 2015. Heteroaggregation of graphene oxide with minerals in aqueous phase. Environ. Sci. Technol. 49(5), 2849-2857.

Zhao, Q., Zhu, X. and Chen, B. 2018. Stable graphene oxide/poly(ethyleneimine) 3D aerogel with tunable surface charge for high performance selective removal of ionic dyes from water. Chem. Eng. J. 334, 1119-1127.

Zhou, D., Ji, Z., Jiang, X., Dunphy, D.R., Brinker, J. and Keller, A.A. 2013. Influence of material properties on TiO_2 nanoparticle agglomeration. PLOS ONE 8(11), e81239.

Appendix A: Supporting Information for Chapter 3

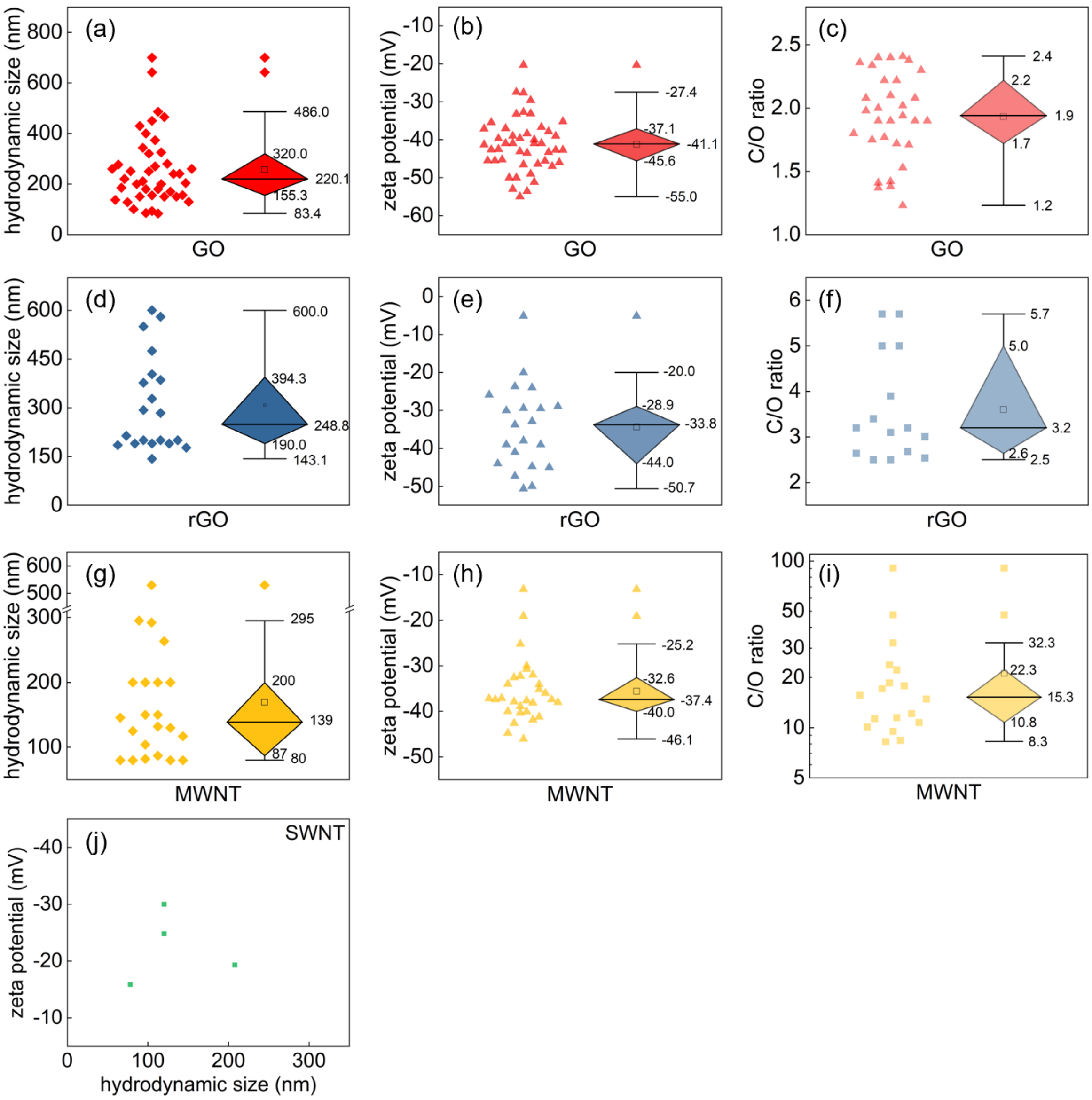

Figure S3.1 Box plots (data distribution shown as well) of (a, d, g) hydrodynamic size, (b, e, g) zeta potential, (c, f, i) C/O ratio of (a-c) GO, (d-f) rGO, (g-i) MWNT. (j) zeta potential of SWNT is plotted against hydrodynamic size.

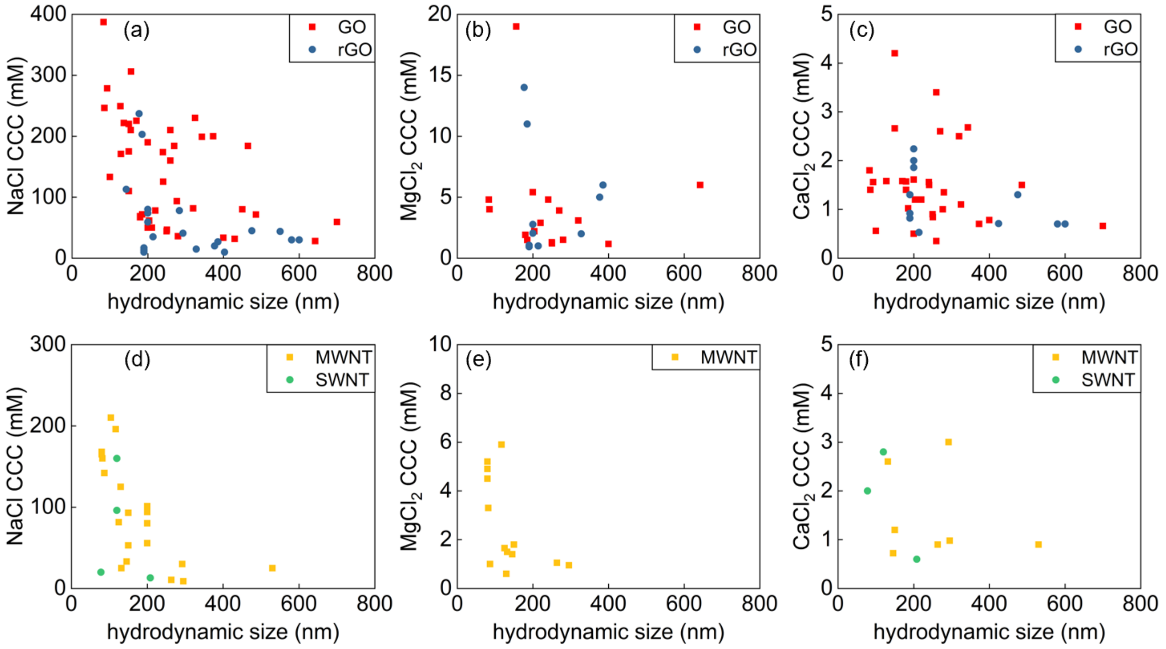

Figure S3.2 The NaCl, MgCl2, and CaCl2 CCC of GO, rGO, MWNT, and SWNT were plotted against material hydrodynamic size; (a and d) NaCl CCC vs. size, (b and e) MgCl2 vs. size, and (c and f) CaCl2 vs. size.

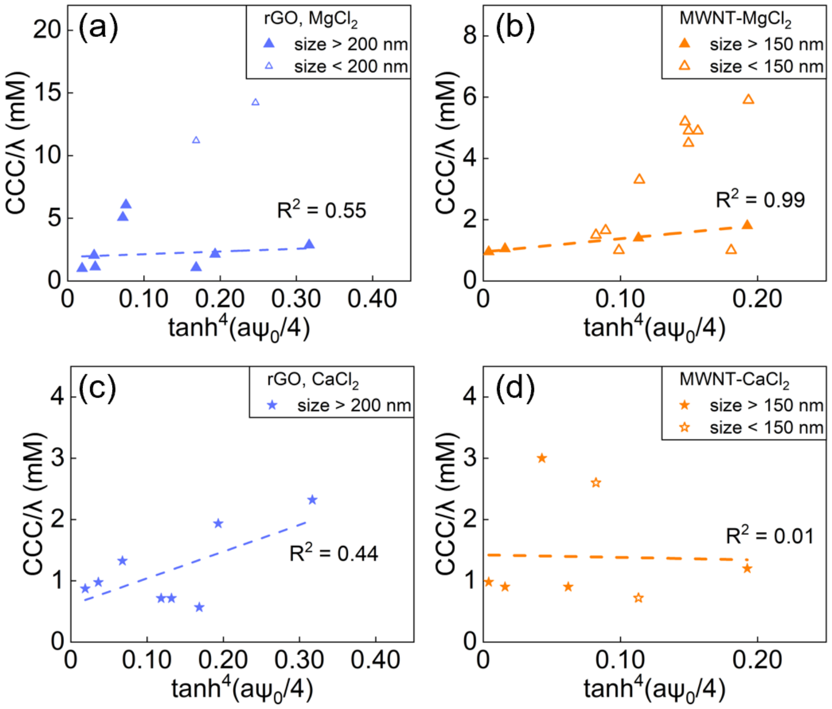

Figure S3.3 Correlation between the (a-b) MgCl2 CCC and (c-d) CaCl2 CCC and zeta potential for nanomaterials with size larger than the threshold size based on the DLVO theory. Dash lines are the regression lines for solid triangles or stars.

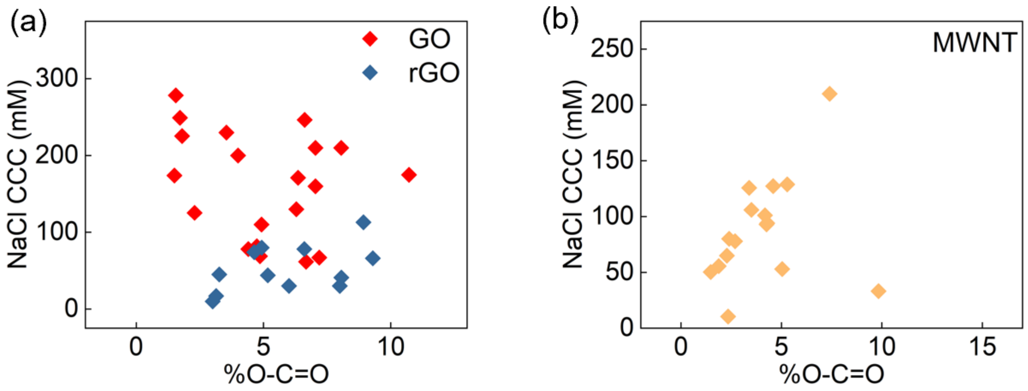

Figure S3.4 The NaCl CCC of (a) GO/rGO and (b) MWNT were plotted against their carboxyl content determined by XPS.

Table S3.1 Physicochemical properties and critical coagulation concentration (CCC) of graphene oxide (GO) reported in literature. Blank cells represent that the corresponding data were not reported. DLS size refers to the hydrodynamic size determined by dynamic light scattering. Zeta potential is calculated from electrophoretic mobility using the Smoluchowski equation. C/O ratio and the fractions of functionalities are determined by XPS.

pH	DLS size (nm)	zeta potential (mV)	C/O ratio	%C-C	%C-O	%C=O	%O-C=O	NaCl CCC (mM)	$MgCl_2$ CCC (mM)	$CaCl_2$ CCC (mM)	Ref.
5	270	-32.7						184	3.9	2.6	(Wu et al., 2013)
5.5	250	-46.6						44	1.3	0.9	(Chowdhury et al., 2013)
5.2	373	-53.6	2.40	42.00	33.00	21.00	4.00	200		0.7	(Chowdhury et al., 2015)
5.5	211	-50.0						50			(Huang et al., 2016)
6	155.3	-43.5	2.10	39.07	49.18	3.93	8.05	210			(Qi et al., 2016)
7	280	-51.2						36	1.5	1.35	(Yang et al., 2016)
6	180	-49.0	1.90	40.57	48.58	5.98	4.86	68.7	1.91	1.57	(Jiang et al., 2016)
6	320	-50.0	2	45.30	46.14	4.69	4.74	81.7	3.09	2.5	(Jiang et al., 2016)
6	180	-38.4	1.90	40.69	48.32	5.95	5.11	67		1.4	(Jiang et al., 2017)
6.6	150	-39.7	1.94	48.33	31.23	15.51	4.92	110		2.66	(Tang et al., 2017)
6.6	150	-43.1	1.72	41.99	31.22	16.07	10.72	175		4.2	(Tang et al., 2017)
6	100							133		0.56	(Wang et al., 2018)
7	642.3	-33.2						28	6		(Azizighannad and Mitra, 2018)
5.5	200	-46.4						190	5.41	1.61	(Sun et al., 2018)
6	240	-41.5	1.38	51.70	38.17	8.26	1.50	173.9		1.56	(Sun et al., 2020)
6	170	-43.2	1.42	51.30	36.85	10.10	1.80	225.3		1.58	(Sun et al., 2020)
6	128		1.41	52.53	35.54	10.20	1.72	249.2		1.58	(Sun et al., 2020)
6	93	-40.9	1.37	47.87	41.21	9.35	1.55	278.4		1.56	(Sun et al., 2020)
5	450		2.22					80			(Szabo et al., 2020)

5	150	-40.0	2.22					220			(Szabo et al., 2020)
7	85.4	-33.1	2.40	45.42	47.42	0.55	6.62	246.4	4	1.4	(Kim et al., 2020)
7	83.4	-43.3	1.98	41.75	53.65	0.07	4.54	387.2	4.8	1.8	(Kim et al., 2020)
5.3	250.7	-42.5	1.23					46.5	1.21	0.84	(Gao et al., 2020)
5.3	185.3	-39.0	2.38					71.7	1.49	1.02	(Gao et al., 2020)
5.5	240.7	-45.3	1.77	36.05	51.31	10.35	2.29	125.4	4.8	1.5	(Sun et al., 2021)
5.5	220.1	-45.6	2.02	48.72	36.28	10.6	4.4	78	2.9	1.2	(Sun et al., 2021)
5.5	203.7	-45.5	2.41	53.26	30.68	9.39	6.67	61.5	2.2	1.2	(Sun et al., 2021)
7	156	-53.0	2.34					306	19.0		(An et al., 2021)
5.9	400	-47.0	2.30					33.5	1.16	0.78	(Gao et al., 2022)
7		-36.7						91.6		1.8	(Zeng et al., 2019)
7	486	-37.0						71.6		1.5	(Zeng et al., 2019)
7		-37.8						62.6		1.4	(Zeng et al., 2019)
7		-39.7						43.2		1.3	(Zeng et al., 2019)
7		-42.7						36.4		1.2	(Zeng et al., 2019)
5.4	430	-20.3						31.6			(Story et al., 2020)
7	277	-45.5	1.71					93.5		1	(Liu et al., 2018)
7	700	-42.6	1.75					59.2		0.66	(Liu et al., 2018)
7		-39.0	1.90					33.4		0.33	(Liu et al., 2018)
5.2	137	-35.4						221.6			(Feng et al., 2017)
7	465	-35.2						184			(Sotirelis and Chrysikopoulos, 2017)
6	260	-42.7	2.08	45.72	39.84	7.40	7.04	160		3.4	(Li et al., 2022)
8	260	-46.0	2.08	45.72	39.84	7.40	7.04	210		0.35	(Li et al., 2022)
7	325	-37.1	1.53	34.15	52.21	9.34	3.54	230		1.1	(Song et al., 2022)
7.5	343.3	-27.6						199		2.68	(Shen et al., 2019)
7	129.5	-27.5	1.80	45.16	43.71	4.77	6.36	171			(Du et al., 2018)

7		-41.3	2.36	57.13	32.62	3.06	7.19	67			(Du et al., 2018)
7		-29.6	1.90	49.15	40.26	4.30	6.29	130			(Du et al., 2018)

Table S3.2 Physicochemical properties and CCC of reduced graphene oxide (rGO) reported in literature. Blank cells represent that the corresponding data were not reported. DLS size refers to the hydrodynamic size determined by dynamic light scattering. Zeta potential is calculated from electrophoretic mobility using the Smoluchowski equation. C/O ratio and the fractions of functionalities are determined by XPS.

pH	DLS size (nm)	zeta potential (mV)	C/O ratio	%C-C	%C-O	%C=O	%O-C=O	NaCl CCC (mM)	$MgCl_2$ CCC (mM)	$CaCl_2$ CCC (mM)	Ref.
5.2	580	-50.7	3.1	52.0	31.0	10.0	6.0	30		0.70	(Chowdhury et al., 2015)
5.2	600	-32.9	3.9	62.0	18.0	12.0	8.0	30		0.70	(Chowdhury et al., 2015)
6	143.1	-44.8	2.5	49.1	39.0	3.0	8.9	113			(Qi et al., 2016)
6	283.6	-38.0	3.4	53.8	38.1	1.7	6.6	78			(Qi et al., 2016)
6	293	-33.8	5.7	56.3	35.6	0.1	8.1	41			(Qi et al., 2016)
6	200	-50.0	3.2	60.5	30.7	4.2	4.6	73.9	2.77	2.24	(Jiang et al., 2016)
6	200	-41.0						59.3	2.05	1.86	(Jiang et al., 2016)
6	190	-24.0						13.4	1.06	0.92	(Jiang et al., 2016)
6	190	-20.0	5	75.0	19.9	2.1	3.0	9.9	0.94	0.82	(Jiang et al., 2016)
6	200	-47.3	3.2	60.6	30.1	4.1	4.9	80		2.00	(Jiang et al., 2017)
6	190	-29.4	5	75.1	19.3	2.1	3.1	17		1.30	(Jiang et al., 2017)
7	385.5	-30.0						27	6.00		(Azizighannad and Mitra, 2018)

7	376.7	-29.5						20	5.00		(Azizighannad and Mitra, 2018)
7	327.9	-23.7						15	2.00		(Azizighannad and Mitra, 2018)
5.3	214	-39.0	2.5					35.1	1.01	0.53	(Gao et al., 2020)
7	185	-39.0	3.01					203	11.00		(An et al., 2021)
7	177	-45.0	2.68					237	14.00		(An et al., 2021)
7	403	-25.9						9.96			(Su et al., 2017)
6.3	424.4	-5.1	5.7	82.4	12.5	0.0	5.2	43.8		0.71	(Park et al., 2018)
7	475	-28.9	2.64	63.6	28.8	6.7	3.3	45		1.30	(Song et al., 2022)
7		-44.0	2.54	62.4	25.1	3.1	9.3	66			(Du et al., 2018)

Table S3.3 Physicochemical properties and CCC of MWNT reported in literature. Blank cells represent that the corresponding data were not reported. DLS size refers to the hydrodynamic size determined by dynamic light scattering. Zeta potential is calculated from electrophoretic mobility using the Smoluchowski equation. C/O ratio and the fractions of functionalities are determined by XPS.

pH	DLS size (nm)	zeta potential (mV)	C/O ratio	%C-C	%C-O	%C=O	%O-C=O	NaCl CCC (mM)	$MgCl_2$ CCC (mM)	CaCl2 CCC (mM)	Ref.
6	132	-30.7						25	1.5	2.6	(Saleh et al., 2008)
6	150	-46.1	11.5	91.91	1.09	1.44	4.26	93	1.8	1.2	(Smith et al., 2009a)
6		-37.6	32.3	97.14	0.59	0.79	1.48	50.3			(Smith et al., 2009b)
6	200	-32.2	22.3	96.43	0.79	0.9	1.88	55.6			(Smith et al., 2009b)
6		-38.9	18.6	95.44	1.19	1.09	2.28	64.9			(Smith et al., 2009b)

6	200	-40.0	17.9	96.32	0.49	0.79	2.4	80.1			(Smith et al., 2009b)
6		-38.1	17.2	95.73	0.59	0.99	2.69	77.9			(Smith et al., 2009b)
6	200	-40.3	12.2	93.63	1	1.19	4.18	101.1			(Smith et al., 2009b)
6	200	-37.9	11.3	93.23	1.09	1.39	4.29	94			(Smith et al., 2009b)
6		-41.8	10.8	93.02	1.59	1.89	3.5	106			(Smith et al., 2009b)
6		-42.6	10.1	94.31	0.9	1.4	3.39	125.8			(Smith et al., 2009b)
6		-35.2	9.5	93.02	0.79	1.6	4.59	127.3			(Smith et al., 2009b)
6		-41.2	8.3	90.82	1.3	2.59	5.29	128.8			(Smith et al., 2009b)
7.1	104	-44.8	8.4	89.84	1.12	1.64	7.4	210			(Yi and Chen, 2011)
7.1	150	-32.0	14.9	93	0.79	1.17	5.04	53			(Yi and Chen, 2011)
6	130	-40.0						125	0.6		(Ntim et al., 2011)
6								170	1.7		(Ntim et al., 2012)
6								170	2.3		(Ntim et al., 2012)
6								200	2.35		(Ntim et al., 2012)
6								190	1.65		(Ntim et al., 2012)
6								205	1.6		(Ntim et al., 2012)
6								130	1.65		(Ntim et al., 2012)
6								85	1.6		(Ntim et al., 2012)
6								160	0.4		(Ntim et al., 2012)
7	125	-30.0						81.5	1.65		(Wu and Mitra, 2014)
7	117	-36.0						196	5.9		(Wu and Mitra, 2014)
6	530	-37.1						25		0.9	(Liu et al., 2016)
7.2	292.4	-25.2	15.7					30		3	(Yang et al., 2017)
6	87	-32.6						142	1		(Wu et al., 2017)
6	82	-34.1						160	3.3		(Wu et al., 2017)

6	80	-37.4						165	4.5		(Wu et al., 2017)
6	80	-37.4						165	4.9		(Wu et al., 2017)
6	80	-38.0						168	4.9		(Wu et al., 2017)
6	80	-37.2						168	5.2		(Wu et al., 2017)
6	295.2	-13.2	90.9					8.78	0.95	0.98	(Xia et al., 2019)
6	263.5	-19.1	47.6	88.6	6.11	0.69	2.34	10.51	1.05	0.9	(Xia et al., 2019)
6	145.6	-34.0	23.8	72.8	11.5	1.88	9.83	33.12	1.4	0.72	(Xia et al., 2019)

Table S3.4 Physicochemical properties and CCC of SWNT reported in literature. Blank cells represent that the corresponding data were not reported. DLS size refers to the hydrodynamic size determined by dynamic light scattering. Zeta potential is calculated from electrophoretic mobility using the Smoluchowski equation. C/O ratio and the fractions of functionalities are determined by XPS.

pH	DLS size (nm)	zeta potential (mV)	C/O ratio	%C-C	%C-O	%C=O	%O-C=O	NaCl CCC (mM)	$MgCl_2$ CCC (mM)	$CaCl_2$ CCC (mM)	Ref.
6	78.1	-15.9						20		2	(Saleh et al., 2010)
6	120		7.1					160			(Li and Huang, 2010)
6.5	120	-24.8	7.4					96		2.8	(Khan et al., 2013)
6.5	208	-19.3	6.5					13		0.6	(Khan et al., 2013)

Table S3.5 Spearman's correlation coefficient between CCC and physicochemical properties of GO (all data included).

Material Property	NaCl		$MgCl_2$		$CaCl_2$	
	Spearman's rank correlation coefficient	*p*-value	Spearman's rank correlation coefficient	*p*-value	Spearman's rank correlation	*p*-value
Hydrodynamic size	-0.540 (n = 40)	**3.6E-04**	-0.300 (n = 16)	0.259	-0.262 (n = 31)	0.155
Zeta potential	0.030 (n = 41)	0.830	0.125 (n = 16)	0.644	0.298 (n = 34)	0.082
C/O ratio	-0.102 (n = 31)	0.586	0.027 (n = 11)	0.936	-0.171 (n = 24)	0.425
%C-C	-0.155 (n = 22)	0.492	-0.396 (n = 7)	0.379	0.064 (n = 18)	0.800
%C-O	0.277 (n = 22)	0.212	0.631 (n = 7)	0.129	-0.099 (n = 18)	0.695
%C=O	-0.044 (n = 22)	0.845	-0.342 (n = 7)	0.452	-0.035 (n = 18)	0.890
%O-C=O	-0.314 (n = 22)	0.155	-0.541 (n = 7)	0.210	0.109 (n = 18)	0.668

Table S3.6 Spearman's correlation coefficient between CCC and physicochemical properties of rGO (all data included).

Material Property	**NaCl**		**$MgCl_2$**		**$CaCl_2$**	
	Spearman's rank correlation coefficient	*p*-value	Spearman's rank correlation coefficient	*p*-value	Spearman's rank correlation	*p*-value
Hydrodynamic size	-0.342 (n = 20)	0.140	-0.134 (n = 10)	0.712	-0.465 (n = 11)	0.149
Zeta potential	-0.699 (n = 21)	**4E-04**	-0.547 (n = 8)	0.102	-0.228 (n = 11)	0.500
C/O ratio	-0.463 (n = 15)	0.082	-0.400 (n = 5)	0.505	0.174 (n = 9)	0.655
%C-C	-0.501 (n = 12)	0.097	- (n = 2)	-	-0.084 (n = 8)	0.843
%C-O	0.578 (n = 12)	0.049	- (n = 2)	-	0.337 (n = 8)	0.414
%C=O	-0.004 (n = 12)	0.991	- (n = 2)	-	-0.301 (n = 8)	0.468
%O-C=O	0.420 (n = 12)	0.174	- (n = 2)	-	-0.554 (n = 8)	0.154

Table S3.7 Spearman's correlation coefficient between CCC and physicochemical properties of MWNT (all data included).

Material Property	NaCl		MgCl$_2$		CaCl$_2$	
	Spearman's rank correlation coefficient	*p*-value	Spearman's rank correlation coefficient	*p*-value	Spearman's rank correlation	*p*-value
Hydrodynamic size	-0.82 (n = 22)	**< 0.001**	-0.367 (n = 14)	0.197	-0.090 (n = 7)	0.848
Zeta potential	-0.47 (n = 29)	**0.011**	-0.257 (n = 14)	0.376	0.162 (n = 7)	0.728
C/O ratio	-0.915 (n = 18)	**< 0.001**	- (n = 4)	-	-0.500 (n = 5)	0.391
%C-C	-0.115 (n = 16)	0.672	- (n = 3)	-	- (n = 3)	-
%C-O	0.028 (n = 16)	0.918	- (n = 3)	-	- (n = 3)	-
%C=O	0.655 (n = 16)	0.006	- (n = 3)	-	- (n = 3)	-
%O-C=O	0.438 (n = 16)	0.090	- (n = 3)	-	- (n = 3)	-

References for Appendix A

An, S., Zeng, Q., Li, W. and Fortner, J. 2021. A graphene oxide cookbook: Exploring chemical and colloidal properties as a function of synthesis parameters. J. Colloid Interface Sci. 588, 725-736.

Azizighannad, S. and Mitra, S. 2018. stepwise reduction of graphene oxide (GO) and its effects on chemical and colloidal properties. Sci. Rep. 8(1), 10083.

Chowdhury, I., Duch, M.C., Mansukhani, N.D., Hersam, M.C. and Bouchard, D. 2013. Colloidal properties and stability of graphene oxide nanomaterials in the aquatic environment. Environ. Sci. Technol. 47(12), 6288-6296.

Chowdhury, I., Mansukhani, N.D., Guiney, L.M., Hersam, M.C. and Bouchard, D. 2015. Aggregation and stability of reduced graphene oxide: Complex roles of divalent cations, pH, and natural organic matter. Environ. Sci. Technol. 49(18), 10886-10893.

Du, T., Adeleye, A.S., Zhang, T., Jiang, C., Zhang, M., Wang, H., Li, Y., Keller, A.A. and Chen, W. 2018. Influence of light wavelength on the photoactivity, physicochemical transformation, and fate of graphene oxide in aqueous media. Environ. Sci.: Nano 5(11), 2590-2603.

Feng, Y., Liu, X., Huynh, K.A., McCaffery, J.M., Mao, L., Gao, S. and Chen, K.L. 2017. Heteroaggregation of graphene oxide with nanometer- and micrometer-sized hematite colloids: Influence on nanohybrid aggregation and microparticle sedimentation. Environ. Sci. Technol. 51(12), 6821-6828.

Gao, Y., Ren, X., Song, G., Chen, D., Zhang, X. and Chen, C. 2020. Colloidal properties and stability of UV-transformed graphene oxide in aqueous solutions: The role of disorder degree. J. Hazard. Mater. 382, 121097.

Gao, Y., Zeng, X., Zhang, W., Zhou, L., Xue, W., Tang, M. and Sun, S. 2022. The aggregation behaviour and mechanism of commercial graphene oxide in surface aquatic environments. Sci. Total Environ. 806, 150942.

Huang, G., Guo, H., Zhao, J., Liu, Y. and Xing, B. 2016. Effect of co-existing kaolinite and goethite on the aggregation of graphene oxide in the aquatic environment. Water Res. 102, 313-320.

Jiang, Y., Raliya, R., Fortner, J.D. and Biswas, P. 2016. Graphene oxides in water: Correlating morphology and surface chemistry with aggregation behavior. Environ. Sci. Technol. 50(13), 6964-6973.

Jiang, Y., Raliya, R., Liao, P., Biswas, P. and Fortner, J.D. 2017. Graphene oxides in water: assessing stability as a function of material and natural organic matter properties. Environ. Sci.: Nano 4(7), 1484-1493.

Khan, I.A., Afrooz, A.R.M.N., Flora, J.R.V., Schierz, P.A., Ferguson, P.L., Sabo-Attwood, T. and Saleh, N.B. 2013. Chirality affects aggregation kinetics of single-walled carbon nanotubes. Environ. Sci. Technol. 47(4), 1844-1852.

Kim, C., Lee, J., Wang, W. and Fortner, J. 2020. Organic functionalized graphene oxide behavior in water. Nanomaterials 10(6), 1228.

Li, M. and Huang, C.P. 2010. Stability of oxidized single-walled carbon nanotubes in the presence of simple electrolytes and humic acid. Carbon 48(15), 4527-4534.

Li, W., Yu, J., Zhang, S., Tang, H. and Huang, T. 2022. The fate of aggregated graphene oxide upon the increasing of pH: An experimental and molecular dynamic study. Sci. Total Environ. 851, 157954.

Liu, W., Zhao, X., Cai, Z., Han, B. and Zhao, D. 2016. Aggregation and stabilization of multiwalled carbon nanotubes in aqueous suspensions: influences of carboxymethyl cellulose, starch and humic acid. RSC Advances 6(71), 67260-67270.

Liu, X., Xu, X., Sun, J., Duan, S., Sun, Y., Hayat, T. and Li, J. 2018. Interaction between Al_2O_3 and different sizes of GO in aqueous environment. Environ. Pollut. 243, 1802-1809.

Ntim, S.A., Sae-Khow, O., Desai, C., Witzmann, F.A. and Mitra, S. 2012. Size dependent aqueous dispersibility of carboxylated multiwall carbon nanotubes. J. Environ. Monit. 14(10), 2772-2779.

Ntim, S.A., Sae-Khow, O., Witzmann, F.A. and Mitra, S. 2011. Effects of polymer wrapping and covalent functionalization on the stability of MWCNT in aqueous dispersions. J. Colloid Interface Sci. 355(2), 383-388.

Park, C.M., Wang, D., Heo, J., Her, N. and Su, C. 2018. Aggregation of reduced graphene oxide and its nanohybrids with magnetite and elemental silver under environmentally relevant conditions. J. Nanopart. Res. 20(4), 93.

Qi, Y., Xia, T., Li, Y., Duan, L. and Chen, W. 2016. Colloidal stability of reduced graphene oxide materials prepared using different reducing agents. Environ. Sci.: Nano 3(5), 1062-1071.

Saleh, N.B., Pfefferle, L.D. and Elimelech, M. 2008. Aggregation kinetics of multiwalled carbon nanotubes in aquatic systems: Measurements and environmental implications. Environ. Sci. Technol. 42(21), 7963-7969.

Saleh, N.B., Pfefferle, L.D. and Elimelech, M. 2010. Influence of biomacromolecules and humic acid on the aggregation kinetics of single-walled carbon nanotubes. Environ. Sci. Technol. 44(7), 2412-2418.

Shen, M., Hai, X., Shang, Y., Zheng, C., Li, P., Li, Y., Jin, W., Li, D., Li, Y., Zhao, J., Lei, H., Xiao, H., Li, Y., Yan, G., Cao, Z. and Bu, Q. 2019. Insights into aggregation and transport of graphene oxide in aqueous and saturated porous media: Complex effects of cations with different molecular weight fractionated natural organic matter. Sci. Total Environ. 656, 843-851.

Smith, B., Wepasnick, K., Schrote, K.E., Bertele, A.R., Ball, W.P., O'Melia, C. and Fairbrother, D.H. 2009a. Colloidal properties of aqueous suspensions of acid-treated, multi-walled carbon nanotubes. Environ. Sci. Technol. 43(3), 819-825.

Smith, B., Wepasnick, K., Schrote, K.E., Cho, H.-H., Ball, W.P. and Fairbrother, D.H. 2009b. Influence of surface oxides on the colloidal stability of multi-walled carbon nanotubes: A structure−property relationship. Langmuir 25(17), 9767-9776.

Song, J., Zeng, Y., Liu, Y. and Jiang, W. 2022. Retention of graphene oxide and reduced graphene oxide in porous media: Diffusion-attachment, interception-attachment and straining. J. Hazard. Mater. 431, 128635.

Sotirelis, N.P. and Chrysikopoulos, C.V. 2017. Heteroaggregation of graphene oxide nanoparticles and kaolinite colloids. Sci. Total Environ. 579, 736-744.

Story, S.D., Boggs, S., Guiney, L.M., Ramesh, M., Hersam, M.C., Brinker, C.J. and Walker, S.L. 2020. Aggregation morphology of planar engineered nanomaterials. J. Colloid Interface Sci. 561, 849-853.

Su, Y., Yang, G., Lu, K., Petersen, E.J. and Mao, L. 2017. Colloidal properties and stability of aqueous suspensions of few-layer graphene: Importance of graphene concentration. Environ. Pollut. 220, 469-477.

Sun, B., Zhang, Y., Chen, W., Wang, K. and Zhu, L. 2018. Concentration dependent effects of bovine serum albumin on graphene oxide colloidal stability in aquatic environment. Environ. Sci. Technol. 52(13), 7212-7219.

Sun, B., Zhang, Y., Li, R., Wang, K., Xiao, B., Yang, Y., Wang, J. and Zhu, L. 2021. New insights into the colloidal stability of graphene oxide in aquatic environment: Interplays of photoaging and proteins. Water Res. 200, 117213.

Sun, B., Zhang, Y., Liu, Q., Yan, C., Xiao, B., Yang, J., Liu, M. and Zhu, L. 2020. Lateral size dependent colloidal stability of graphene oxide in water: impacts of protein properties and water chemistry. Environ. Sci.: Nano 7(2), 634-644.

Szabo, T., Maroni, P. and Szilagyi, I. 2020. Size-dependent aggregation of graphene oxide. Carbon 160, 145-155.

Tang, H., Zhao, Y., Yang, X., Liu, D., Shao, P., Zhu, Z., Shan, S., Cui, F. and Xing, B. 2017. New Insight into the Aggregation of graphene oxide using molecular dynamics simulations and extended Derjaguin–Landau–Verwey–Overbeek theory. Environ. Sci. Technol. 51(17), 9674-9682.

Wang, M., Gao, B., Tang, D., Sun, H., Yin, X. and Yu, C. 2018. Effects of temperature on aggregation kinetics of graphene oxide in aqueous solutions. Colloids Surf. A Physicochem. Eng. Asp. 538, 63-72.

Wu, L., Liu, L., Gao, B., Muñoz-Carpena, R., Zhang, M., Chen, H., Zhou, Z. and Wang, H. 2013. Aggregation kinetics of graphene oxides in aqueous solutions: Experiments, mechanisms, and modeling. Langmuir 29(49), 15174-15181.

Wu, Z. and Mitra, S. 2014. Length reduction of multi-walled carbon nanotubes via high energy ultrasonication and its effect on their dispersibility. J. Nanopart. Res. 16(8), 2563.

Wu, Z., Wang, Z., Yu, F., Thakkar, M. and Mitra, S. 2017. Variation in chemical, colloidal and electrochemical properties of carbon nanotubes with the degree of carboxylation. J. Nanopart. Res. 19(1), 16.

Xia, T., Guo, X., Lin, Y., Xin, B., Li, S., Yan, N. and Zhu, L. 2019. Aggregation of oxidized multi-walled carbon nanotubes: Interplay of nanomaterial surface O-functional groups and solution chemistry factors. Environ. Pollut. 251, 921-929.

Yang, K., Chen, B., Zhu, X. and Xing, B. 2016. Aggregation, adsorption, and morphological transformation of graphene oxide in aqueous solutions containing different metal cations. Environ. Sci. Technol. 50(20), 11066-11075.

Yang, X., Wang, Q., Qu, X. and Jiang, W. 2017. Bound and unbound humic acids perform different roles in the aggregation and deposition of multi-walled carbon nanotubes. Sci. Total Environ. 586, 738-745.

Yi, P. and Chen, K.L. 2011. Influence of surface oxidation on the aggregation and deposition kinetics of multiwalled carbon nanotubes in monovalent and divalent electrolytes. Langmuir 27(7), 3588-3599.

Zeng, Z., Wang, Y., Zhou, Q., Yang, K. and Lin, D. 2019. New insight into the aggregation of graphene oxide in synthetic surface water: Carbonate nanoparticle formation on graphene oxide. Environ. Pollut. 250, 366-374.

Chapter 4 Aggregation of Engineered DNA-Grafted Nanoparticles in Water: Critical Role of Sequence-Dependent Conformation of DNA Coating

(This chapter is based on Peng, B., Liu, Z., & Jiang, Y. (2022). Aggregation of DNA-grafted nanoparticles in water: The critical role of sequence-dependent conformation of DNA coating. *The Journal of Physical Chemistry B*, *126*(4), 847-857. DOI: 10.1021/acs.jpcb.1c09450)

Abstract

Aggregation behavior of nanoparticles in water, particularly in the presence of surface coating, is a fundamental behavior to understand as it closely relates to the material function, reactivity, and toxicity. Engineered DNA, an important type of surface coating, is essentially different from conventional polymeric coatings with homogeneous repeating units. The heterogeneous nature of DNA with numerous combinations of the four nucleotides poses a challenge to understand the aggregation of nanoparticles coated with them. In this study, we use both experimental and computational approaches to study how DNA properties influence the aggregation of DNA-conjugated gold nanoparticles (DNA-AuNPs). Aggregation kinetics under different pH values and in three salts (NaCl, $CaCl_2$, and $MgCl_2$) were investigated. Overall, DNA-AuNPs demonstrated similar aggregation behavior of electrosterically stabilized nanoparticles, where the surface coating layer thickness played a determining role. The underlying interactions between DNA-AuNPs were analyzed by an extended DLVO model, and the excluded volume repulsion, which varied as a function of layer thickness, was the dominant stabilizing repulsion. Interestingly, the DNA sequence was found to cause different layer thicknesses and thus profoundly different aggregation behaviors in the presence of cations.

The interactions between DNA strands with different sequences and surrounding counterions were investigated via molecular dynamics simulations. The simulation results were consistent with experimental observations and supported the sequence-dependent conformational change of DNA coating. Our study provides new molecular-level insights into aggregation of nanoparticles with heterogeneous surface coating such as DNA.

4.1 Introduction

Aggregation of nanoparticles (NPs) reduces available surface area, in turn leading to altered material function, reactivity, and toxicity (Hotze et al., 2010). As such, the aggregation behavior of engineered NPs has attracted extensive research attention, e.g., metal (oxide) NPs (Chowdhury et al., 2012; El Badawy et al., 2010; Nason et al., 2012; Phenrat et al., 2008), C_{60} (Chen and Elimelech, 2006; 2007), carbon nanotube (Saleh et al., 2008; 2010; Yi and Chen, 2011), graphene (oxide) (Chowdhury et al., 2013; Chowdhury et al., 2015; Jiang et al., 2016; Jiang et al., 2017), and emerging 2D materials (MoS_2, WS_2, h-BN, and MXene) (Mohona et al., 2019; Xie et al., 2020), among others. Surface functionalization of engineered NPs (e.g., with small molecules, synthetic polymers, biomacromolecules) is common for material processing convenience and/or specific functionality (Hotze et al., 2010), and it alters the aggregation behavior of engineered NPs (Ditsch et al., 2005; Golas et al., 2010; Moore et al., 2003; Phenrat et al., 2008; Surette and Nason, 2016). It is thus important to study the effects of surface coatings on aggregation of NPs, however, it remains a challenge due to difficulty in resolving the structures of these surface coatings under various solution conditions.

Engineered DNA emerges as an important type of surface coating, due to its remarkable binding specificity and thermodynamic stability. As a long-chain polyelectrolyte, DNA has the most predictable and programmable interactions of any natural or synthetic molecule (Seeman and Sleiman, 2017). It consists of nucleotides in a specific order. Each nucleotide contains a deoxyribose sugar, a phosphate group, and one of the four nitrogenous bases, namely adenine (A), thymine (T), cytosine (C), and guanine (G). Applications of engineered DNA-coated NPs range across diverse scientific and technological fields, such as materials synthesis (Macfarlane et al., 2011), diagnostics (Taton et al., 2000), and therapeutics (Rosi et al., 2006). The colloidal stability of such particles is of essence in its functionality, particularly in cell culture media or other challenging buffers. For example, the crystallization of DNA-functionalized NPs into well-defined structures relied on the excluded volume repulsion to counterbalance the DNA hybridization attraction (Seo et al., 2017); the assembly of DNA-coated gold nanorods into DNA origami structure for the detection of RNA was performed in solution with ionic strength as high as 14 mM $MgCl_2$ and 500 mM NaCl (Funck et al., 2018); the enhanced drug (Paclitaxel) effectiveness in aqueous media was due to its significantly enhanced stability and solubility by attaching the drug onto gold NP surface via DNA linkers (Zhang et al., 2011). A fundamental understanding of the molecular interactions of DNA coatings can also benefit the design and applications of nanomaterial-based aptasensors, e.g., the detection of bacteria (Zhang et al., 2019) and heavy metals (Zong et al., 2019). An earlier study showed the aggregation of NPs with self-complementary DNA sequences is driven by combinatorial entropy (Sciortino et al., 2020). However, overall, very limited attention has been devoted to reveal the mechanisms governing the aggregation of DNA-grafted NPs, especially with the non-complementary DNA coatings.

Conventional polymer coatings are organic macromolecules consisting of repeating monomer units. They stabilize NPs by providing extra (electro)steric repulsion, the magnitude of which is determined by the properties and structure of the polymer coating. For example, the stability of NPs was found to be positively related to the layer thickness and molecular weight of adsorbed polymers (carboxymethyl cellulose and Pluronic) (Moore et al., 2003; Phenrat et al., 2008). The structure of the coating changes under different solution conditions. For instance, the conformation of polystyrenesulfonate (PSS) brushes tethered on a surface showed a dependency on the valency of surrounding counterions (Yu et al., 2016). While monovalent counterions induced a homogeneous shrinkage of the brushes, multivalent counterions could trigger a pinned micelle-like heterogeneous collapse with a thinner layer. Furthermore, the span of the adsorbed polymer layer, which represents a layer thickness taking into account a greater contribution from the tails, was considered to greatly contribute to the colloidal stability of the coated NPs (Goodwin et al., 2013).

DNA is a polymer with unique material features. As loading increases, end-grafted DNA takes the form of wrapping around the NPs, to a more upright and random coil conformation, and eventually to a stretched shape with DNA standing perpendicularly to the surface (Parak et al., 2003). For densely packed DNA strands, short DNA (< 30 bases) is fully stretched on particle surface, while longer DNA has a mixture of fully stretched inner parts and randomly coiled outer parts (Parak et al., 2003). DNA, however, differs from conventional polymer in its intrinsic structural complexity, i.e., sequence. Different interaction/reaction potentials of the nucleobases toward NPs and solutes affect the structure of the DNA coating. For example, thymine was found to have lower affinity towards gold NP surface compared to other bases, allowing for a higher packing density of DNA strands containing a thymine spacer (Hurst et al., 2006). Furthermore, different positions of the bases in a strand were observed to affect the DNA loading on a NP (Brown et al., 2008) and the height of DNA strands grafted on a surface (Holland and Geiger, 2012). Also, variation in the affinities of bases with surrounding metal ions (e.g., Na^+, Mg^{2+}, Ca^{2+}) influenced the folding structure of DNA strands (Kolev et al., 2018). These molecular-level heterogeneity can add extreme complexity to the aggregation behavior of DNA-coated NPs. It has been reported that the aggregation of DNA-coated NPs in $MgCl_2$ was affected by the DNA sequence (Storhoff et al., 2002). However, the study was limited to homobase strands (poly-adenine/thymine/cytosine), the effects of guanine and the heterogeneous nature of DNA, as well as the cation-induced structural change of the DNA coating, remain largely unknown.

The objective of this study therefore is to obtain a molecular-level understanding of the structure (change) of DNA coatings in presence of ubiquitous cations and the subsequent impact on the aggregation behavior of engineered DNA NPs. Specifically, DNA functionalized gold nanoparticle (DNA-Au NP) was used as model particles; their aggregation kinetics under the influence of systematically varied DNA properties (i.e., length and sequence) and aquatic chemistries (pH and presence of NaCl, $MgCl_2$, or $CaCl_2$ salts) were studied. An extended DLVO model was used to gain a theoretical understanding of the interactions between DNA-Au NPs. Molecular dynamic (MD) simulation was performed to investigate the interactions between counterions and DNA coatings. Supported by both experimental and theoretical results, our study highlights the sequence-dependent conformational change of DNA coating in presence of cations and its subsequent impact on the aggregation behaviors of DNA-Au NPs. The findings from this study reveal the fundamental aspects of the aggregation behavior of DNA-grafted nanomaterials in a structure-activity manner, benefiting the design and applications of such materials.

4.2 Experimental

4.2.1 Materials and Chemicals

Spherical Au NPs (citrate-capped, 20 nm, Ted Pella, Inc., denoted as Citrate-Au hereafter) were used as the NP core for synthesis of DNA-Au NPs. Single-stranded DNA (ssDNA), based on our given design, was purchased from Integrated DNA Technologies, Inc. (IDT). Upon receipt it was dissolved in 10 mM Tris buffer and stored at 4 °C. Four DNA strands (denoted as DNA_{15}, DNA_{25}, DNA_{25C}, and DNA_{40}) were carefully designed: each strand has two regions, starting with a 10-base region of adenine (A10) as a spacer, followed by another 5- to 30-base region of systematically varied sequences (Table 4.1). Namely, the DNA_{15} includes the first five bases after the A10 spacer in DNA_{25}, and DNA_{40} has two repeated 15-base segments that appear (once) in DNA_{25}. Such design with repeated segments was aimed at singling out the effect of DNA length. Furthermore, to evaluate the effect of the DNA sequence, DNA_{25C} was designed with sequence being complementary to that of DNA_{25} except the A10 spacer region.

The DNA strands were modified with a thiol group at 3’ end to allow covalent Au-S bonding between DNA and Au NP (Mirkin et al., 1996).

Table 4.1 Single-stranded DNA sequences and modifications

DNA	Sequence (3’ to 5’)
DNA_{15}	$HS-(CH_2)_3$-AAAAAAAAAA GACTC
DNA_{25}	$HS-(CH_2)_3$-AAAAAAAAAA GACTCATACTCACCT
DNA_{25C}	$HS-(CH_2)_3$-AAAAAAAAAA CTGAGTATGAGTGGA
DNA_{40}	$HS-(CH_2)_3$-AAAAAAAAAA GACTCATACTCACCT GACTCATACTCACCT

4.2.2 Synthesis of DNA-Au NPs

Au NPs were functionalized with DNA strands using the salt-aging method described in literature (Liu and Liu, 2017; Mirkin et al., 1996). Briefly, thiol modified DNA (2 μM) was firstly treated with Tris(2-carboxyethyl)phosphine hydrochloride (TCEP) at a 100:1 ratio (TCEP:DNA) for at least 90 min to cleave the disulfide bond. Afterwards, Au NP suspension was added to a final concentration of 1.16 nM. The mixture was incubated in the dark overnight (DNA: Au NP = 1720:1). Then, NaCl solution (2 M) was added in a stepwise manner to reach a final concentration of 0.1 M. The solution was allowed to age under these conditions for another 24 hr. Excess reagents were then removed by centrifugation at 11,000 g for 20 min. The Au NP pellets were redispersed with DI water. The procedure was repeated for another two times to ensure the unbonded DNA was completely removed from the dispersion. The as-synthesized DNA-Au NPs were eventually dispersed in DI water and stored at 4 °C until any characterization or experiment.

4.2.3 Characterization of Citrate-Au and DNA-Au NPs

The morphology and size of Citrate-Au and DNA-Au NPs were examined by transmission electron microscopy (TEM, JOEL JEM-2010). Hydrodynamic diameter (D_h) and electrophoretic mobility (EPM) were characterized using dynamic/electrophoretic light scattering with ZetaSizer Nano ZS90 (Malvern Instruments). Optical property was measured by UV/Vis spectroscopy (Biochrom Libra S35) and the absorbance at 522 nm for Citrate-Au and 526 nm for DNA -Au was used to calculate the concentration of Au NPs via the Beer–Lambert law. An extinction coefficient (ε) of 8.7×10^8 L/(mol·cm) was used for the 20 nm Au NPs (Pellegrino et al., 2007). The concentration of Citrate-Au calculated with the extinction coefficient was consistent with the concentration provided by the manufacturer. Surface chemistry information was obtained with X-ray photoelectron spectroscopy (XPS, PHI 5000 VersaProbe III, operating with monochromatic Al Kα X-ray source) and the data were analyzed using software PHI MultiPak. Raman Spectra of the DNA_{25}-Au and DNA_{25C}-Au with or without the presence of electrolyte (NaCl, $MgCl_2$, $CaCl_2$) were recorded with a Raman spectrometer (i-Raman Plus, B&W TEK). KBr was added into the sample and the mixture was freeze-dried and homogenized, then pressed into a pellet for measurement.

4.2.4 Quantification of DNA Loading on Au NPs

First, mercaptoethanol (ME) was added into DNA-Au NPs to displace anchored DNA from Au NPs (final concentration of 12 mM) (Demers et al., 2000). The dispersion was allowed to incubate at room temperature for 24 hr with intermittent shaking, then centrifuged (11,000 *g*, 20 min) to separate detached DNA from Au NPs. The supernatant containing the detached DNA was replaced into an Amicon Ultra centrifugal filter (MWCO: 3k Da) and centrifuged at 14,000 *g* for 30 min following the manufacturer's procedure. Excessive ME solution was forced to pass through the filter while DNA was retained. DI water was added after centrifugation and the washing process was repeated for a total of four times to completely remove ME. The UV absorbance at 260 nm of retained DNA solution was measured with a Thermo Scientific NanoDrop 2000c Spectrophotometer and the corresponding concentration was determined via the Beer-Lambert law. The extinction coefficients (ε) for each DNA provided by IDT are listed in Table S4.1 (Appendix B: Supporting Information, S.I.). Control experiment with known DNA concentration confirms the recovery rates for each DNA were similar and all higher than 90%. Finally, DNA loading (DNA per Au NP) was calculated by dividing the number of DNA strands by that of Au NP.

4.2.5 Aggregation Kinetics of Citrate-Au and DNA-Au NPs

To investigate the aggregation kinetics of DNA-Au NPs, time-resolved dynamic light scattering (TR-DLS) was used to track the initial change of hydrodynamic diameter (D_h) of NPs upon addition of electrolytes. In early stage of aggregation, initial rate constant (k_i) is proportional to the initial rate of increase in the D_h and inversely proportional to the initial particle concentration N_0 (Equation 4.1) (Chen and Elimelech, 2007; Holthoff et al., 1996).

$$k_{\mathrm{i}} = \frac{1}{N_0}\left(\frac{\mathrm{d}}{\mathrm{d}t}D_{\mathrm{h}}(t)\right)_{t\to 0} \tag{4.1}$$

Attachment efficiency (α, also known as the inverse stability ratio) at various electrolyte concentrations can be calculated by normalizing the initial rate constant to the rate constant obtained under diffusion-limited regime (k_{fast}), where electrostatic repulsion is completely screened and aggregation is only limited by diffusion (Equation 4.2) (Chen and Elimelech, 2007; Holthoff et al., 1996).

$$\alpha = \frac{k_{\mathrm{i}}}{k_{\mathrm{fast}}} = \frac{\frac{1}{N_0}\left(\frac{\mathrm{d}}{\mathrm{d}t}D_{\mathrm{h}}(t)\right)_{t\to 0}}{\frac{1}{N_{0,\mathrm{fast}}}\left(\frac{\mathrm{d}}{\mathrm{d}t}D_{\mathrm{h}}(t)\right)_{t\to 0,\mathrm{fast}}} \tag{4.2}$$

In the experiment, Citrate-Au or DNA-Au suspension and electrolyte solution (NaCl, $CaCl_2$, and $MgCl_2$ at various concentrations) of equal volume (0.5 mL) were mixed in a cuvette to reach desired concentrations (NP = 10 mg/L; NaCl = 0−4 M; $CaCl_2$ = 0−100 mM; $MgCl_2$ = 0−100 mM). After vortex for 1 s, the cuvette was placed into the testing chamber of the DLS instrument. Having reached equilibrium after 15 s, the D_h of the suspension was measured at a 15 s interval for a period of 1200 s. Initial rate of change of D_h was calculated for the period between t = 0 and the time when D_h reached $1.30D_{h0}$ (Chen and Elimelech, 2007). pH of the suspension was unadjusted and determined to be 6.0 ± 0.2. Because the concentrations of Citrate-Au/DNA-Au remained identical ($N_0 = N_{0,fast}$), α was then determined to be the ratio of the initial rate of change of D_h in the reaction-limited regime over that in the diffusion-limited regime. Critical coagulation concentrations (CCC) were determined as the intersection of extrapolated lines through the diffusion- and reaction-limited regimes.

4.2.6 Molecular Dynamics Simulation

MD simulations of DNA_{25} and DNA_{25C} were performed using GROMACS 2016.2 simulation package (Abraham et al., 2015) in rectangular simulation boxes under three-dimensional periodic boundary conditions. The Amber 14SB (Maier et al., 2015) force field with OL15 (Zgarbová et al., 2015) modification for DNA and all ions, and the SPC/E force field (Berendsen et al., 1987) for water were employed in the simulation. Five DNA strands were grafted to a gold surface in the simulation box, according to the grafting density of DNA_{25}-Au and DNA_{25C}-Au as determined by the experiment. Calcium ions were initially randomly placed in the total simulation box and well separated from each other (60/90/120 ions, corresponding to 100/150/200% of the charges of DNA strands neutralized by Ca^{2+}). In the cases of 150% and 200% neutralization, Cl^- was used to maintain the electroneutrality of the simulation box. The simulations were equilibrated in the isothermal-isobaric ensemble for 100 ns, where the Parrinello-Rahman barostat/Nosé-Hoover thermostat (Hoover, 1985; Parrinello and Rahman, 1981) with pressure/temperature coupling time constant of 0.4 ps/2 ps was chosen. After equilibration, a subsequent 50 ns production simulation was executed in a canonical ensemble with a coupling time of 1 ps. The time step was 2 fs. The system configuration for each simulation cell and the periodic lengths after equilibrations are listed in

Table S4.2 and S4.3. The radial distribution functions (RDFs) and the number of associated calcium ions with respect to specific DNA atoms were analyzed. Counting of the associated calcium ions was carried out by using the proximity method with a cutoff distance of 5 Å.

4.3 Results and Discussion

4.3.1 Materials Characterization

Figure 4.1a shows the normalized UV/Vis spectra of Citrate-Au and DNA-Au aqueous suspensions. Compared to Citrate-Au, DNA-Au displayed similar UV/Vis spectra, but with a slight red-shift of the localized surface plasmon resonance peak (from 522 to 526 nm, 1a inset), consistent with a previous study (Storhoff et al., 1998). This shift was induced by successful DNA functionalization which increased the local refractive index at the surface of Au NPs (Raschke et al., 2003). The XPS survey spectrum of DNA_{40}-Au (Figure 4.1b) reveals the emergence of nitrogen and phosphorus signals, corresponding to the nitrogenous base and phosphate backbone of DNA, respectively, further confirming the successful DNA functionalization. Figure 4.1c shows the intensity-based hydrodynamic size (D_h) distribution of Citrate-Au and DNA-Au NPs suspended in DI water. An increase of the D_h was observed upon DNA displacement of citrate group, which could be attributed to the stretched conformation of DNA strands on the Au particle surface (Carnerero et al., 2017; Cutler et al., 2012; Parak et al., 2003). The average D_h increased from 22 nm of Citrate-Au to 30.8 ± 1.5 nm of DNA_{15}-Au, 31.2 ± 1.7 nm of DNA_{25}-Au, 33.1 ± 0.5 nm of DNA_{25C}-Au, and 35.4 ± 1.5 nm of DNA_{40}-Au (Table S4.1). Particles remained monodispersed (polydispersity index < 0.3). The TEM image shows that DNA functionalization did not alter the spherical shape of Au NPs, and the DNA coating was not observable (Figure S4.1a). With the presence of cations, a ring around the Au NPs was observed, likely attributable to condensed DNA coating (Figure S4.1b-d). Analysis of particle diameter by software ImageJ yielded an average size of 21.7 ± 1.3 nm, consistent with that obtained from DLS measurement and that provided by the manufacturer

(20.5 nm). The loading of DNA per Au particle is shown in Figure 4.1d. Under our DNA design scheme (detail in the Experimental section), DNA_{15}-Au possessed the highest loading (116 ± 19 strands per particle), which could be attributed to the shortest length of DNA_{15}. Statistical analysis (one-way ANOVA test followed by the Tukey test for multiple comparisons, $p < 0.05$) did not show a significant difference in the loadings between DNA_{25}-Au and DNA_{40}-Au, as well as between DNA_{25}-Au and DNA_{25C}-Au. The loadings of DNA_{25}-Au and DNA_{25C}-Au were comparable to that of a previous study by Hill et al. (2009), in which similar DNA lengths and synthesis conditions resulted in ca. 60 strands/particle, and the maximum loading was as high as 180 strands/particle.

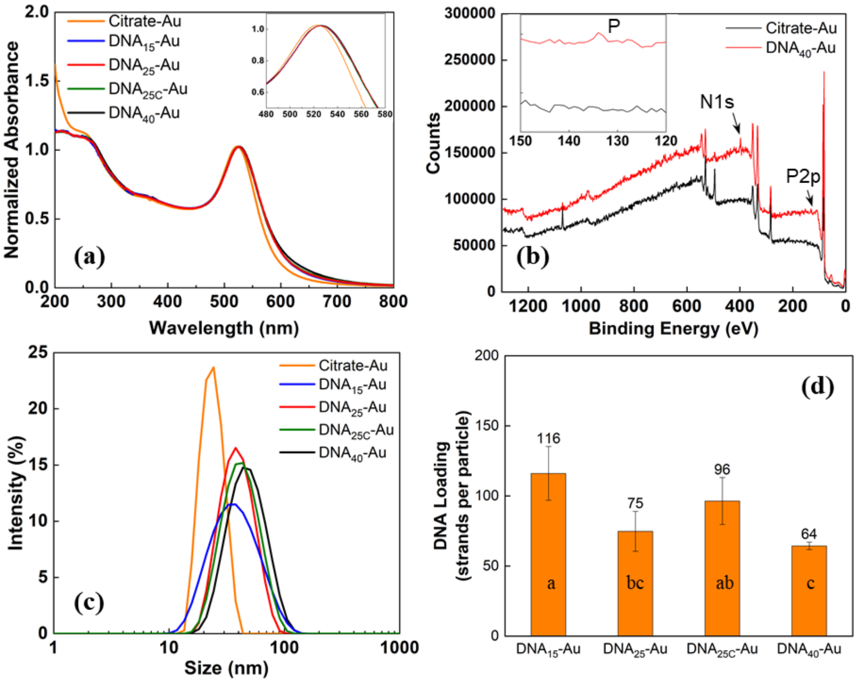

Figure 4.1 Material characterization of Citrate-Au and DNA-Au: (a) UV/Vis spectra of Citrate-Au and DNA-Au, with enlarged spectra from 480 nm to 580 nm shown in the inset; (b) XPS spectra of Citrate-Au and DNA_{40}-Au; the inset shows the enlarged spectra with binding energy levels from 120 to 150 eV; (c) intensity-based size distribution of Citrate-Au and DNA-Au measured by dynamic light scattering (10 mg/L aqueous solution); and (d) number of DNA strands per DNA-Au NP. Error bars indicate one standard deviation of at least four replicates. Different letters indicate significant difference (one-way ANOVA test followed by the Tukey test for multiple comparisons, $p < 0.05$).

4.3.2 Effect of pH on Electrokinetic and Hydrodynamic Properties

The effect of pH on the electrokinetic and hydrodynamic properties DNA-Au NPs were performed from pH 2 to 10 (Figure S4.2). The results suggested that pH may have limited effects on the stability of DNA-Au NPs in a typical pH range of 5-9 (Crittenden et al., 2012). Details are provided in Text S4.2 (Appendix B).

4.3.3 Aggregation Kinetics in the Presence of Electrolytes

Early-stage aggregation kinetics of Citrate-Au and DNA-Au NPs under various electrolyte conditions (i.e., concentration and type of electrolyte) were monitored via TR-DLS (Figure S4.3). By normalizing the initial rate constants to the rate constants obtained under diffusion-limited aggregation regime, attachment efficiencies (α) at different electrolyte concentrations were obtained and plotted as a function of NaCl, $CaCl_2$, and $MgCl_2$ concentrations (Figure 4.2). Distinct reaction-limited and diffusion-limited aggregation regimes were observed for Citrate-Au and DNA-Au NPs in all three electrolytes (Chen and Elimelech, 2006; Verwey, 1947). In the reaction-limited aggregation regime, attachment efficiency (α) increases with electrolyte concentration. When electrolyte concentration is above the CCC, van der Waals force becomes dominant and the energy barrier towards aggregation no longer exists, leading to diffusion-limited aggregation (i.e., $\alpha = 1$). The intersections of extrapolated lines through reaction-limited and diffusion-limited aggregation regimes generate the CCC in respective electrolytes, which are listed in Table 4.2.

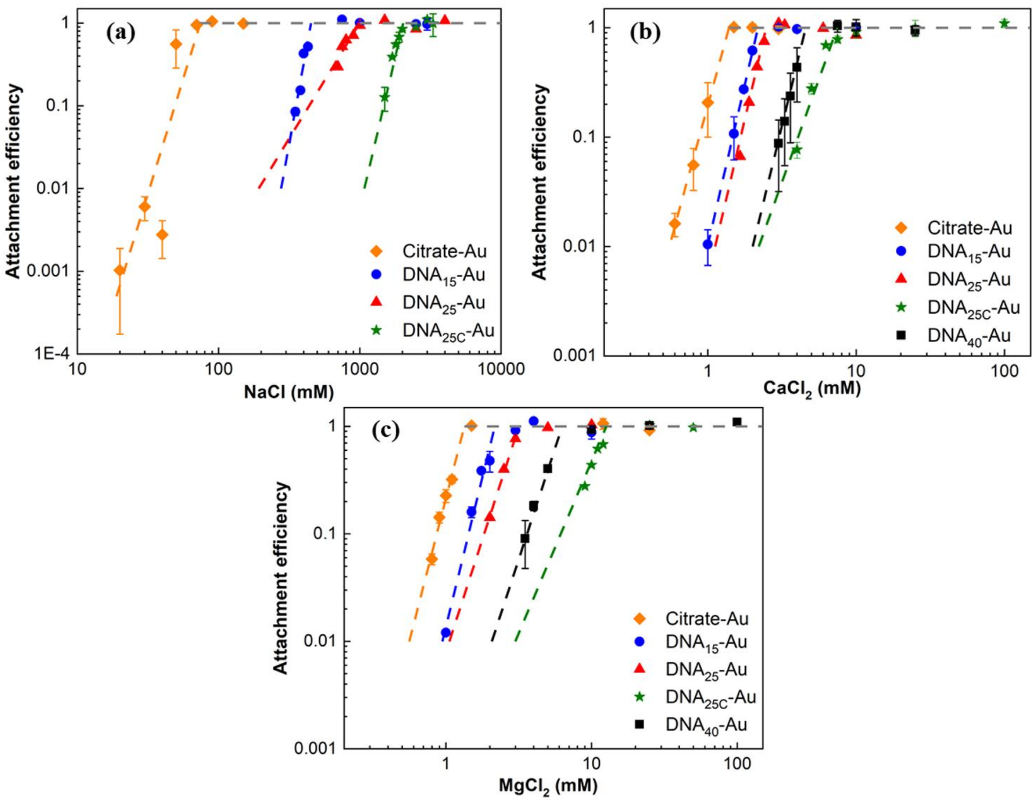

Figure 4.2 Attachment efficiencies (α) of Citrate-Au and DNA-Au as a function of (a) NaCl, (b) $CaCl_2$, and (c) $MgCl_2$ concentrations. pH was unadjusted at 6.0 ± 0.2. CCC values were calculated as the intersection of extrapolations through reaction-limited and diffusion-limited aggregation regimes.

Compared to Citrate-Au, DNA-Au displayed significantly enhanced colloidal stability, consistent with a previous report stating that DNA-Au NPs remained stable in 1 M NaCl (Hurst et al., 2006). Here, the NaCl CCC increased dramatically from 74 mM of Citrate-Au to 451 mM of DNA_{15}-Au, to 996 mM of DNA_{25}-Au, and to 2030 mM of DNA_{25C}-Au. DNA_{40}-Au was the most stable in NaCl electrolyte and a CCC value was not obtained due to a lack of observed diffusion-limited aggregation regime under even the highest NaCl concentration tested. Likewise, the enhanced stability of DNA-Au over Citrate-Au was also observed in two divalent electrolytes ($CaCl_2$ and $MgCl_2$), but to a smaller extent. The $CaCl_2$ CCC increased from 1.4 mM of Citrate-Au to 2.2 mM of DNA_{15}-Au, 2.5 mM of DNA_{25}-Au, 4.6 mM of DNA_{40}-Au, and 7.5 mM of DNA_{25C}-Au. A similar trend was also observed in $MgCl_2$ electrolyte (Table 4.2).

While the relative stability largely remained the same in divalent electrolytes as that in monovalent electrolyte, the CCC values of DNA_{40}-Au became smaller than those of DNA_{25C}-Au, e.g., 4.6 mM versus 7.5 mM $CaCl_2$, and 6.3 mM versus 12.6 mM $MgCl_2$.

Altogether, the CCC values of DNA-Au NPs are much larger than other NPs without surface coating, such as 68.7 mM NaCl, 1.6 mM $CaCl_2$, and 1.9 mM $MgCl_2$ for graphene oxide (Jiang et al., 2016); and 37 mM NaCl and 3 mM $CaCl_2$ for MoS_2 (Mohona et al., 2019), among many others. Meanwhile, they are comparable to those with polymer coatings, e.g., the CCC values of Ag NPs with PVP coating are 1010 mM NaCl and 18.8 mM $CaCl_2$ (Zhang et al., 2012), but lower than Au NPs with PEG (10 kDa) coating, which could withstand 1 M $CaCl_2$ (Surette and Nason, 2016). Such discrepancy highlights the influence of the characteristics of surface coating on colloidal stability.

Table 4.2 Critical coagulation concentration (CCC) values of Citrate-Au and DNA-Au and fitting of the Schulze-Hardy rule (last two columns, with Z being the valence of Ca^{2+}/Mg^{2+} ions (Z = 2)). The NaCl CCC value of DNA_{40}-Au was not obtained due to a lack of observed diffusion-limited aggregation.[a]

Particle	NaCl (mM)	$CaCl_2$ (mM)	$MgCl_2$ (mM)	$CaCl_2$/ NaCl	$MgCl_2$/ NaCl
Citrate-Au	74	1.4	1.3	$Z^{-5.7}$	$Z^{-5.8}$
DNA_{15}-Au	451	2.2	2.2	$Z^{-7.7}$	$Z^{-7.7}$
DNA_{25}-Au	996	2.5	3.2	$Z^{-8.7}$	$Z^{-8.3}$
DNA_{25C}-Au	2030	7.5	12.6	$Z^{-8.1}$	$Z^{-7.3}$
DNA_{40}-Au	N/A	4.6	6.3	N/A	N/A

[a] The NaCl CCC value of DNA40-Au was not obtained due to a lack of observed diffusion-limited aggregation.

Following the classical DLVO theory and Schultz-Hardy rule (Elimelech et al., 1995), the ratio of CCC values for divalent cation and monovalent cation should be proportional to Z^{-6} for particles with large surface potential and Z^{-2} for particles with low surface potential, with Z being the valence of divalent cation (Z = 2). Our results show that the ratios of CCC values of Citrate-Au had a good fit with Z^{-6} (Table 4.2), suggesting that its colloidal behavior can be well described by the classical DLVO theory, i.e., combined interactions of van der Waals attraction and electrostatic repulsion (Elimelech et al., 1995). On the other hand, the ratios of CCC values of DNA-Au did not fall into the range of Z^{-6} and Z^{-2}, suggesting that additional interaction(s) needs to be taken into account.

4.3.4 Steric Repulsion as the Major Stabilization Mechanism

It is generally considered that polymeric surface coating (electro)sterically stabilizes the coated NPs (Israelachvili, 2015; Napper, 1983). Single-stranded DNA is a highly negatively charged polymer (i.e., polyelectrolyte) (Liu and Liu, 2017), grafting of which on particles provides a combination of steric and electrostatic stabilization, i.e., electrosteric stabilization (Israelachvili, 2015). Figure S4.4 presents the EPM of DNA-Au NPs at varied salt concentrations. Overall, the EPM of four DNA-Au NPs changed similarly in all three electrolytes and approached -1.8 and -1 μm·cm/V·s along with increasing NaCl and $MgCl_2$/$CaCl_2$ concentrations. The approaching of EPMs towards a non-zero limiting value, which stems from the fixed charges of polyelectrolyte chains, is consistent with Ohshima's soft particle theory (Ohshima, 1995). The increase of ionic strength leads to the (gradual) screening of electrostatic repulsion, and steric repulsion becomes more important. Considering similar changes of EPM as a function of electrolyte concentrations for all DNA-Au NPs, the markedly different stability was thus attributed to the (varied) steric repulsions.

The coating layer thickness is considered to be a major factor determining the effect of steric stabilization (Elimelech et al., 1995; Stenkamp and Berg, 1997). The effective thickness of the coating could be measured by hydrodynamic methods as the hydrodynamic thickness appears to include the full influence of tails (Stenkamp and Berg, 1997). Krueger et al. (2007) demonstrated that a structural model, assuming that the hydrodynamic size of particle equal to the core size plus two times the coating layer thickness, was qualitatively applicable to polystyrene-coated NPs. Using the same structural model, we measured the hydrodynamic size of DNA-Au NPs at relatively low electrolyte concentrations (before particle aggregation occurred) using DLS. This was performed to track the change of DNA layer thickness upon electrolyte addition.

In NaCl electrolyte, a higher concentration of cations induced a stronger screening of the negative charges along the DNA phosphate backbone, therefore the hydrodynamic sizes of the four DNA-Au NPs gradually decreased (Figure 4.3a). For example, the size of DNA_{15}-Au decreased from 27.2 ± 0.4 nm in 1 mM NaCl to 26.2 ± 0.2 nm in 50 mM NaCl. The decrease of particle size reached a plateau due to the excluded volume effect when there was no free space for the DNA strands to shrink anymore. For example, the sizes of DNA_{15}-Au and DNA_{25}-Au NPs barely changed when NaCl concentration increased from 50 mM to 100 mM. The order of the DNA layer thickness coincided with that of particle colloidal stability as suggested by CCC values, i.e., DNA_{40}-Au > DNA_{25C}-Au > DNA_{25}-Au > DNA_{15}-Au. For example, at 50 mM NaCl, the sizes of DNA_{40}-Au, DNA_{25C}-Au, DNA_{25}-Au, DNA_{15}-Au were 29.7, 29.2, 26.9, and 26.2 nm, respectively, corresponding to DNA layer thickness of 3.7, 3.5, 2.4, and 2.0 nm. Similarly, a positive correlation between the DNA layer thickness and particle stability was observed in divalent electrolytes ($MgCl_2$ and $CaCl_2$, Figure 4.3b-c). Both followed the order: DNA_{25C}-Au > DNA_{40}-Au > DNA_{25}-Au. For DNA_{15}-Au in divalent electrolytes of concentrations from 0.1 mM to 0.5 mM, particle aggregation was observed, which caused the increase of size along the concentrations tested (0.01 – 0.5 mM $CaCl_2$/$MgCl_2$) and negatively influenced the accuracy of evaluating its DNA layer thickness, therefore DNA_{15}-Au was excluded in the comparison. Interestingly, although DNA_{25} and DNA_{25C} had the same number of nucleobases and their loadings on Au NP were similar, the DNA layer thickness of DNA_{25C}-Au was found to be larger than that of DNA_{25}-Au in all three electrolytes, which was also consistent with the higher CCC values of DNA_{25C}-Au.

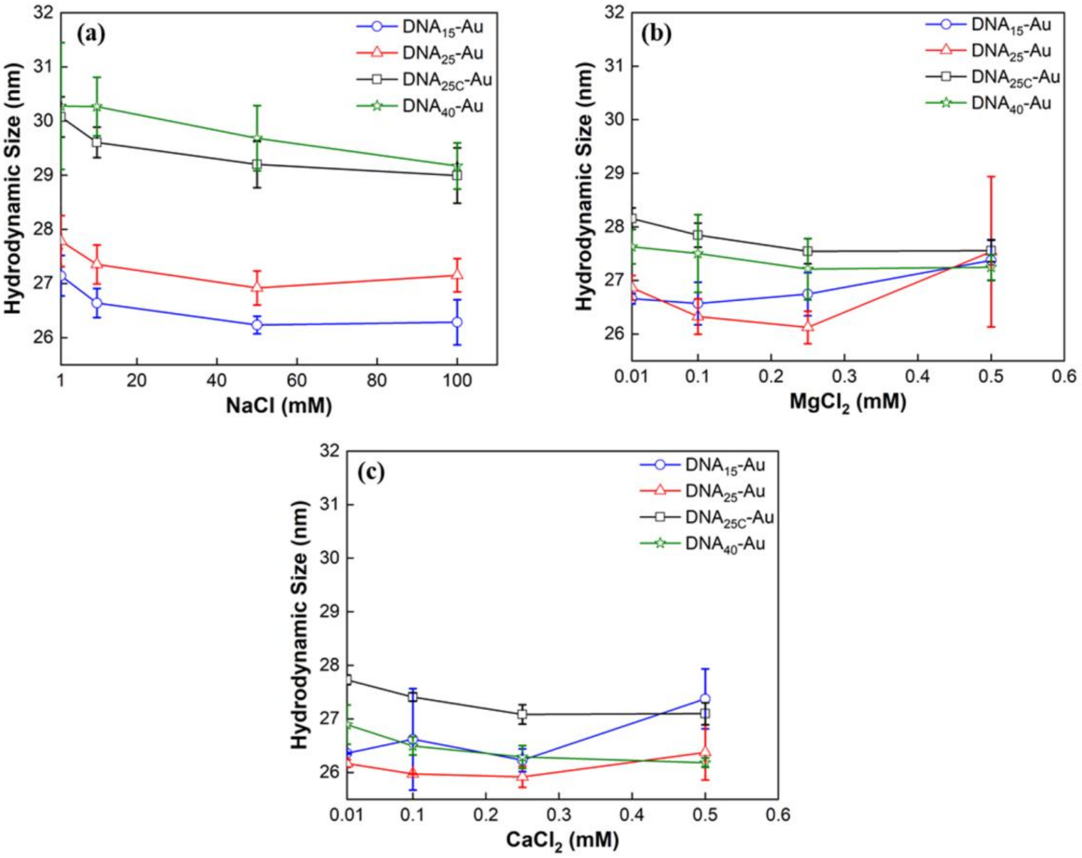

Figure 4.3 Hydrodynamic size of DNA-Au NPs as functions of (a) NaCl; (b) $MgCl_2$, and (c) $CaCl_2$ concentrations.

The classical theory of grafted polyelectrolyte brushes predicts a power law relationship between layer thickness and (monovalent) salt concentration ($L \propto c_s^{-1/3}$, where L is layer thickness, and c_s is the external salt concentration), and as the grafting density increases, the layer thickness becomes less sensitive to added salt (Pincus, 1991). A scaling behavior was evident in our experimental results, however, only a weak power law was observed (roughly $L \propto c_s^{-0.04}$, Figure 4.4a), which could be attributed to the high grafting density of DNA strands. For polyelectrolyte brushes at a high grafting density, they behave like neutral polymer brushes (quasineutral brush) and the excluded volume interaction (short-range intermonomer interaction) becomes dominant in determining the layer structure, where a scaling relationship applies (Borisov et al., 1994):

$$L \propto N\sigma^{1/3} \tag{4.3}$$

where N is the degree of polymerization and σ is the grafting density. N could be related to the molecular weight (M_w) by the following relation in a homogeneous polymer (Krueger et al., 2007):

$$N = M_w/S_w \tag{4.4}$$

where S_w is the molecular weight of a monomer. Then, the layer thickness L can be related to molecular weight of the polymer M_w by:

$$L \propto (M_w/S_w)\sigma^{1/3} \propto M_w\sigma^{1/3} \tag{4.5}$$

A linear scaling relationship was obtained (Figure 4.4b). The scaling of the layer thickness with grafting density suggests the presence of excluded volume interaction between DNA strands on (one) NP surface (Bracha et al., 2013), supporting the role of steric repulsion in stabilizing DNA-Au NPs.

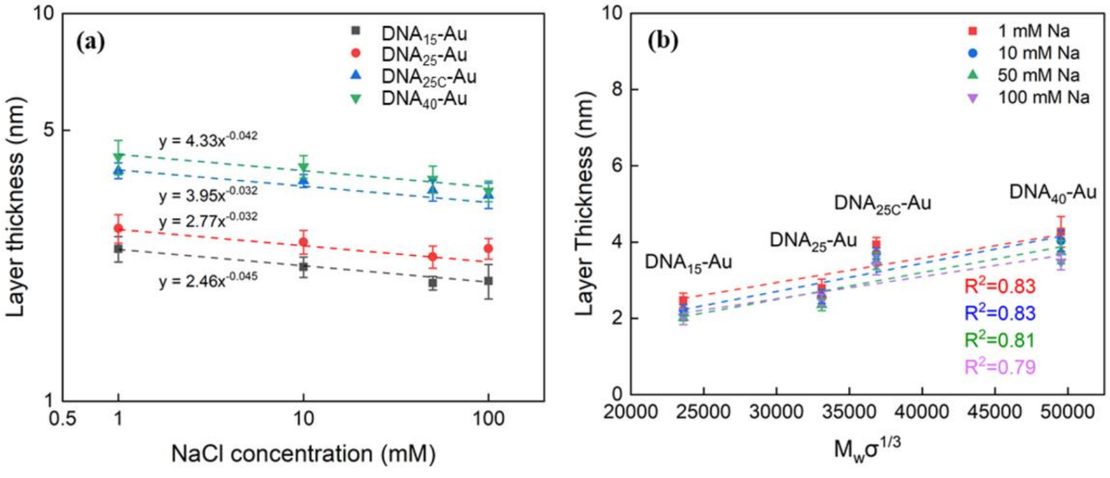

Figure 4.4 (a) DNA layer thickness as a function of NaCl concentration, both axes are in logarithmic scale. (b) DNA layer thickness in NaCl electrolyte is graphed as a function of molecular weight and grafting density.

4.3.5 Potential Energy Calculation for Interactions between DNA-Au NPs

To gain a theoretical understanding of the role of steric repulsion in stabilizing DNA-Au NPs, an extended DLVO model was used to investigate the contributions of both attractive and repulsive energies to the interaction between DNA-Au NPs. In this model, the major attractive energy was the van der Waals energy (V_{vdW}) of Au NPs, while the repulsive energy was composed of steric energy, which included excluded volume energy (V_{EV}) stemming from the overlap of polymers and elastic energy (V_{EL}) due to the compression of polymers (Napper, 1983), and osmotic energy (V_{CI}) from the trapped counterions inside the DNA layer (Jusufi et al., 2002; Kegler et al., 2007) (Figure 4.5a). It has been reported that the potential energies vary as a function of layer thickness (Seo et al., 2017); however, it is difficult to obtain the exact DNA layer thickness when the particles start to aggregate. Therefore, we used the layer thickness measured at relatively high salt concentrations (i.e., 100 mM NaCl, 0.25 mM $MgCl_2$/$CaCl_2$), where the DNA layer has been largely compressed, to predict the interaction between DNA-Au NPs when they start to aggregate. Consequently, the electrostatic repulsion was neglected as it should be effectively screened at high salt concentrations. Details for the calculation are provided in the Test S4.1 (Appendix B).

The potential energy of interactions for DNA_{15}-Au in 100 mM NaCl is shown in Figure 4.5b. The contributions from elastic repulsion and the entropic effects of the trapped counterions were minimal compared with the excluded volume repulsion, coinciding with a previous study (Seo et al., 2017). The potential energies of interactions for DNA_{25}-Au, DNA_{25C}-Au, and DNA_{40}-Au are shown in Figure S4.5, all suggesting the dominant role of excluded volume repulsion. The total interaction energy (V_{T}), the sum of all contributing energies, of DNA-Au NPs in 100 mM NaCl is presented in Figure 4.5c. The energy barriers for DNA_{15}-Au, DNA_{25}-Au, DNA_{25C}-Au, and DNA_{40}-Au were 18.8, 42.7, 191.1, and 209.3 $k_{\mathrm{B}}T$, respectively. The order of which was consistent with the order of stability of DNA-Au NPs determined by the experiment, i.e., DNA$_{40}$-Au > DNA$_{25C}$-Au > DNA$_{25}$-Au > DNA$_{15}$-Au.

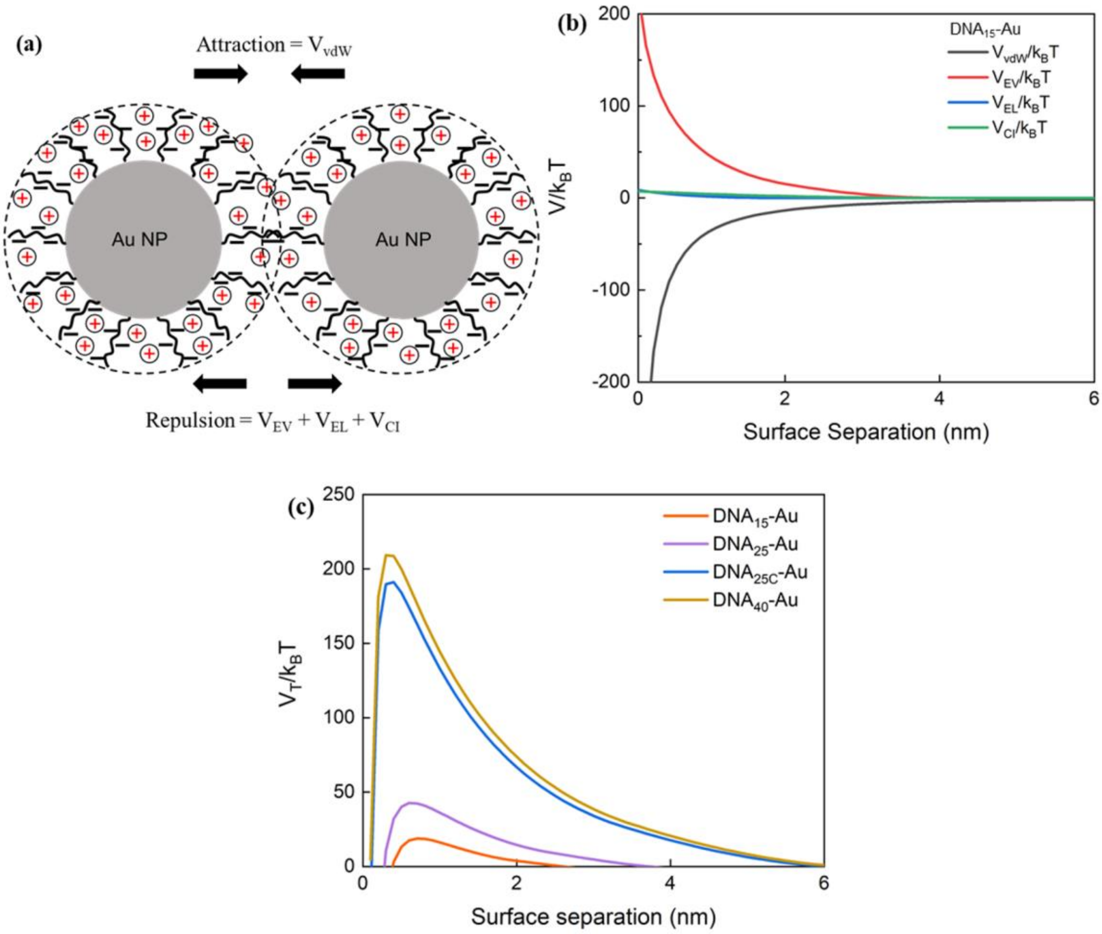

Figure 4.5 (a) Schematic representation of interactions between DNA-Au NPs, including van der Waals attraction (V_{vdW}), excluded volume repulsion (V_{EV}), elastic repulsion (V_{EL}), and osmotic repulsion of counterions (V_{CI}). (b) Potential energy of interaction for a pair of DNA$_{15}$-Au particles in 100 mM NaCl. (c). Total interaction energy (V_T) of DNA-Au NPs in 100 mM NaCl.

Similarly, we performed the free energy calculation for DNA-Au NPs in $CaCl_2$ and $MgCl_2$. The total interaction energies for DNA$_{25}$-Au, DNA$_{25C}$-Au, and DNA$_{40}$-Au are shown in Figure S4.6, and DNA$_{15}$-Au was excluded as we did not obtain reliable layer thickness (Figure 4.3b-c). While the order of energy barriers of DNA-Au in $CaCl_2$ was of the same order as the experimentally determined stability, i.e., DNA$_{25C}$-Au > DNA$_{40}$-Au > DNA$_{25}$-Au, we observed similar energy barriers of DNA_{40}-Au and DNA_{25C}-Au in $MgCl_2$ (both were around 143 k_BT), contradicting with the higher particle stability of DNA_{25C}-Au in $MgCl_2$. However, this discrepancy in the order of energy barriers might be induced by the experimental error in measuring DNA layer thickness. For example, if by using a lower value of layer thickness for DNA_{40}-Au (2.22 nm, obtained by subtracting the standard deviation from the average layer thickness), we would observe a higher energy barrier of DNA_{25C}-Au (143 k_BT) than that of DNA_{40}-Au (123 k_BT). On the other hand, the discrepancy in the order of energy barriers might be attributed to that we assumed a same Flory-Huggins parameter (χ) when calculating the potential energy of excluded volume interaction (Equation S4.2 and S4.3). The Flory-Huggins parameter describes the interaction between polymer and solvent. For simplicity we assumed the same value of χ for all DNA-Au NPs. However, for a homogenous polymer, χ is dependent on polymer concentration and molecular weight and the presence of non-solvent (such as salt in our case) (Napper, 1983; Post and Zimm, 1982). As for heterogeneous polymers such as DNA, the varied hydrophilicity of bases (Amutha et al., 2001) might also contribute to different values of χ. We could not precisely determine χ for the four DNA-Au NPs, and the determination of which is beyond the scope of this work. We note that the model presented here has its limitation; nevertheless, this model still semi-quantitatively supports the experimentally observed effect of DNA on the aggregation of DNA-Au NPs and suggests the dominant role of excluded volume repulsion in stabilizing DNA-Au NPs.

4.3.6 Role of DNA Sequence in the Conformational Change of DNA Layer

The presence of salts screens the charges along the strands and reduces DNA layer thickness. In monovalent salt, due to the weak interaction between monovalent ions and polyelectrolyte chains, DNA brushes went through a homogeneous collapse (Yu et al., 2016). Therefore, the order of layer thickness of DNA_{40}-Au > DNA_{25}-Au > DNA_{15}-Au was easy to understand, but what was more interesting was the thicker DNA layer of DNA_{25C}-Au than that of DNA_{25}-Au.

As the DNA loadings of DNA_{25}-Au and DNA_{25C}-Au were not statistically different (Figure 4.1d), such discrepancy in DNA layer thickness should be attributed to the difference in the DNA sequence (Table 4.1). In divalent salts, the divalent cations could strongly interact with polymer chains and condense onto two separate chains to form an ionic cross-link, potentially inducing a pinned-micelle-like heterogeneous collapse structure (Yu et al., 2018; Yu et al., 2016). Raman spectroscopic analysis of DNA_{25}-Au and DNA_{25C}-Au revealed that the signature Raman peaks for adenine (734 cm^{-1}, in-ring breathing mode) and phosphate (1106 cm^{-1}, phosphate symmetric stretching) significantly decreased when DNA strands interacted with divalent cations (Ca^{2+}, Mg^{2+}), but remained same in presence of Na^{+} (Figure S4.7). This supports that divalent cations not only screens charge, but also bridges the DNA molecules via bases and/or phosphate groups, which is consistent with the reported inter-strand phosphate bridging by Ca^{2+} and Mg^{2+} (Sundaresan et al., 2006). For the difference of DNA layer thickness between DNA_{25}-Au and DNA_{25C}-Au, it could again be attributed to the difference in the DNA sequence. In the case of DNA_{25C}-Au and DNA_{40}-Au, besides the difference in DNA sequence, their DNA loadings were significantly different, with DNA_{25C}-Au possessing more DNA strands per particle (Figure 4.1d). In the quasineutral regime, excluded-volume interaction between polymer segments becomes significant (Borisov et al., 1994). It is proposed that the higher DNA surface coverage of DNA_{25C}-Au also contributed to its thicker DNA layer compared to DNA_{40}-Au due to limited free space among polymer segments upon collapse.

To provide certain qualitative information about the role of DNA sequence in the salt-induced conformational change of DNA layer, MD simulations of DNA_{25} and DNA_{25C} with the presence of Ca^{2+} were performed. In the simulations, Ca^{2+} were introduced to screen the anionic phosphates of DNA (60/90/120 calcium ions, corresponding to 100/150/200% of the brush charge being neutralized). Both DNA_{25C} and DNA_{25} had the same number of adenine and thymine, and the main difference between DNA_{25C} and DNA_{25} was that DNA_{25C} possessed six guanines in each strand, while each DNA_{25} strand had only one guanine. To assess the interaction between DNA and Ca^{2+} cations, we calculated the RDFs of specific atoms of DNA (phosphates and bases) coordinated with Ca^{2+} cations (Figure S4.8). For both DNA_{25} and DNA_{25C}, two particularly strong, well-defined peaks of phosphates were observed, corresponding to the first and second coordination shell (cutoff distance at 3 and 5 Å, respectively). For the bases in DNA_{25C} (Figure S4.8a), only guanine and adenine were found to be within the two coordination shells, while for DNA_{25} (Figure S4.8b), on the other hand, all four bases were found to be within the two coordination shells. Based on the results of RDFs, we used a cutoff distance of 5 Å to evaluate the distribution of Ca^{2+} cations among DNA bases (any Ca^{2+} that were within 5 Å of the bases). The results show that adenine and guanine of DNA_{25C} were the only two bases to associate with Ca^{2+} (Figure 4.6a). Due to the dominant number of adenine (A) in our DNA design (in total 14 A out of 25 bases), the association of Ca^{2+} with adenine was expected. This is also supported by Raman characterization results (Figure S4.7). What is more interesting is the preferential binding of Ca^{2+} to guanine, which is consistent with previous reports of guanine as the preferential binding site for divalent cations (Egli, 2002; Holland et al., 2011; Long et al., 2020). On the other hand, even though each DNA_{25} strand had only one guanine, the binding of Ca^{2+} to which was comparable to thymine and cytosine. For example, at 150% neutralization, 4.81 Ca^{2+} associated with guanine, while 2.89 Ca^{2+} associated with thymine and 7.32 Ca^{2+} associated with cytosine (Figure 4.6b). Taken together, these results suggested the strongest affinity of Ca^{2+} towards guanine among four bases.

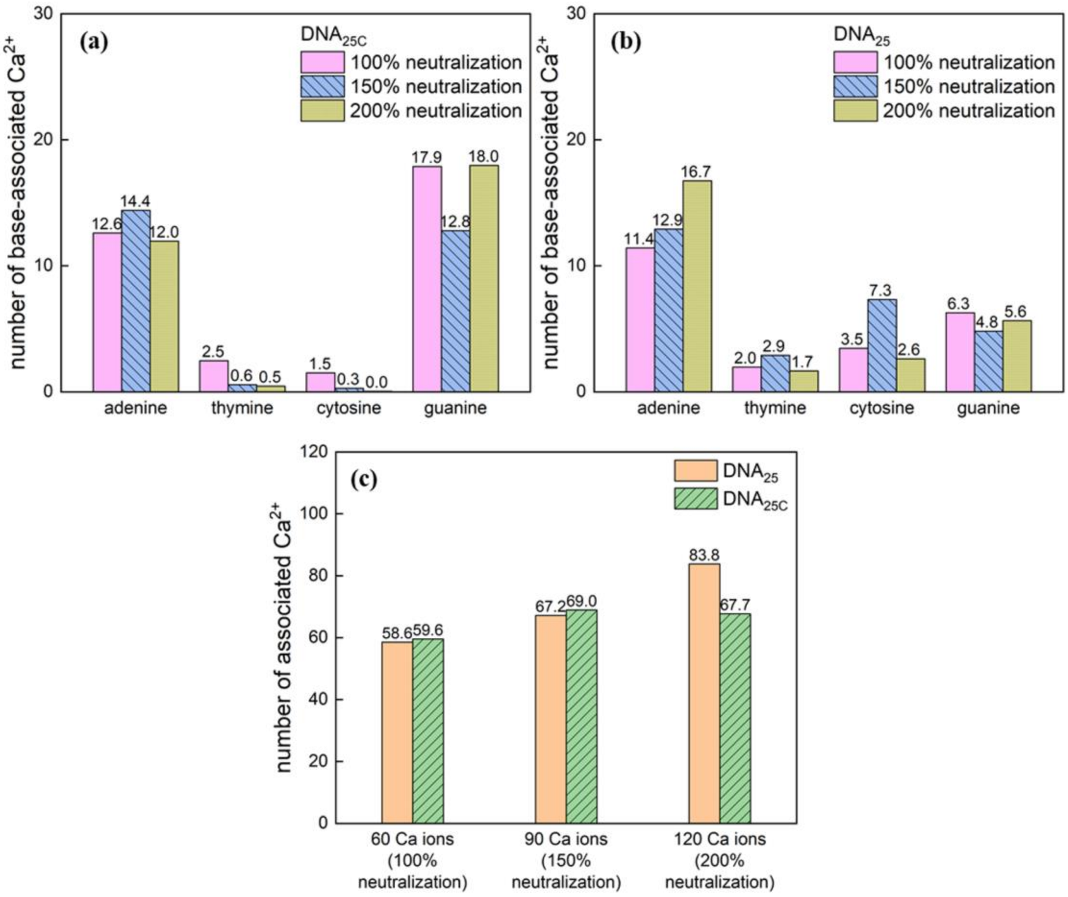

Figure 4.6 MD simulation results of DNA$_{25}$ and DNA$_{25C}$ in the presence of Ca^{2+} (60/90/120 ions, corresponding to 100/150/200% neutralization). (a) Distribution of Ca^{2+} cations among bases of DNA$_{25C}$, (b) distribution of Ca^{2+} cations among bases of DNA$_{25}$, and (c) the number of associated Ca^{2+} on DNA strands.

A previous study showed a negative correlation between the number of bounded counterions and the height of surface-bound DNA strands, where the decrease of the height of DNA strands was attributed to the resultant screening of Coulombic repulsions and/or specific binding (Holland and Geiger, 2012). As such, we counted the number of Ca^{2+} associated with DNA strands by subtracting the number of unassociated Ca^{2+} (any Ca^{2+} that were 5 Å away from phosphates or bases) from the total number of Ca^{2+} in the system. The results are presented in Figure 4.6c. As the total number of Ca^{2+} in the system increased, we observed that DNA$_{25}$ attracted more Ca^{2+} than DNA$_{25C}$ did, i.e., 83.83 vs. 67.74 ions at 200% neutralization, which was qualitatively in accordance with the lower DNA layer thickness of DNA$_{25}$-Au experimentally measured in $CaCl_2$ electrolyte. We propose that the difference in associated Ca^{2+} between DNA_{25} and DNA_{25C} was caused by the number and location of guanine in the strand. As reported in an earlier study (Holland and Geiger, 2012), for surface-bound DNA strands with 10 guanine bases at the strand end close to the bulk solution and 10 adenine bases at the other end close to the surface, the strong binding affinity of Mg^{2+} ions to guanine bases leads to the accumulation of positive charges near the end close to the bulk solution, which prevents cations from penetrating into the other end close to surface and binding to the adenine bases. Similarly, the six guanine bases in DNA_{25C} located at the strand end (close to the bulk solution) attracted a high density of positive charge, which prevented the penetration and binding of Ca^{2+} to the other end near the surface, therefore fewer Ca^{2+} were associated. The lack of guanine in DNA_{25} allowed the binding of Ca^{2+} to the end near the surface and thus overall, more associated Ca^{2+}. This hypothesis is graphically depicted in Figure S4.9. Taken together, the results of MD simulation suggested the role of DNA sequence in affecting the thickness of DNA layer on particle surface and (eventually) their colloidal stability in water.

4.4 Conclusions

Engineered DNA NPs have emerged as a new class of nanomaterial with their unique properties being widely leveraged in multiple fields, such as material synthesis and environmental applications (e.g., aptasensors). Understanding the colloidal stability of such material in a structure-activity manner is important as the stability of the material influences its functionality. This work shows that steric stabilization (mainly excluded volume repulsion) is the major contributor to the stability of DNA-Au NPs, and the effect of which is related to DNA layer thickness. The sequence and loading of DNA strands on particle surface and their interaction with surrounding counterions affect the thickness of the DNA layer. Among the nucleobases, guanine has the highest affinity towards counterions, and their preferential interactions influence the ion distribution along DNA strands. Guanine located at the far-away end of the surface-bound DNA strands may prevent the penetration and binding of cations to the other end near the surface, therefore decreasing the effect of reducing the DNA layer thickness. Divalent cations induce the heterogeneous collapse of the DNA layer, significantly reducing the layer thickness compared to monovalent cations. These results highlight the role of specific interactions between DNA and surrounding counterions in determining the aggregation behavior of engineered DNA NPs, providing molecular-level information for their design for applications. Such information is also beneficial to interpreting the aggregation behavior of NPs with other heterogeneous surface coatings.

Acknowledgement

The authors acknowledge partial financial support from the Guangdong-Hong Kong-Macau Joint Laboratory for Environmental Pollution and Control (ZGBX), and thank Zhiying Deng for her help with partial experimental work on the aggregation kinetics of DNA-Au NPs.

References

Abraham, M.J., Murtola, T., Schulz, R., Páll, S., Smith, J.C., Hess, B. and Lindahl, E. 2015. GROMACS: High performance molecular simulations through multi-level parallelism from laptops to supercomputers. SoftwareX 1-2, 19-25.

Amutha, R., Subramanian, V. and Unni Nair, B. 2001. Free energy calculation for DNA bases in various solvents using Flory–Huggins theory. Chem. Phys. Lett. 335(5), 489-495.

Berendsen, H.J.C., Grigera, J.R. and Straatsma, T.P. 1987. The missing term in effective pair potentials. J. Phys. Chem. 91(24), 6269-6271.

Borisov, O., Zhulina, E. and Birshtein, T. 1994. Diagram of the states of a grafted polyelectrolyte layer. Macromolecules 27(17), 4795-4803.

Bracha, D., Karzbrun, E., Shemer, G., Pincus, P.A. and Bar-Ziv, R.H. 2013. Entropy-driven collective interactions in DNA brushes on a biochip. Proc. Natl. Acad. Sci. U. S. A. 110(12), 4534-4538.

Brown, K.A., Park, S. and Hamad-Schifferli, K. 2008. Nucleotide−Surface Interactions in DNA-Modified Au−Nanoparticle Conjugates: Sequence Effects on Reactivity and Hybridization. J. Phys. Chem. C 112(20), 7517-7521.

Carnerero, J.M., Jimenez-Ruiz, A., Castillo, P.M. and Prado-Gotor, R. 2017. Covalent and Non-Covalent DNA-Gold-Nanoparticle Interactions: New Avenues of Research. ChemPhysChem 18(1), 17-33.

Chen, K.L. and Elimelech, M. 2006. Aggregation and Deposition Kinetics of Fullerene (C60) Nanoparticles. Langmuir 22(26), 10994-11001.

Chen, K.L. and Elimelech, M. 2007. Influence of humic acid on the aggregation kinetics of fullerene (C60) nanoparticles in monovalent and divalent electrolyte solutions. J. Colloid Interface Sci. 309(1), 126-134.

Chowdhury, I., Cwiertny, D.M. and Walker, S.L. 2012. Combined Factors Influencing the Aggregation and Deposition of nano-TiO2 in the Presence of Humic Acid and Bacteria. Environ. Sci. Technol. 46(13), 6968-6976.

Chowdhury, I., Duch, M.C., Mansukhani, N.D., Hersam, M.C. and Bouchard, D. 2013. Colloidal Properties and Stability of Graphene Oxide Nanomaterials in the Aquatic Environment. Environ. Sci. Technol. 47(12), 6288-6296.

Chowdhury, I., Mansukhani, N.D., Guiney, L.M., Hersam, M.C. and Bouchard, D. 2015. Aggregation and Stability of Reduced Graphene Oxide: Complex Roles of Divalent Cations, pH, and Natural Organic Matter. Environ. Sci. Technol. 49(18), 10886-10893.

Crittenden, J.C., Trussell, R.R., Hand, D.W., Howe, K. and Tchobanoglous, G. (2012) MWH's water treatment: principles and design, John Wiley & Sons.

Cutler, J.I., Auyeung, E. and Mirkin, C.A. 2012. Spherical Nucleic Acids. J. Am. Chem. Soc. 134(3), 1376-1391.

Demers, L.M., Mirkin, C.A., Mucic, R.C., Reynolds, R.A., Letsinger, R.L., Elghanian, R. and Viswanadham, G. 2000. A Fluorescence-Based Method for Determining the Surface Coverage and Hybridization Efficiency of Thiol-Capped Oligonucleotides Bound to Gold Thin Films and Nanoparticles. Anal. Chem. 72(22), 5535-5541.

Ditsch, A., Laibinis, P.E., Wang, D.I. and Hatton, T.A. 2005. Controlled clustering and enhanced stability of polymer-coated magnetic nanoparticles. Langmuir 21(13), 6006-6018.

Egli, M. 2002. DNA-Cation Interactions: Quo Vadis? Chem. Biol. 9(3), 277-286.

El Badawy, A.M., Luxton, T.P., Silva, R.G., Scheckel, K.G., Suidan, M.T. and Tolaymat, T.M. 2010. Impact of Environmental Conditions (pH, Ionic Strength, and Electrolyte Type) on the Surface Charge and Aggregation of Silver Nanoparticles Suspensions. Environ. Sci. Technol. 44(4), 1260-1266.

Elimelech, M., Gregory, J. and Jia, X. (1995) Particle Deposition and Aggregation: Measurement, Modelling and Simulation, Butterworth-Heinemann.

Funck, T., Nicoli, F., Kuzyk, A. and Liedl, T. 2018. Sensing Picomolar Concentrations of RNA Using Switchable Plasmonic Chirality. Angew. Chem. Int. Ed. 57(41), 13495-13498.

Golas, P.L., Louie, S., Lowry, G.V., Matyjaszewski, K. and Tilton, R.D. 2010. Comparative study of polymeric stabilizers for magnetite nanoparticles using ATRP. Langmuir 26(22), 16890-16900.

Goodwin, D.J., Sepassi, S., King, S.M., Holland, S.J., Martini, L.G. and Lawrence, M.J. 2013. Characterization of Polymer Adsorption onto Drug Nanoparticles Using Depletion Measurements and Small-Angle Neutron Scattering. Mol. Pharmaceutics 10(11), 4146-4158.

Hill, H.D., Millstone, J.E., Banholzer, M.J. and Mirkin, C.A. 2009. The Role Radius of Curvature Plays in Thiolated Oligonucleotide Loading on Gold Nanoparticles. ACS Nano 3(2), 418-424.

Holland, J.G. and Geiger, F.M. 2012. Importance of Length and Sequence Order on Magnesium Binding to Surface-Bound Oligonucleotides Studied by Second Harmonic Generation and Atomic Force Microscopy. J. Phys. Chem. B 116(22), 6302-6310.

Holland, J.G., Malin, J.N., Jordan, D.S. and Geiger, F.M. 2011. Specific and Nonspecific Metal Ion−Nucleotide Interactions at Aqueous/Solid Interfaces Functionalized with Adenine, Thymine, Guanine, and Cytosine Oligomers. J. Am. Chem. Soc. 133(8), 2567-2570.

Holthoff, H., Egelhaaf, S.U., Borkovec, M., Schurtenberger, P. and Sticher, H. 1996. Coagulation Rate Measurements of Colloidal Particles by Simultaneous Static and Dynamic Light Scattering. Langmuir 12(23), 5541-5549.

Hoover, W.G. 1985. Canonical dynamics: Equilibrium phase-space distributions. Phys. Rev. A 31(3), 1695-1697.

Hotze, E.M., Phenrat, T. and Lowry, G.V. 2010. Nanoparticle Aggregation: Challenges to Understanding Transport and Reactivity in the Environment. J. Environ. Qual. 39(6), 1909-1924.

Hurst, S.J., Lytton-Jean, A.K.R. and Mirkin, C.A. 2006. Maximizing DNA Loading on a Range of Gold Nanoparticle Sizes. Anal. Chem. 78(24), 8313-8318.

Israelachvili, J.N. (2015) Intermolecular and Surface Forces, Academic Press.

Jiang, Y., Raliya, R., Fortner, J.D. and Biswas, P. 2016. Graphene Oxides in Water: Correlating Morphology and Surface Chemistry with Aggregation Behavior. Environ. Sci. Technol. 50(13), 6964-6973.

Jiang, Y., Raliya, R., Liao, P., Biswas, P. and Fortner, J.D. 2017. Graphene oxides in water: assessing stability as a function of material and natural organic matter properties. Environ. Sci.: Nano 4(7), 1484-1493.

Jusufi, A., Likos, C.N. and Löwen, H. 2002. Counterion-induced entropic interactions in solutions of strongly stretched, osmotic polyelectrolyte stars. J. Chem. Phys. 116(24), 11011-11027.

Kegler, K., Salomo, M. and Kremer, F. 2007. Forces of Interaction between DNA-Grafted Colloids: An Optical Tweezer Measurement. Phys. Rev. Lett. 98(5), 058304.

Kolev, S.K., Petkov, P.S., Rangelov, M.A., Trifonov, D.V., Milenov, T.I. and Vayssilov, G.N. 2018. Interaction of Na^+, K^+, Mg^{2+} and Ca^{2+} counter cations with RNA. Metallomics 10(5), 659-678.

Krueger, K.M., Al-Somali, A.M., Mejia, M. and Colvin, V.L. 2007. The hydrodynamic size of polymer stabilized nanocrystals. Nanotechnology 18(47), 475709.

Liu, B. and Liu, J. 2017. Methods for preparing DNA-functionalized gold nanoparticles, a key reagent of bioanalytical chemistry. Anal. Methods 9(18), 2633-2643.

Long, M.P., Alland, S., Martin, M.E. and Isborn, C.M. 2020. Molecular dynamics simulations of alkaline earth metal ions binding to DNA reveal ion size and hydration effects. Phys. Chem. Chem. Phys. 22(10), 5584-5596.

Macfarlane, R.J., Lee, B., Jones, M.R., Harris, N., Schatz, G.C. and Mirkin, C.A. 2011. Nanoparticle Superlattice Engineering with DNA. Science 334(6053), 204-208.

Maier, J.A., Martinez, C., Kasavajhala, K., Wickstrom, L., Hauser, K.E. and Simmerling, C. 2015. ff14SB: Improving the Accuracy of Protein Side Chain and Backbone Parameters from ff99SB. J. Chem. Theory Comput. 11(8), 3696-3713.

Mirkin, C.A., Letsinger, R.L., Mucic, R.C. and Storhoff, J.J. 1996. A DNA-based method for rationally assembling nanoparticles into macroscopic materials. Nature 382, 607-609.

Mohona, T.M., Gupta, A., Masud, A., Chien, S.-C., Lin, L.-C., Nalam, P.C. and Aich, N. 2019. Aggregation Behavior of Inorganic 2D Nanomaterials Beyond Graphene: Insights from Molecular Modeling and Modified DLVO Theory. Environ. Sci. Technol. 53(8), 4161-4172.

Moore, V.C., Strano, M.S., Haroz, E.H., Hauge, R.H., Smalley, R.E., Schmidt, J. and Talmon, Y. 2003. Individually Suspended Single-Walled Carbon Nanotubes in Various Surfactants. Nano Lett. 3(10), 1379-1382.

Napper, D.H. (1983) Polymeric Stabilization of Colloidal Dispersions, Academic Press, London; New York.

Nason, J.A., McDowell, S.A. and Callahan, T.W. 2012. Effects of natural organic matter type and concentration on the aggregation of citrate-stabilized gold nanoparticles. J. Environ. Monit. 14(7), 1885-1892.

Ohshima, H. 1995. Electrophoresis of soft particles. Adv. Colloid Interface Sci. 62(2), 189-235.

Parak, W.J., Pellegrino, T., Micheel, C.M., Gerion, D., Williams, S.C. and Alivisatos, A.P. 2003. Conformation of Oligonucleotides Attached to Gold Nanocrystals Probed by Gel Electrophoresis. Nano Lett. 3(1), 33-36.

Parrinello, M. and Rahman, A. 1981. Polymorphic transitions in single crystals: A new molecular dynamics method. J. Appl. Phys. 52(12), 7182-7190.

Pellegrino, T., Sperling, R.A., Alivisatos, A.P. and Parak, W.J. 2007. Gel Electrophoresis of Gold-DNA Nanoconjugates. J. Biomed. Biotechnol. 2007, 26796.

Phenrat, T., Saleh, N., Sirk, K., Kim, H.-J., Tilton, R.D. and Lowry, G.V. 2008. Stabilization of aqueous nanoscale zerovalent iron dispersions by anionic polyelectrolytes: adsorbed anionic polyelectrolyte layer properties and their effect on aggregation and sedimentation. J. Nanopart. Res. 10(5), 795-814.

Pincus, P. 1991. Colloid stabilization with grafted polyelectrolytes. Macromolecules 24(10), 2912-2919.

Post, C.B. and Zimm, B.H. 1982. Theory of DNA condensation: Collapse versus aggregation. Biopolymers 21(11), 2123-2137.

Raschke, G., Kowarik, S., Franzl, T., Sönnichsen, C., Klar, T.A., Feldmann, J., Nichtl, A. and Kürzinger, K. 2003. Biomolecular Recognition Based on Single Gold Nanoparticle Light Scattering. Nano Lett. 3(7), 935-938.

Rosi, N.L., Giljohann, D.A., Thaxton, C.S., Lytton-Jean, A.K.R., Han, M.S. and Mirkin, C.A. 2006. Oligonucleotide-Modified Gold Nanoparticles for Intracellular Gene Regulation. Science 312(5776), 1027-1030.

Saleh, N.B., Pfefferle, L.D. and Elimelech, M. 2008. Aggregation Kinetics of Multiwalled Carbon Nanotubes in Aquatic Systems: Measurements and Environmental Implications. Environ. Sci. Technol. 42(21), 7963-7969.

Saleh, N.B., Pfefferle, L.D. and Elimelech, M. 2010. Influence of Biomacromolecules and Humic Acid on the Aggregation Kinetics of Single-Walled Carbon Nanotubes. Environ. Sci. Technol. 44(7), 2412-2418.

Sciortino, F., Zhang, Y., Gang, O. and Kumar, S.K. 2020. Combinatorial-Entropy-Driven Aggregation in DNA-Grafted Nanoparticles. ACS Nano 14(5), 5628-5635.

Seeman, N.C. and Sleiman, H.F. 2017. DNA nanotechnology. Nat. Rev. Mater. 3(1), 17068.

Seo, S.E., Li, T., Senesi, A.J., Mirkin, C.A. and Lee, B. 2017. The Role of Repulsion in Colloidal Crystal Engineering with DNA. J. Am. Chem. Soc. 139(46), 16528-16535.

Stenkamp, V.S. and Berg, J.C. 1997. The Role of Long Tails in Steric Stabilization and Hydrodynamic Layer Thickness. Langmuir 13(14), 3827-3832.

Storhoff, J.J., Elghanian, R., Mirkin, C.A. and Letsinger, R.L. 2002. Sequence-Dependent Stability of DNA-Modified Gold Nanoparticles. Langmuir 18(17), 6666-6670.

Storhoff, J.J., Elghanian, R., Mucic, R.C., Mirkin, C.A. and Letsinger, R.L. 1998. One-Pot Colorimetric Differentiation of Polynucleotides with Single Base Imperfections Using Gold Nanoparticle Probes. J. Am. Chem. Soc. 120(9), 1959-1964.

Sundaresan, N., Pillai, C.K.S. and Suresh, C.H. 2006. Role of Mg^{2+} and Ca^{2+} in DNA Bending: Evidence from an ONIOM-Based QM-MM Study of a DNA Fragment. J. Phys. Chem. A 110(28), 8826-8831.

Surette, M.C. and Nason, J.A. 2016. Effects of surface coating character and interactions with natural organic matter on the colloidal stability of gold nanoparticles. Environ. Sci.: Nano 3(5), 1144-1152.

Taton, T.A., Mirkin, C.A. and Letsinger, R.L. 2000. Scanometric DNA Array Detection with Nanoparticle Probes. Science 289(5485), 1757-1760.

Verwey, E.J.W. 1947. Theory of the Stability of Lyophobic Colloids. J. Phys. Chem. 51(3), 631-636.

Xie, Y., Gao, Y., Ren, X., Song, G., Alsaedi, A., Hayat, T. and Chen, C. 2020. Colloidal Behaviors of Two-Dimensional Titanium Carbide in Natural Surface Waters: The Role of Solution Chemistry. Environ. Sci. Technol. 54(6), 3353-3362.

Yi, P. and Chen, K.L. 2011. Influence of Surface Oxidation on the Aggregation and Deposition Kinetics of Multiwalled Carbon Nanotubes in Monovalent and Divalent Electrolytes. Langmuir 27(7), 3588-3599.

Yu, J., Jackson, N.E., Xu, X., Morgenstern, Y., Kaufman, Y., Ruths, M., de Pablo, J.J. and Tirrell, M. 2018. Multivalent counterions diminish the lubricity of polyelectrolyte brushes. Science 360(6396), 1434-1438.

Yu, J., Mao, J., Yuan, G., Satija, S., Jiang, Z., Chen, W. and Tirrell, M. 2016. Structure of Polyelectrolyte Brushes in the Presence of Multivalent Counterions. Macromolecules 49(15), 5609-5617.

Zgarbová, M., Šponer, J., Otyepka, M., Cheatham, T.E., Galindo-Murillo, R. and Jurečka, P. 2015. Refinement of the Sugar–Phosphate Backbone Torsion Beta for AMBER Force Fields Improves the Description of Z- and B-DNA. J. Chem. Theory Comput. 11(12), 5723-5736.

Zhang, H., Smith, J.A. and Oyanedel-Craver, V. 2012. The effect of natural water conditions on the anti-bacterial performance and stability of silver nanoparticles capped with different polymers. Water Res. 46(3), 691-699.

Zhang, X.Q., Xu, X., Lam, R., Giljohann, D., Ho, D. and Mirkin, C.A. 2011. Strategy for Increasing Drug Solubility and Efficacy through Covalent Attachment to Polyvalent DNA–Nanoparticle Conjugates. ACS Nano 5(9), 6962-6970.

Zhang, Z., Liu, D., Bai, Y., Cui, Y., Wang, D. and Shi, X. 2019. Identification and characterization of two high affinity aptamers specific for Salmonella Enteritidis. Food Control 106, 106719.

Zong, C., Zhang, Z., Liu, B. and Liu, J. 2019. Adsorption of Arsenite on Gold Nanoparticles Studied with DNA Oligonucleotide Probes. Langmuir 35(22), 7304-7311.

Appendix B: Supporting Information for Chapter 4

Text S4.1 Calculation of the Extended DLVO Model

Classical DLVO theory describes the interaction energies between two particles consisted of an attractive van der Waals interaction energy (V_{vdW}) and a repulsive electrostatic interaction energy (which is neglected in our calculation due to the strong screening in high salt concentration) (Elimelech et al., 1995). For two identical spherical particles with radius R_c at surface separation h, the van der Waals attractive energy can be expressed as (Elimelech et al., 1995):

$$\frac{V_{vdW}}{k_B T} = \frac{-A}{6k_B T}\left[\frac{2{R_c}^2}{h(4R_c+h)} + \frac{2{R_c}^2}{(2R_c+h)^2} + \ln\left(\frac{h(4R_c+h)}{(2R_c+h)^2}\right)\right] \tag{S4.1}$$

where A is the Hamaker constant of gold (2.7×10^{-19} J) (Petosa et al., 2010), k_B is Boltzmann constant; T is temperature. In the presence of a polymer layer on the particle surface, namely sterically stabilized particles, an extended DLVO theory including the mixing/excluded-volume free energy (V_{EV}), the elastic free energy (V_{EL}), and osmotic energy (V_{CI}) from the trapped counterions inside DNA layer is needed (Jusufi et al., 2002; Kegler et al., 2007; Napper, 1983).

Regarding the separation between two sterically stabilized particles, three domains of close approach are used to describe the interaction energies. The first one is the non-interactional domain where the separation (h) between particle surfaces is larger than twice the polymer layer thickness (L). In this domain, no significant interaction between the layers is expected. The second domain is the interpenetrational domain ($L \leq h \leq 2L$) where the polymer layers of two particles start to interpenetrate each other. In this domain, the dominant free energy generating the stabilization effect comes from the mixing free energy of polymers. Upon the interpenetration of polymer layers, the local polymer segment density increases and the molecules of the dispersion medium are excluded, thus raising a difference in the osmotic pressure (of polymers) and a repelling force. In a strict manner, there is also an entropic contribution to the total free energy induced by the minor conformational change of the polymer chains in this domain (Osmond et al., 1975). However, it is concluded that the magnitude of contribution from the polymer conformational change in this domain is insignificant and acceptable to ignore it (Napper, 1983). Thus, in the interpenetrational domain (subscript I), the excluded volume energy can be expressed as (Napper, 1983):

$$V_{EV,I} = \frac{4\pi R_c k_B T \omega^2 v_2^2}{v_1} (\frac{1}{2} - \chi)(1 - \frac{h}{2L})^2 \qquad (L \leq h \leq 2L) \qquad \text{(S4.2)}$$

where ω is weight of polymer per unit surface area, v_2 is the polymer specific volume which equals to the reciprocal of polymer density, v_1 is the volume of one solvent molecule, χ is the Flory-Huggins parameter which describes the interaction between polymer and solvent molecules. DNA is hydrophilic, suggesting a good interaction between DNA molecules and water molecules, therefore we only considered the situation of good solvent ($\chi < 0.5$). A value of $\chi = 0.4$ was assumed for all DNA in this model. Lowering the value of χ only increased the scale of V_{EV}. As the particles get closer with each other and enter the last domain, interpenetrational-plus-compressional (subscript $I + C$) domain ($L < h$), the presence of opposing particle surface reduces the spatial expansion of the polymer chains, leading to a decrease in configurational entropy, which generates a repulsive elastic repulsion. At the meantime, the excluded volume term is also operative in this domain, so the steric free energy equals to the summation of the excluded volume energy (V_{EV}) and the elastic free energy (V_{EL}) (Napper, 1983):

$$V_{EV,I+C} = \frac{2\pi R_c k_B T \omega^2 v_2^2}{v_1} (\frac{1}{2} - \chi) \left\{3 \ln\left(\frac{L}{h}\right) + 2\frac{h}{L} - 1.5\right\} \qquad (L < h) \qquad \text{(S4.3)}$$

$$V_{EL,I+C} = \frac{2\pi R_c k_B T \omega N_A}{M_w} L \left\{1 - \frac{h}{L} + \frac{h}{L} \ln\left(\frac{h}{L}\right)\right\} \qquad (L < h) \qquad \text{(S4.4)}$$

where N_A is Avogadro's constant, M_W is the molecular weight of the polymer.

Furthermore, an analytical expression for energy of entropic effect from trapped counterions (V_{CI}) for two spherical polyelectrolyte brush has been given as (Jusufi et al., 2004):

$$\frac{V_{CI}}{k_B T} = \frac{Q}{|e|} \left\{ \frac{1}{2RK} \left[D ln^2 \left(\frac{D}{2R} \right) + 8R_c ln \left(\frac{R_c}{R} \right) \right] + ln \left(\frac{2L}{RK} \right) - 2 \frac{R_c}{L} ln \left(\frac{R_c}{R} \right) \right\} \qquad \text{(S4.5)}$$

$$K = 1 - 2 \frac{R_c}{R} + \frac{D}{2R} \left[1 - ln \left(\frac{D}{2R} \right) \right] \qquad \text{(S4.6)}$$

where $Q/|e|$ is the number of free counterions within the brush layer; R_c is the core radius, L is the brush layer thickness, and $R = R_c + L$; D is the center-to-center separation. Since one phosphate group carries one negative charge (Liu and Liu, 2017):

$$Q/|e| = f \times \sigma \times n \qquad \text{(S4.7)}$$

where f is the fraction of unbounded counterions within DNA layer and assumed to be about 10% (Kegler et al., 2008; Seo et al., 2017). σ is DNA grafting density, and n is the number of bases per chain. The total interaction energy V_T equals the sum of V_{EV}, V_{EL}, and V_{CI}.

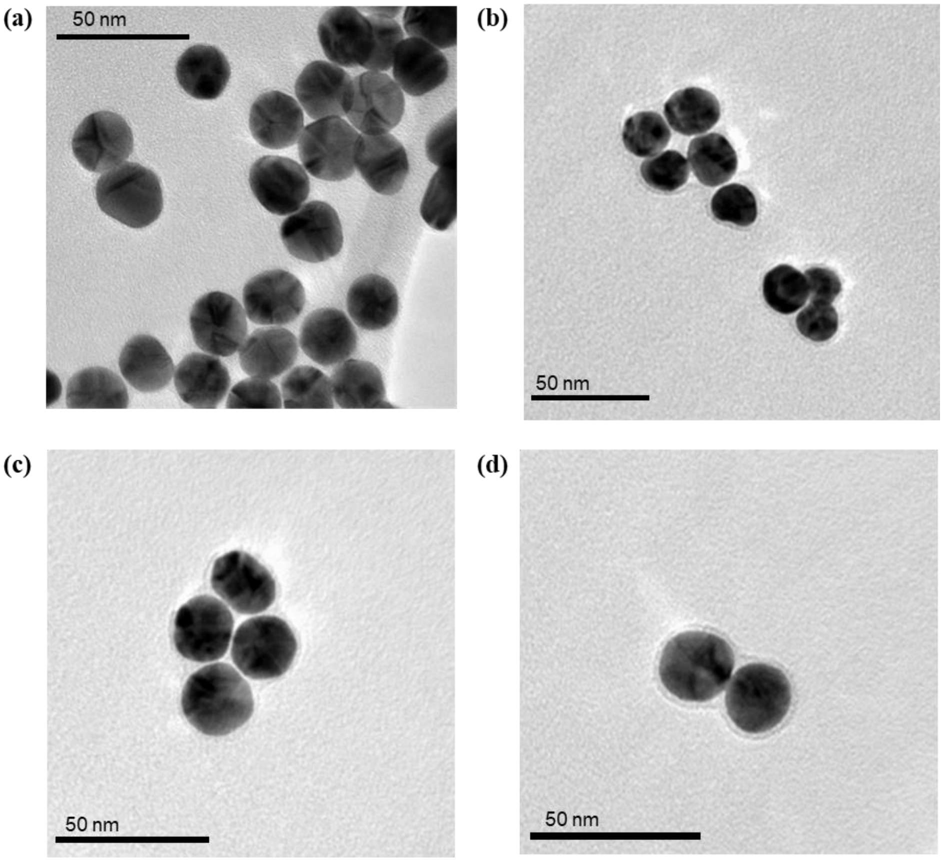

Figure S4.1 TEM images of DNA$_{25}$-Au NPs in (a) DI water; (b) 15 mM NaCl; (c) 5 mM MgCl$_2$; (d) 5 mM CaCl$_2$.

Text S4.2 Electrokinetic and Hydrodynamic Properties of Citrate-Au and DNA-Au NPs as a Function of pH.

Both Citrate-Au and DNA-Au NPs remain negatively charged in a wide pH range (2 to 11, Figure S4.2a). After DNA displacement, the EPM values of DNA-Au become more negative than that of Citrate-Au, and no significant difference is observed among the four DNA-Au NPs (pH 6.0). When pH decreases from 6 to 3, the EPM values of DNA-Au increase more sharply than that of Citrate-Au, and the absolute values of EPM of DNA-Au are smaller. Previous studies have demonstrated that Au NPs with various coatings have distinct EPM behavior when pH changes. For instance, Au NPs with PVP (Stankus et al., 2011) or PEG (Surette and Nason, 2016) coatings also exhibited a negative surface charge, but the absolute EPM values were much lower than those of Au NPs with DNA coating at neutral pH. On the contrary, Au NPs with MPTMA (Stankus et al., 2011) or BPEI (Surette and Nason, 2016) coatings displayed a positive surface charge at neutral pH.

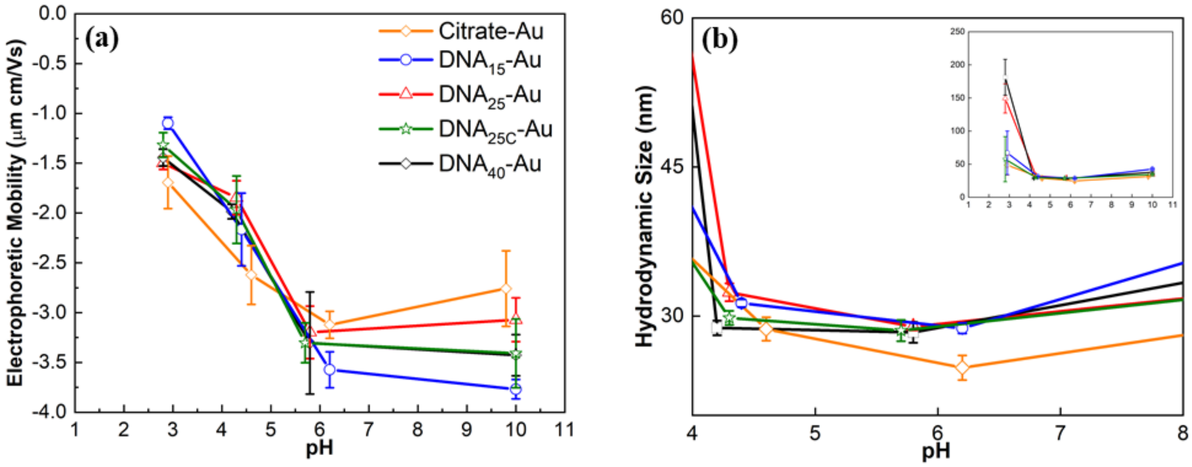

Figure S4.2 (a) Electrophoretic mobility (EPM) of Citrate-Au and DNA-Au as a function of pH; (b) Hydrodynamic diameter as a function of pH. Particles were suspended in DI water at concentration of 10 mg/L. 0.1 M HCl/NaOH were used to adjust the pH to desired values (2.8-10). Measurements were conducted at approximately 2 minutes after the desired pH reached. Error bars indicate one standard deviation of duplicate experiments.

The D_h of Citrate-Au and DNA-Au NPs as a function of pH is presented in Figure S4.2b. Both Citrate-Au and DNA-Au NPs remain relatively stable over a wide range of pH (4 to 10), while aggregation and/or sedimentation is observed when pH drops to 2.9. It is to be noted that at pH 2.9, the color of Citrate-Au and DNA-Au suspensions rapidly change from red to blue (due to aggregation), and then colorless (due to sedimentation). This sedimentation as a result confounded our measurement of D_h using DLS.

Overall, the distinctive electrokinetic and hydrodynamic properties between Citrate-Au and DNA-Au NPs could be attributed to the difference in surface coating. Citrate ligand is weakly associated on the Au NP surface via complexation of the carboxylate groups, preventing Au NP from aggregation mainly via electrostatic stabilization (Liu and Liu, 2017; Park and Shumaker-Parry, 2014). pH decrease leads to the protonation of citrate group on the Au surface and screens the electrostatic interaction between particles. On the other hand, DNA is anchored to the Au NP surface via a much stronger Au-S covalent bond (Liu and Liu, 2017), stabilizing Au NP via electrosteric interactions (i.e., a combination of electrostatic and steric interactions). DNA-Au NPs remain negatively charged over a wide range of pH due to the (ionized) phosphate backbone of the DNA molecule, whose pK_a is smaller than 2.0 (Liu and Liu, 2017). Bases of DNA are charge neutral between pH 5 and 8. But as pH drops lower, adenine (pK_a = 3.5) and cytosine (pK_a = 4.2) are protonated, corresponding to the rapid change of EPM at pH < 6.0. Further, Guanine (pK_a = 2.1) can only be protonated in extreme acidic condition (Liu and Liu, 2017).

The above results show that pH may have limited effects on the stability of DNA-Au in a typical aquatic environment (pH 5-9) (Crittenden and Montgomery Watson, 2005).

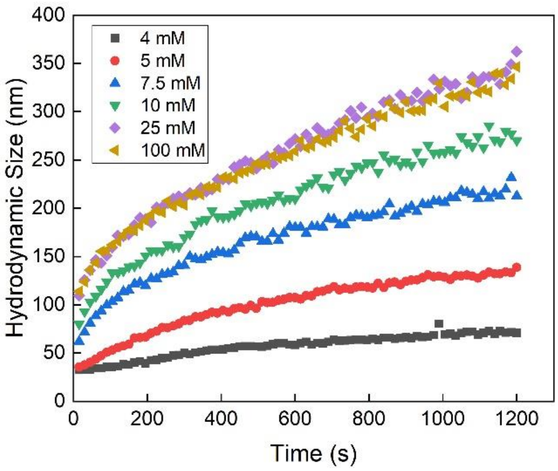

Figure S4.3 Representative TR-DLS (time-resolved dynamic light scattering) profiles of DNA$_{25C}$-Au NPs (10 mg/L) in CaCl$_2$ electrolytes of different concentrations.

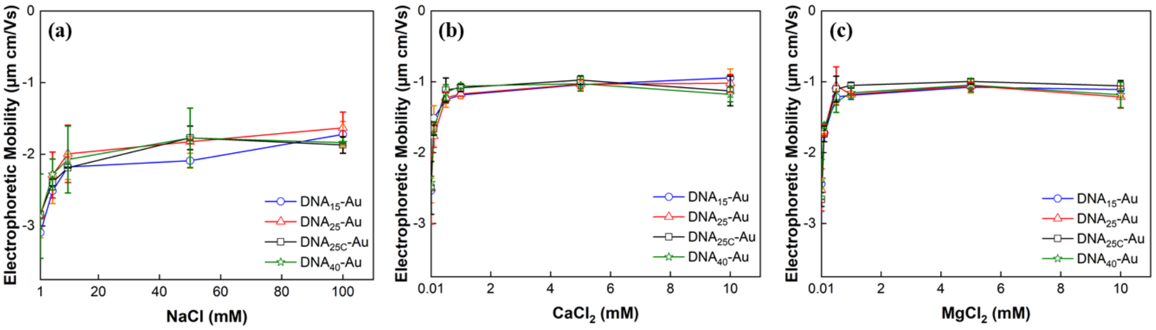

Figure S4.4 Electrophoretic mobility (EPM) of DNA-Au NPs as a function of (a) NaCl, (b) CaCl$_2$, and (c) MgCl$_2$ concentration, respectively.

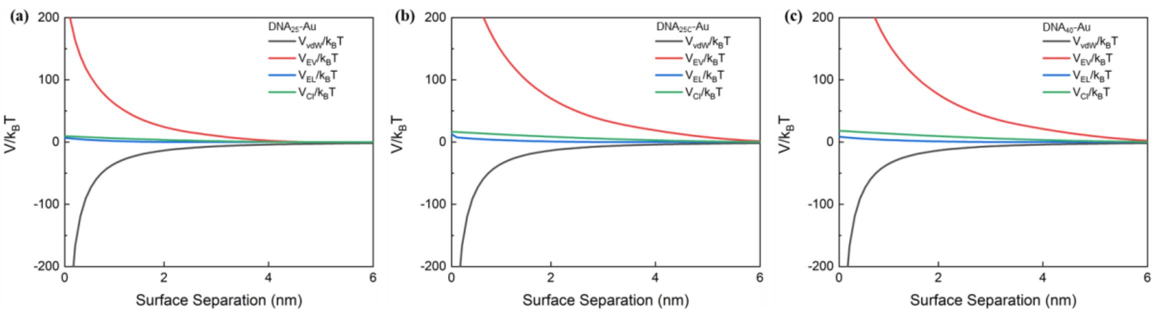

Figure S4.5 Potential energy of interaction for a pair of (a) DNA$_{25}$-Au; (b) DNA$_{25C}$-Au; (c) DNA$_{40}$-Au in 100 mM NaCl.

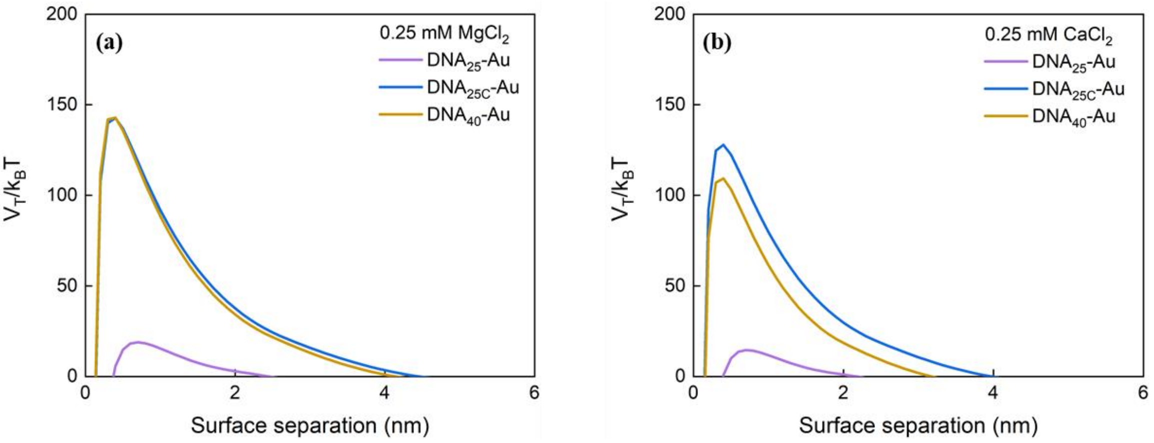

Figure S4.6 Total energy of DNA_{25}-Au, DNA_{25C}-Au, and DNA_{40}-Au in (a) 0.25 mM $MgCl_2$ and (b) 0.25 mM $CaCl_2$.

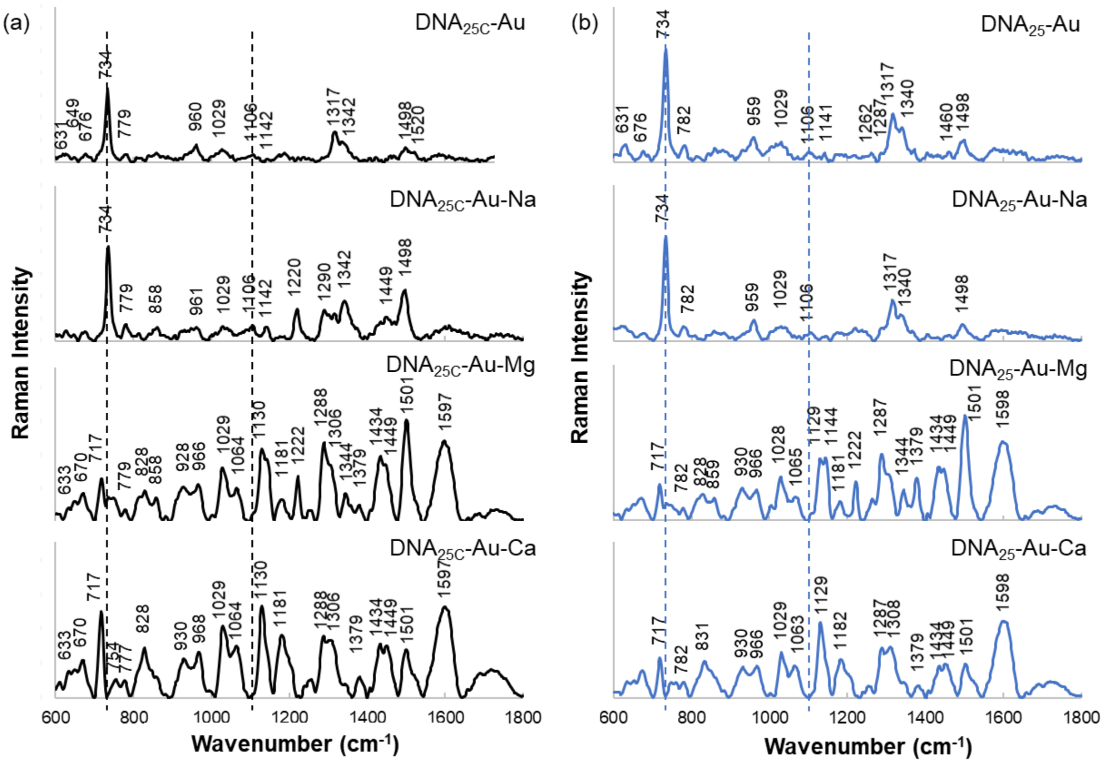

Figure S4.7 Raman spectrum of (a) DNA_{25C}-Au and (b) DNA_{25}-Au with or without the presence of electrolytes (NaCl, $MgCl_2$, or $CaCl_2$).

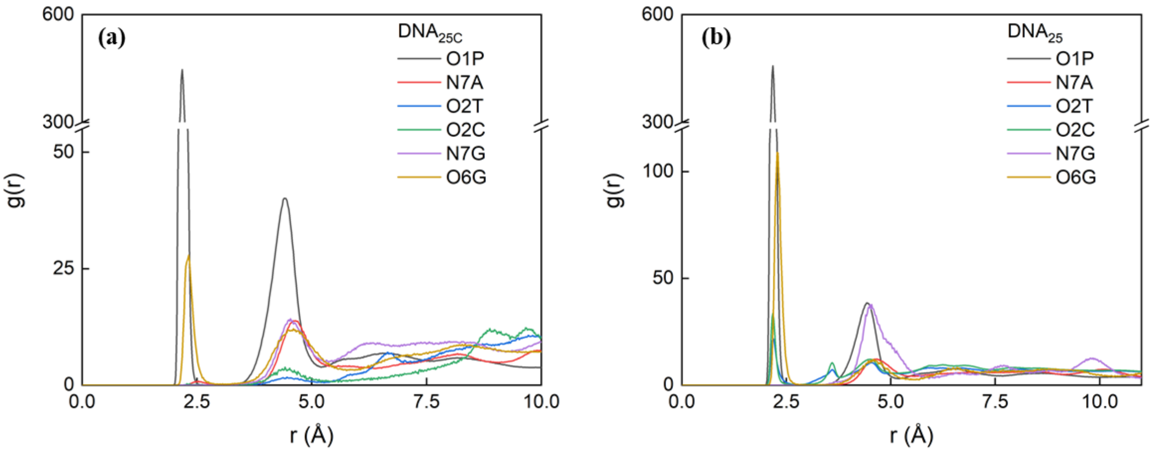

Figure S4.8 Radial distribution function (RDF) of specific atoms of DNA coordination with the Ca^{2+} cations, (a) DNA_{25C} (150% neutralization); (b) DNA_{25} (150% neutralization).

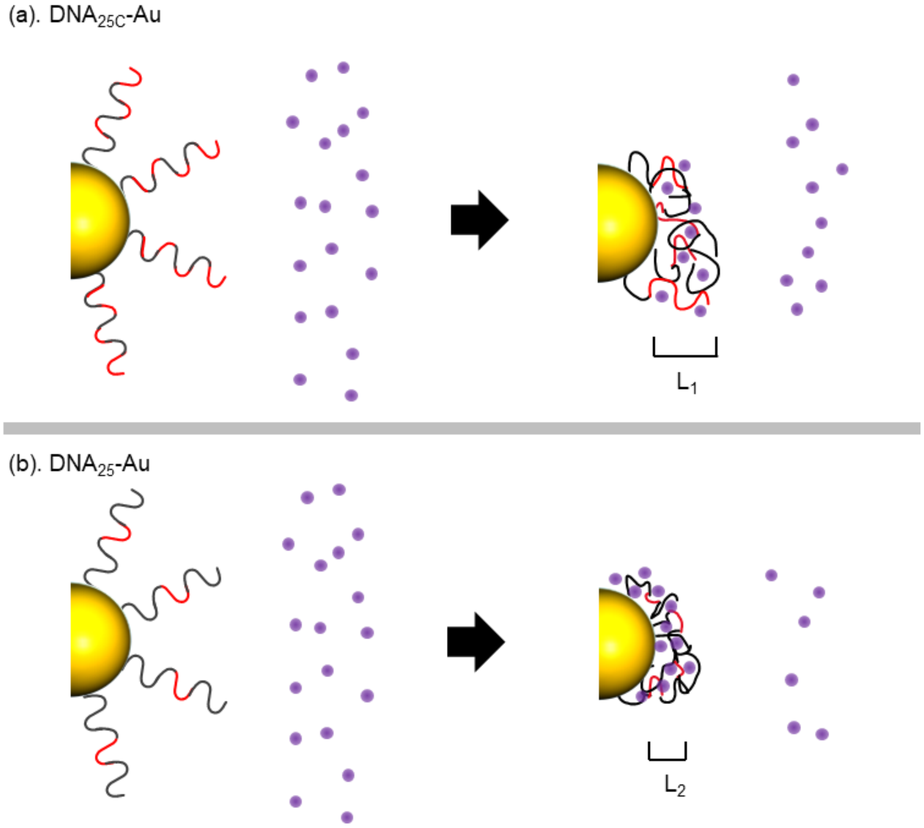

Figure S4.9 Depiction of proposed effect of guanine on the binding of Ca(II) ions to (a) DNA_{25C}-Au and (b) DNA_{25}-Au. The gold circles represent Au nanoparticle, the curves (black and red, where red part refers guanine) on particle represent DNA strands, the purple dots represent Ca(II) ions, and the black arrows represent the process of ion binding. The number of guanine bases and bounded ions only serve as illustration.

Table S4.1 Characteristics of DNA-Au NPs and corresponding DNA strand

	Hydrodynamic Size (nm)	DNA Molecular Weight* (g/mol)	DNA Extinction Coefficient* L/(mol·cm)
DNA_{15}-Au	30.8 ± 1.5	4839.4	167,800
DNA_{25}-Au	31.2 ± 1.7	7848.3	260,400
DNA_{25C}-Au	33.1 ± 0.5	8048.4	398,900
DNA_{40}-Au	35.4 ± 1.5	12382.3	279,200

*provided by manufacturer Integrated DNA Technologies, Inc. (IDT)

Table S4.2 System configuration of the simulation cell in MD simulations for DNA_{25}.

Neutralization (%)	Number of Ca^{2+}	Number of Cl^-	Number of H_2O	X(Y) (nm)	Z (nm)
100	60	0	26004	8.508	12.012
150	90	60	25982	8.528	12.040
200	120	120	25957	8.528	12.039

Table S4.3 System configuration of the simulation cell in MD simulations for DNA_{25C}.

Neutralization (%)	Number of Ca^{2+}	Number of Cl^-	Number of H_2O	X(Y) (nm)	Z (nm)
100	60	0	25988	8.508	12.011
150	90	60	25955	8.524	12.034
200	120	120	25922	8.524	12.034

References for Appendix B

Crittenden, J. and Montgomery Watson, H. (2005) Water Treatment Principles and Design, John Wiley, Hoboken, N.J.

Elimelech, M., Gregory, J. and Jia, X. (1995) Particle Deposition and Aggregation: Measurement, Modelling and Simulation, Butterworth-Heinemann.

Jusufi, A., Likos, C.N. and Ballauff, M. 2004. Counterion distributions and effective interactions of spherical polyelectrolyte brushes. Colloid Polym. Sci. 282(8), 910-917.

Jusufi, A., Likos, C.N. and Löwen, H. 2002. Counterion-induced entropic interactions in solutions of strongly stretched, osmotic polyelectrolyte stars. J. Chem. Phys. 116(24), 11011-11027.

Kegler, K., Konieczny, M., Dominguez-Espinosa, G., Gutsche, C., Salomo, M., Kremer, F. and Likos, C.N. 2008. Polyelectrolyte-compression forces between spherical DNA brushes. Phys. Rev. Lett. 100(11), 118302.

Kegler, K., Salomo, M. and Kremer, F. 2007. Forces of interaction between DNA-grafted colloids: An optical tweezer measurement. Phys. Rev. Lett. 98(5), 058304.

Liu, B. and Liu, J. 2017. Methods for preparing DNA-functionalized gold nanoparticles, a key reagent of bioanalytical chemistry. Anal. Methods 9(18), 2633-2643.

Napper, D.H. (1983) Polymeric Stabilization of Colloidal Dispersions, Academic Press, London; New York.

Osmond, D., Vincent, B. and Waite, F. 1975. Steric stabilisation: A reappraisal of current theory. Colloid and Polym. Sci. 253(8), 676-682.

Park, J.-W. and Shumaker-Parry, J.S. 2014. structural study of citrate layers on gold nanoparticles: Role of intermolecular interactions in stabilizing nanoparticles. J. Am. Chem. Soc. 136(5), 1907-1921.

Petosa, A.R., Jaisi, D.P., Quevedo, I.R., Elimelech, M. and Tufenkji, N. 2010. Aggregation and deposition of engineered nanomaterials in aquatic environments: Role of physicochemical interactions. Environ. Sci. Technol. 44(17), 6532-6549.

Seo, S.E., Li, T., Senesi, A.J., Mirkin, C.A. and Lee, B. 2017. The role of repulsion in colloidal crystal engineering with DNA. J. Am. Chem. Soc. 139(46), 16528-16535.

Stankus, D.P., Lohse, S.E., Hutchison, J.E. and Nason, J.A. 2011. Interactions between natural organic matter and gold nanoparticles stabilized with different organic capping agents. Environ. Sci. Technol. 45(8), 3238-3244.

Surette, M.C. and Nason, J.A. 2016. Effects of surface coating character and interactions with natural organic matter on the colloidal stability of gold nanoparticles. Environ. Sci.: Nano 3(5), 1144-1152.

Chapter 5 Preferential Interactions of Surface-Bound Engineered Single Stranded DNA with Highly Aromatic Natural Organic Matter: Mechanistic Insights and Implications for Optimizing Practical Aquatic Applications

(This chapter is based on Peng, B., Liao, P., & Jiang, Y. (2022). Preferential interactions of surface-bound engineered single stranded DNA with highly aromatic natural organic matter: Mechanistic insights and implications for optimizing practical aquatic applications. *Water Research*, *223*, 119015. DOI: 10.1016/j.watres.2022.119015)

Abstract

Engineered short-chain single stranded DNA (ssDNA) are emerging materials with various environmental applications, such as aptasensor, selective adsorbent, and hydrological tracer. However, the lack of fundamental understanding on the interactions of such materials with natural organic matter (NOM) hinders the improvement of their application performance in terms of sensitivity, selectivity, and stability. In this study, we investigated the interactions of ssDNA (four strands with systematically varied length and sequence) with two humic acids (Suwannee River humic acid (SRHA) and Aldrich humic acid (AHA)) and two humic-like NOM present in local aquatic matrices (ROM in river water and WOM in wastewater). Detailed, molecular-level interaction mechanisms were obtained by probing the colloidal stability of the ssDNA-coated gold nanoparticles, coupled with product characterization using a suite of microscopic and spectroscopic techniques. Our study revealed that π-π interactions and divalent cation bridging were the major mechanisms for ssDNA-NOM interactions. ssDNA preferentially interacted with NOM with high aromaticity (AHA > SRHA/WOM/ROM). With divalent cations present (especially Ca^{2+}), even a small amount of AHA could completely

shield ssDNA, whereas the extent of shielding by SRHA/WOM/ROM depended on the relative content of ssDNA and NOM and whether bridges formed. The extent of shielding of ssDNA by NOM provides a potential answer to the reported conflicting effects of natural water matrices on the performance of DNA-based sensors. Taken together, our findings provide insights into the transformations of engineered ssDNA under environmentally relevant conditions as well as implications for their performance optimization in practical aquatic applications (e.g., from DNA design to pretreatment strategy).

5.1 Introduction

Engineered DNA strands with desired sequences and a wide range of useful modifications, such as fluorescent tags and linkage molecules, can now be synthesized/purchased at low (and decreasing) costs. The DNA consists of nucleotides in a specific order, and each nucleotide contains a deoxyribose sugar, a phosphate group, and one of the four nitrogenous bases, namely adenine (A), thymine (T), cytosine (C), and guanine (G). They are unique from other synthetic polymers due to their intrinsic functions or embedded information. For example, a short-chain single-stranded DNA (ssDNA) aptamer binds targets with high sensitivity and selectivity, being very promising for rapid, point-of-use, multiplex environmental sensing of organic contaminants (Akki et al., 2015; Fan et al., 2014), ions (Qing et al., 2017), and pathogens (Yu et al., 2018), etc. Aptasensors have the potential to rival some state-of-the-art chemical/biological analytical methods. Also, DNA aptamer has been demonstrated as a highly selective adsorbent to remove arsenic (Kim et al., 2009) and illicit pharmaceuticals (Hu et al., 2011). Engineered DNA with programmed information (i.e., the sequence of nucleotides) can also be used as a tracer to track the source and migration pathways of pollutants in hydrological environment investigations (Liao et al., 2018). The number of DNA tracers is theoretically unlimited (i.e., the combination of four nucleobases) and the unique sequence of each DNA tracer makes it easily distinguishable from environmental background and allows for multipoint tracing.

While the potential of engineered DNA in aquatic applications has been well recognized as described above, little is known about the interactions of engineered DNA with natural organic matter (NOM) in typical aquatic environments. Natural organic matter, including humic substances, proteins, polysaccharides, etc., is ubiquitous in the environment (Philippe and Schaumann, 2014), and their interactions with engineered DNA interfere the performance of DNA-based applications. For aptasensors, a positive correlation between NOM concentration

(0–3.6 mg C/L) and the extent of performance degradation has been observed (Vogiazi et al., 2021), however, higher NOM concentrations (from 4 to 16 mg C/L) were also reported to exert no significant influence on the performance (Akki et al., 2015; Park et al., 2022). Among various types of aptasensor, colorimetric aptasensors typically involve the use of DNA-coated gold nanoparticles (Au NPs). The Au NPs are stabilized by the DNA coating in the presence of high salt concentrations, and the introduction of the target triggers preferential binding of DNA aptamer and causes the aggregation of Au NPs. Such systems are dependent on salt-induced aggregation and susceptible to the interferences from matrices (e.g., NOM or other constituents) (Akki and Werth, 2018). For example, low recovery of target was observed when the target was doped in milk samples (Yan et al., 2017). Other than aptasensors, NOM can also impact the functionality of DNA tracers. Adsorption of DNA tracers to NOM can lead to low recovery and unprecise detection (Liao et al., 2018; Pang et al., 2020). These reports highlight the need to elucidate the interaction(s) between engineered DNA and NOM, and the associated change of nanoparticle aggregation behaviors, which will benefit the development of DNA-based applications in more realistic scenarios.

Previous studies investigating the interactions between DNA and NOM have been mostly conducted with (natural) double-stranded DNA (dsDNA) with a long chain (thousands of base pairs) (Lu et al., 2012; Nguyen and Chen, 2007; Nguyen and Elimelech, 2007; Qin et al., 2018). For example, divalent cations formed bridges between the phosphate groups of DNA and the carboxyl groups of NOM, while monovalent cations only screened the negative charges (Nguyen and Chen, 2007; Nguyen and Elimelech, 2007). However, variations in DNA properties (e.g., double- or single-stranded, length, and sequence) may increase the complexity of their interactions with NOM. Smaller DNA fragments (2.69 kbp) were reported to have preferential adsorption to soil compared to larger fragments (11.19 and 23 kbp) due to their faster diffusion rates and/or the size exclusion of available binding sites (Ogram et al., 1994).

The phosphate groups of dsDNA were deemed as the major interaction sites with NOM (Lu et al., 2012; Nguyen and Chen, 2007; Nguyen and Elimelech, 2007) while the exposed nucleobases of ssDNA also participated in the interaction with graphene oxide (He et al., 2010; Liu et al., 2020). The preferential interaction of cations with guanine bases in the ssDNA affected the ion distribution along the DNA strands, resulting in varied DNA layer thickness and drastically different colloidal stability of the coated particles (Peng et al., 2022). Little attention has been paid to (engineered) short-chain ssDNA (e.g., < 100 nucleobases, the typical length of a DNA aptamer (Zhou et al., 2010)), which behaves distinctively from natural dsDNA in aquatic systems. As such, there is a critical knowledge gap in understanding the interactions of short-chain ssDNA with NOM, which expectedly have profound implications for the rational design of engineered DNA for aquatic applications, such as DNA-based sensor/adsorbent and DNA tracer, among other emerging applications.

In this study, we investigated the interaction(s) between ssDNA and NOM by examining the impact of NOM on the colloidal stability of ssDNA-coated nanoparticles. Molecular-level interaction mechanisms were revealed by characterizing the resulting products using a suite of microscopic and spectroscopic techniques (FTIR, Raman, Fluorescence, and TEM). Following our earlier work (Peng et al., 2022), ssDNA-coated gold nanoparticles (DNA-Au NPs) with four different ssDNA coatings (systematically varied in length and sequence) were studied. Two humic acids (Suwannee River humic acid (SRHA), an aquatic humic substance, and Aldrich humic acid (AHA), a terrestrial humic substance (Hur and Schlautman, 2003)), along with two humic-like NOM from local water matrices in Hong Kong (river water and wastewater effluent) were studied as the representative NOM. Our study revealed the dependences of ssDNA-NOM interaction on the aromaticity of NOM and the cation bridging effect (especially Ca^{2+}). A strong interaction could result in a complete shielding of the ssDNA by NOM, potentially sabotaging the functionality of ssDNA (e.g., the specific binding of aptamer to target and the hybridization of DNA barcode). Our findings provide new insights into the functioning of engineered ssDNA in complex aquatic matrices and directions to optimize the general design of DNA-based system for various aquatic applications (e.g., selection of DNA tracer and DNA aptamer and proper pretreatment strategy).

5.2 Experimental

5.2.1 Materials

Citrate-capped 20 nm spherical Au nanoparticles (Ted Pella, Inc.) were used for the synthesis of DNA-Au NPs. Four ssDNA with carefully designed sequences and 3’ end thiol modification were purchased from IDT (Integrated DNA Technologies, Inc.; denoted as DNA_{15}, DNA_{25}, DNA_{25C}, and DNA_{40}, Figure 5.1). The design of DNA_{15}, DNA_{25}, and DNA_{40} aimed at investigating the effect of DNA length, while the design of DNA_{25} and DNA_{25C} was to evaluate the effect of DNA sequence (Peng et al., 2022). Suwannee River humic acid (SRHA) was purchased from International Humic Substances Society (IHSS, standard III), and Aldrich humic acid (AHA) was purchased from Sigma-Aldrich.

5.2.2 Synthesis of DNA-Au NPs

DNA-Au NPs were synthesized using the salt-aging method (Liu and Liu, 2017; Mirkin et al., 1996), and the detailed procedure has been provided previously (Peng et al., 2022). Briefly, the ssDNA and Au NP suspension were incubated with stepwise addition of NaCl solution (2 M) to increase the salt concentration to 0.1 M. Excess reagents were removed by centrifugation three times. The DNA-Au NPs were redispersed in deionized water and stored at 4 °C until use.

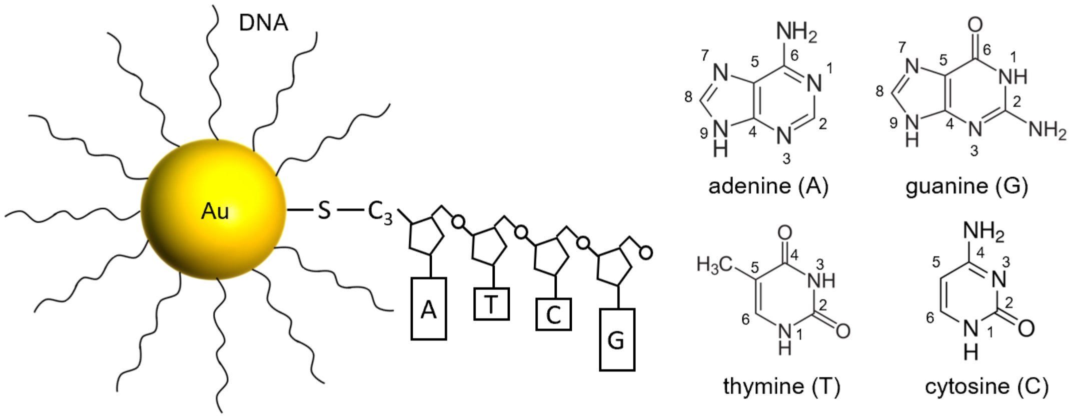

	DNA Sequences (3' to 5')
DNA_{15}	$HS-(CH_2)_3$-AAAAAAAAAA GACTC
DNA_{25}	$HS-(CH_2)_3$-AAAAAAAAAA GACTCATACTCACCT
DNA_{25C}	$HS-(CH_2)_3$-AAAAAAAAAA CTGAGTATGAGTGGA
DNA_{40}	$HS-(CH_2)_3$-AAAAAAAAAA GACTCATACTCACCT GACTCATACTCACCT

Figure 5.1 Schematic of a DNA-coated gold nanoparticle (DNA-Au NP) and the molecular structure of the four nitrogenous bases. The schematics are not drawn to scale and for illustrative purposes only. Sequences of the four DNA strands used in this study are listed in the table.

5.2.3 Preparation of NOM Solutions

SRHA and AHA stock solutions were prepared by dissolving humic substances in MilliQ water under pH 10.5 and subsequently filtering the mixture using a 0.45 μm membrane filter. The chemical characteristics of SRHA and AHA were assessed by UV/vis spectroscopy (Biochrom Libra S35), fluorescence spectroscopy (FLS920, Edinburgh Instruments), Raman spectroscopy (i-Raman Plus, B&W TEK), and FTIR (Spectrum Two PerkinElmer) (Details in Text S5.1, Appendix C). Specific UV absorbance at 254 nm ($SUVA_{254}$) was calculated as the UV absorbance at 254 nm divided by the total organic carbon (TOC; mg C/L, determined by TOC-L, Shimadzu) and 1 cm quartz cell path length. Bulk elemental compositions and functional group compositions of SRHA and AHA retrieved from previous works are summarized in Table S5.1 (Appendix C).

5.2.4 Aggregation Kinetics of DNA-Au NPs in the Presence of NOM and Electrolytes

Aggregation kinetics of DNA-Au NPs (10 mg Au/L) in the presence of NOM (SRHA or AHA, 2.7 mg C/L) were analyzed in three electrolytes (NaCl: 0.1–4 M; $CaCl_2$: 0–100 mM; $MgCl_2$: 0–100 mM) by time-resolved dynamic light scattering (TR-DLS; Zetasizer Nano ZS90, Malvern Instruments) following our previous work (Peng et al., 2022). The pH was unadjusted and determined to be 6.4 ± 0.2. Stock solution of SRHA or AHA was mixed with DNA-Au NPs, followed by the addition of salts. Attachment efficiency (α) was determined to be the ratio of the initial rate of change in the reaction-limited regime over that in the diffusion-limited regime. Critical coagulation concentration (CCC), served as an indicator for colloidal stability, was obtained from the intersection of extrapolated lines of reaction-limited and diffusion-limited regime.

5.2.5 Stability of DNA-Au NPs in Complex Aquatic Matrices

River water was collected from the Lam Tsuen River located in Tai Po, Hong Kong. Wastewater effluent was obtained from the secondary effluent of Tai Po Wastewater Treatment Plant in Hong Kong. The water samples were filtered by 0.45 μm filters and analyzed with regard to pH, TOC, conductivity, and cation concentration (Dionex Integrion HPIC System, Thermo Scientific). The organic matter in river water and wastewater (denoted as ROM and WOM, respectively) were characterized by fluorescence and Raman spectroscopies.

Initial aggregation kinetics (30 mins) of DNA-Au NPs in river water or wastewater effluent were performed at a particle concentration of 5 mg Au/L with or without dosed SRHA/AHA (10 mg C/L). Particle size was monitored via TR-DLS at 30 s interval for 30 mins. For long-term stability (21 days) of DNA-Au NPs, initial dosing of DNA-Au NPs was 500 μg Au/L and the concentration of suspended DNA-Au NPs was determined by inductively coupled plasma optical emission spectroscopy (ICP-OES, Agilent 720). The dosing of SRHA/AHA was 1 mg C/L or 5 mg C/L.

5.2.6 Characterization of DNA-NOM Interactions

The hydrodynamic diameter and electrophoretic mobility (EPM) of SRHA/AHA-adsorbed DNA-Au NPs were determined using Zetasizer Nano ZS90. The structures of DNA-Au NP aggregates with SRHA/AHA present in three electrolytes (NaCl, $MgCl_2$, and $CaCl_2$) were examined by transmission electron microscopy (TEM, JEOL JEM-2010) and scanning transmission electron microscopy (STEM, Talos™ F200X G2) equipped with high angle annular dark field (HAADF) detector and energy-dispersive X-ray spectroscopy (EDS) detector. The Raman and FTIR spectra of NOM-adsorbed DNA-Au NPs were recorded. Detailed procedures are provided in Text S5.1.

5.2.7 Urea/SDS Induced Desorption of NOM from DNA-Au NPs

NOM (5 mg C/L) was incubated with DNA_{25}-Au NPs (5 mg Au/L) in 50 mM NaCl overnight to allow adsorption to reach equilibrium (pH 6.3 ± 0.2). After centrifugation (11000 rpm, 20 min) and removal of the supernatant, the NOM-adsorbed DNA-Au NPs were dispersed in solutions containing different solutes (50 mM NaCl; 50 mM NaCl, and 1 or 6 M urea; 50 mM NaCl, and 1% or 10% sodium dodecyl sulfate (SDS)). After 45 min, the released NOM was quantified by fluorescence spectroscopy.

5.3 Results and Discussion

5.3.1 Characterization of DNA-Au NPs and NOM

DNA strands were thiol-modified at their 3’ end and attached to the particle surface via Au-S covalent bonds, forming a densely-packed DNA layer (Mirkin et al., 1996) (Figure 5.1). Four DNA strands with systematically varied sequences and lengths were used to synthesize DNA-Au NPs, denoted as DNA_{15}-Au, DNA_{25}-Au, DNA_{25C}-Au, and DNA_{40}-Au, respectively. Such design aimed at singling out the effect of DNA length (i.e., DNA_{15}, DNA_{25}, and DNA_{40}) and the effect of DNA sequence (i.e., DNA_{25} and DNA_{25C}) on their interactions with NOM.

Detailed characterization of these particles has been reported in our earlier work (Peng et al., 2022). The hydrodynamic sizes of the four DNA-Au NPs were 35.4 ± 1.5 nm of DNA_{40}-Au, 33.1 ± 0.5 nm of DNA_{25C}-Au, 31.2 ± 1.7 nm of DNA_{25}-Au, and 30.8 ± 1.5 nm DNA_{15}-Au, respectively.

Figure 5.2a presents the UV/vis spectra of SRHA and AHA (2.7 mg C/L in water). AHA had higher absorbance than SRHA in both the UV and visible light wavelength ranges. Absorbance at 254 nm is characteristic of aromatic regions (Korshin et al., 2009), whereas absorbance at 280 nm is positively correlated to molecular weight (Chin et al., 1994). The observed higher absorbance of AHA at 280 nm was consistent with the reported more high-molecular-weight portion (> 100 kDa) in AHA than SRHA (*ca*. 20% for AHA vs 5% for SRHA) (Kim et al., 2006). Due to different humification environments, SRHA is typically comprised of relatively small and polar moieties, while AHA has more nonpolar and aromatic contents (Grasso et al., 1990; Hong and Elimelech, 1997). The $SUVA_{254}$ of SRHA and AHA were calculated to be 6.2 ± 0.1 and 9.0 ± 0.1, respectively, suggesting a higher aromatic content of AHA (Abbt-Braun et al., 2004) and being in agreement with our previously reported values (Jiang et al., 2017).

The excitation emission matrix (EEM) of SRHA and AHA showed a similar excitation maximum at around 330 nm, and SRHA showed an obvious emission peak at around 460 nm while AHA had a broad emission peak from 450 to 550 nm (Figure 5.2c-d). The excitation/emission wavelengths are representative of humic-like peak C fluorophore (Coble, 1996). Emission scan at 330 nm excitation confirmed the emission peak of AHA at around 520 nm (Figure 5.2b). A blue-shifted emission maximum of SRHA indicates a decrease in the π-electron system, such as a lower number of aromatic rings (Coble, 1996), consistent with the lower aromaticity as suggested by the smaller $SUVA_{254}$ value of SRHA. Also, it has been suggested that long emission wavelengths (> 500 nm) could be attributed to the presence of greatly conjugated systems, such as linearly condensed aromatic rings and other unsaturated bond systems (Rodríguez et al., 2014; Sierra et al., 2005), in accordance with the higher aromaticity of AHA as suggested by a larger SUVA$_{254}$ value.

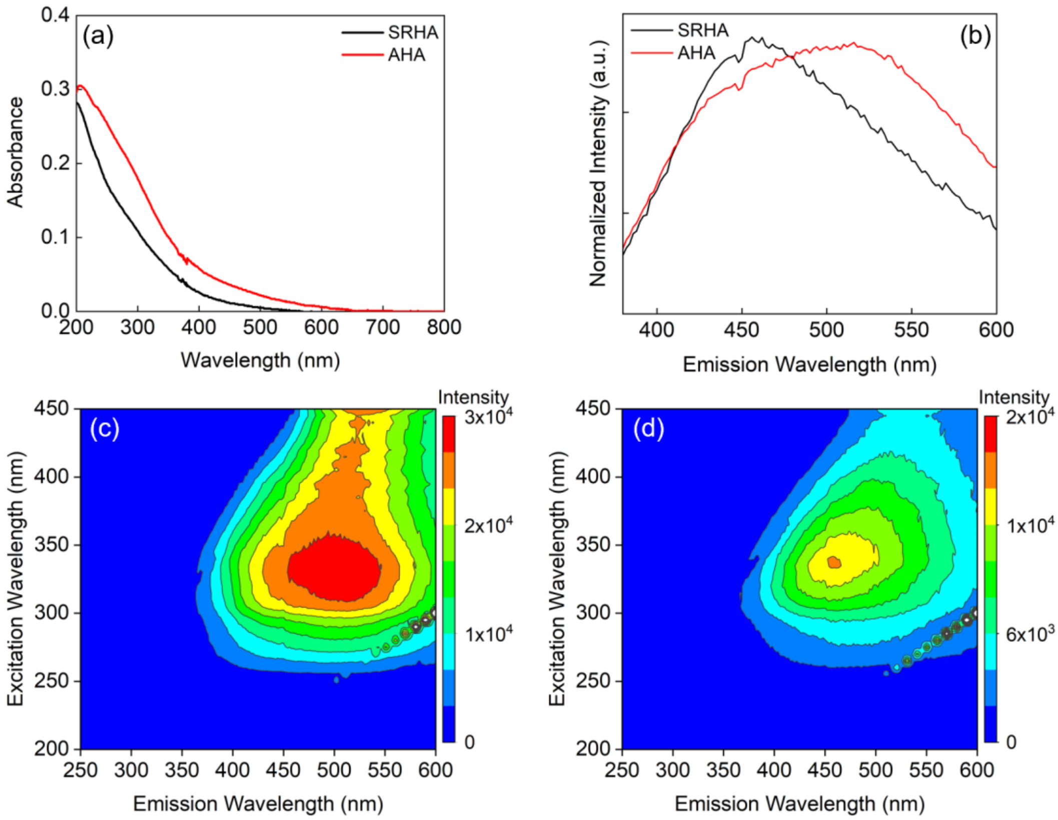

Figure 5.2 Spectroscopic characterization of SRHA and AHA; (a) UV/vis spectra (2.7 mg C/L); (b) normalized emission scan spectra at excitation wavelength of 330 nm; (c) and (d) excitation emission matrix (EEM) of SRHA and AHA, respectively.

5.3.2 Aggregation Kinetics of DNA-Au NPs in the Presence of NOM

The aggregation kinetics of DNA-Au NPs in the presence of SRHA or AHA were investigated in NaCl, $MgCl_2$, and $CaCl_2$ electrolytes, respectively. Distinct reaction-limited and diffusion-limited regimes of DNA-Au NPs were observed (Figure S5.1, Appendix C). The CCC values were determined as the intersections of the extrapolated lines of these two regimes and compared in Figure 5.3. The CCC values of DNA-Au NPs without NOM were retrieved from our previous work (Peng et al., 2022).

The presence of SRHA increased the CCC values of DNA_{15}-Au from 451 mM to 489 mM NaCl, from 2.2 mM to 3 mM $MgCl_2$, and from 2.2 mM to 2.7 mM $CaCl_2$, respectively (Figure 5.3). Similar enhanced colloidal stability was observed for the other three DNA-Au NPs, regardless of the DNA sequence and length. The enhancement of colloidal stability by the presence of NOM has been extensively reported (Jiang et al., 2017; Loosli et al., 2013; Nason et al., 2012), and such effect was attributed to the enhanced (electro)steric repulsion imparted by adsorbed NOM (Chen and Elimelech, 2007). The EPMs of SRHA-adsorbed DNA-Au NPs were either less negative (in NaCl electrolyte) or similar (in $MgCl_2$ or $CaCl_2$ electrolyte) to the 'bare' DNA-Au NPs (Text S5.2 and Figure S5.3), indicating that the enhanced colloidal stability mainly arose from stronger steric repulsion. The order of stability among the four DNA-Au NPs with the presence of SRHA was the same as that without SRHA (Peng et al., 2022), i.e., (1) in NaCl electrolyte: DNA_{40}-Au > DNA_{25C}-Au > DNA_{25}-Au > DNA_{15}-Au and (2) in $MgCl_2$ and $CaCl_2$ electrolytes: DNA_{25C}-Au > DNA_{40}-Au > DNA_{25}-Au > DNA_{15}-Au.

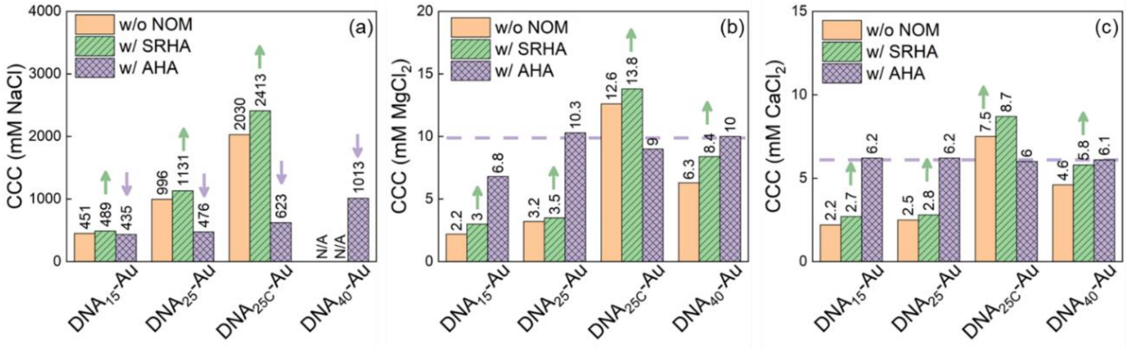

Figure 5.3 Critical coagulation concentration (CCC) of DNA-Au NPs (10 mg Au/L) with or without the presence of NOM (2.7 mg C/L) in (a) NaCl; (b) $MgCl_2$; (c) $CaCl_2$. The CCC values of DNA-Au NPs without NOM were retrieved from our previous work (Peng et al., 2022). The NaCl CCC values of DNA_{40}-Au without NOM or with SRHA were not obtained due to a lack of observed diffusion-limited aggregation in the NaCl concentrations tested. Upward/downward arrows (green/purple) indicate increased/decreased CCC values with the presence of NOM compared to those without NOM. Dash lines (purple) indicate similar CCC values with the presence of AHA.

Unlike SRHA, the presence of AHA significantly changed the stability of DNA-Au NPs, and the effect showed a strong dependency on the co-existing cations. In NaCl electrolyte, the presence of AHA lowered the CCC values of all four DNA-Au NPs (Figure 5.3a). For example, the CCC value of DNA_{25C}-Au decreased significantly from 2030 mM to 623 mM NaCl. Although the colloidal stability of DNA-Au NPs was reduced by the presence of AHA, the order of stability did not change compared to that without AHA present, i.e., DNA_{40}-Au > DNA_{25C}-Au > DNA_{25}-Au > DNA_{15}-Au. In divalent electrolytes ($MgCl_2$ and $CaCl_2$), interestingly, the presence of AHA brought the stability of DNA-Au NPs to a similar level (i.e., similar CCCs, Figure 5.3b-c) regardless of the original ssDNA coatings, which was completely different from the effect of SRHA. The CCC values of DNA-Au NPs with AHA present were *ca.* 6 mM $CaCl_2$ and *ca.* 10 mM $MgCl_2$ (with the exception of DNA_{15}-Au in $MgCl_2$ electrolyte, 6.8 mM). In either electrolyte, the similar EPMs of DNA-Au NPs with or without the presence of AHA (Figure S5.3) indicated that mechanism(s) other than electrostatic interactions should be accounted for inducing such change in colloidal stability.

5.3.3 Mechanisms Underlying the Distinct Effects of NOM on Particle Stability

5.3.3.1 Adsorption of NOM onto DNA-Au NPs

The interaction between DNA-Au NPs and NOM (SRHA/AHA) was first probed by fluorescence spectroscopy (Text S5.3 and Figure S5.4-S5.6). Due to fluorescence quenching of Au NPs (Liu and Liu, 2017), the fluorescence intensity of NOM was lowered after adsorption (Figure S5.4a and e, S5.5a and e, and S5.6). Stronger quenching of the AHA fluorescence by DNA-Au NPs was observed compared to SRHA (Figure S5.6), suggesting a stronger interaction (i.e., adsorption) between AHA and the ssDNA coating. For example, by calculating the intensity change at emission maximum (460 nm for SRHA and 520 nm for AHA, excitation wavelength = 330 nm), the peak intensity of SRHA was reduced by 8%, while that of AHA was reduced by 24%. When additional salts (NaCl/$MgCl_2$/$CaCl_2$) were introduced, the fluorescence intensity of AHA was further decreased while the emission peak intensity of SRHA barely changed (Text S5.3 and Figure S5.4-S5.6). Both NOM and DNA-Au NPs were negatively charged, therefore the adsorption of NOM should be attributed to interactions other than electrostatic attraction, such as hydrogen bonding, hydrophobic interactions, π-π interactions, cation bridging, etc. (Philippe and Schaumann, 2014).

To understand the NOM-DNA interaction mechanism(s), we first examined the FTIR spectra of NOM-adsorbed DNA-Au NPs in $CaCl_2$/NaCl electrolytes, respectively. The adsorption of NOM in $CaCl_2$ electrolyte induced a spectral change at *ca*. 1580 cm^{-1} (Figure 5.4a and c), and the extent of which is more pronounced in the spectra of AHA-adsorbed ones and proportional to the adsorbed amount (AHA:Au = 1:1). The results suggested that the ssDNA coating interacted more strongly with AHA than SRHA, consistent with the aforementioned fluorescence study. Due to the strong overlap of absorption in the IR spectra of the four nucleobases (Alex and Dupuis, 1989; Tsuboi, 1970), correlating the interaction between SRHA/AHA and a specific nucleobase was difficult. Nevertheless, an attenuation of the peak at 1466 cm^{-1} after NOM adsorption, which symbolizes the in-plane vibrations of the nucleobases (e.g., NH and CH in the ring structures (Tsuboi, 1970); molecular structures shown in Figure 5.1), was observed in both electrolytes ($CaCl_2$ and NaCl; Figure 5.4a, c, and e), implying that the ssDNA-NOM interactions could have occurred through π-π interactions.

Furthermore, we observed attenuated peaks at 1730 cm^{-1} (C=O stretching of nucleobases (guanine, thymine, and cytosine, Figure 5.1)), 1277 cm^{-1} (asymmetric stretching of phosphate), and 1073 cm^{-1} (symmetric stretching of phosphate) (Alex and Dupuis, 1989; Tsuboi, 1970), which may stem from the binding of cations and/or hydrogen bonding (Park et al., 2013) between NOM and the ssDNA coating. These interaction sites (i.e., C=O of nucleobases and phosphate groups) indicated by the FTIR results were consistent with our previous work (Peng et al., 2022), in which we used molecular dynamics simulations to investigate the interaction

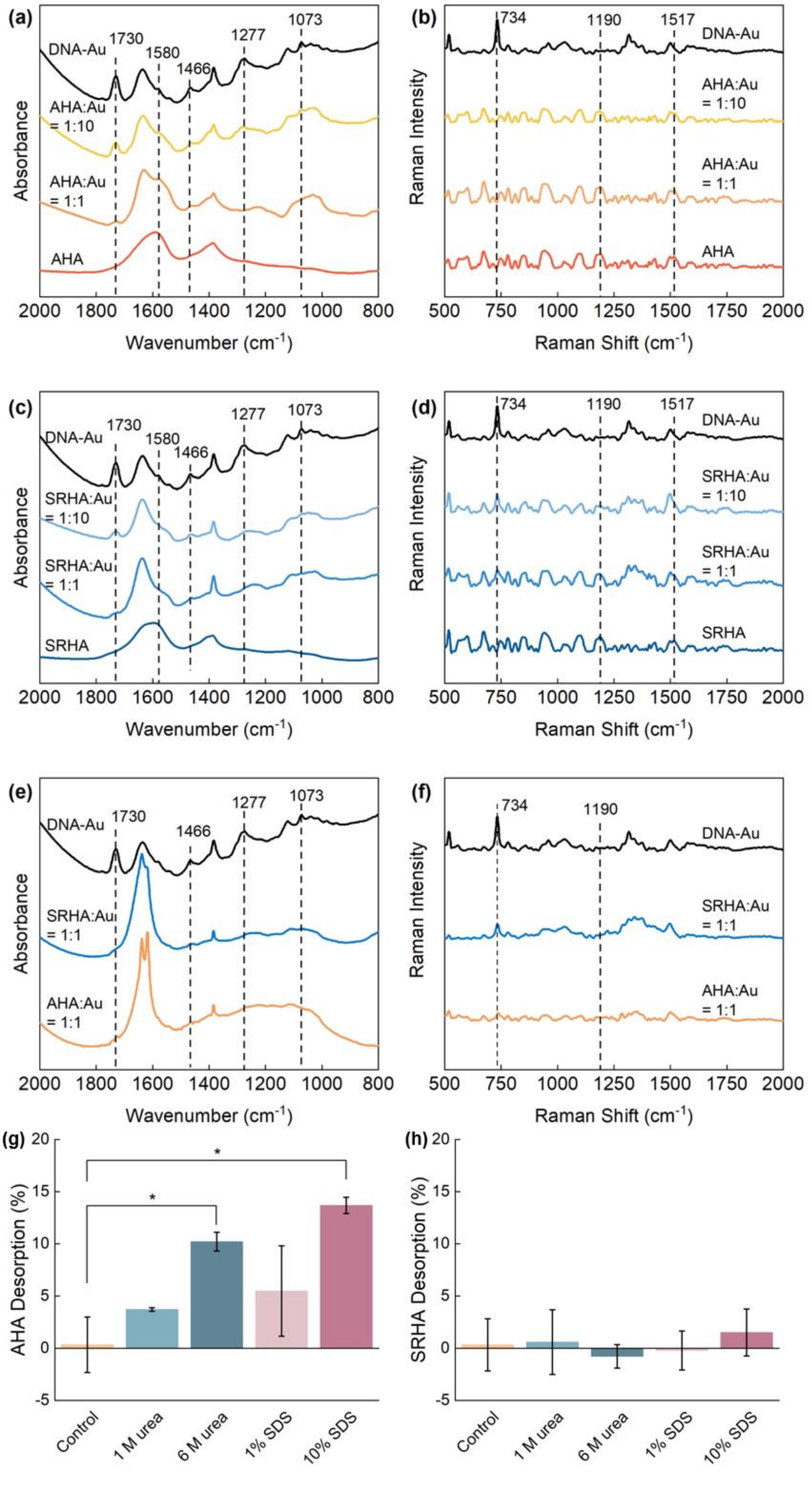

Figure 5.4 (a-f) FTIR and Raman spectra of SRHA/AHA adsorbed DNA$_{25}$-Au in (a-d) 0.5 mM CaCl$_2$ or (e-f) 50 mM NaCl. SRHA/AHA:Au refers to the carbon-to-gold ratio during sample preparation (see details in Text S1). (g-h) Urea or SDS induced desorption of (g) AHA or (h) SRHA from NOM-adsorbed DNA$_{25}$-Au NPs. Error bars indicate one standard deviation of at least three replicates. Asterisks indicate significant difference (one-way ANOVA test followed by the Tukey test for multiple comparisons, $p < 0.05$).

between Ca^{2+} and DNA strands. To further probe the interactions, we used urea and SDS to induce possible desorption of NOM from DNA-Au NPs in NaCl electrolyte (excluding cation bridging). Urea breaks hydrogen bonds (Liu et al., 2020) and SDS breaks both hydrogen bonds and hydrophobic interactions (Schmid et al., 2017), while π-π interactions are not disturbed. As shown in Figure 5.4g, urea induced the desorption of AHA from DNA-Au NPs, and the effect of which was more pronounced at higher urea concentration (6 M, *ca.* 10% AHA desorbed). SDS also induced the desorption of AHA (*ca.* 14% AHA desorbed with 10% SDS). These results suggest that hydrogen bonding and/or hydrophobic interactions contributed to the adsorption of AHA onto DNA-Au NPs, however, a quantitative distribution of each AHA adsorption mechanism cannot be achieved. Overall, less than 15% of AHA were desorbed even at 6 M urea or 10% SDS condition, suggesting that π-π interaction was the major mechanism responsible for AHA adsorption. On the other hand, desorption of SRHA induced by urea or SDS was not observed (Figure 5.4h), indicating that π-π interaction was likely the only mechanism responsible for SRHA adsorption. Therefore, the exposed nucleobases of ssDNA played a significant role in its interaction with NOM via π-π interactions. The stronger adsorption of AHA than SRHA onto DNA-Au NPs was due to its higher aromaticity (indicated by the aromatic carbon content (Table S5.1) and $SUVA_{254}$) and capability to form hydrogen/hydrophobic bonds with the ssDNA coating.

Raman spectra revealed more details of the interaction between NOM and the ssDNA. The adsorption of AHA in $CaCl_2$ electrolyte completely shielded the characteristic peaks of adenine (734 cm^{-1}) and nucleobases (1250-1500 cm^{-1}) (Alex and Dupuis, 1989; Otto et al., 1986) (Figure 5.4b). The spectra of AHA-adsorbed DNA-Au NPs became the same as that of pure AHA even at a low carbon-to-gold ratio (AHA:Au = 1:10). On the other hand, the characteristic peaks of adenine and nucleobases after SRHA adsorption remained in the spectra, albeit attenuated (Figure 5.4d). With more SRHA adsorbed (SRHA:Au increased from 1:10 to 1:1), the peak of adenine became weaker and the peaks from SRHA (e.g., 1190 and 1517 cm^{-1}) became apparent. Similar pattern was observed for the NOM-adsorbed DNA$_{25C}$-Au NPs in CaCl$_2$ electrolyte as well (Figure S5.7), likely due to that the minor differences in DNA$_{25}$ and DNA$_{25C}$ did not significantly impact their interactions with NOM. In NaCl electrolyte, neither SRHA nor AHA was able to completely shield the original ssDNA coating, as suggested by the remaining peaks of adenine and nucleobases after adsorption (Figure 5.4f). The relatively weaker peaks of adenine and nucleobases in the spectrum of AHA-adsorbed DNA$_{25}$-Au compared to the SRHA-adsorbed one was in line with the stronger interaction between AHA and the ssDNA coating. The lack of complete shielding by adsorbed AHA in NaCl electrolyte suggested that divalent cation bridging between the phosphate groups of DNA and the carboxyl groups of NOM (Lu et al., 2012; Nguyen and Chen, 2007) also played a significant role in the adsorption process of AHA in CaCl$_2$ electrolyte.

5.3.3.2 Intermolecular Interactions of NOM

Aggregation of Au NPs shortens their interparticle distance and causes the suspension color to change from red to purple (Storhoff et al., 2000). Such color change was observed for the aggregated DNA-Au NPs without NOM present or with SRHA present in all three electrolytes (Figure 5.5c inset and S5.8b-c). However, the colors of aggregated DNA-Au NPs with AHA present were reddish-purple (Figure 5.5a inset) and showed a dependency on the presence of cations (Figure S5.8d-e). From Na$^+$, Mg^{2+}, to Ca^{2+}, the color of the suspensions gradually transitioned from purple to magenta, suggesting increased interparticle distance of the aggregated Au NPs. More details regarding the colors of aggregated DNA-Au NPs are given in Text S5.4.

To elucidate the underlying mechanism(s) causing the discrepancy in color change, we examined the structure of aggregated DNA$_{25}$-Au with NOM present via TEM and EDS elemental mapping. In the presence of both Ca^{2+} and AHA, we observed light shadowy areas bridging DNA-Au NPs (Figure 5.5a and S5.9a-c). Such bridging areas were also observed in the HAADF images as well (Figure 5.5b). The corresponding EDS elemental mapping showed that the elemental distribution of P (from DNA backbone) and S (from thiol group in DNA, Figure 5.1) matched well with that of Au, suggesting that the DNA strands were on Au NPs. The elemental distribution of N and O highly overlapped with the bridging areas (Figure 5.5b insets), especially the O distribution, indicating the areas were indeed AHA molecules. The intermolecular bridging of AHA molecules (both adsorbed and unadsorbed) likely occurred via calcium complexation (Chen and Elimelech, 2007; Liu et al., 2011; Schwyzer et al., 2013). On the contrary, the intermolecular bridging of SRHA molecules was hardly observed (Figure 5.5c-d and S5.10a-c), and the aggregate structure was similar to the aggregated DNA-Au NPs without NOM present (Figure S5.11). The interparticle distance observed with AHA present was apparently larger than the other two scenarios (with SRHA or without NOM), in agreement with its magenta color of aggregate suspension (Figure 5.5a inset). The aggregated particles with SRHA present or without NOM were closely packed, in line with the purple colors of their aggregate suspensions (Figure 5.5c inset).

Similar bridging of the AHA molecules by Mg^{2+} was observed (Figure S5.9d-f), but to a less extent and only occurred at high concentrations (e.g., 20 mM Mg^{2+}) (Text S5.5 and Figure S5.12-S5.13), in agreement with the intermediate reddish-purple color of aggregate suspension (Figure S5.8e). Such discrepancy in the effect of Mg^{2+} and Ca^{2+} stemmed from the weaker electronegativity and larger hydrated radius of Mg^{2+} (Stankus et al., 2011). Interestingly, although the bridging effect was not expected in NaCl electrolyte because Na^{+} only screens the negative charges, similar light shadowy areas linking aggregated particles was observed with the presence of AHA (Figure S5.9g-l), but not with SRHA (Figure S5.10d-f). Such intermolecular interactions of AHA molecules are speculated to occur through π-π interaction due to their high aromaticity (Ghosh et al., 2008; Nason et al., 2012).

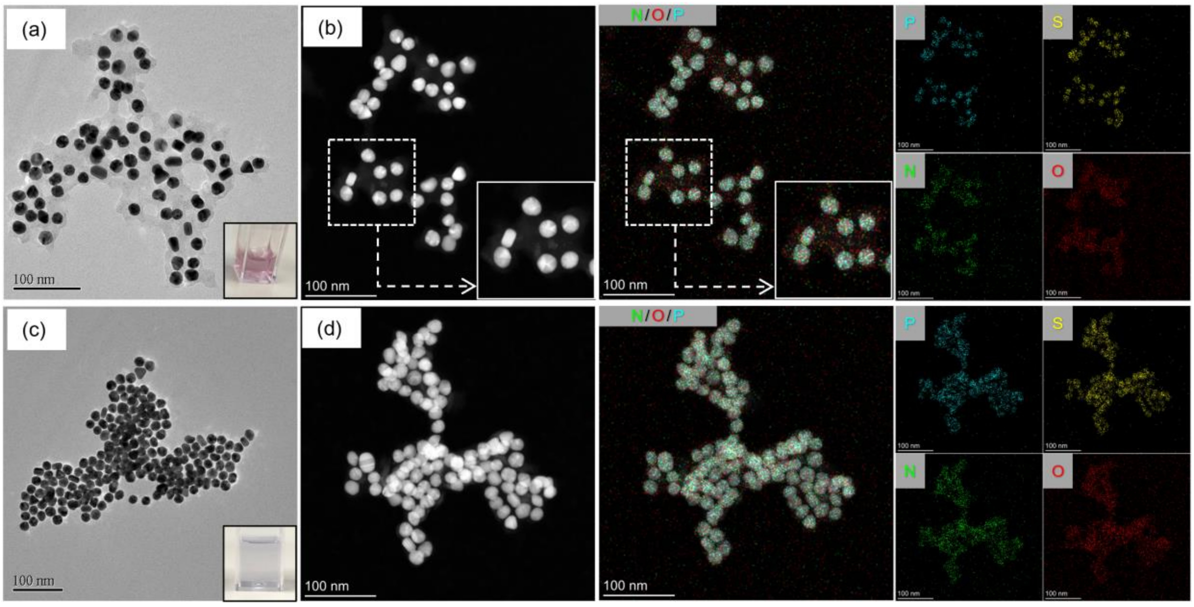

Figure 5.5 Morphology and microscopic structure of aggregated DNA25-Au NPs (10 mg/L) in the presence of 10 mM Ca^{2+} and 2.7 mg C/L NOM. (a-b) aggregated particles with AHA present examined by (a) TEM and (b) HAADF-STEM and the corresponding EDS elemental mapping; insets show the enlarged selected area (white dashed box). (c-d) aggregated particles with SRHA present examined by (c) TEM and (d) HAADF-STEM and the corresponding EDS elemental mapping.

The bridging of NOM molecules by divalent cations has been widely reported (Chen and Elimelech, 2007; Ghosh et al., 2008; Huynh and Chen, 2011; Liu et al., 2011; Nason et al., 2012; Stankus et al., 2011), and the carboxyl groups have been recognized as the binding sites for cations. Although the carboxyl group density was found to be positively related to the bridging effectiveness (Lu et al., 2012), it does not seem to be the only parameter determining the bridging effect. For example, the bridging of SRHA (standard II), which has 15% carboxyl carbon (Table S5.1), has been reported (Chen and Elimelech, 2007; Huynh and Chen, 2011; Liu et al., 2011), but the bridging of SRHA (standard I) with a higher carboxyl content (19% carboxyl carbon, Table S5.1) was not observed (Huangfu et al., 2013). Other parameters, such as the position of carboxyl groups in the polymer chain (Labille et al., 2005), might also need to be taken into consideration. In our study, the bridging mediated by divalent cations was only observed with AHA but not SRHA, which was consistent with the aggregation profile of pure

SRHA/AHA in the electrolytes (Figure S5.2). Only in $CaCl_2$ electrolyte of a high concentration (50 mM), the SRHA molecules formed clusters that can be steadily detected by the DLS instrument (Figure S5.2d), while the aggregation of AHA molecules was observed in both $CaCl_2$ and $MgCl_2$ electrolytes (Figure S5.2b-c). The higher carboxyl content of AHA than SRHA (standard III used in this study) (Table S5.1) may partially contribute to the observed phenomenon. More efforts are required to reveal the underlying mechanism of such divalent cation bridging in future.

5.3.3.3 Proposed Interaction Mechanisms

The adsorption of NOM to ssDNA and subsequent impact on the colloidal stability of DNA-Au NPs in simple electrolytes showed a dependency on both the properties of NOM and cations (Figure 5.6). In divalent electrolytes ($MgCl_2$ and $CaCl_2$), the adsorbed AHA molecules completely shielded the original ssDNA coating, which was facilitated mainly by both π-π interaction and divalent cation bridging. The AHA coating determined the stability of the coated nanoparticles, which explained the similar CCC values of the four AHA-adsorbed DNA-Au NPs in divalent electrolytes (Figure 5.3b-c). On the contrary, the adsorption of AHA in NaCl electrolyte did not completely shield the original ssDNA coating. As such, the original ssDNA coating still played a role in the colloidal stability, explaining the same order of stability to the 'bare' DNA-Au NPs (Figure 5.3a). The order of stability for the four 'bare' DNA-Au NPs was determined by ssDNA coating thickness, which was influenced by the coating properties (DNA strand length, sequence, and loading) and cations (preferential interaction with guanine base), as discussed in our previous work (Peng et al., 2022). The intermolecular attractions from the adsorbed AHA molecules led to the reduced colloidal stability (lower CCC values).

The adsorption of SRHA onto DNA-Au NPs was limited, largely due to the relatively weak π-π interactions between SRHA and ssDNA. Furthermore, the stabilization of DNA-Au NPs by adsorbed SRHA was only observed in high SRHA concentration (100 mg C/L) in $CaCl_2$ electrolyte but not in $MgCl_2$ electrolyte (Text S5.5 and Figure S5.12), suggesting that Ca^{2+} bridged the ssDNA with SRHA while Mg^{2+} did not, and the bridging effect was relatively weaker compared to that with AHA. As a result, the adsorption of SRHA did not completely shield the original ssDNA coating in all three electrolytes. The original ssDNA coating determined the particle stability, explaining the same order of colloidal stability of the four SRHA-adsorbed DNA-Au NPs as the 'bare' DNA-Au NPs (Figure 5.3). The limited intermolecular interaction of SRHA molecules and the extra steric repulsion provided by the adsorbed SRHA molecules collectively contributed to the minor increase of CCC values.

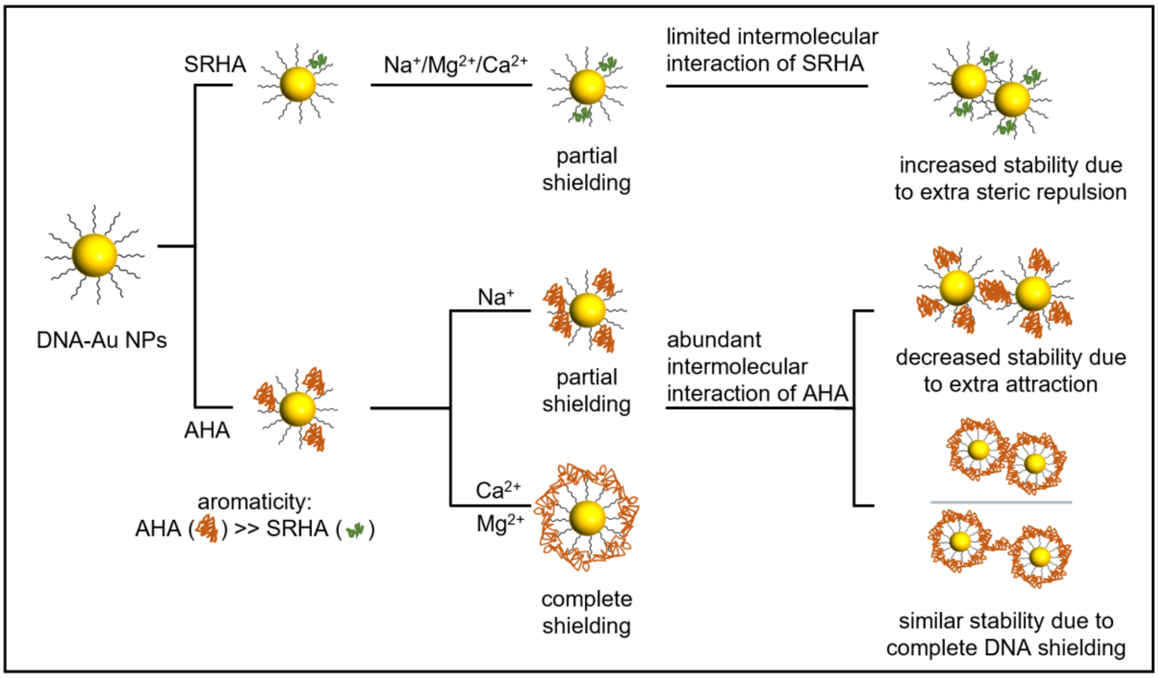

Figure 5.6 Schematic illustration of the interactions between SRHA/AHA and DNA-Au NPs, and the subsequent impact on the colloidal stability of DNA-Au NPs. The schematics are not drawn to scale and for illustrative purposes only.

5.3.4 Interaction of ssDNA with NOM in Real Water Samples

5.3.4.1 Interaction with the Real Water Organic Matter

Characteristics of the wastewater effluent and river water are summarized in Table S5.2. The high ionic strength of the wastewater effluent (conductivity = 13360 μS/cm, saline wastewater, a unique feature in Hong Kong due to seawater toilet flushing), especially high concentration of divalent cations (10 mM Mg^{2+} and 2.9 mM Ca^{2+}), induced the rapid aggregation of both DNA_{25}-Au and DNA_{25C}-Au in the 30-min kinetics study (Figure 5.7a-b; more details in Text S5.6). A slower aggregation of DNA_{25C}-Au was observed due to the guanine-rich sequence of DNA_{25C} (Peng et al., 2022). On the contrary, the stability of DNA_{25}-Au and DNA_{25C}-Au did not differ in the 21-day study (Figure 5.7c and S5.14a), with approximately 20% of the particles remaining in suspension after 21 days. This discrepancy in the 30-min/21-day studies was due to the varied overcoating of wastewater organic matter (WOM, TOC = 7.0 mg C/L) onto the DNA-Au NPs. The fluorescence analysis of WOM revealed their humic-like nature (a maximum fluorescence of peak C, Figure S5.15a) and slightly lower aromaticity than SRHA (Figure S5.15c) (Coble, 1996; Rodríguez et al., 2014). Different dosing of DNA-Au NPs in the 30-min (5 mg Au/L) and the 21-day (0.5 mg Au/L) studies resulted in different carbon-to-gold or carbon-to-DNA (mass) ratios (WOM:Au = 1.4 and 14, respectively; WOM:DNA = 140 and 1400, respectively), which impacted the amount of adsorbed WOM. The Raman spectra of WOM-adsorbed DNA-Au NPs confirmed that more WOM were adsorbed at higher WOM:Au ratio (Figure 5.7e). The peak of adenine (734 cm^{-1}) disappeared and WOM peaks became apparent (e.g., 942 and 1003 cm^{-1}) when WOM:Au ratio increased from 1.4 to 14. Nevertheless, the remaining peaks from nucleobases (1250–1500 cm^{-1}) at WOM:Au = 14 and the different spectra of WOM-adsorbed DNA-Au NPs and pure WOM (in contrast to the identical spectra of AHA-adsorbed DNA-Au NPs and pure AHA in Figure 5.4b) suggested that the complete shielding of ssDNA coating by WOM was unlikely. These observations are consistent with the humic nature of the WOM, which was more SRHA like. The similar long-term stability of DNA$_{25}$-Au and DNA$_{25C}$-Au in wastewater effluent was likely due to the large amount of WOM adsorbed that have weakened the role of DNA properties in controlling the colloidal stability of DNA-Au NPs.

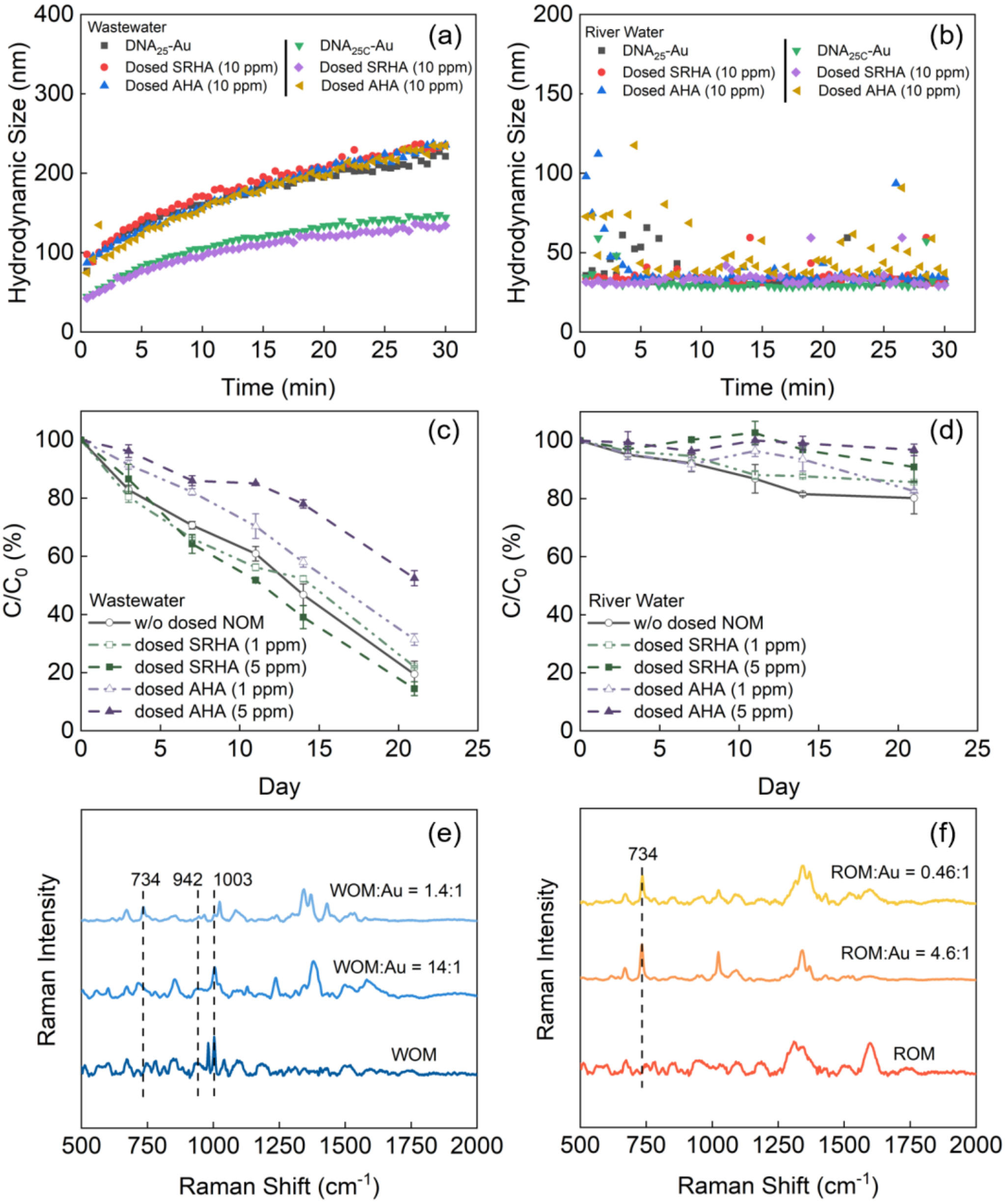

Figure 5.7 (a-b) Aggregation kinetics (30-min) of DNA$_{25}$-Au and DNA$_{25C}$-Au (C_0 = 5 mg Au/L) in filtered (a) wastewater effluent and (b) river water with or without dosed SRHA or AHA (10 mg C/L). (c-d) Long-term (21-day) stability of DNA$_{25}$-Au (C_0 = 0.5 mg Au/L) in (c) wastewater effluent and (d) river water with or without dosed SRHA or AHA (1 or 5 mg C/L). Error bars are standard deviation of duplicates. (e-f) Raman spectra of (e) WOM-adsorbed and (f) ROM-adsorbed DNA$_{25}$-Au.

The low ionic conditions of river water (divalent cations < 0.1 mM, conductivity = 43.5 μS/cm; Table S5.2) favored the suspension of DNA-Au NPs. Aggregation was not observed in the 30-min kinetics study (Figure 5.7b), and approximately 80% of the particles remained suspended after 21 days (Figure 5.7d and S5.14c), similar to their suspension in deionized water (Figure S5.16). The river water organic matter (ROM, TOC = 2.3 mg C/L) shared a similar humic nature as SRHA (Figure S5.15b-c). The lack of divalent cations in river water and low aromaticity of ROM suggested a weak interaction between the ROM and ssDNA coating, which was confirmed by the Raman spectra of ROM-adsorbed DNA-Au NPs, where the peak of adenine remained prominent (Figure 5.7f).

5.3.4.2 Impact of Dosed SRHA/AHA

Adding additional AHA into wastewater effluent or river water prolonged the suspension of DNA-Au NPs, and the effect of which was positively related to the dosing concentration of AHA (Figure 5.7c-d and Figure S5.14a and c). Such effect could be attributed to the high aromaticity of AHA compared to WOM and ROM, and the ssDNA coating preferentially adsorbed AHA molecules. The adsorption of AHA in wastewater effluent could occur via both divalent cation bridging and π-π interactions, while in river water it mainly occurred via π-π interaction.

Dosing of additional SRHA to wastewater effluent posed little impact on the colloidal stability of DNA-Au NPs (Figure 5.7c and S5.14b) mainly due to the low aromaticity of SRHA and the already high WOM:Au ratio (14.1). As a result, the adsorption of SRHA onto DNA-Au NPs was limited and cannot provide sufficient stabilization against the high ionic strength, particularly rich divalent cations (2.9 mM Ca^{2+} and 10 mM Mg^{2+}), of the wastewater effluent. In river water, dosing of additional SRHA at 5 mg C/L slightly enhanced the stability of DNA-Au NPs (e.g., 90% of DNA-Au NPs remained suspended after 21 days, Figure 5.7d and S5.14d), which was a result of the substantial increased carbon-to-Au ratio (from 4.6 to 14.6). The adsorption of either SRHA or ROM was very limited due to their low aromaticity and the lack of divalent cations in river water.

Overall, these results in the real water samples highlighted the preferential interaction of ssDNA with NOM with high aromaticity, consistent with the studies in simple electrolytes. For NOM with low aromaticity, divalent cation bridging (especially by Ca^{2+}) played an essential role in their enhanced adsorption onto ssDNA.

5.3.5 Implications for Practical Aquatic Applications of Engineered DNA Materials

As discussed in the Introduction, interactions between NOM and engineered DNA have been reported to cause either negative or negligible influence on the performance of DNA-based applications. The observed discrepancy in literatures could possibly be induced by the difference in the carbon-to-DNA ratio (instead of NOM concentration alone), NOM properties and the subsequent (differential) interactions of NOM and DNA, as demonstrated in our earlier results. For instance, in these studies that reported no significant influence from NOM, the carbon-to-DNA ratios were around 30 and the divalent cation concentrations were low (< 1 mM) (Akki et al., 2015; Park et al., 2022). These values are considerably lower than those with which we observed significant change of the colloidal stability of DNA-Au NPs (SRHA:DNA = 1000, 4 mM Ca^{2+}, Text S5.5). Most noteworthy, our study revealed that the highly aromatic NOM like AHA may have the determining role in the engineered DNA functionality in typical aquatic matrices. Other less aromatic SRHA-like NOM are not likely to make the function completely fail in typical natural water chemistries. These findings have important implications for designing pretreatment strategies for terrestrial samples that may contain highly aromatic NOM. Future studies can be conducted to establish such quantitative insights.

Furthermore, our findings facilitate the general designs of aptamers and hydrological tracers for environmental applications. For aptamers, NOM (with high aromaticity) could be incorporated into the aptamer selection process to produce aptamers with higher selectivity/binding affinity to targets, thereby improving the performance of aptasensor in real water samples. For DNA tracers, certain hydrological environments are not suitable for the use of encapsulated DNA tracers (e.g., in alluvial gravel aquifer (Pang et al., 2020)). However, adsorption of naked DNA tracers to NOM can lead to low recovery and unprecise detection (Liao et al., 2018; Pang et al., 2020). Therefore, by understanding the properties of NOM present in the field to be investigated (and other conditions such as Ca^{2+} concentrations), our work provides recommendations on whether naked DNA tracers could be directly used or certain protection to the tracers will be required.

5.4 Conclusions

Our study bridged the critical knowledge gap regarding the interactions between engineered short-chain ssDNA and a major natural matrix factor, i.e., NOM. The interactions between ssDNA and NOM mainly depended on the properties of NOM (i.e., carboxyl group and aromaticity), the presence of cations (i.e., valency and concentration), and the relative content of ssDNA and NOM in the system. The π-π interactions between the aromatic regions of NOM and the exposed nucleobases of ssDNA (AHA > SRHA/WOM/ROM) and the cation bridging effect ($Ca^{2+} > Mg^{2+}$, but not via Na^{+}) control whether the adsorbed NOM fully shield the ssDNA. With divalent cations present (specifically Ca^{2+}), even a small amount of NOM with high aromaticity (e.g., AHA) can fully shield ssDNA, whereas the extent of shielding by NOM with low aromaticity (e.g., SRHA, ROM, and WOM) depends on the relative content of ssDNA and NOM in the aquatic system and the occurrence of bridging. The extent of shielding by NOM has a major impact on the performance of engineered DNA applications, providing a partial answer to previously reported conflicting impacts of natural matrices on system performance. Overall, our findings provide new insights into the transformations of engineered ssDNA under environmentally relevant conditions, as well as implications for the rational design of engineered DNA-based environmental applications, such as selecting anti-interference aptamers and designing strategies for the protection of DNA tracers.

Acknowledgement

The authors acknowledge partial funding support from the Guangdong-Hong Kong-Macau Joint Laboratory for Environmental Pollution and Control (K-ZGBX) and Hong Kong Research Grants Council Theme-based Research Scheme (T21-711/16-R).

References

Abbt-Braun, G., Lankes, U. and Frimmel, F.H. 2004. Structural characterization of aquatic humic substances – The need for a multiple method approach. Aquat. Sci. 66(2), 151-170.

Akki, S.U. and Werth, C.J. 2018. Critical review: DNA aptasensors, are they ready for monitoring organic pollutants in natural and treated water sources? Environ. Sci. Technol. 52(16), 8989-9007.

Akki, S.U., Werth, C.J. and Silverman, S.K. 2015. Selective aptamers for detection of estradiol and ethynylestradiol in natural waters. Environ. Sci. Technol. 49(16), 9905-9913.

Alex, S. and Dupuis, P. 1989. FT-IR and Raman investigation of cadmium binding by DNA. Inorg. Chim. Acta 157(2), 271-281.

Chen, K.L. and Elimelech, M. 2007. Influence of humic acid on the aggregation kinetics of fullerene (C60) nanoparticles in monovalent and divalent electrolyte solutions. J. Colloid Interface Sci. 309(1), 126-134.

Chin, Y.-P., Aiken, G. and O'Loughlin, E. 1994. Molecular weight, polydispersity, and spectroscopic properties of aquatic humic substances. Environ. Sci. Technol. 28(11), 1853-1858.

Coble, P.G. 1996. Characterization of marine and terrestrial DOM in seawater using excitation-emission matrix spectroscopy. Mar. Chem. 51(4), 325-346.

Fan, L., Zhao, G., Shi, H., Liu, M., Wang, Y. and Ke, H. 2014. A femtomolar level and highly selective 17β-estradiol photoelectrochemical aptasensor applied in environmental water samples analysis. Environ. Sci. Technol. 48(10), 5754-5761.

Ghosh, S., Mashayekhi, H., Pan, B., Bhowmik, P. and Xing, B. 2008. Colloidal behavior of aluminum oxide nanoparticles as affected by pH and natural organic matter. Langmuir 24(21), 12385-12391.

Grasso, D., Chin, Y.-P. and Weber, W.J. 1990. Structural and behavioral characteristics of a commercial humic acid and natural dissolved aquatic organic matter. Chemosphere 21(10), 1181-1197.

He, S., Song, B., Li, D., Zhu, C., Qi, W., Wen, Y., Wang, L., Song, S., Fang, H. and Fan, C. 2010. A graphene nanoprobe for rapid, sensitive, and multicolor fluorescent DNA analysis. Adv. Funct. Mater. 20(3), 453-459.

Hong, S. and Elimelech, M. 1997. Chemical and physical aspects of natural organic matter (NOM) fouling of nanofiltration membranes. J. Membr. Sci. 132(2), 159-181.

Hu, X., Mu, L., Zhou, Q., Wen, J. and Pawliszyn, J. 2011. ssDNA aptamer-based column for simultaneous removal of nanogram per liter level of illicit and analgesic pharmaceuticals in drinking water. Environ. Sci. Technol. 45(11), 4890-4895.

Huangfu, X., Jiang, J., Ma, J., Liu, Y. and Yang, J. 2013. Aggregation kinetics of manganese dioxide colloids in aqueous solution: influence of humic substances and biomacromolecules. Environ. Sci. Technol. 47(18), 10285-10292.

Hur, J. and Schlautman, M.A. 2003. Molecular weight fractionation of humic substances by adsorption onto minerals. J. Colloid Interface Sci. 264(2), 313-321.

Huynh, K.A. and Chen, K.L. 2011. Aggregation kinetics of citrate and polyvinylpyrrolidone coated silver nanoparticles in monovalent and divalent electrolyte solutions. Environ. Sci. Technol. 45(13), 5564-5571.

Jiang, Y., Raliya, R., Liao, P., Biswas, P. and Fortner, J.D. 2017. Graphene oxides in water: assessing stability as a function of material and natural organic matter properties. Environ. Sci.: Nano 4(7), 1484-1493.

Kim, H.C., Yu, M.J. and Han, I. 2006. Multi-method study of the characteristic chemical nature of aquatic humic substances isolated from the Han River, Korea. Appl. Geochem. 21(7), 1226-1239.

Kim, M., Um, H.J., Bang, S., Lee, S.H., Oh, S.J., Han, J.H., Kim, K.W., Min, J. and Kim, Y.H. 2009. Arsenic removal from Vietnamese groundwater using the arsenic-binding DNA aptamer. Environ. Sci. Technol. 43(24), 9335-9340.

Korshin, G., Chow, C.W.K., Fabris, R. and Drikas, M. 2009. Absorbance spectroscopy-based examination of effects of coagulation on the reactivity of fractions of natural organic matter with varying apparent molecular weights. Water Res. 43(6), 1541-1548.

Labille, J., Thomas, F., Milas, M. and Vanhaverbeke, C. 2005. Flocculation of colloidal clay by bacterial polysaccharides: effect of macromolecule charge and structure. J. Colloid Interface Sci. 284(1), 149-156.

Liao, R., Yang, P., Wu, W., Luo, D. and Yang, D. 2018. A DNA tracer system for hydrological environment investigations. Environ. Sci. Technol. 52(4), 1695-1703.

Liu, B. and Liu, J. 2017. Methods for preparing DNA-functionalized gold nanoparticles, a key reagent of bioanalytical chemistry. Anal. Methods 9(18), 2633-2643.

Liu, B., Zhao, Y., Jia, Y. and Liu, J. 2020. Heating drives DNA to hydrophobic regions while freezing drives DNA to hydrophilic regions of graphene oxide for highly robust biosensors. J. Am. Chem. Soc. 142(34), 14702-14709.

Liu, X., Wazne, M., Chou, T., Xiao, R. and Xu, S. 2011. Influence of Ca2+ and Suwannee River Humic Acid on aggregation of silicon nanoparticles in aqueous media. Water Res. 45(1), 105-112.

Loosli, F., Le Coustumer, P. and Stoll, S. 2013. TiO2 nanoparticles aggregation and disaggregation in presence of alginate and Suwannee River humic acids. pH and concentration effects on nanoparticle stability. Water Res. 47(16), 6052-6063.

Lu, N., Mylon, S.E., Kong, R., Bhargava, R., Zilles, J.L. and Nguyen, T.H. 2012. Interactions between dissolved natural organic matter and adsorbed DNA and their effect on natural transformation of Azotobacter vinelandii. Sci. Total Environ. 426, 430-435.

Mirkin, C.A., Letsinger, R.L., Mucic, R.C. and Storhoff, J.J. 1996. A DNA-based method for rationally assembling nanoparticles into macroscopic materials. Nature 382, 607-609.

Nason, J.A., McDowell, S.A. and Callahan, T.W. 2012. Effects of natural organic matter type and concentration on the aggregation of citrate-stabilized gold nanoparticles. J. Environ. Monit. 14(7), 1885-1892.

Nguyen, T.H. and Chen, K.L. 2007. Role of divalent cations in plasmid DNA adsorption to natural organic matter-coated silica surface. Environ. Sci. Technol. 41(15), 5370-5375.

Nguyen, T.H. and Elimelech, M. 2007. Adsorption of plasmid DNA to a natural organic matter-coated silica surface: kinetics, conformation, and reversibility. Langmuir 23(6), 3273-3279.

Ogram, A.V., Mathot, M.L., Harsh, J.B., Boyle, J. and Pettigrew, C.A. 1994. Effects of DNA polymer length on its adsorption to soils. Appl. Environ. Microbiol. 60(2), 393-396.

Otto, C., van den Tweel, T.J.J., de Mul, F.F.M. and Greve, J. 1986. Surface-enhanced Raman spectroscopy of DNA bases. J. Raman Spectrosc. 17(3), 289-298.

Pang, L., Abeysekera, G., Hanning, K., Premaratne, A., Robson, B., Abraham, P., Sutton, R., Hanson, C., Hadfield, J., Heiligenthal, L., Stone, D., McBeth, K. and Billington, C. 2020. Water tracking in surface water, groundwater and soils using free and alginate-chitosan encapsulated synthetic DNA tracers. Water Res. 184, 116192.

Park, J., Yang, K.A., Choi, Y. and Choe, J.K. 2022. Novel ssDNA aptamer-based fluorescence sensor for perfluorooctanoic acid detection in water. Environ. Int. 158, 107000.

Park, J.S., Na, H.K., Min, D.H. and Kim, D.E. 2013. Desorption of single-stranded nucleic acids from graphene oxide by disruption of hydrogen bonding. Analyst 138(6), 1745-1749.

Peng, B., Liu, Z. and Jiang, Y. 2022. Aggregation of DNA-grafted nanoparticles in water: the critical role of sequence-dependent conformation of DNA coating. J. Phys. Chem. B 126(4), 847-857.

Philippe, A. and Schaumann, G.E. 2014. Interactions of Dissolved Organic Matter with Natural and Engineered Inorganic Colloids: A Review. Environ. Sci. Technol. 48(16), 8946-8962.

Qin, C., Zhang, W., Yang, B., Chen, X., Xia, K. and Gao, Y. 2018. DNA facilitates the sorption of polycyclic aromatic hydrocarbons on montmorillonites. Environ. Sci. Technol. 52(5), 2694-2703.

Qing, Z., Zhu, L., Li, X., Yang, S., Zou, Z., Guo, J., Cao, Z. and Yang, R. 2017. A target-lighted dsDNA-indicator for high-performance monitoring of mercury pollution and its antagonists screening. Environ. Sci. Technol. 51(20), 11884-11890.

Rodríguez, F.J., Schlenger, P. and García-Valverde, M. 2014. A comprehensive structural evaluation of humic substances using several fluorescence techniques before and after ozonation. Part I: Structural characterization of humic substances. Sci. Total Environ. 476-477, 718-730.

Schmid, M., Prinz, T.K., Stäbler, A. and Sängerlaub, S. 2017. Effect of sodium sulfite, sodium dodecyl sulfate, and urea on the molecular interactions and properties of whey protein isolate-based films. Front. Chem. 4, 49.

Schwyzer, I., Kaegi, R., Sigg, L. and Nowack, B. 2013. Colloidal stability of suspended and agglomerate structures of settled carbon nanotubes in different aqueous matrices. Water Res. 47(12), 3910-3920.

Sierra, M.M.D., Giovanela, M., Parlanti, E. and Soriano-Sierra, E.J. 2005. Fluorescence fingerprint of fulvic and humic acids from varied origins as viewed by single-scan and excitation/emission matrix techniques. Chemosphere 58(6), 715-733.

Stankus, D.P., Lohse, S.E., Hutchison, J.E. and Nason, J.A. 2011. Interactions between natural organic matter and gold nanoparticles stabilized with different organic capping agents. Environ. Sci. Technol. 45(8), 3238-3244.

Storhoff, J.J., Lazarides, A.A., Mucic, R.C., Mirkin, C.A., Letsinger, R.L. and Schatz, G.C. 2000. What controls the optical properties of DNA-linked gold nanoparticle assemblies? J. Am. Chem. Soc. 122(19), 4640-4650.

Tsuboi, M. 1970. Application of infrared spectroscopy to structure studies of nucleic acids. Appl. Spectrosc. Rev. 3(1), 45-90.

Vogiazi, V., de la Cruz, A.A., Varughese, E.A., Heineman, W.R., White, R.J. and Dionysiou, D.D. 2021. Sensitive electrochemical detection of microcystin-LR in water samples Via target-induced displacement of aptamer associated $[Ru(NH_3)_6]^{3+}$. ACS ES&T Eng. 1(11), 1597-1605.

Yan, J., Huang, Y., Zhang, C., Fang, Z., Bai, W., Yan, M., Zhu, C. and Chen, A. 2017. Aptamer based photometric assay for the antibiotic sulfadimethoxine based on the inhibition and reactivation of the peroxidase-like activity of gold nanoparticles. Microchimica Acta 184(1), 59-63.

Yu, X., Chen, F., Wang, R. and Li, Y. 2018. Whole-bacterium SELEX of DNA aptamers for rapid detection of E.coli O157:H7 using a QCM sensor. J. Biotechnol. 266, 39-49.

Zhou, J., Battig, M.R. and Wang, Y. 2010. Aptamer-based molecular recognition for biosensor development. Anal. Bioanal. Chem. 398(6), 2471-2480.

Appendix C: Supporting Information for Chapter 5

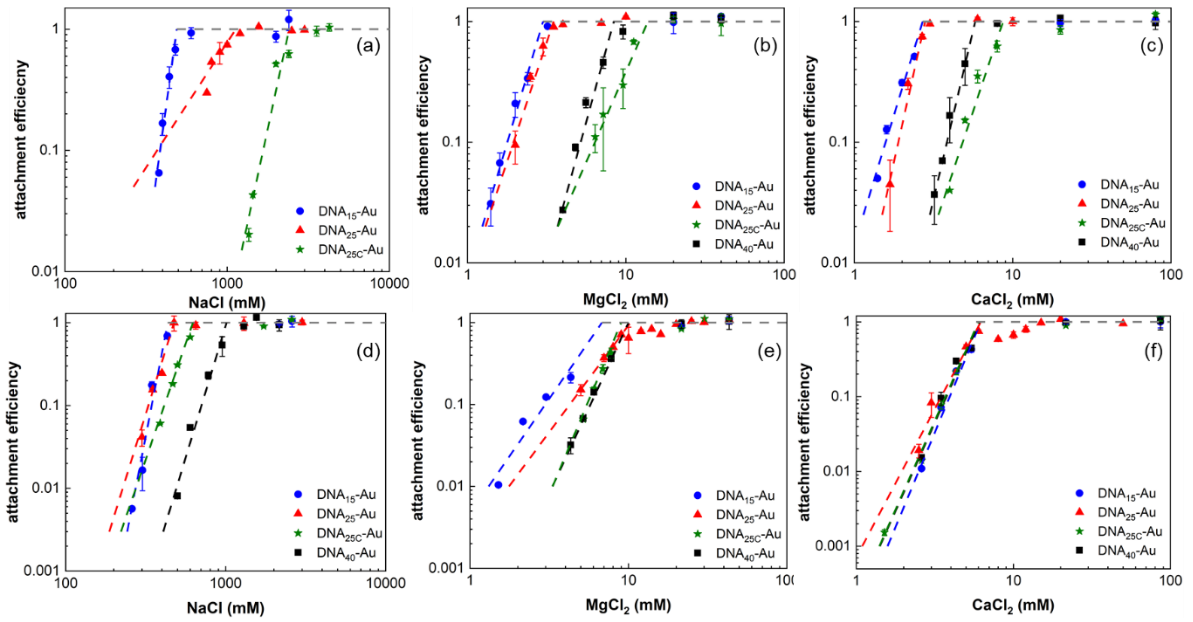

Figure S5.1 Attachment efficiencies (α) of DNA-Au NPs (10 mg Au/L) in the presence of 2.7 mg C/L SRHA (a-c) or AHA (d-f) as functions of (a and d) NaCl, (b and e) $MgCl_2$, and (c and f) $CaCl_2$ concentrations. The critical coagulation concentration (CCC) values were calculated as the intersection of extrapolations through reaction-limited and diffusion-limited aggregation regimes.

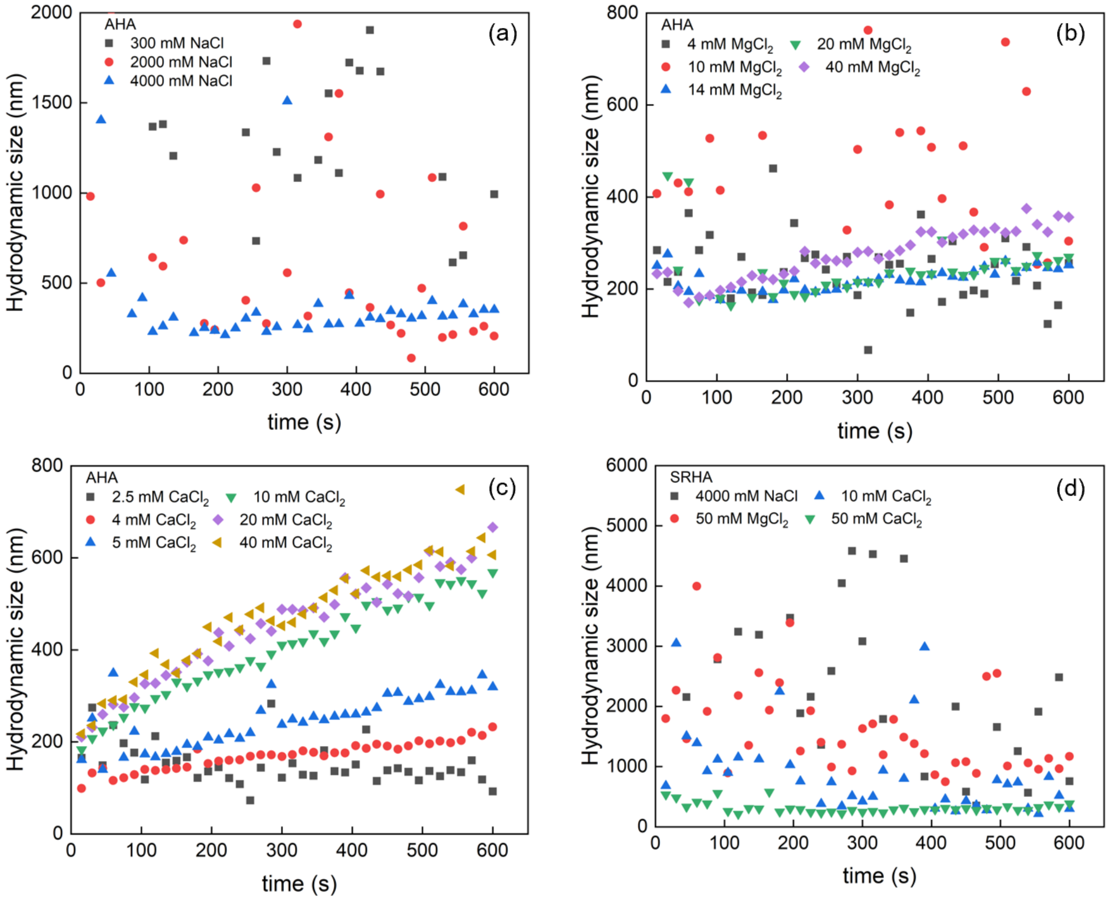

Figure S5.2 (a-c) Aggregation profile of pure AHA (2.7 mg C/L) in (a) NaCl; (b) $MgCl_2$; (c) $CaCl_2$. (d) Aggregation profile of pure SRHA (10 mg C/L) in three salts. Because the SRHA molecules at 2.7 mg/L could not scatter sufficient light for DLS analysis, higher concentration (10 mg C/L) was used.

Text S5.1 Sample Preparation for FTIR, Raman, Fluorescence Spectroscopy and TEM Characterization

To probe the interactions between the ssDNA and NOM (SRHA/AHA/ROM/WOM), the Raman and FTIR spectra of NOM-adsorbed DNA-coated gold nanoparticles (DNA-Au NPs) were recorded. For SRHA and AHA, DNA_{25}-Au (25 mg Au/L) were incubated with SRHA or AHA (2.5 mg C/L or 25 mg C/L, corresponding to TOC:Au = 1:10 or 1:1, respectively) in 0.5 mM $CaCl_2$ or 50 mM NaCl for 48 hr to allow the adsorption to reach equilibrium. Then the suspension was centrifuged at 10,000 g for 15 mins and the supernatant was discarded to remove unadsorbed NOM. Electrolyte solution (0.5 mM $CaCl_2$ or 50 mM NaCl) was used to redisperse the particles. The suspension was centrifuged again, and the supernatant was discarded. The particles were redispersed in DI water. KBr was then added, and the mixture was freeze-dried and homogenized, then pressed into a pellet for Raman and FTIR analyses. For ROM and WOM, DNA_{25}-Au (0.5 or 5 mg Au/L) was suspended in river water and wastewater effluent for 24 hr to allow the adsorption. The suspensions were centrifuged and washed with deionized water to obtain ROM/WOM-adsorbed DNA-Au NPs. KBr was added into the washed suspensions and the mixtures were freeze-dried and pressed into a pellet for analysis.

TEM (transmission electron microscopy) images of aggregated DNA_{25}-Au NPs with or without the presence of NOM and salts were collected on a transmission electron microscope (JEOL JEM-2010). DNA_{25}-Au NPs (10 mg Au/L) were first mixed with NOM (2.7 or 10 mg C/L of SRHA or AHA). Then salts ($CaCl_2$, $MgCl_2$, or NaCl) were added to reach a concentration of 10 mM Ca^{2+}/Mg^{2+} or 1000 mM Na^+ to induce the aggregation of DNA-Au NPs, and the mixture was immediately dripped onto a TEM grid. The drip was allowed to stay on the grid for 15 mins and the excess liquid was gently removed by Kimwipe tissues.

Fluorescence excitation emission matrix (EEM) and emission scan (at fixed excitation wavelength, 330 nm) spectra of SRHA or AHA (2.7 mg C/L) with or without the presence of DNA_{25}-Au NPs (10 mg Au/L) were performed in three electrolytes (50 mM NaCl, 0.5 mM $MgCl_2$, or 0.5 mM $CaCl_2$). The mixtures were left in dark for 24 hr for the adsorption of SRHA/AHA to reach equilibrium. For EEM scans, the fluorescence intensity was measured at excitation wavelengths from 200 nm to 450 nm at 5 nm increments and at emission wavelengths from 250 nm to 600 nm at 2 nm increments. Excitation and emission slit width were 3 nm. For emission scan (380 nm to 600 nm), excitation wavelength was fixed at 330 nm. All spectra were processed by subtracting the fluorescence intensity of deionized water at corresponding wavelengths.

Text S5.2 Electrophoretic Mobility of DNA-Au NPs in the Presence of NOM

Similar changes of electrophoretic mobility (EPM) were observed for four DNA-Au NPs in salts (NaCl, $MgCl_2$, and $CaCl_2$) (Peng et al., 2022). Here DNA_{25}-Au and DNA_{25C}-Au were used to probe their EPM in the presence of SRHA/AHA and three salts (Figure S5-3). Overall, DNA_{25}-Au and DNA_{25C}-Au had similar EPM behavior with the presence of NOM in different salts. In NaCl, the presence of SRHA decreased the absolute surface charge of DNA-Au NPs (less negative) while AHA maintained similar surface charge compared to the case without NOM present (Figure S5-3a). For example, the EPM of DNA_{25C}-Au in 100 mM NaCl was -1.87 μm•cm/Vs without NOM, -1.07 μm•cm/Vs with SRHA, and -1.56 μm•cm/Vs with AHA, respectively. In divalent salts ($MgCl_2$/$CaCl_2$, Figure S5-3b-c), the EPMs of DNA-Au NPs were observed to be independent of the NOM (with or without SRHA/AHA), DNA coating (DNA_{25} or DNA_{25C}), and cations (Ca^{2+} or Mg^{2+}). The EPMs increased to around -1 μm•cm/Vs for all scenarios, i.e., 1 or 5 mM $MgCl_2$/$CaCl_2$, with or without SRHA/AHA.

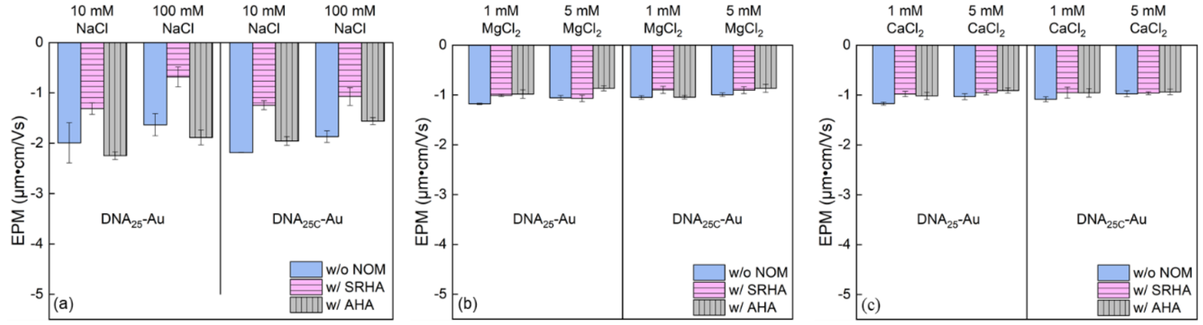

Figure S5.3 Electrophoretic mobility (EPM) of DNA$_{25}$-Au and DNA$_{25C}$-Au (10 mg Au/L) with or without the presence of SRHA or AHA (2.7 mg C/L) in (a) NaCl; (b) MgCl$_2$; (c) CaCl$_2$.

Text S5.3 Fluorescence Spectroscopic Analysis of NOM Molecules with or without the Presence of DNA-Au NPs

Figure S5.4 and S5.5 show the excitation emission matrix (EEM) spectra of NOM (SRHA or AHA, 2.7 mg C/L) with or without the presence of DNA$_{25}$-Au (10 mg Au/L) and/or salts (50 mM NaCl, 0.5 mM MgCl$_2$ or CaCl$_2$). Overall, the presence of DNA-Au NPs and/or salts did not change the peak location of the NOM (excitation maximum at 330 nm, emission maximum in the range of 450-550 nm), but fluorescence intensity. The presence of DNA-Au NPs lowered the fluorescence intensity of NOM (Figure S5.4a and e and Figure S5.5a and e), which could be attributed to the adsorption of NOM onto the DNA-Au NPs and subsequent fluorescence quenching by Au nanoparticles (Liu and Liu, 2017). On the other hand, the presence of salts (without DNA-Au present) slightly increased the fluorescence intensity of SRHA (Figure S5.4b-d) but decreased that of AHA (Figure S5.5b-d), especially in the presence of Ca^{2+}. The decreased fluorescence intensity of AHA could be induced by the self-quenching in larger aggregates (Sharpless and McGown, 1999), consistent with the observed aggregation of AHA molecules in divalent salts (Figure S5.2b-c). Figure S5.6 shows the emission spectra of NOM at excitation wavelength of 330 nm. When salt was not added, we observed a stronger quenching of the AHA fluorescence by Au NPs than that of SRHA fluorescence. For example, by calculating the intensity change at emission maximum (460 nm for SRHA and 520 nm for AHA), the intensity of SRHA was reduced by 8% while the intensity of AHA was reduced by 24%. Overall, as salt (NaCl/$MgCl_2$/$CaCl_2$) were introduced, the intensity of AHA further decreased, especially for $CaCl_2$ (Figure S5.6b). Such decreased intensity of AHA indicated the enhanced adsorption of AHA onto DNA-Au NPs. On the other hand, the intensity of SRHA with the presence of both DNA-Au NPs and salts barely changed (Figure S5.6a).

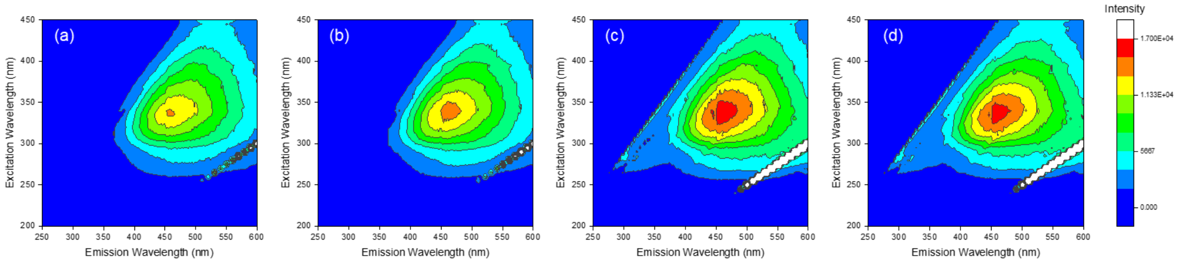

SRHA SRHA + Ca SRHA + Mg SRHA+ Na

Au + SRHA Au + SRHA + Ca Au + SRHA + Mg Au + SRHA+ Na

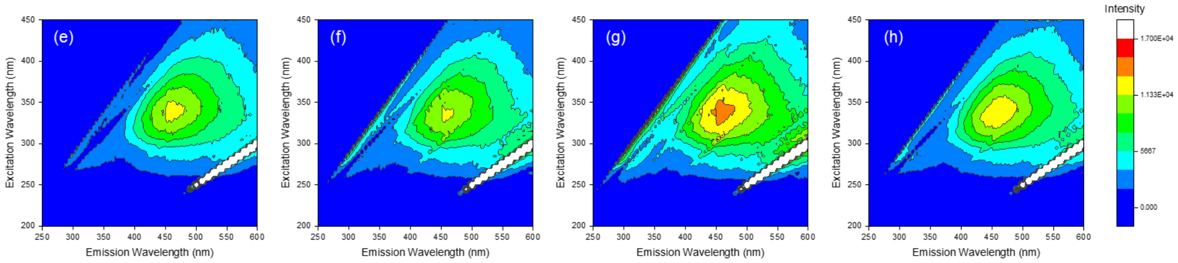

Figure S5.4 Fluorescence excitation emission matrix (EEM) of SRHA (2.7 mg C/L) with or without the presence of DNA_{25}-Au NPs (10 mg Au/L) and/or salts (50 mM NaCl, 0.5 mM $MgCl_2$, or 0.5 mM $CaCl_2$).

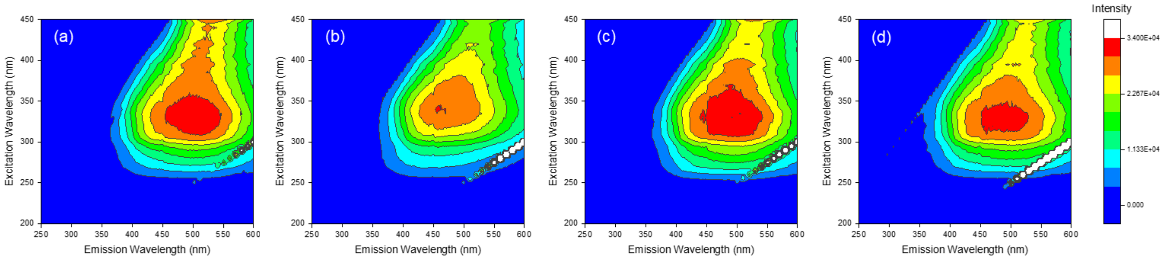

AHA
Au + AHA

AHA + Ca
Au + AHA + Ca

AHA + Mg
Au + AHA + Mg

AHA+ Na
Au + AHA+ Na

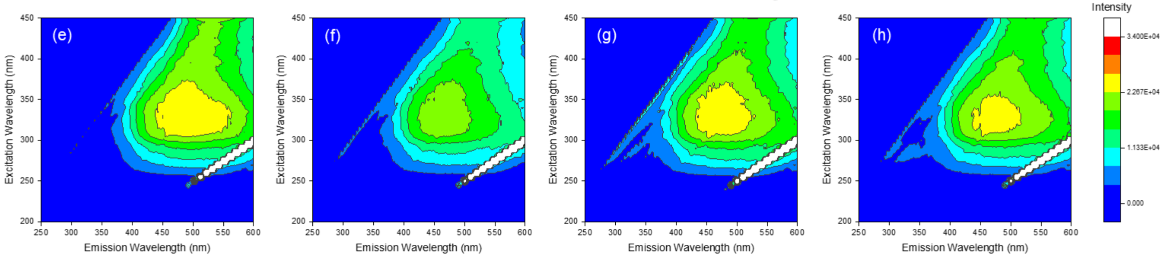

Figure S5.5 Fluorescence excitation emission matrix (EEM) of AHA (2.7 mg C/L) with or without the presence of DNA_{25}-Au NPs (10 mg Au/L) and/or salts (50 mM NaCl, 0.5 mM $MgCl_2$, or 0.5 mM $CaCl_2$).

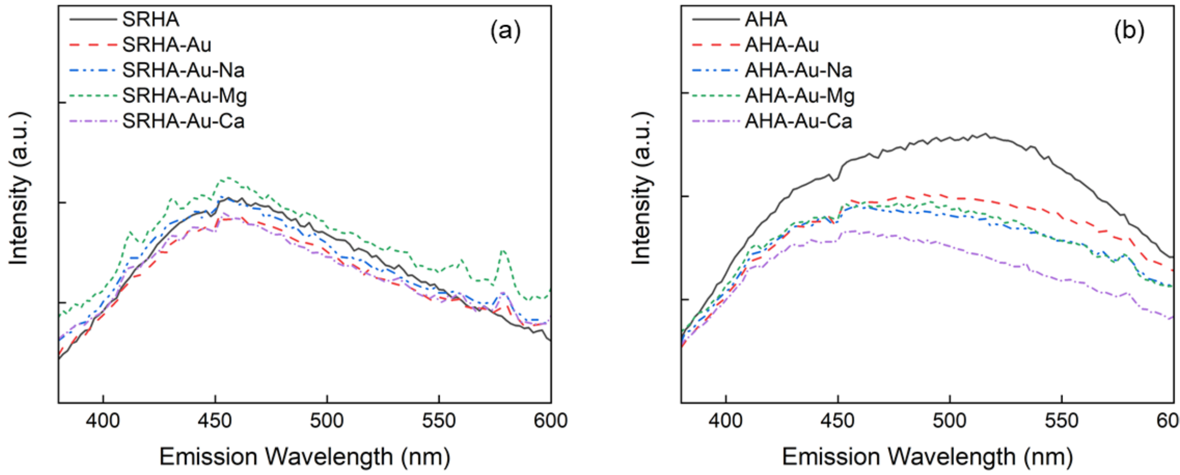

Figure S5.6 Emission scan spectra (excitation wavelength = 330 nm) of (a) SRHA and (b) AHA (2.7 mg C/L) with or without the presence of DNA_{25}-Au NPs (10 mg Au/L) and salts (50 mM NaCl, 0.5 mM $MgCl_2$, or 0.5 mM $CaCl_2$).

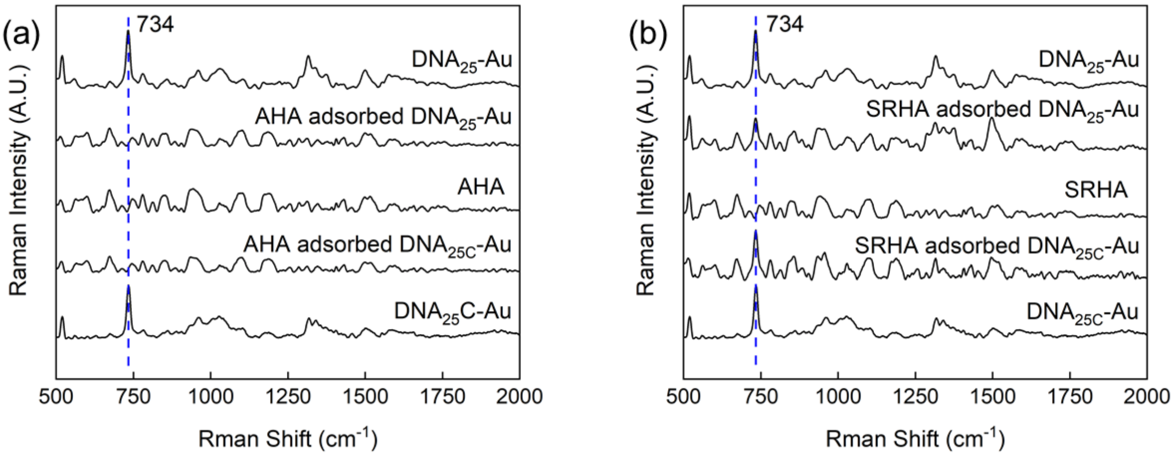

Figure S5.7 Raman spectra of (a) AHA- and (b) SRHA-adsorbed DNA$_{25}$-Au and DNA$_{25C}$-Au in 0.5 mM $CaCl_2$ at NOM:Au = 1:10.

Text S5.4 Distinguishable Colors of the Aggregates of DNA-Au NPs with NOM Present

Au NPs have distance-dependent optical properties, where the color of well dispersed Au NPs (with a diameter around 20 nm) is red (Figure S5.8a), and the color of aggregated Au NPs turns to purple due to shortened interparticle distance (Storhoff et al., 2000). When studying the aggregation kinetics (Section 5.3.2), we observed distinguishable colors of the aggregates. In the presence of SRHA, the aggregated DNA-Au NPs settled to the cuvette bottom and formed a bluish-purple layer while the supernatant was clear (Figure S5.8b). After a mild sonication (30 s), the aggregates were resuspended, but the suspension remained bluish-purple (Figure S5.8c). Similar color change was observed for the aggregated DNA-Au NPs without NOM present (photos not shown), suggesting a similar aggregation mechanism between these two scenarios. However, when AHA was present, the precipitates turned reddish-purple (Figure S5.8d), and the redispersed suspensions had a reddish-purple color (Figure S5.8e). The color was easily distinguishable from that of the redispersed suspension with SRHA present and without NOM present, especially in the $CaCl_2$ electrolyte. This difference suggested distinct aggregation mechanisms of DNA-Au NPs with AHA present. Interestingly, the color of the redispersed suspensions with AHA present also showed a dependency on the presence of cations. From Na^+, Mg^{2+}, to Ca^{2+}, the color of the suspensions gradually transitioned from purple to magenta, suggesting that the interparticle distance of aggregated DNA-Au NPs increased accordingly.

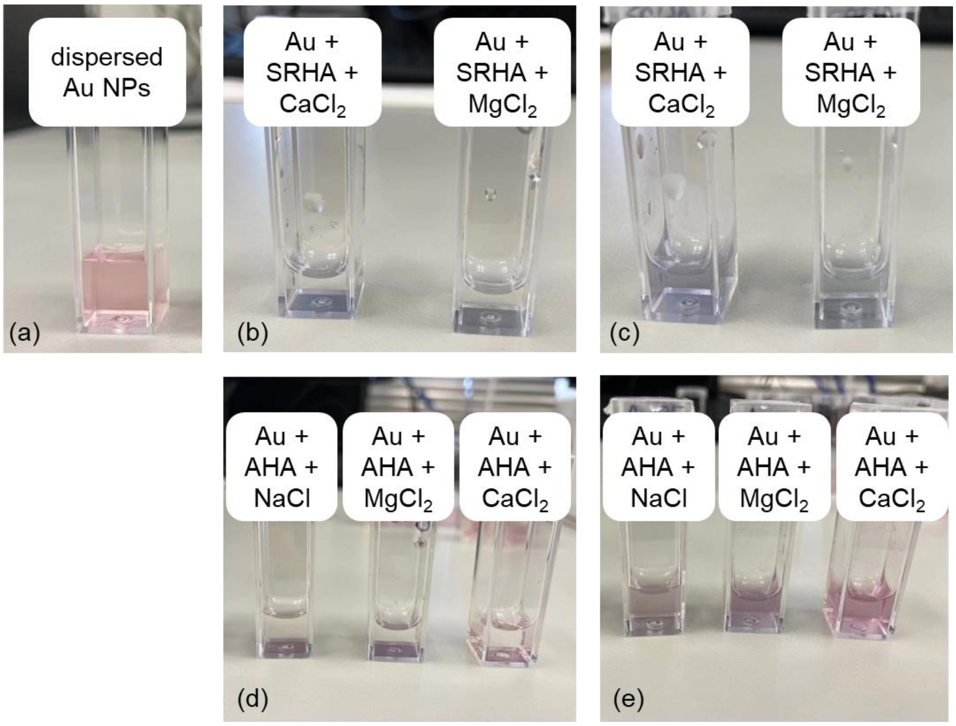

Figure S5.8 Photos of DNA_{25}-Au suspensions. (a) Well dispersed DNA_{25}-Au (10 mg Au/L) in DI water; (b) in the presence of SRHA (2.7 mg C/L), aggregated DNA_{25}-Au settled and formed a bluish-purple layer at the bottom; (c) samples from (b) after water-bath sonication, suspensions were bluish-purple. (d) In the presence of AHA (2.7 mg C/L), aggregated DNA_{25}-Au settled and formed a reddish-purple layer at the bottom, easily distinguishable from (b); (e) samples from (d) after water-bath sonication, suspensions were more reddish, especially in $CaCl_2$.

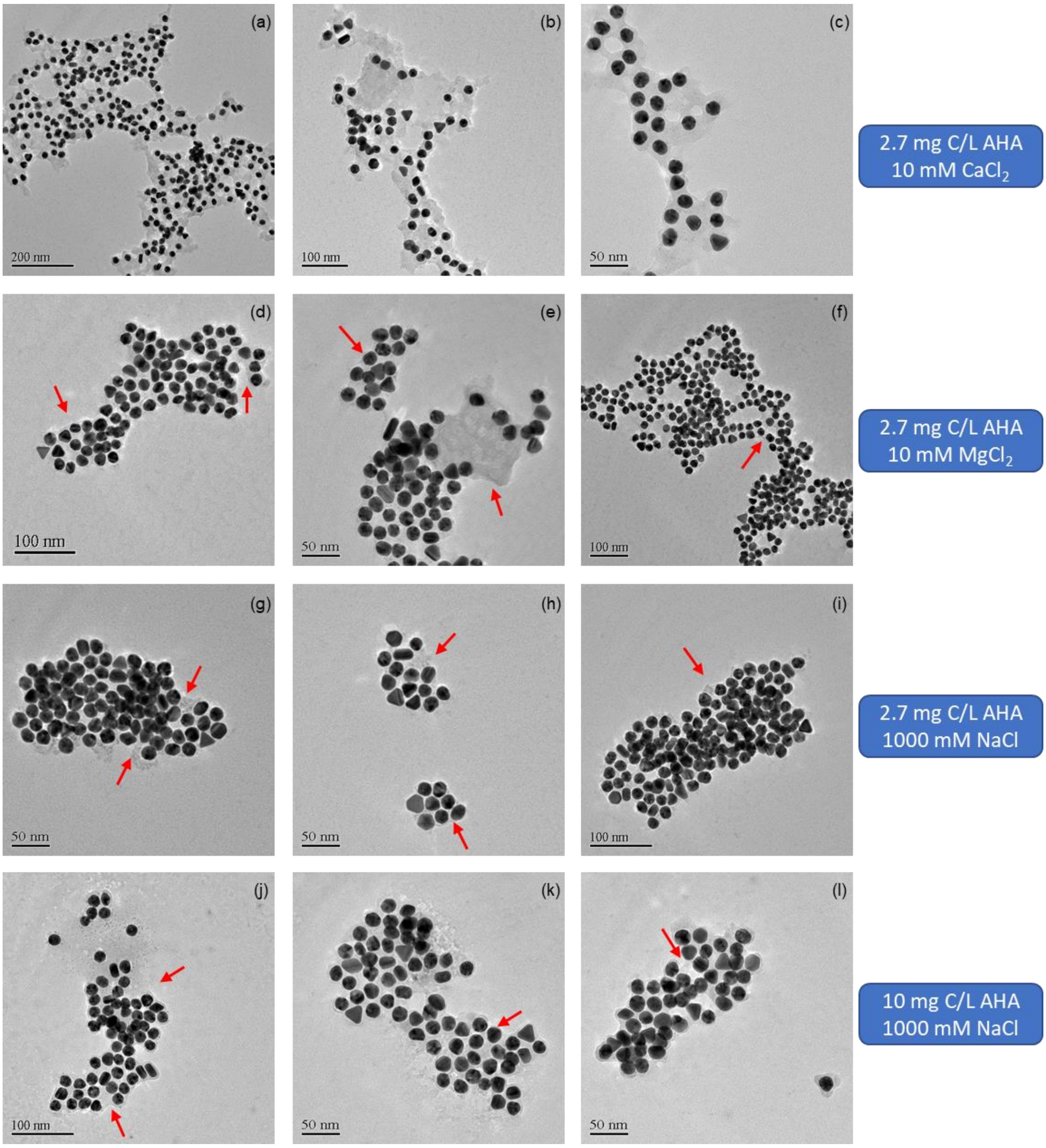

Figure S5.9 TEM images of aggregated DNA$_{25}$-Au (a-i) with AHA (2.7 mg C/L) in (a-c) 10 mM CaCl$_2$, (d-f) 10 mM MgCl$_2$, (g-i) 1000 mM NaCl; and (j-l) with AHA (10 mg C/L) in 1000 mM NaCl. Red arrows indicate light shadowy areas due to the intermolecular interactions of AHA molecules.

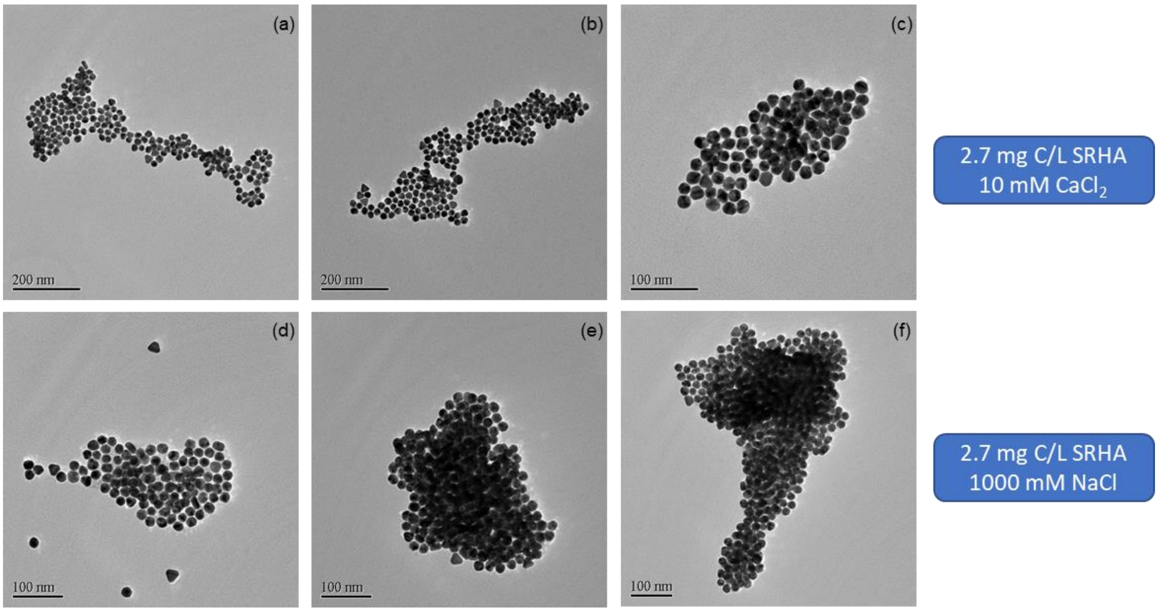

Figure S5.10 TEM images of aggregated DNA25-Au with SRHA present (2.7 mg C/L) in (a-c) 10 mM $CaCl_2$, (d-f) 1000 mM NaCl.

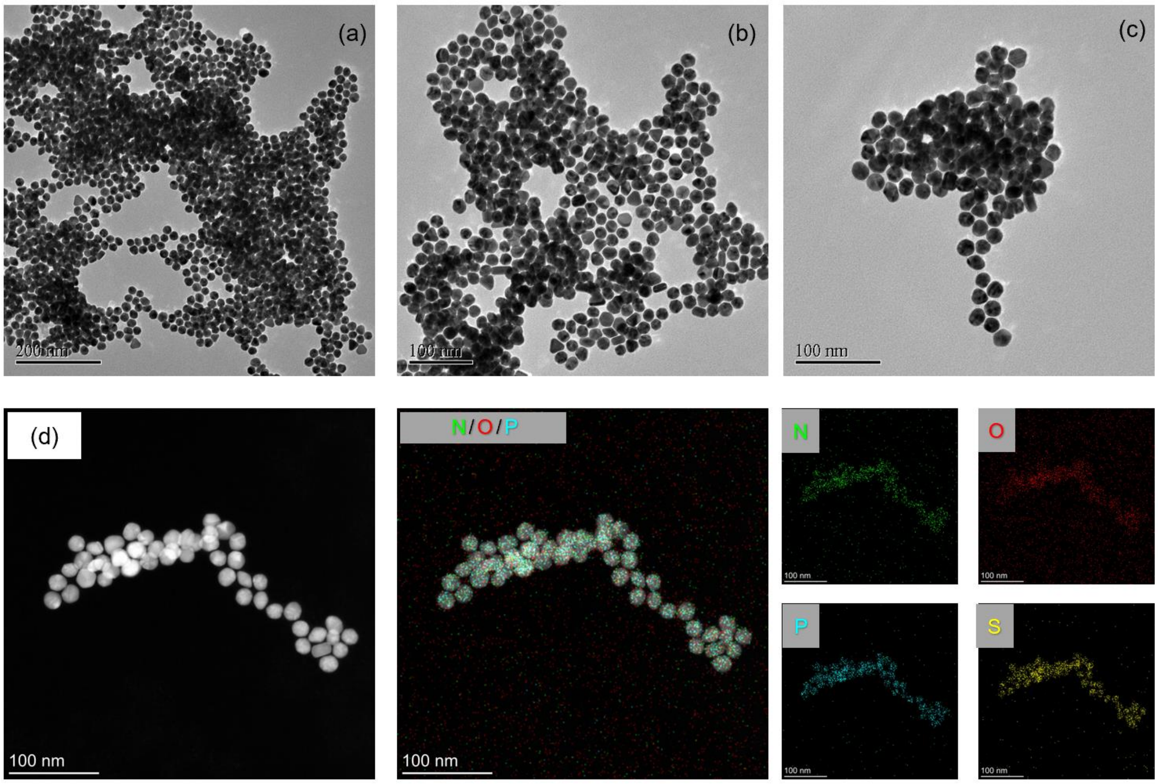

Figure 5.11 (a-c) TEM images of aggregated DNA25-Au NPs (10 mg/L) without NOM present in 10 mM $CaCl_2$. (d) HAADF-STEM image and the corresponding EDS elemental mapping images of aggregated particles in 10 mM $CaCl_2$.

Text S5.5 Impact of the Concentrations of Divalent Cation and NOM on the Aggregation Behavior of DNA-Au NPs

The aggregation kinetics of DNA$_{25}$-Au (10 mg Au/L) in fixed salt concentration (4 or 20 mM $MgCl_2$, 4 mM $CaCl_2$) as a function of NOM concentration (SRHA or AHA, 0-100 mg C/L) were investigated by TR-DLS. Aggregation rates were determined as the slope of a linear fitting across data points until the hydrodynamic size was larger than 1.3× the initial size. Results are presented in Figure S5.12 and S5.13. Overall, the interaction of the DNA coating with AHA was stronger than with SRHA, consistent with the results from Raman and Fluorescence spectroscopy measurements. Enhanced particle aggregation was observed with the presence of AHA only, but not SRHA.

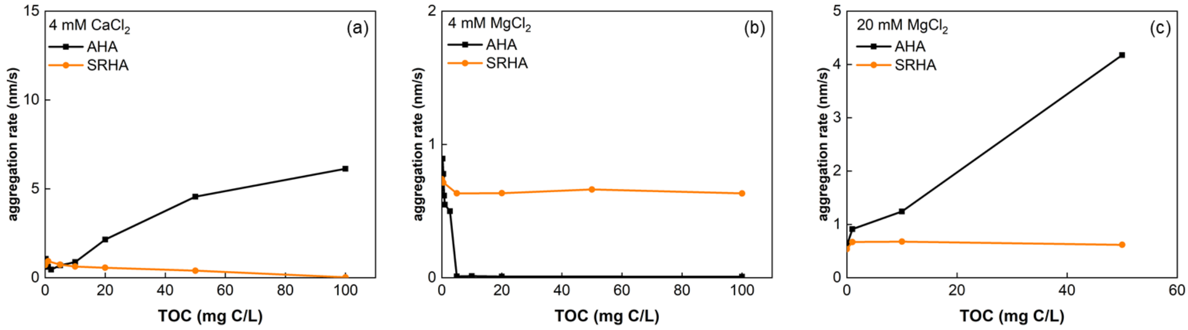

Figure S5.12 Aggregation rates of DNA$_{25}$-Au (10 mg Au/L) as a function of SRHA/AHA concentration in (a) 4 mM $CaCl_2$; (b) 4 mM $MgCl_2$; (c) 20 mM $MgCl_2$.

In 4 mM $CaCl_2$, the presence of 2 mg C/L AHA stabilized DNA-Au NPs (Figure S5.12a). However, at higher AHA concentrations (10 – 100 mg C/L), the aggregation of DNA-Au NPs was enhanced, because the Ca^{2+} induced intermolecular bridging of AHA molecules (both adsorbed and unadsorbed) (Chen and Elimelech, 2007; Liu et al., 2011; Liu et al., 2010; Schwyzer et al., 2013). The color of the aggregate suspension transitioned from purple to red as more AHA were present (Figure S5.13b-c), suggesting a larger interparticle distance of aggregated DNA-Au NPs (Storhoff et al., 2000). At a high AHA concentration (e.g., 100 mg

C/L), we observed similar aggregation profiles of DNA-Au NPs with AHA present and the AHA control (without DNA-Au NPs) (Figure S5.13a). On the other hand, increasing SRHA concentration from 1 to 100 mg C/L (SRHA:Au from 0.1:1 to 10:1) only stabilized DNA-Au NPs in the presence of Ca^{2+}, which could be attributed to that more SRHA molecules adsorbed on particle surface via calcium-mediated bridging between DNA and SRHA (Lu et al., 2012; Nguyen and Chen, 2007), engendering a stronger (electro)steric repulsion (Sun et al., 2018). The intermolecular bridging of SRHA molecules was not observed, consistent with the aggregation profile of pure SRHA (Figure S5.2d) and the TEM images of aggregated SRHA-adsorbed DNA-Au NPs (Figure S5.10a-c).

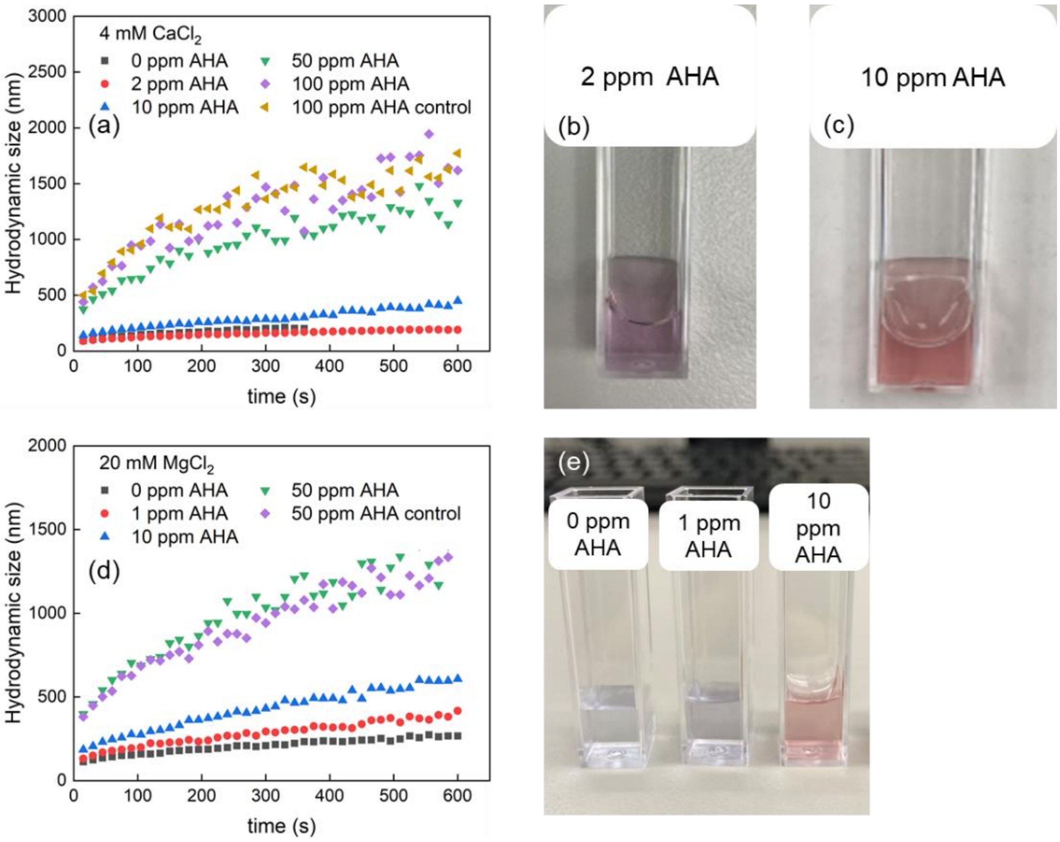

Figure 5.13 (a) Aggregation profile of DNA$_{25}$-Au (10 mg Au/L) in 4 mM CaCl$_2$ in the presence of different concentrations of AHA; AHA control refers to pure AHA molecules; (b and c) photos of DNA$_{25}$-Au suspension in the presence of 2 or 10 mg C/L AHA after aggregation study in 4 mM CaCl$_2$; (d) aggregation profile in 20 mM MgCl$_2$; (e) photos of DNA$_{25}$-Au suspension in the presence of 0, 1, or 10 mg C/L AHA after aggregation study in 20 mM MgCl$_2$.

In 4 mM $MgCl_2$, the enhanced aggregation of DNA-Au NPs with AHA present was not observed (Figure S5.12b). Increasing AHA up to 100 mg C/L (AHA:Au from 0:1 to 10:1) gradually decreased the aggregation rate to near zero due to more AHA molecules adsorbed and thus stronger (electro)steric repulsion (Sun et al., 2018). However, similar enhanced aggregation of particles and color change of the aggregate suspension with increasing AHA concentration as that in 4 mM $CaCl_2$ was observed in 20 mM $MgCl_2$ (Figure S5.12c and S5.13d-e), suggesting that Mg^{2+} could also induce the intermolecular bridging of AHA molecules, but the process is less favorable than when Ca^{2+} is present. Such discrepancy may stem from the weaker electronegativity and larger hydrated radius of Mg^{2+} compared to Ca^{2+} (Stankus et al., 2011). On the contrary, with SRHA in $MgCl_2$ electrolyte, the aggregation rate of DNA-Au NPs did not change significantly (Figure S5.12b-c), suggesting Mg^{2+} was not able to form bridges neither between DNA and SRHA nor among SRHA molecules.

Test S5.6 Early-Stage Aggregation Kinetics of DNA-Au NPs with River Water and Wastewater Effluent

Due to instrumental detection limit, the early-stage aggregation kinetics of DNA-Au NPs in the absence and presence of SRHA/AHA (10 mg C/L) in river water and wastewater effluent were performed at a particle concentration of 5 mg Au/L. The aggregation profiles are shown in Figure 5.7, a-b. In wastewater effluent, the high concentration of divalent cations (10 mM Mg^{2+} and 2.9 mM Ca^{2+}) induced the rapid aggregation of both DNA_{25}-Au and DNA_{25C}-Au. DNA_{25C}-Au were more resistant to aggregation induced by divalent cations compared to DNA_{25}-Au (Figure 5.3), therefore a slower aggregation of DNA_{25C}-Au was observed (Figure 5.7a). The presence of SRHA or AHA did not show a significant impact on the aggregation of DNA_{25}-Au NPs, which could be attributed to high ionic strength (especially rich divalent cations) of wastewater and the aggregation of particles was in the diffusion-limited regime. In river water, due to the overall low ionic strength, both DNA25-Au and DNA25C-Au NPs remained stable and no obvious effect of SRHA/AHA on colloidal stability was observed (Figure 5.7b).

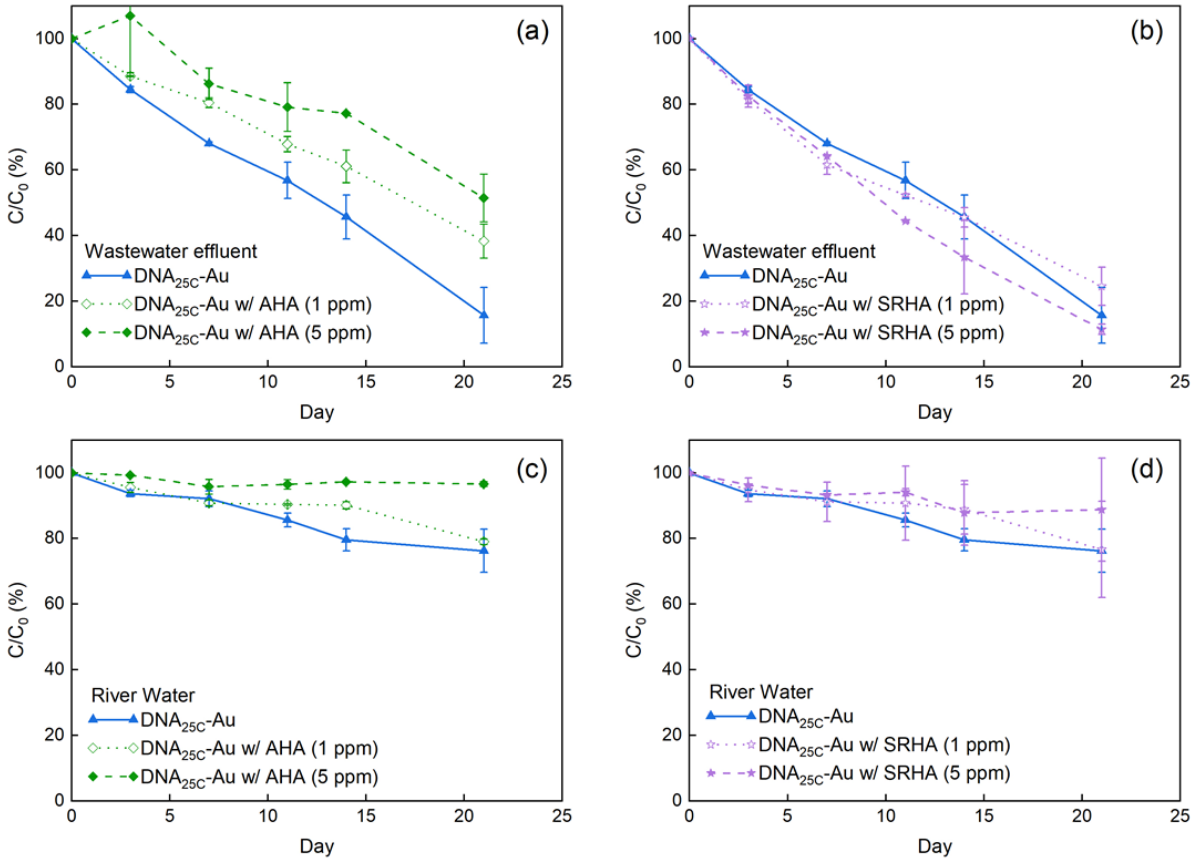

Figure S5.14 Long-term stability of DNA25C-Au (C_0 = 500 μg Au/L) in filtered (a-b) wastewater effluent and (c-d) river water with or without the dosed SRHA or AHA (C = 1 or 5 mg C/L). Error bars are standard deviation of duplicates.

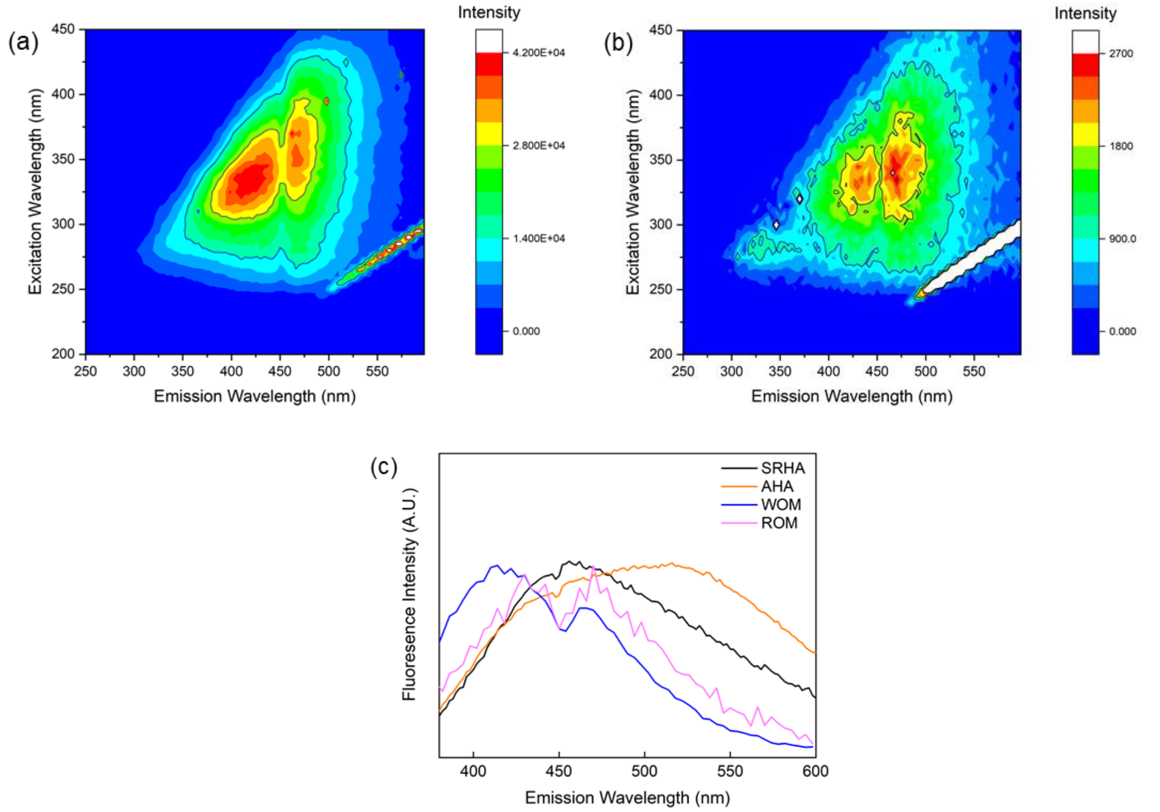

Figure S5.15 Fluorescence excitation emission matrix (EEM) of filtered (a) wastewater effluent and (b) river water; (c) emission scan of SRHA, AHA, WOM, and ROM at excitation wavelength of 330 nm

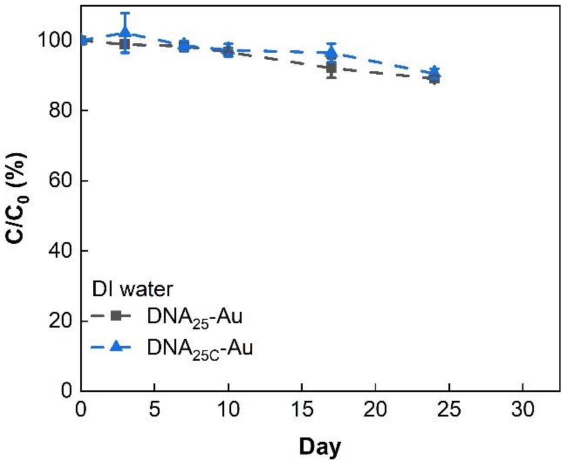

Figure S5.16 Long-term stability of DNA$_{25}$-Au and DNA$_{25C}$-Au (C_0 = 1000 µg Au/L) in DI water.

Table S5.1 Characteristics of NOM isolates*

Sample	Bulk Elemental Composition (%)					Functional Group Composition				$SUVA_{254}$
	C	H	O	N	S	Carbonyl	Carboxyl	Aromatic	Aliphatic	L/(mg·m)
AHA	60.0	4.5	34.5	1.0	-	-	15.6 ± 2.2	45.1 ± 6.3	33.4 ± 3.0	9.0 ± 0.1
SRHA III (Used in this study)	54.6	3.9	40.0	1.5	0.6	3.9	12.8	35.3	23.9	6.2 ± 0.1
SRHA II	52.6	4.3	42.0	1.2	0.5	6	15	31	29	-
SRHA I	52.6	4.4	42.5	1.2	0.6	8	19	37	21	-

*Bulk elemental compositions and Functional group composition of SRHA (I/II/III) were provided by International Humic Substances society (IHSS, http://humic-substances.org/); bulk elemental compositions of AHA were determined by Vario Micro cube elemental analyzer (Li et al., 2019); functional group composition of AHA were determined by ^{13}C nuclear magnetic resonance (NMR) (Mao et al., 2000). Specific UV absorbance at 254 nm ($SUVA_{254}$) of SRHA and AHA were calculated as the UV absorbance at 254 nm divided by the TOC concentration (mg C/L) and 1 cm quartz cell path length.

Table S5.2 Characteristics of river water and wastewater effluent used in this study

	River Water	Wastewater Effluent
pH	7.3	7.8
TOC (mg C/L)	2.3	7.0
Conductivity* (µS/cm)	43.5	13360
Cation Concentration** (mM)		
Na^+	0.18	103.35
K^+	0.04	2.42
Mg^{2+}	0.02	9.95
Ca^{2+}	0.08	2.91

*The high conductivity and concentration of cations in wastewater effluent is due to the use of seawater for toilet flushing in Hong Kong.

**Only common cations are measured.

References for Appendix C

Chen, K.L. and Elimelech, M. 2007. Influence of humic acid on the aggregation kinetics of fullerene (C60) nanoparticles in monovalent and divalent electrolyte solutions. J. Colloid Interface Sci. 309(1), 126-134.

Li, Q., Xie, L., Jiang, Y., Fortner, J.D., Yu, K., Liao, P. and Liu, C. 2019. Formation and stability of NOM-Mn(III) colloids in aquatic environments. Water Res. 149, 190-201.

Liu, B. and Liu, J. 2017. Methods for preparing DNA-functionalized gold nanoparticles, a key reagent of bioanalytical chemistry. Anal. Methods 9(18), 2633-2643.

Liu, X., Wazne, M., Chou, T., Xiao, R. and Xu, S. 2011. Influence of Ca^{2+} and Suwannee River Humic Acid on aggregation of silicon nanoparticles in aqueous media. Water Res. 45(1), 105-112.

Liu, X., Wazne, M., Han, Y., Christodoulatos, C. and Jasinkiewicz, K.L. 2010. Effects of natural organic matter on aggregation kinetics of boron nanoparticles in monovalent and divalent electrolytes. J. Colloid Interface Sci. 348(1), 101-107.

Lu, N., Mylon, S.E., Kong, R., Bhargava, R., Zilles, J.L. and Nguyen, T.H. 2012. Interactions between dissolved natural organic matter and adsorbed DNA and their effect on natural transformation of Azotobacter vinelandii. Sci. Total Environ. 426, 430-435.

Mao, J.D., Hu, W.G., Schmidt-Rohr, K., Davies, G., Ghabbour, E.A. and Xing, B. 2000. Quantitative characterization of humic substances by solid-state carbon-13 nuclear magnetic resonance. Soil Sci. Soc. Am. J. 64(3), 873-884.

Nguyen, T.H. and Chen, K.L. 2007. Role of divalent cations in plasmid DNA adsorption to natural organic matter-coated silica surface. Environ. Sci. Technol. 41(15), 5370-5375.

Peng, B., Liu, Z. and Jiang, Y. 2022. Aggregation of DNA-grafted nanoparticles in water: The critical role of sequence-dependent conformation of DNA coating. J. Phys. Chem. B 126(4), 847-857.

Schwyzer, I., Kaegi, R., Sigg, L. and Nowack, B. 2013. Colloidal stability of suspended and agglomerate structures of settled carbon nanotubes in different aqueous matrices. Water Res. 47(12), 3910-3920.

Sharpless, C.M. and McGown, L.B. 1999. Effects of aluminum-induced aggregation on the fluorescence of humic substances. Environ. Sci. Technol. 33(18), 3264-3270.

Stankus, D.P., Lohse, S.E., Hutchison, J.E. and Nason, J.A. 2011. Interactions between natural organic matter and gold nanoparticles stabilized with different organic capping agents. Environ. Sci. Technol. 45(8), 3238-3244.

Storhoff, J.J., Lazarides, A.A., Mucic, R.C., Mirkin, C.A., Letsinger, R.L. and Schatz, G.C. 2000. What controls the optical properties of DNA-linked gold nanoparticle assemblies? J. Am. Chem. Soc. 122(19), 4640-4650.

Sun, B., Zhang, Y., Chen, W., Wang, K. and Zhu, L. 2018. Concentration dependent effects of bovine serum albumin on graphene oxide colloidal stability in aquatic environment. Environ. Sci. Technol. 52(13), 7212-7219.

Chapter 6 Conclusions, Impacts, and Future Directions

6.1 Conclusions

This thesis has considerably improved our fundamental understanding of the aggregation behavior of engineered nanomaterials in aquatic environments. The major conclusions are as follows:

1) The seemingly contradictory property-aggregation relationships observed in previous literature are resolved. The critical coagulation concentration (CCC) of nanomaterials increases with decreasing nanomaterial size, increasing surface charge, and increasing surface oxidation degree (for carbon nanomaterials).
2) The inconsistencies between experimental observations and theoretical predictions based on the DLVO theory in previous literature are rationalized. The negative relationship between CCC and material size is qualitatively consistent with the theoretical prediction, but with a much smaller threshold size (*ca.* 200 vs. 2000 nm). Beyond the threshold size, material zeta potential can be correlated to CCC as predicted by the DLVO theory ($CCC/\lambda \propto \tanh^4\left(\frac{a\psi_0}{4}\right)$).
3) Using the Smoluchowski Equation to calculate the zeta potential of nanomaterials only remains valid for nanomaterials with moderate/low surface charge, e.g., graphene oxide with a C/O ratio larger than *ca.* 3.0.
4) Engineered ssDNA surface coating improves the colloidal stability of the coated nanomaterials mainly through the excluded volume repulsion, which is largely affected by the ssDNA coating layer thickness. Thicker DNA coating results in more stable coated nanomaterials.
5) DNA sequence has a major impact on the thickness of DNA coating. Among the nucleobases, guanine has the highest affinity towards cations, and their preferential interactions influence the ion distribution along the ssDNA strands. Guanine located at

the end closer to the bulk solution may prevent the penetration and binding of cations to the other end near the surface, therefore leading to a thicker DNA coating and more aggregation-resistant coated nanomaterials.

6) ssDNA preferentially interacts with highly aromatic natural organic matter (NOM), and such interactions considerably alter the aggregation behavior of engineered DNA-coated nanoparticles. Interaction(s) between NOM and ssDNA occur via π-π interactions between the aromatic regions of NOM and the exposed nucleobases of ssDNA.
7) The high aromaticity of NOM and divalent cation bridging collectively lead to the complete shielding of ssDNA coating by NOM, rendering the stability of particles to be mainly dependent on the properties of adsorbed NOM. When the ssDNA coating is partially shielded by adsorbed NOM, the particle stability is largely determined by the properties of the original ssDNA coating.

6.2 Impacts

Aggregation of nanomaterials not only affects their functionality in applications, but also their fate and behavior in the environment (Hotze et al., 2010; Lowry et al., 2012; Petosa et al., 2010; Zhang, 2014). The structure-activity type of knowledge obtained in this thesis on the aggregation behavior of nanomaterials will be useful for their better design in applications and an improved understanding of their environmental fate and behavior. For instances, the location and number of the guanine base could be considered in the sequence design of the DNA coating to produce more stable DNA-coated nanomaterials, since many applications of DNA-coated nanomaterials are performed in cell culture media or other challenging buffers (e.g., the DNA-based assembly of gold nanorods for RNA detection was performed in solution with ionic strength as high as 14 mM $MgCl_2$ and 500 mM NaCl (Funck et al., 2018)); the preferential interactions of DNA with the aromatic regions of NOM could serve as an analog to DNA-protein interactions to predict the behavior of DNA-coated nanomaterials in biological fluids;

the extent of shielding of nanomaterials could be considered in modeling their fate and behavior in the environment. Also, in this thesis, the successful use of a meta-analytic approach to synthesize previous data to determine the property-aggregation relationships of nanomaterials demonstrates that this approach is suitable for discovering and defining (more) relationships between the properties of nanomaterials and their behaviors (e.g., chemical activity). As more analytical data are being generated and to be included in the future (e.g., more types of nanomaterials and physicochemical properties), more advanced meta-analytic techniques, such as machine learning, could be used to understand the interplay of multiple properties on the behavior of nanomaterials, thereby facilitating the better design of nanomaterials.

Furthermore, knowledge obtained from this thesis could be useful for optimizing the performance of DNA-based nanomaterials for environmental applications, such as DNA tracer and aptasensor. For example, the presence of NOM has been shown to degrade the performance of aptasensor (Vogiazi et al., 2021). Introducing aromatic NOM to the SELEX (Sequential Evolution of Ligands by Exponential Enrichment) process of DNA aptamer could generate an aptamer sequence that is more resistant to the interferences from (aromatic) NOM, thereby improving the selectivity and sensitivity of aptasensor. On the other hand, a protective layer could be applied to naked DNA tracers if they are to be applied in fields with aromatic NOM present, since the adsorption of DNA tracers to NOM can lead to low recovery and unprecise detection (Liao et al., 2018; Pang et al., 2020).

6.3 Future Directions

While this study advances our knowledge of the dominant factors influencing the aggregation behavior of engineered nanomaterials, there are several questions that should be explored in the future.

1) A threshold size of *ca.* 200 nm is observed for carbon nanomaterials, below which the effect of size on nanomaterial stability (i.e., CCC) becomes prominent. A smaller

threshold size (*ca.* 50 nm) for silver nanomaterials is also reported (Afshinnia et al., 2017). The deviation of experimental observation from the prediction of the DLVO theory requires more (theoretical) efforts to uncover the cause(s).

2) An improved characterization of the surface charge (e.g., zeta potential or other parameter(s) serving the same purpose) of highly charged (carbon) nanomaterials will be needed to validate the correlations between surface charge and nanomaterial stability as predicted by the DLVO theory.
3) Meta-analysis has been proven to be a very promising tool to identify patterns and make predictions by synthesizing pre-existed data. This approach could be used to include more types of nanomaterials and/or properties of nanomaterials for a broader analysis on the property-aggregation relationships of nanomaterials.
4) The configuration of adsorbed NOM on engineered ssDNA coating impacts the steric repulsion and subsequently the colloidal stability of the coated nanomaterials, thereby requiring further investigation, preferably quantitatively and at a molecular-level. To reveal such information, experiments can be combined with computational approaches (e.g., molecular dynamics simulation).
5) Specific interaction(s), especially divalent cation bridging, are important in the interactions between NOM and ssDNA and among themselves. The density (Lu et al., 2012) and position (Labille et al., 2005) of carboxyl groups likely play a role, as well as the species and concentration of divalent cations revealed in this thesis. However, the trigger mechanism of the divalent cation bridging has yet to be systematically investigated and requires further investigation.
6) Additional studies are needed to describe the kinetics of NOM adsorption onto ssDNA coating. Results in this thesis show that highly aromatic NOM completely shields the ssDNA coating at equilibrium, yet the kinetics of this process are unexplored. Other

transformations of the ssDNA coating may occur faster in the realistic environment and pose a more significant impact on the aggregation behavior of engineered ssDNA-coated nanomaterials.

7) The aggregation behavior of engineered DNA-coated nanomaterial should be further assessed in more realistic environmental scenarios, e.g., in environmentally relevant concentrations. The highest NOM-nanomaterial ratio (10:1) used in this thesis is still at least one magnitude lower than the realistic scenarios, in which the NOM is in mg/L and the nanomaterial is expected in ng/L.
8) In addition to interaction(s) with NOM, other transformations of the engineered DNA coating need to be probed to comprehensively understand the colloidal stability of the coated nanomaterials in typical aquatic environment. These transformations could include interactions with organisms (biodegradation) or biological macromolecules (e.g., protein), redox reactions, photochemical reactions, etc. (Lead et al., 2018; Lowry et al., 2012). Under these challenging conditions, the engineered DNA coating might experience conformational change, be displaced by other adsorbing species, or be degraded.
9) The preferential interactions of ssDNA with highly aromatic NOM might provide a potential answer to the reported conflicting effects of NOM on the performance of engineered DNA-based sensors (Akki et al., 2015; Park et al., 2022; Vogiazi et al., 2021). However, the hypothesis has yet to be validated by experiment. Future studies could systematically investigate the effect of NOM with varied properties on the performance of engineered ssDNA-based sensors (and other practical aquatic applications).

References

Afshinnia, K., Sikder, M., Cai, B. and Baalousha, M. 2017. Effect of nanomaterial and media physicochemical properties on ag nm aggregation kinetics. J. Colloid Interface Sci. 487, 192-200.

Akki, S.U., Werth, C.J. and Silverman, S.K. 2015. Selective aptamers for detection of estradiol and ethynylestradiol in natural waters. Environ. Sci. Technol. 49(16), 9905-9913.

Funck, T., Nicoli, F., Kuzyk, A. and Liedl, T. 2018. Sensing picomolar concentrations of RNA using switchable plasmonic chirality. Angew. Chem. Int. Ed. 57(41), 13495-13498.

Hotze, E.M., Phenrat, T. and Lowry, G.V. 2010. Nanoparticle aggregation: Challenges to understanding transport and reactivity in the environment. J. Environ. Qual. 39(6), 1909-1924.

Labille, J., Thomas, F., Milas, M. and Vanhaverbeke, C. 2005. Flocculation of colloidal clay by bacterial polysaccharides: Effect of macromolecule charge and structure. J. Colloid Interface Sci. 284(1), 149-156.

Lead, J.R., Batley, G.E., Alvarez, P.J.J., Croteau, M.N., Handy, R.D., McLaughlin, M.J., Judy, J.D. and Schirmer, K. 2018. Nanomaterials in the environment: Behavior, fate, bioavailability, and effects—an updated review. Environ. Toxicol. Chem. 37(8), 2029-2063.

Liao, R., Yang, P., Wu, W., Luo, D. and Yang, D. 2018. A DNA tracer system for hydrological environment investigations. Environ. Sci. Technol. 52(4), 1695-1703.

Lowry, G.V., Gregory, K.B., Apte, S.C. and Lead, J.R. 2012. Transformations of nanomaterials in the environment. Environ. Sci. Technol. 46(13), 6893-6899.

Lu, N., Mylon, S.E., Kong, R., Bhargava, R., Zilles, J.L. and Nguyen, T.H. 2012. Interactions between dissolved natural organic matter and adsorbed DNA and their effect on natural transformation of azotobacter vinelandii. Sci. Total Environ. 426, 430-435.

Pang, L., Abeysekera, G., Hanning, K., Premaratne, A., Robson, B., Abraham, P., Sutton, R., Hanson, C., Hadfield, J., Heiligenthal, L., Stone, D., McBeth, K. and Billington, C. 2020. Water tracking in surface water, groundwater and soils using free and alginate-chitosan encapsulated synthetic DNA tracers. Water Res. 184, 116192.

Park, J., Yang, K.A., Choi, Y. and Choe, J.K. 2022. Novel ssDNA aptamer-based fluorescence sensor for perfluorooctanoic acid detection in water. Environ. Int. 158, 107000.

Petosa, A.R., Jaisi, D.P., Quevedo, I.R., Elimelech, M. and Tufenkji, N. 2010. Aggregation and deposition of engineered nanomaterials in aquatic environments: Role of physicochemical interactions. Environ. Sci. Technol. 44(17), 6532-6549.

Vogiazi, V., de la Cruz, A.A., Varughese, E.A., Heineman, W.R., White, R.J. and Dionysiou, D.D. 2021. Sensitive electrochemical detection of microcystin-lr in water samples via target-induced displacement of aptamer associated $[Ru(NH_3)_6]^{3+}$. ACS ES&T Eng. 1(11), 1597-1605.

Zhang, W. (2014). Nanoparticle aggregation: principles and modeling. In: Capco, D., Chen, Y. (eds) Nanomaterial: Advances in experimental medicine and biology, vol 811. Springer, Dordrecht.